Università di Genova

Doctoral Course on Neurosciences

Curriculum: Clinical and Experimental Neurosciences

DINOGMI - University of Genoa

PhD thesis

Molecular and functional study of genes associated with epilepsy and movement disorders

Candidate:

Morinelli Lisastella

Supervisor:

Prof. Corradi Anna Margherita

Academic year 2024/2025 - XXXVIII cycle

INDEX

Abstract

Paroxysmal neurological disorders, including early-onset epilepsies and movement disorders, arise from alterations in neuronal excitability and network stability. The identification of disease-associated genes has provided crucial insights into the molecular mechanisms underlying these conditions. A powerful approach to investigate such mechanisms is the functional characterization of pathogenic variants identified in patients. In this PhD project, I studied disease-causing variants in ***SCN2A***, ***PRRT2***, and ***TMEM151A***, three genes implicated in epilepsy and paroxysmal movement disorders, with the aim of elucidating their pathogenic mechanisms, refining genotype–phenotype correlations, and gaining insight into their physiological roles in neuronal function.

Pathogenic variants in ***SCN2A***, encoding the voltage-gated sodium channel NaV1.2, are associated with a broad spectrum of neurodevelopmental disorders. I report on the clinical and functional characterization of two de novo *SCN2A* missense variants, c.4976C>T (p.A1659V) and c.710T>A (p.I237N), identified in patients with neonatal-onset, drug-resistant epilepsy and severe neurodevelopmental impairment, characterized by somatic mosaicism. Despite clinical features suggestive of a gain-of-function mechanism and in silico predictions supporting pathogenicity, electrophysiological analyses revealed a marked reduction in sodium current density for both variants and altered gating properties for the A1659V variant, consistent with an overall loss-of-function effect. These findings highlight the complexity of *SCN2A* genotype–phenotype relationships and have important implications for precision treatment strategies.

PRRT2 is a neuronal protein that regulates intrinsic excitability and synaptic function through modulation of voltage-gated sodium channels. Pathogenic variants in *PRRT2* are a major cause of Benign Familial Infantile Seizures (BFIS) and Paroxysmal Kinesigenic Dyskinesia (PKD), two paroxysmal disorders that frequently co-occur or segregate within the same families. Focusing on missense variants within its transmembrane domain, we demonstrated that PRRT2 variants can differentially affect NaV1.2 channel regulation, resulting in either loss- or gain-of-function phenotypes at the channel level, despite similar clinical presentations. In silico docking analyses further identified putative interaction interfaces between PRRT2 and NaV1.2, guiding targeted mutagenesis to functionally validate residues involved in channel modulation. These data underscore the central role of PRRT2–NaV interactions in disease pathogenesis and suggest that paroxysmal manifestations arise when PRRT2 function deviates from its physiological range.

TMEM151A, recently identified as a causative gene for PKD, remains poorly characterized. Notably, *TMEM151A*-associated PKD overlaps with the same paroxysmal disorder classically caused by *PRRT2* variants, indicating a shared disease phenotype and potentially a shared disease mechanism. Using molecular dynamics simulations, immunocytochemistry, and electron microscopy, we defined its membrane topology, revealing a protein predominantly oriented toward the cytosol with a structured transmembrane domain. Functional analyses showed that pathogenic *TMEM151A* variants impair protein expression and subcellular localization, supporting a loss-of-function mechanism. TMEM151A overexpression promoted neurite outgrowth and dendritic arborization in primary neurons, whereas pathogenic variants impaired neuronal maturation. Moreover, analysis of a human *TMEM151A* heterozygous knockout iNeuron model revealed impaired network formation and reduced structural complexity, confirming a key role for TMEM151A in neuronal development and excitability.

Finally, electrophysiological studies demonstrated a selective modulation of NaV1.1 channels by TMEM151A.

Overall, this work provides converging molecular, cellular, and functional evidence that alterations in sodium channel regulation and neuronal network maturation represent shared pathogenic mechanisms linking epilepsy and paroxysmal movement disorders. By integrating the study of *SCN2A*, *PRRT2*, and *TMEM151A*, this thesis contributes to a deeper understanding of disease mechanisms and highlights potential targets for genotype-informed therapeutic strategies.

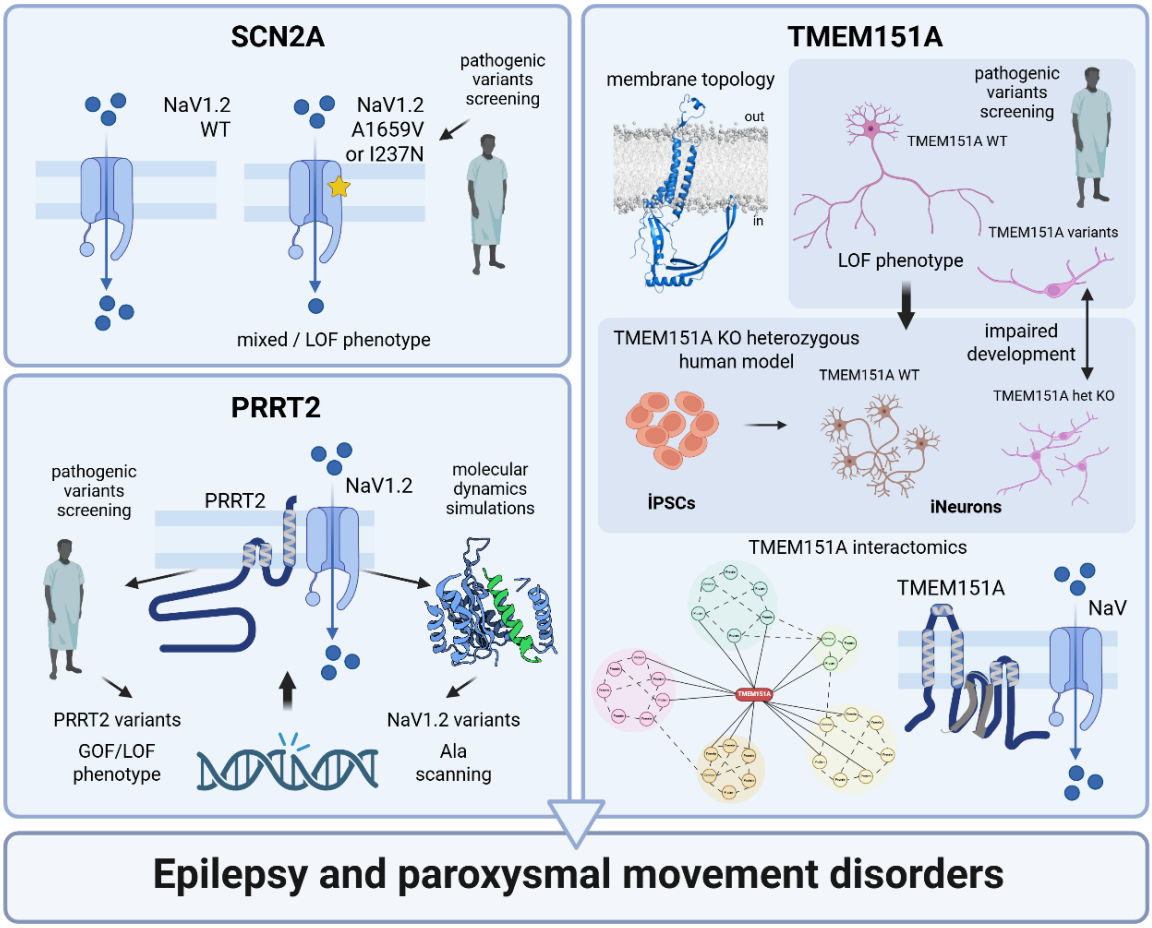

Graphical abstract. Created with BioRender.com

Introduction

Epilepsy

Epilepsy is a chronic neurological disorder characterized by recurrent, unprovoked seizures arising from abnormal, excessive, or synchronous neuronal activity within the brain. It affects approximately 50 million people worldwide. Epidemiological studies indicate that epilepsy comprises a broad spectrum of syndromes rather than a single disease entity, with clinical presentations that vary widely in terms of seizure type, age at onset, comorbidities, severity, and treatment response. [1] Epileptic syndromes are divided into focal (when seizures are generated in a unilateral local network) and generalized ones (when seizures are generated in bilateral networks).

The etiologies of epilepsy are diverse and can be categorized into structural, metabolic, infectious, immune-mediated, and genetic causes. Structural causes include cortical malformations, tumors, traumatic injuries, stroke, and perinatal brain insults that disrupt neuronal networks and lead to chronic hyperexcitability. Metabolic disorders - including inborn errors of metabolism, disorders of energy production, or transporter deficiencies - may also result in epileptic activity due to impaired neuronal homeostasis. Immune-mediated epilepsies, often associated with neural-specific autoantibodies, highlight the contribution of neuroinflammation to seizure generation. Infectious etiologies remain relevant worldwide, especially in low-resource settings, where neurotropic viral or parasitic infections can cause both acute symptomatic seizures and chronic epileptic sequelae. [2]

Genetic Epilepsies: A Heterogeneous Landscape

Over the past decade, advances in genomic sequencing technologies have significantly reshaped our understanding of epilepsy. Many epilepsies previously labeled “idiopathic” have been shown to involve underlying genetic factors, including both monogenic and complex polygenic risk. In fact, up to 40% of rare epilepsies are now estimated to have an identifiable genetic cause. [3] These genetic forms often manifest in early childhood, may be associated with neurodevelopmental delay or intellectual disability, and frequently overlap with other neurological phenotypes such as movement disorders or migraine.

Molecular mechanisms underlying genetic epilepsies include ion-channel dysfunction, impairments in synaptic transmission, abnormalities in neuronal development, and altered network organization. Ion-channel disorders (“channelopathies”) represent one of the most extensively studied categories.

Beyond channelopathies, a growing number of genes involved in synaptic vesicle regulation, presynaptic release, receptor trafficking and intracellular signaling have been associated with epileptic phenotypes. [3], [4], [5] These “synaptopathies” highlight the importance of precise control of neurotransmitter release and synaptic plasticity in maintaining normal network function.

Additionally, many genes implicated in neuronal migration and cortical development can cause malformations or subtle architectural abnormalities that predispose to epilepsy. Abnormal neuronal positioning, altered dendritic morphology, or impaired circuit formation may result in persistent network instability, thereby lowering the seizure threshold.

Although specific genes play important roles and will be discussed in subsequent chapters, the broader picture is that genetic epilepsies represent a highly heterogeneous group. Their phenotypic manifestations reflect not only the pathogenic variant itself but also

developmental stage, brain region–specific expression patterns, genetic background, and environmental modifiers.

In summary, epilepsy arises from a wide array of biological processes that converge on the final pathway of neuronal hyperexcitability. Identifying the underlying cause in each patient is essential for accurate diagnosis, prognosis, and optimal treatment, particularly as precision medicine becomes increasingly feasible. Next-generation sequencing, functional studies, and integrative neurobiological approaches continue to expand our understanding of the genetic landscape of epilepsy and its mechanistic diversity.

Channelopathies in Epilepsy

A significant proportion of genetic epilepsies arise from channelopathies, caused by dysfunction in ion channels or associated regulatory proteins. Voltage-gated sodium (NaV), potassium, calcium, and chloride channels, as well as ligand-gated channels (GABA and glutamate receptors), are the most commonly implicated. [6] These variants can alter action potential generation, synaptic transmission, or inhibitory–excitatory balance, thereby predisposing to seizures. Channelopathies frequently present in infancy or childhood with paroxysmal or episodic symptoms, reflecting transient disruptions of neuronal excitability. Here we will focus on NaV channels, in particular on NaV1.2 related epilepsies, that will be discussed in the following paragraphs.

Voltage-gated Sodium channels (NaV)

Sodium channels are transmembrane proteins, fundamental for the generation of the action potential at the level of the neural membrane. Voltage-gated Sodium channels can be present in 3 stages: closed, open, refractory for inactivation (Fig. 1A).

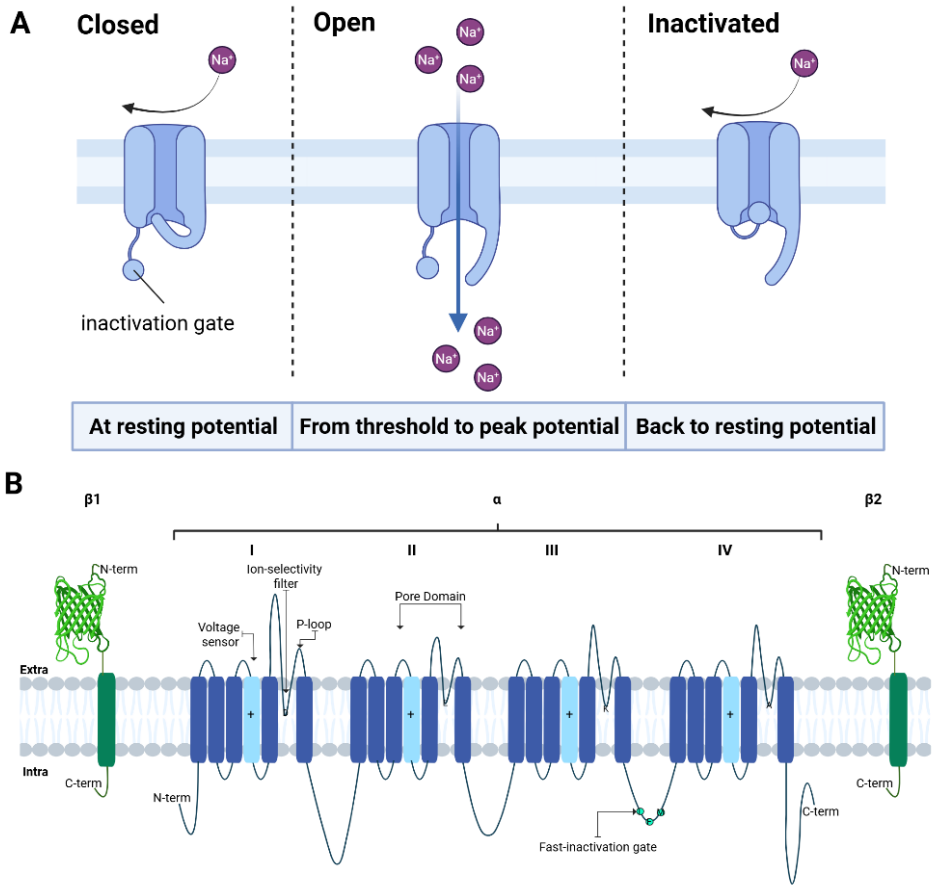

Figure 1: Schematic representation of NaV channels cycle and structure. A: Schematic representation of NaV channels closed – open – inactivated states. B: Schematic representation of NaV channels α-subunit and β accessory subunits at the membrane level. Created with BioRender.com

A positively charged α-helix works as a voltage sensor: the membrane depolarization determines a charge repulsion and the movement of the molecular sensor; this conformational change allows the channel opening, so the Na^+ passage. After 1 msec of the opening phase, the channel enters the refractory state, so that even if the stimulus persists, the ion passage cannot occur, due to the inactivation gate, a stretch of amino acids creating a steric block. When the membrane repolarization occurs, the channel goes back to the initial state and becomes ready for a new cycle. Nine NaV subtypes exist in the different human tissues; they are formed by an α-subunit constituting the pore, characterized by four transmembrane domains (DI – DIV), each one formed by six transmembrane helices (S1-S6), and by one or more β accessory subunits, which instead are involved in the plasma membrane expression (Fig. 1B). In each transmembrane domain of the α-subunit, the fourth helix is the segment responsible for the voltage-sensitive sensor for activation. The fifth and sixth transmembrane helices, and the loops connecting them in each domain, are implicated in the formation of the selectivity filter, for selective passage of Na^+ ions [7]. Site-specific mutagenesis studies have shown that four residues are responsible for sodium selectivity: aspartate in DI, glutamic acid in DII, lysine in DIII, and alanine in DIV, also known as DEKA locus [8]. Aspartate and glutamic acid provide a high field strength site, which facilitates the partial dehydration of sodium ions, arriving to the channel pore covered by a hydration shell. The intracellular loop connecting the third and the fourth domains is responsible for the inactivation gate, with a IFM motif (Isoleucine-Phenylalanine-Methionine) which is involved in the allosteric inhibition of the channel [9], [10]. When these channels open, they determine the membrane depolarization needed to obtain the action potential, the auto regenerative electric event fundamental for the neuronal stimuli conduction.

The subtypes expressed in the nervous system are the NaV 1.1 (encoded by *SCN1A*), NaV 1.2 (encoded by *SCN2A*) and NaV 1.6 (encoded by *SCN8A*), which are localized at high density at the level of the axon initial segment (AIS), where the action potential originates [11], [12]. Considering NaV pathogenic variants, there is a considerable overlap among clinical conditions caused by variants of *SCN1A*, *SCN2A* and *SCN8A*. The differences in molecular mechanisms reflect divergence among the channels in function and neuronal distribution, considering that NaV1.2 and NaV1.6 are expressed in excitatory neurons, while NaV1.1 are found in inhibitory neurons.

NaV1.2

NaV1.2, as previously mentioned, is expressed in excitatory neurons and has a critical role in the initiation and propagation of action potentials (APs). During fetal development, NaV1.2 is the sole sodium channel expressed at the axon initial segment (AIS), where APs originate. Consequently, in this stage of life, NaV1.2 is crucial for APs generation and propagation [13], [14]. In later stages of development, NaV1.2 is replaced by the orthologous channel NaV1.6, which generates APs starting from a lower voltage threshold and is expressed at the level of the nodes of Ranvier and in the distal portion of the AIS. At this point, NaV1.2 carries on the role of maintaining APs towards the soma of the neuron [12], [15]. However, during postnatal development NaV1.2 is also expressed in the somato-dendritic neuronal compartment where it takes part in regulating synapses maturation and function, particularly in the prefrontal cortex [16].

SCN2A-Related Epilepsies

Variants in *SCN2A* may determine changes in the biophysical and electrophysiological properties of the encoded channel and have been recognized to cause a spectrum of neurodevelopmental disorders (NDs) encompassing different epileptic syndromes.

From first discovery in the early 2000's, genotype-phenotype correlations have been proposed for *SCN2A*-related disorders and a rough dichotomy has been created based on the biophysical properties of the mutated channel. Gain-of-function (GOF) variants typically enhance channel activity and seem more likely associated to early-infantile onset seizures, both self-limited or featuring later encephalopathy. Conversely, loss-of-function (LOF) variants reduce channel function and have shown to be associated to later-onset epilepsy [17], or non-epileptic phenotypes such as ASD/ID [18].

Based on disease severity, anticipated clinical outcome, and underlying functional mechanisms, *SCN2A*-related phenotypes can be grouped into the following clinical categories [19], [20], [21], [22], [23]:

- self-limited conditions, including benign familial neonatal–infantile seizures / benign infantile epilepsy (BFNIS/BFIE), characterized by neonatal or early-infantile seizure onset, spontaneous remission, absence of long-term neurodevelopmental impairment, and most commonly associated with GOF missense variants.
- Early-onset epileptic encephalopathies, encompassing Ohtahara syndrome, epilepsy of infancy with migrating focal seizures, West syndrome, and Lennox–Gastaut syndrome (LGS), in which seizures represent a predominant clinical feature and are invariably associated with impaired neurodevelopmental trajectories; these phenotypes are more frequently linked to GOF variants, although LOF variants have also been reported. [17], [18]
- Neurodevelopmental disorders with or without epilepsy, including ASD and/or ID with seizures that may be absent or occur later in life and are not constitutive features of the phenotype; these presentations are most often associated with LOF variants, particularly those affecting critical functional domains such as the ion-selectivity filter.
- Mixed epilepsy–movement disorder phenotypes, such as neonatal seizures with later-onset episodic ataxia or paroxysmal motor manifestations, in which GOF variants give rise to combined epileptic and paroxysmal movement features.

Phenotypic variability reflects the functional impact of the variant, its location within the channel, and the developmental context in which NaV1.2 contributes to neuronal excitability and synaptic integration. *SCN2A* variants exemplify the intersection of channelopathies, neurodevelopmental disorders, and epilepsy. [20]

Recently, new variants in *SCN2A* have been identified as causative of epilepsy in a mosaic state. Mosaicism refers to a condition in which an individual has two or more populations of cells with different genetic backgrounds, all originating from a single fertilized egg. This means that a variant occurred at some point after fertilization, during cell division, resulting in a percentage of cells carrying the genetic alteration and the remaining not. The different ratios of mutant and wild-type cells could have a different impact on the brain functionality resulting in phenotypes of variable intensity.

Paroxysmal Movement Disorders

Paroxysmal movement disorders (PMDs) are a group of rare neurological conditions characterized by sudden, transient, and recurrent episodes of involuntary movements. These

episodes can include dystonia, chorea, athetosis, ballism, or combinations thereof, and typically occur in otherwise neurologically normal individuals between attacks. PMDs are distinct from continuous movement disorders such as primary dystonia or Huntington's disease because of their episodic nature, short duration, and often precise triggers. [24]

PMDs can present across a wide age range, from childhood to adulthood, and may significantly impact quality of life depending on frequency, duration, and severity of attacks. The disorders are frequently underdiagnosed or misdiagnosed, partly due to their episodic nature and overlapping features with epilepsy, functional movement disorders, or other paroxysmal conditions. [25]

Classification and Subtypes

PMDs are broadly classified based on precipitating factors [26], [27]:

1. Paroxysmal Kinesigenic Dyskinesia (PKD): Attacks triggered by sudden voluntary movement or startle. It often has a genetic basis (e.g., *PRRT2*, *TMEM151A*). [24], [25], [28]
2. Paroxysmal Non-Kinesigenic Dyskinesia (PNKD): Attacks not precipitated by movement, but often by fatigue, stress, or alcohol intake. Episodes are usually longer (minutes to hours) compared with PKD.
3. Paroxysmal Exercise-Induced Dyskinesia (PED): Triggered by prolonged exercise or repetitive activity. Duration of episodes can range from several minutes to hours.
4. Secondary PMDs: Resulting from metabolic, structural, vascular, or neurodegenerative conditions. Identification of secondary causes is crucial to guide management.

Clinical Features

Despite variability across subtypes, PMDs share some common clinical characteristics:

- Sudden onset and brevity
- Preserved consciousness: Unlike epileptic seizures, awareness is generally intact.
- Stereotyped movements: Individual attacks are often similar in phenomenology within the same patient.
- Normal interictal neurological examination: Most patients exhibit no neurological deficits between episodes.
- Trigger specificity: Movement, startle, fatigue, or stress can precipitate attacks depending on the subtype.

Pathophysiologically, PMDs are considered disorders of neuronal excitability and network modulation. The episodic nature is thought to reflect transient network destabilization, often triggered by specific external or internal stimuli. [27], [28]

Genetics of Paroxysmal Movement Disorders

While epilepsy and movement disorders have historically been classified as distinct clinical entities, genetic and molecular evidence increasingly demonstrates substantial overlap between these conditions. [5]

Multiple genes linked to episodic movement disorders are involved in synaptic transmission, ion-channel function, or neuronal excitability, suggesting convergence onto pathways also relevant to epilepsy. For example, some channelopathies initially identified in epileptic syndromes have since been associated with paroxysmal dyskinesias, and vice versa. Likewise, variants in presynaptic proteins can lead to both epileptic seizures and movement paroxysms, depending on how neuronal circuits are affected. Subtle changes in circuit architecture, excitability or plasticity may lower the threshold for pathological activity bursts in motor or cortical networks leading to both epilepsy and movement disorders. Moreover, the same variant may have different phenotypic effects depending on when (and where) the affected protein is required during brain maturation resulting.

Genes specifically associated with paroxysmal movement disorders (including *PRRT2* and *TMEM151A*) will be discussed in detail in later chapters. [29]

Paroxysmal Kinesigenic Dyskinesia (PKD): Clinical Features and Pathophysiology

What is PKD

Paroxysmal Kinesigenic Dyskinesia (PKD) is the most common form among the paroxysmal dyskinesias. As previously mentioned, in PKD, attacks are typically induced by sudden voluntary movements, such as standing up, initiating gait, turning, or performing abrupt motor actions. In some patients, other triggers - including startle, psychological stress, or hyperventilation, may also provoke attacks. [28], [30]

PKD usually presents in childhood or adolescence, most often during the first or second decade of life. The highly episodic nature of the disorder - combined with otherwise normal motor function between attacks - and the very short duration of episodes (usually seconds to less than one minute) distinguish PKD from other movement disorders with persistent or continuous manifestations. [31]

Clinical and Phenotypic Features

During PKD attacks, involuntary movements may manifest as dystonia (sustained muscle contractions), chorea or choreoathetosis (rapid or writhing movements), ballism (violent flinging movements), or mixed patterns of these hyperkinetic features. [30] The limbs are most frequently involved, though trunk, cervical, or facial muscles can also be affected. Importantly, consciousness remains preserved throughout the episodes; patients maintain full awareness. [31]

Between attacks, neurological examination is generally normal, and brain MRI or CT imaging, as well as electroencephalography (EEG), typically show no abnormalities. PKD is primarily a clinical diagnosis, following the above mentioned key features, but because interictal evaluations are usually unremarkable, PKD is frequently misdiagnosed - often as a functional/psychogenic movement disorder. [31]

Attack frequency and severity vary considerably among individuals. Some patients may experience multiple daily episodes, whereas others have infrequent or mild attacks. Over time, especially with increasing age, many individuals show a spontaneous reduction in the frequency or intensity of episodes. [30] A positive family history is common in primary (hereditary) PKD, consistent with a genetic etiology, although sporadic cases are also well documented. [28], [30]

Pathophysiology and Genetic Background

Although the precise pathophysiological mechanisms underlying PKD are not yet fully clarified, the disorder is widely considered to reflect a channelopathy, a synaptopathy, or a combination of both. [28] This hypothesis is supported by two main lines of evidence: the marked therapeutic response to ion-channel–blocking antiepileptic drugs and the accumulating genetic findings linking PKD to proteins involved in synaptic and neuronal excitability. [28]

Genetic studies have identified several genes associated with PKD. Historically, *PRRT2* was the first and remains the most frequently implicated gene. However, *PRRT2* variants are not found in all patients, indicating genetic heterogeneity. [30] More recently, additional candidate genes - including *TMEM151A* and, in some *PRRT2*-negative individuals, variants in ion-channel–related genes such as *KCNA1* - have been reported.

From a physiological standpoint, neurophysiological studies in PKD patients have demonstrated reduced short-interval intracortical inhibition (SICI), decreased transcallosal inhibition, and diminished spinal reciprocal inhibition - alterations consistent with heightened motor-circuit excitability and impaired inhibitory neuronal regulation. Notably, these abnormalities differ from those found in primary dystonia or epilepsy, suggesting that PKD possesses a distinct neurophysiological signature.

Taken together, PKD represents a point of convergence between paroxysmal movement disorders and disorders of neuronal excitability and synaptic regulation, making it an informative model for studying shared mechanisms such as ion-channel dysfunction, synaptic dysregulation, altered network modulation, and genetically mediated susceptibility.

Prognosis and Natural History

PKD typically follows a favorable course. In many patients, the frequency and severity of attacks decrease with age. Pharmacological treatment is highly effective in most cases, enabling remission of attacks and preservation of quality of life. [30], [32]

However, genetic penetrance may be incomplete. For instance, *PRRT2* variants exhibit an estimated penetrance of approximately 75–80%, meaning that carriers may remain asymptomatic. This complicates genetic counseling and prognostic assessment.

Sodium-Channel Blockers in *SCN2A* Epilepsy and PKD (*PRRT2*, *TMEM151A*)

Sodium-channel blockers (SCBs) represent a cornerstone of therapy for multiple paroxysmal neurological disorders, including genetic epilepsies and paroxysmal movement disorders. Their efficacy is particularly notable in conditions caused by variants in genes encoding NaV channels or associated regulatory proteins. In this context, *SCN2A*-related epilepsy and PKD associated with *PRRT2* or *TMEM151A* variants exemplify disorders in which SCBs are often the first-line therapy.

NaVs, as previously described, are critical for the initiation and propagation of action potentials in excitable cells. SCBs - such as carbamazepine, oxcarbazepine, and lamotrigine - stabilize the inactivated state of NaVs, thereby reducing repetitive neuronal firing and hyperexcitability. [33] This mechanism is particularly effective when disease-causing variants result in GOF effects, as seen in many pathogenic variants of *SCN2A*, which enhance persistent or resurgent sodium currents and lower the seizure threshold. [34] Conversely, in patients carrying LOF variants of NaV channels, SCBs are proven to be less effective,

inefficient or even exacerbate seizures due to further reduction of sodium currents, highlighting the need for genotype-guided therapy. [35] In these cases, patients may necessitate alternative therapies such as sodium-channel agonists or non-SCB antiepileptics.

In PKD, variants in *PRRT2* or *TMEM151A* are thought to dysregulate presynaptic release, NaV channels activity and indirectly affect neuronal excitability, as it will be discussed in the following paragraphs. Although these proteins are not sodium channels per se, SCBs reduce the hyperexcitability of motor circuits by dampening action potential propagation, thereby preventing trigger-induced paroxysmal episodes. [36], [37] In primary PKD, Carbamazepine remains the first-line treatment, with most patients achieving complete or near-complete remission of paroxysmal attacks. Oxcarbazepine and lamotrigine are effective alternatives in cases of intolerance. [38]

In summary, SCBs are highly effective in *SCN2A* gain-of-function epilepsies and in *PRRT2*/*TMEM151A*-associated PKD, acting primarily by stabilizing neuronal excitability. Their clinical success depends on variant type, channel functionality, and individual patient tolerance. While SCBs remain first-line therapy in these genetic disorders, careful genetic and phenotypic characterization is essential to optimize treatment and avoid paradoxical worsening in cases of LOF variants or complex genetic backgrounds.

PRRT2

PRRT2 is a neuron-specific protein that plays important roles in the control of intrinsic excitability and synaptic transmission [39], [40]. PRRT2 is composed of a large proline-rich intracellular NH2-terminal domain and a COOH-terminal transmembrane (TM) domain composed of two hydrophobic segments of which the first one forms a helix-loop-helix structure within the inner leaflet of the membrane and the second one is fully transmembrane [41], [42].

In nerve terminals, PRRT2 participates in the protein complex including SNARE proteins, synaptotagmins1/2 and P/Q Ca^{2+} channels, increasing the Ca^{2+} sensitivity neurotransmitter release and decreasing synaptic facilitation [43], [44], [45], [46]. More recently, PRRT2 was demonstrated to inhibit intrinsic neuronal excitability by negatively modulating NaV1.2/1.6 channels [41], [45], [47], [48] and enhancing the activity and pump current of Na^+/K^+-ATPase [49].

PRRT2 is the causative gene for a wide spectrum of neurological disorders with paroxysmal manifestations [36], [50]. *PRRT2* pathogenic variants account for a large fraction of cases of Benign Familial Infantile Epilepsy (BFIE), Paroxysmal Kinesigenic Dyskinesia (PKD) and Paroxysmal Kinesigenic Dyskinesia with Infantile Convulsions (PKD/IC) and, conversely, 95% of *PRRT2* patients have a diagnosis within the BFIE-PKD/IC-PKD spectrum. The remaining *PRRT2* patients display other disorders that share the paroxysmal character of the attacks, such as episodic ataxia or hemiplegic migraine [39], [51], [52], [53]. Relatively rare patients characterized by compound heterozygosity or homozygosity present with a severe developmental encephalopathic phenotype with developmental delay and intellectual disability [30], [54], [55]. To date, over 130 different variants have been reported, mostly of familial origin, with over 75% of patients carrying the same frameshift variant (c.649dupC) resulting in haploinsufficiency, that is consistent with a loss-of-function (LOF) mechanism for *PRRT2*-associated diseases.

Genetic deletion of the *PRRT2* gene in the mouse (*PRRT2*-KO) mimics the human pathology with an increased epileptic propensity, complex movement disorders and paroxysmal attacks

triggered by sensory stimuli [56], [57]. *PRRT2*-KO mouse neurons and iPSC-derived human neurons from homozygous patients display increased Na^+ current densities that are responsible for network hyperexcitability. Such network instability is particularly noticeable in brain areas where PRRT2 is highly expressed, such as the cerebellum and the hippocampus that are responsible for the paroxysmal phenotype of *PRRT2*-KO mice [56], [57], [58], [59], [60], [61].

Interestingly, while PRRT2 is a physiological inhibitor of NaV1.2/NaV1.6 which sustain the firing of excitatory neurons, it does not affect NaV1.1 channels that are fundamental for the excitability of inhibitory neurons [62], [63], thus generating an excitatory/inhibitory unbalance [45], [47]. While the increased synaptic facilitation in the absence of PRRT2 can contribute to network hyperexcitability, the dysfunction of NaV channels seems to play a central role in the pathogenesis of *PRRT2*-linked disorders, as demonstrated by the successful therapeutic control of *PRRT2* symptoms by NaV blockers, but not by other antiepileptic drugs with different targets [38], [64], [65], [66], [67]. PRRT2 negatively modulates NaV1.2/1.6 channels by decreasing their targeting to the plasma membrane, widening the voltage range in which NaVs are inactivated and slowing down NaV recovery after inactivation [45], [47], [48]. All these biophysical effects are largely opposite to those promoted by NaV β-subunits, of which PRRT2 appears as a physiological, but not molecular, antagonist [48], [68].

Besides nonsense variants, about 60 missense variants of *PRRT2* are documented in *PRRT2*-related disorders [69], [70], [71]. Although most of these variants also cause degradation or decreased targeting to the plasma membrane, some of them display a normal membrane expression and location. The latter ones are particularly interesting for physiological studies, as they can reveal important structure-function relationships and information on the subcellular targeting and downstream interactors of PRRT2. In this respect, two-thirds of the described pathogenic point variants concentrate in the relatively short (79 amino acids) COOH-terminal domain of PRRT2, characterized by a stable TM configuration [41], [42]. This observation suggests a crucial role of this domain in the PRRT2 function, as well as in the binding to downstream interactors. Indeed, the COOH-terminal domain of PRRT2 was recently demonstrated to be responsible for the specific regulation of NaV1.2 function [41]. However, a very low number of *PRRT2* pathogenic variants has been functionally studied thus far [43], [69], [72].

TMEM151A

In 2011, *PRRT2* was identified as the first causative gene of PKD [52], [73]. As described, *PRRT2* encodes for a protein that controls neuronal excitability and network stability by negatively modulating the function of NaV channels and regulating synaptic activity [41], [46], [47], [49], [74], [75]. Very recently, few reports identified *TMEM151A* as a causative gene for PKD in *PRRT2*-negative cohorts [28], [30], [37], [76], [77], [78], [79], [80], [81], [82], [83]. While we do have an extended knowledge about the function of PRRT2, we have no knowledge about the *TMEM151A* gene encoded protein, other than that it is localized in the brain [76] and that the drug treatment of choice, as already mentioned, for PKD caused by *TMEM151A*, as well as by *PRRT2* variants, is Carbamazepine, a SCB. Both PRRT2 and TMEM151A are membrane associated proteins with similar expression patterns in the nervous system. Therefore, our hypothesis is that *PRRT2* and *TMEM151A* could share the same pathophysiological mechanisms.

TMEM151A consists of two exons encoding a 468-amino acid protein. In mice, *TMEM151A* mRNA is expressed at the level of the nervous system in the cortex, hippocampus, brainstem

and spinal cord. Importantly, TMEM151A expression showed a strong developmental regulation, being higher during early postnatal stages and progressively decreasing in adulthood, in line with the age-dependent onset and spontaneous remission of paroxysmal kinesigenic dyskinesia (PKD) symptoms observed in patients. There are no protein expression data except for overexpression experiments suggesting a higher association of TMEM151A with endoplasmic reticulum membranes (ER) [76].

TMEM151A is part of the TMEM proteins, a large family of poorly described membrane proteins containing at least one putative transmembrane segment that spans completely or partially biological membranes [84].

Depending on their membrane topology and domains' orientation, TMEM proteins are involved in extracellular functions such as cell-cell communication and adhesion processes or in intracellular functions like mechanisms of exo or endocytosis. In the neuronal setting, cell membrane proteins with large extracellular domains may be involved in the neuronal/glial interactions or in synapse formation and functioning. Otherwise, cell membrane proteins with large intracellular domains, like PRRT2, may interact and regulate other membrane proteins, like channels, or be involved in membrane trafficking mechanisms or in neurotransmitter release [42], [44], [47]. Therefore, the different orientation of protein domains as well as the NH2 and COOH termini of a protein with respect to the cell membrane may determine a completely diverse set of putative protein interactors, and the formulation of different hypotheses about their function.

TMEM151A is predicted to have two transmembrane helices connected by an extramembranous loop, followed by a quite large extramembranous domain. The orientation of the NH2 and COOH termini is unknown and as a consequence its membrane topology and the location of the protein domains with respect to cell membranes is still unclear. The definition of the topology of TMEM151A, and therefore of the orientation of the large extramembranous domain, may represent a first fundamental step forward in the understanding of TMEM151A function at the membrane level. I will discuss along this work the recent results published by our group about the TMEM151A topology [85].

Recent work by Zhou *et al*. has provided the first in vivo functional characterization of TMEM151A through the generation and analysis of a murine loss-of-function model [86]. In this study, TMEM151A expression was confirmed to be highly enriched in the central nervous system, with prominent expression in cortical and subcortical regions involved in motor control. Moreover, they demonstrated that TMEM151A is mostly expressed in excitatory glutamatergic neurons rather than in inhibitory ones [86].

Behavioral analysis of Tmem151a-deficient mice revealed a paroxysmal movement disorder characterized by sudden, brief episodes of involuntary motor activity triggered by voluntary movement, closely recapitulating the core clinical features of human PKD. These episodes were responsive to carbamazepine treatment, further supporting the validity of this model and suggesting a shared pathophysiological mechanism with PRRT2-related PKD [86]. Notably, baseline motor coordination and general neurological function were largely preserved outside the paroxysmal events, indicating a specific defect in movement initiation or control rather than a global motor impairment. Together, these findings establish TMEM151A as a critical regulator of motor circuit stability *in vivo*.

AIMS

Epilepsy and paroxysmal movement disorders comprise a heterogeneous group of neurological conditions frequently caused by pathogenic variants in genes regulating neuronal excitability and synaptic function. Among these, *SCN2A*, *PRRT2*, and *TMEM151A* are strongly associated with epilepsy and paroxysmal movement disorders and often present overlapping clinical phenotypes. While the pathogenic mechanisms of *SCN2A*- and *PRRT2*-related disorders have been partially elucidated, the physiological function and disease mechanisms associated with *TMEM151A* remain largely unknown.

The overall aim of this PhD project is to elucidate the molecular and functional mechanisms through which pathogenic variants in *SCN2A*, *PRRT2*, and *TMEM151A* disrupt neuronal excitability and network stability, leading to epilepsy and movement disorders, and to identify convergent pathogenic pathways underlying paroxysmal neurological phenotypes, given the similarities observed in patient phenotypes.

Aim 1 – *SCN2A*

To define the functional consequences of disease-associated *SCN2A* variants on sodium channel activity and neuronal excitability.

This aim focuses on the functional characterization of pathogenic *SCN2A* variants identified in patients with developmental epileptic encephalopathy, including mosaic variants. By combining clinical data, in silico predictions, and electrophysiological analyses in heterologous expression systems, this work aims to determine how these *de-novo SCN2A* variants alter NaV1.2 channel biophysical properties and contribute to epileptic phenotypes, with implications for genotype-informed therapeutic strategies.

Aim 2 – *PRRT2*

To elucidate the molecular mechanisms by which PRRT2 regulates voltage-gated sodium channels and contributes to epilepsy and paroxysmal movement disorders.

This aim seeks to define the role of PRRT2 in the control of neuronal excitability through its interaction with voltage-gated sodium channels, with particular emphasis on NaV1.2. Functional analyses of PRRT2 pathogenic variants will be performed to assess their impact on channel regulation. In parallel, in silico docking approaches combined with targeted mutagenesis aim to identify the molecular interface mediating PRRT2–NaV1.2 interaction, providing mechanistic insight into *PRRT2*-linked disorders and highlighting potential therapeutic targets.

Aim 3 – *TMEM151A*

To characterize the physiological role of TMEM151A in neuronal development and excitability and define its contribution to paroxysmal movement disorders.

This aim focuses on defining the membrane topology, subcellular localization, and functional role of TMEM151A. Using biochemical, imaging, electrophysiological analyses, as well as human iNeurons model, this work aims to determine how TMEM151A loss of function affects neuronal maturation, network formation, and sodium channel activity. Furthermore, proteomic analyses will be used to identify TMEM151A interacting proteins and signaling pathways, with particular attention to mechanistic convergence with PRRT2- and *SCN2A*-dependent regulation of neuronal excitability.

Materials and methods

Structural modeling of TMEM151A

The predicted structure of full-length TMEM151A was retrieved from the AlphaFold2 (AF2) database [87]. Amino-acids M1 to P21 and S323 to L468, characterized by low values of the AF2 confidence metrics (the predicted local distance difference test score, pLDDT) were removed. All the retained protein segments show optimal values of pLDDT, except for a two-turns helix in the short extramembranous loop. The resulting model was submitted to the Orientations of Proteins in Membranes [88] (OPM-PPM) web server to predict its orientation within a membrane-like environment. PyMOL [89] was used for visual inspection and image generation.

All-atom molecular dynamics simulations of truncated TMEM151A

The membrane builder plug-in of the CHARMM-GUI [90] web server was utilized for setting up the system and for generating input file to be used in MD simulations. The protein model (residues L22 to S322) was inserted into a 1-palmitoyl-2-oleoyl-sn-glycero-3-phosphocholine (POPC) lipid bilayer and solvated with TIP3P water molecules in a [170.09 × 170.09 × 159.03] Å3 rectangular box. [91] Na^+ and Cl^- ions were added to neutralize the total system's charge at a concentration of 0.15 M. The whole system amounts to ~435000 atoms.

Simulations were performed with namd2.14 [92] using the CHARMM36m force field. [93], [94] Periodic boundary conditions (PBC) were applied. Electrostatic interactions were treated with the Particle Mesh Ewald method,[95] with a maximum grid spacing of 1 Å and an interpolation order of 6. A cut-off of 12 Å was employed for Lennard-Jones interactions, which were smoothly switched off starting at 10 Å. Chemical bond distances involving hydrogen atoms were constrained using the SHAKE/RATTLE algorithm. [96] A time-step of 2 fs was employed.

Before production stage, the system was energy minimized and equilibrated for 40 ns in the isobaric-isothermal ensemble (NPT), extending the protocol suggested by CHARMM-GUI, with P = 1 atm and T = 310 K. Pressure and temperature were maintained constant using the Nosé-Hoover Langevin piston [97] and the Langevin thermostat, respectively. Afterwards, three independent, 500-ns-long unbiased all-atom MD simulations were performed in the NPT ensemble.

Structural analysis of TMEM151A

The VMD software [98] and TcL scripting were used to compute root mean square deviations (RMSDs) for the transmembrane (TMD) and the extramembrane domains. The integrity of TMD's helices spatial arrangement was monitored by computing cross-distances between Cα atoms. The TrajMap [99] program was utilized to calculate each residue's backbone shift (defined as the Euclidean distance after alignment) from the starting position of the simulation. To this goal, each of the three trajectories was filtered by extracting two configurations per 10 ns. Derived structures were aligned to eliminate rotations and translations. A structural alignment between AF3 [100] and AF2 models of human TMEM151A was performed.

Multiple sequence alignment

Human TMEM151A full-length sequence served as a query for a homology search which was carried out using the NCBI-blastp [101] (protein–protein BLAST) algorithm. The Reference proteins (refseq_protein) database was scanned while excluding models; the maximum number of aligned hits was set to 50, while the expect threshold was set to 0.005 with a word

size of 5. The BLOSUM62 scoring matrix was chosen and penalties for the insertion and extension of a gap were set to 11 and 1, respectively. Eleven sequences were retrieved which were subsequently aligned with M-Coffee. [102], [103] The multiple sequence alignment file was later visualized and edited using Espript3.0. [104] A similarity score for each column of the MSA was calculated considering the percentage of strictly conserved residues. The results of the conservation analysis were converted in a structural map.

Constructs and mutagenesis

Recently, DeKeyser and colleagues identified the presence of cryptic bacterial promoter–like elements within NaV genes that induce toxic effects in bacterial cells, thereby hindering DNA manipulation and functional studies. [105] The optimized plasmid pIR-CMV-*SCN2A*-Variant-1-IRES-mScarlet, produced by the laboratory of Al George (Addgene plasmid no. 162279; http://n2t.net/addgene:162279; RRID: Addgene162279, Watertown, MA, USA), which encodes NaV1.2, was used to introduce the selected variants of interest into the *SCN2A* gene by site-directed mutagenesis using the QuikChange Lightning Site-Directed Mutagenesis Kit (Cat. no. 210518; Agilent Technologies, Santa Clara, CA, USA) with primers containing the variants (p.A1659V and p.I237N) at the center of their sequence. The used forward primers are:
I237N - CCTGAAGACCAATGTGGGGGCCC
A1659V – GATGATGTCCCTTCCTGTGTGTTTAACATCGGCCTC
About the *SCN2A* mutant constructs used to investigate NaV1.2 – PRRT2 interactions, triple mutant *SCN2A* constructs have been purchased by GenScript Biotech (Netherlands) BV, starting from the above mentioned plasmid and following the table reported in the results section.
For the NaV constructs used to investigate NaV-TMEM151A interactions, the following plasmids have been used:
NaV1.1 - pIR-CMV-SCN1A-Variant-1-IRES-mScarlet was a gift from Al George (Addgene plasmid # 162278 ; http://n2t.net/addgene:162278 ; RRID:Addgene_162278)
NaV1.2 – Above mentioned pIR-CMV-*SCN2A*-Variant-1-IRES-mScarlet
NaV1.6 - pcDNA4TO-SCN8A-Variant-1-IRES-mScarlet was a gift from Al George (Addgene plasmid # 162280 ; http://n2t.net/addgene:162280 ; RRID:Addgene_162280)

The used plasmids related to the *PRRT2* results are: *PRRT2*-HA: pKH3-*PRRT2*-HA vector encoding for the human *PRRT2* cDNA tagged at COOH-terminal with the 3xHA epitope [42]; *BAP*-HA: pKH3-*BAP*-HA vector encoding for Bacterial Alkaline Phosphatase with HA tags fused at C terminus. The pKH3-*PRRT2*-HA vector was used as template to obtain mutant *PRRT2* isoforms by site-directed mutagenesis using the QuikChange Lightning site-directed mutagenesis kit (Agilent). The used forward primers are:
R266W - GTGAAGGCACCCAGAAACCTTGGGACTACATCATC;
I270N – CTCGGGACTACATCAACCTTGCCATCCTGTC;
V286M – GTGGCCTGTCAACATCATGGCCTTCGCTTATGC;
R308C – GTGGACGGGGCCCAGTGTCTGGGCCGGGTAG;
R311W – GGCCCAGCGTCTGGGCTGGGTAGCCAAGCTCTTAAGC;
V319L – CAAGCTCTTAAGCATCTTGGCGCTGGTGGG;
A320V – CTCTTAAGCATCGTGGTGCTGGTGGGGGGA;
I327M – GGGGAGTCCTCATGATCATCGCCTCCTGC.

For the L336X *PRRT2* variant, a new pKH3-HA-*PRRT2* vector has been designed to generate the truncated variant without the removal of the HA tag. The *hPRRT2* cDNA has been cloned in EcoRI site of the pKH3 vector and the correct insertion orientation was checked by sequencing

(pKH3 was a gift from Ian Macara, Addgene plasmid #12555; https://n2t.net/addgene:12555; RRID:Addgene_12555) [106]. The resulting vector was used as template to obtain the mutant PRRT2 isoform by site-directed mutagenesis using the QuikChange Lightning site-directed mutagenesis kit (Agilent). The used forward primer is:
L336X - GTCATCAACTGAGGCGTGTATAAG

For the *TMEM151A* results, we purchased the pCMV3-*TMEM151A* plasmid (Cat.# HG28144-UT; Sino Biological) containing the human *TMEM151A* coding sequence and the pCMV6-*Tmem151a* (Cat.#MC205299; Origene), containing the mouse *Tmem151a* coding sequence.
We generated four distinct HA constructs using the pKH3 plasmid and the human pCMV3-*TMEM151A*: 3xHA tags at the N terminus of *TMEM151A* (HA-*TMEM151A*), with the *TMEM151A* human coding sequence cloned in EcoRI site; 3xHA tags at the C terminus of *TMEM151A* (*TMEM151A*-HA), with the *TMEM151A* human coding sequence without a stop codon cloned in HindIII-SalI; 2xHA tags between the two hydrophobic transmembrane segments in the putative extramembranous loop of the protein (*TMEM151A*-HA-LOOP), obtained by cloning *TMEM151A* in HindIII-EcoRI and then by cloning 2xHA tags in XmaI site in the *TMEM151A* sequence; 2xHA tags between the two β-sheet forming segments (*TMEM151A*-HA-βsheet), obtained by cloning *TMEM151A* in HindIII-EcoRI and then, by cloning into PstI-XhoI, we inserted a modified sequence with 2xHA tags after Asparagine 170 (generated by Genscript Synthesis Service).
For the double tagged *TMEM151A*-HA-LOOP + V5 construct, the *TMEM151A*-HA-LOOP construct was modified with the addition of a V5 tag at the C terminus after the removal of the stop codon by cloning the V5 tag in XbaI-EcoRI sites (top oligo 5'-[PHO] CTA GAG GTA AGC CTA TCC CTA ACC CTC TCC TCG GTC TCG ATT CTA CGT AGG; bottom oligo 5'-[PHO] AAT TCC TAC GTA GAA TCG AGA CCG AGG AGA GGG TTA GGG ATA GGC TTA CCT).
The *TMEM151A*-HA vector was used as template to obtain mutant *TMEM151A* isoforms (G56R, V149del, V264A, S297L) by site-directed mutagenesis using the Q5® Site-Directed Mutagenesis Kit (Cat.#E0554S; New Englad Biolabs). The HA-*TMEM151A* vector was used as template to obtain mutant TMEM151A isoforms causative of truncation (C125*, L300Pfs*118). The used primers are:

variant	Forward primer 5'-3'	Reverse primer 5'-3'
G56R	CACGCCTGCCGGGCCGTGGTG	GATGAGCAGCGTGAGGAGCAGGCACTTCC
V149del	TGGTGGAAGGCCACCAGCTATCACTACG	GCACGGCGGCGCCTGC
V264A	CTGAAGGACGCAGACTTCCGCGAG	GTGCATGCCCTCGCGCG
S297L	GGCCACGCTGTTGTGGCCCCTGCG	GCCGACACGAGCCAGAAGACCCAGGCGC
C125*	GTGCGGTCCTGACAGGCGCCACG	GTGACAGTGCCAGCACTCAGCCAG
L300Pfs118*	GCCTATGGCACGGCTCACGTGC	GGCCACGACAGCGTGGCC

The same variants were also generated on the *TMEM151A*-HA-LOOP construct.

I generated the pKH3-GFP and pKH3-*TMEM151A*-GFP constructs by cloning the GFP cDNA in the empty pKH3 and in the pKH3-*TMEM151A*-HA vectors respectively, using the SalI and EcoRI restriction sites. Vectors were then checked for sequence by Sanger sequencing.

We generated the HA-*Tmem151a* and *Tmem151a*-HA in the pKH3 construct encoding for the mouse Tmem151a protein respectively tagged with 3xHA tags at the N terminus and at the C terminus, by cloning the insert from the pCMV6-*Tmem151a* construct in the HindIII-SalI sites (C terminus tag) or in the EcoRI site (N terminus tag).

pLVX-UbC-rtTA-Ngn2:2A:EGFP was a gift from Fred Gage (Addgene plasmid # 127288; http://n2t.net/addgene:127288; RRID:Addgene_127288) [20].

All primers were purchased from Eurofins Genomics (Kholn, Germany) as well as all the Sanger sequencing checks.

HEK293 Cell culture and transfection

HEK293 cell lines were maintained in DMEM/F12 (1:1) supplemented with 10% fetal bovine serum, 100 U/ml penicillin and 100 µg/ml streptomycin. HEK293 cells stably expressing human NaV1.2 were kind gifts from Drs. Enzo Wanke and Marzia Lecchi (Milano-Bicocca University, Italy). For selection of stable NaV clones, 500 µg/ml G418 was used. Cell lines were transfected according to the manufacturer's recommendations at 70% confluency using Lipofectamine 2000. All reagents were purchased from ThermoFisher Scientific.

To identify transfected HEK293 cells for electrophysiology, the reporter EGFP or Tomato protein reporter (Clontech) was co-transfected. For electrophysiological experiments, transfected cells were dissociated, re-plated at low density about 24 h post-transfection and recorded after further 24 h. To study the effect of *PRRT2* pathogenetic mutants, HEK293 /NaV1.2 were transfected with the MOCK, WT-*PRRT2*, A320V-*PRRT2* or V286M-*PRRT2* tagged with HA. For all electrophysiology experiments involving *SCN2A* mutations, as well as those involving co-expression of neuronal Na^+ channels and WT or mutant TMEM151A, transient transfection was performed using a total of 400 ng of cDNA per condition. HEK293 cells were transfected at 80% confluence with Lipofectamine 2000 (Life Technologies, Carlsbad, CA, USA) according to the manufacturer's instructions. For electrophysiological experiments, cells were also co-transfected with an empty vector as negative control.

Mouse primary neuronal culture and transfection

Hippocampal primary neurons were derived from embryos at E15-16. Each embryo was treated independently. Hippocampi were dissected under a stereomicroscope in ice-cold HBSS. Hippocampi were incubated for 10 minutes with 0,25% trypsin (Gibco) at 37°C. Then, trypsin was replaced with Neurobasal medium (Gibco, 1X) supplemented with 10% Fetal Bovine Serum (FBS, Gibco), 1% GlutaMAX (Gibco) and 1% Penicillin-Streptomycin (Gibco). The digested tissues were mechanically dissociated, cells were counted and plated on 25 mm coverslips or Petri dishes coated with Poly-L-Lysine (0.1 mg/mL for Petri dishes and 1 mg/mL for coverslips). After at least 2 hours from plating, the medium was replaced with new Neurobasal medium supplemented with B27 (Gibco, 1X), 1% GlutaMAX (Gibco) and 1% penicillin-streptomycin (Gibco) (hereby, complete Neurobasal medium). Cultures were maintained in a 5% CO2 humidified incubator at 37°C. Cells were transfected using Lipofectamine 2000 at seven days in vitro (div) and fixed after 48 hours from trasfection.

Rat primary fibroblast culture

Rat fibroblasts were derived from embryos at E15-16. Each embryo was treated independently. Cortices were dissected under a stereomicroscope in ice-cold HBSS and tissues were mechanically dissociated. Cells were counted and plated on T75 flasks in Advanced DMEM medium supplemented with 20% FBS, 1% PenStrep and 1% Glutamax. Cultures were maintained in a 5% CO2 humidified incubator at 37°C.

iPSC generation, maintenance and checks

Cells were purchased from Applied Stem cells. The following gRNAs have been used for the generation of the heterozygous clone #C2.

gRNA1: tcgccgtccgggatgagcgc

gRNA2: gtgcccgcgctcatcccgga

These gRNAs are targeting the cDNA sequence of *hTMEM151A*, at the level of the exon 1. They cause the deletion of a large portion of the sequence, comprising the ATG start codon as depicted in the Results section.

Cells were cultured in Geltrex coated plates (Gibco, A14132-02) and StemFlex medium (Gibco, A3349401). Cells were splitted using Versene Solution (Gibco, 15040066) after 1 × wash of HBSS (Gibco, 14175129) into Stemflex medium with ROCK Inhibitor (RI, Y-27632 dihydrochloride) [1ul/mL]. Freezing solution was prepared using half volume of DMSO 20% (Sigma, D2650) /Fetal Bovine Serum (FBS) (Gibco, 10500064) and half volume of Stemflex medium and ROCK Inhibitor. For freezing, cells were washed once with HBSS, then aspirated HBSS and added Versene solution, kept the cells at 37 °C for 3 min then aspirated the Versene solution and added the Freezing solution. The mycoplasma test is performed routinely.

The iPSCs were checked for gene editing as described in the results section. Genomic DNA was extracted via the DNeasy Blood and Tissue Kit (Qiagen; #69504). The following primers were used for PCR on the extracted genomic DNA:

Fg: CCAGAGGGTTAGACCAGCTC

Rg: CTTTTGCACTGGTCCCTCTC

The used PCR kit was the Q5 High-Fidelity DNA Polymerase kit (New England Biolabs, # M0491S).

iPSC lentiviral Infection

At day −2, in a 6 well plate, 50.000 single cells iPSC were plated. To do so, cells were treated with 0.05% Trypsin solution (Gibco, 25050014) after a single wash with HBSS. Cells were incubated at 37 °C for 3 min, followed by the addition of DMEM/F12 (Gibco, 11330057) and 10% FBS solution to neutralize the Trypsin activity. The cell suspension was then centrifuged at 500 g for 5 min. At day 0, cells were infected with 1 MOI of Lentivirus generated with pLVX-UbC-rtTA-Ngn2:2A:EGFP vector (Addgene plasmid, #127288). The next day Lentivirus was removed and on day 2 we started the puromycin selection with increases doses, identified previously testing different puromycin concentration for each cell line, for 5 days.

iPSC FACS Sorting

Doxycycline (4 µg/mL) was added on day 6 for overnight induction of GFP expression the sorting experiment was performed the following day. Cells were treated with 0.05% Trypsin solution (Gibco, 25050014) after a single wash with HBSS. Cells were incubated at 37 °C for 3 min, followed by the addition of DMEM/F12 (Gibco, 11330057) and 10% FBS solution to neutralize the Trypsin activity. The cell suspension was then centrifuged at 500 g for 5 min. Subsequently, the cells were resuspended in HBSS with 5% FBS and passed through a 70 µm cell strainer (Greiner easy strainer 542040) to obtain a single-cell suspension. FACS was performed using the BD FACSymphony S6 cell sorter to collect an homogeneous pool of GFP-positive cells. All FACS procedures were conducted under low-pressure conditions with a 100 µm nozzle. After sorting, pooled cells were centrifuged at 2000 rpm for 5 min and subsequently plated in Stemflex medium containing RI and Primocin (1:500) (InvivoGen; ant-pm-05). The next day, the rock Inhibitor was removed, and the iPSC-NGN2 cells were expanded.

iNeurons Differentiation

In order to generate induced Neurons (iNeurons) we employed a two-step protocol outlined in the timeline of Fig. 35. Briefly, 300.000 single iPSC stable-NGN2 cells were plated in Geltrex

coated 6 wells plate (counted using the automated cell counter Countess 3, Thermofisher), then cells were cultured for 3 days with pre-differentiation media prepared as following: Knockout DMEM/F12 (Thermofisher; #12660012), N2 supplement 100x 1% (Thermofisher; #17502-048), MEM Non essential AA 100x 1% (Gibco; #11-140-050) and freshly added BDNF 10 ng/mL (Thermofisher; # 450–02), NT-3 10 ng/mL (Thermofisher; #450–03), Laminin 10 ng/mL (Sigma-Aldrich; #L2020-1mg) and Doxycycline 4 ug/mL (Sigma-Aldrich; #D9891-1g). After 3 days, we cryopreserved the NPC using the iNeurons freezing solution [(80% KnockOut Serum Replacement (Gibco, 10828028) and 20% DMSO (Sigma, D2650)] and half solution of pre-differentiation media. After thawing, neuroprogenitor iNeurons were plated respectively on Cytoview 48 well (M768-tMEA-48B BLACK) for MEA recording, on petri dish (3 cm of diameters) for RNA extraction, and on IBIDI (Twin Helix, 80806) or glass coverslips for immunostaining assay. Previously, all supports were coated with Poly-L-ornithine hydrobromide (PLO) 50 µg/mL (Sigma-Aldrich, P3655) overnight, then washed three times with UltraPure water (Invitrogen, 10977049) and then coated with Laminin (10 µg/mL) (Sigma_Merck; L2020) in DMEM/F12 for 2 h at 37 °C. Then we plated dropwise 20 uL of iNeurons and primary rat astrocytes (ratio 1:3) with density of 1200 cell/mm2 on MEA supports. For petri dishes and ibidi plating was done at full surface (not dropwisely). Then iNeurons were cultured for 56 days with two half media change per week, using Differentiation Media composed by Neurobasal medium (Gibco, 21103049) with B-27 2% (Gibco, 17504044), BDNF 10 ng/mL (Thermofisher; # 450–02), NT-3 10 ng/mL (Thermofisher; #450–03), Laminin 10 ng/mL and Doxycycline 4 ug/mL (that was removed after 14 days).

SDS-PAGE and Western blotting

For sodium dodecylsulfate gel electrophoresis (SDS-PAGE), samples were quantified with the BCA assay (ThermoFisher Scientific) and heated to 50 ˚C for 5 min without boiling and successively run on 10% (w/v) polyacrylamide gels and blotted onto nitrocellulose membranes (Whatman). Blotted membranes were blocked for 1 h in 5% milk in Trisbuffered saline (10 mM Tris, 150 mM NaCl, pH 8.0) plus 0.1% Triton X100 and incubated overnight at 4 ˚C with the appropriate primary antibody. Membranes were washed and incubated at room temperature for 1 h with peroxidase-conjugated anti-mouse (Cat.#1706516; 1:3000; BioRad, Hercules, CA) or anti-rabbit (Cat.#1706515; 1:3000; BioRad, Hercules, CA) antibodies. Bands were revealed with the ECL chemiluminescence detection system (ThermoFisher Scientific) and imaged by the ChemiDoc Imaging System (Bio-Rad). Immunoblots were quantified by densitometric analysis of the fluorograms (Quantity One software; Bio-Rad, Hercules, CA) obtained in the linear range of the emulsion response.

Immunolabeling

In the live-labeling protocol, the cells are incubated with the primary antibody diluted in the culture medium; without the permeabilization step, the primary antibodies can bind just to epitopes exposed on the extracellular side of the cell membrane. For both PRRT2 and TMEM151A results, transfected HEK293 cells were maintained for 10 min at 4 °C, and then were live labeled by incubation with primary anti-HA mouse antibody (Cat.#05-904; Merck Millipore, 1:200 diluted in culture medium) for 20 min at 4 °C to detect surface epitopes. Samples were washed in PBS and then incubated with the Alexa Fluor 488-conjugated secondary antibody (Invitrogen, 1:500 diluted in culture medium) for 20 min at 4 °C and then were fixed by 4% paraformaldehyde (PFA) for 20 min at room temperature (RT). After washes in PBS, for TMEM151A double staining, we performed a standard IF staining: cells were permeabilized with 0.1% Triton X-100 in PBS for 10 min at RT, and after washes, blocking was performed with 3% bovine serum albumin (BSA) for 45 min at RT. Samples were then

incubated with anti-TMEM151A rabbit antibody (Cat.#HPA041035, immunogenic sequence: EVPALIPDGEPLREEQRPLKQSLGSSLC; Sigma Aldrich, 1:500 diluted in 3% BSA), washed in PBS, and incubated with Alexa Fluor 594-conjugated secondary antibody (Invitrogen; 1:500 in 3% BSA). After several washes in PBS, coverslips were mounted using Prolong Gold antifade reagent (Invitrogen) containing 4',6'-diamidino-2-phenylindole (DAPI) for nuclear staining. For the *TMEM151A*-HA-LOOP + V5 construct experiments, the primary anti-HA mouse antibody (Cat.#05-904; Merck Millipore) and the primary anti-V5 rabbit antibody (Cat.#13202; Cell Signaling Technology) were used, in different combinations of live-labeling and standard IF.

For NaV1.2 results, HEK293 cells transfected with *SCN2A* constructs, were labeled with anti-PanNaV (Cat. #S8809; 1:200; Sigma-Aldrich, St. Louis, MO, USA) following the above mentioned protocol of standard IF staining. For PRRT2 results, HEK293 cells transfected with *PRRT2* variants were labeled with anti-HA antibody following the above mentioned protocol of standard IF staining.

For iNeurons immunostaining cells were fixed for 10 min with 4%(v/v) paraformaldehyde (PFA) and 4% (w/v) sucrose, then cells were washed 3 times with PBS and permeabilized with 0.2% Triton X-100 in PBS for 10 min, followed by three washes with PBS. A blocking solution (0.2% Triton X-100 and 10% FBS in PBS) was added for 45 min. Subsequently, primary antibodies were diluted in the incubation solution (0.2% Triton X-100 and 5% FBS in PBS) and added for overnight incubation. The following antibodies were used: MAP2 (Sigma; #M9942; 1:200 and Synaptic Systems; #188003; 1:200), Synapsin 1/2 (Synaptic Systems; #106004; 1:100), NeuN (Millipore; #MAB377; 1:200). The next day, for both protocols, cells were washed three times with PBS for 5 min, followed by the addition of the secondary antibody. Secondary antibodies were used at a dilution of 1:500 in the same dilution buffer for 1 h in the dark. The secondary antibody was then removed, and Hoechst (1:300) was added for 15 min, followed by three washes with HBSS for 5 min.

Pull-down and surface biotinylation assays

Both protocols were performed at 4 °C. *Naïve* HEK293 cells were transfected as previously described with HA-tagged WT-PRRT2 and its mutant isoforms, using HA-tagged bacterial alkaline phosphatase (BAP-HA) as control. For pull-down assays, 24 h after transfection, cells were harvested in lysis buffer (150 mM NaCl, 50 mM Tris, 1 mM EDTA and 1% Triton X-100 supplemented with protease inhibitor cocktail) and centrifuged at 10,000 xg for 10 min. Kept an aliquot for the input sample, the supernatant was incubated with 50 µl of monoclonal antiHA-agarose affinity beads (Sigma-Aldrich) for 2 h. After 3 washes in lysis buffer, beads were incubated with cell extracts from HEK293 cells stably expressing NaV1.2 for 3 h. After extensive washes in lysis buffer and detergent-free lysis buffer, samples were resolved by SDS-PAGE and subjected to western blotting with anti-panNaV (Sigma-Aldrich; #s8809; 1:300) and anti-HA (ThermoFisher Scientific; # 71–5500; 1:1,000) specific antibodies.

For biotinylation experiments, HEK293 cells stably expressing Nav1.2 were transfected with either WT-PRRT2 or its variants tagged with HA. Twenty-four hours after transfection, cells were incubated with 1 mg/ml of EZ-Link™ Sulfo-NHS-SS-Biotin (ThermoFisher Scientific) in cold phosphate buffered saline (PBS, pH 8) for 35 min, with constant mixing. Free biotin was quenched, twice with 100 mM Tris pH 8, and once with cold PBS to remove the excess of biotin. Cells were then lysed in lysis buffer (150 mM NaCl, 50 mM Tris, 1 mM EDTA and 1% Triton X-100) supplemented with protease inhibitor cocktail (Cell Signaling). Total cell lysates were centrifuged at 10,000 xg for 10 min. Kept an aliquot for the input sample, the supernatant fraction was incubated with 150 µl of NeutrAvidin conjugated agarose beads (ThermoFisher

Scientific) at 4 ◦C for 3 h. After extensive washes of the beads, samples were eluted, resolved by SDS-PAGE and subjected to western blotting with anti-panNav (Sigma-Aldrich; # s8809; 1:300), anti-NKA 1 (Merck, # 05–369; 1:1,000), anti-Actin (Sigma Aldrich; # A4700; 1:1,000) or HA (ThermoFisher Scientific; # 71–5500; 1:1,000) antibodies.

For the TMEM151A proteomics investigation, the same pull-down protocol was used, but the isolated anti HA-agarose beads – TMEM151A-HA, HA-TMEM151A or BAP-HA complexes have been incubated with adult mouse brain lysate for 3 h. After washes, the eluted material was then analyzed by mass-spectrometry analysis at the Gaslini Institute Proteomics facility as described below.

Mass spectrometry proteomics and analysis

From the pull-down experiment previously described, 80 ul of eluted samples were reduced and alkylated in 80 ul of 80 mM Chloroacetamide and 10 mM Tris(2-carboxyethyl)phosphine. Proteins were isolated and digested by PAC method automated on a KingFisher™ Apex robot (Thermo Fisher Scientific) in 96-well format [107]. Briefly, the tip plate was stored in plate #1. Lysate samples were stored in plate #2, in a final concentration of 70% acetonitrile and with magnetic beads in a protein/bead ratio of 1:4 (1:1 SpeedBead Magnetic Carboxylate, 45152105050250 and 65152105050250). Washing solutions were in plates #3–5 (acetonitrile), plate #6 (70% Ethanol) and plate #7 (isopropanol). Plate #8 contained 100 ul digestion solution of 25 mM Tris HCl pH 8, LysC (Wako) in an enzyme/protein ratio of 1:100 (w/w) and trypsin (Promega) in an enzyme:protein ratio of 1:50. The protein aggregation was carried out in two steps of 1 min mixing at medium mixing speed, followed by a 10 min pause each. The sequential washes were performed in 2.5 min and slow speed, without releasing the beads from the magnet. The digestion was set to 4 h at 37 degrees with slow speed.

Obtained peptides were desalted in Stage-Tips [108] and analyzed by a miniaturized ultra-high performance liquid chromatography-tandem mass spectrometry system (nano-UHPLC-MS/MS) using an Ultimate 3000 RSLC coupled to an Orbitrap Q Exactive Plus mass spectrometer (Thermo Scientific Instrument). Elution was performed with an EASY spray column (75 µm × 50 cm, 2 µm particle size, Thermo Scientific) at a flow rate of 250 nL min-1 using a non-linear gradient from 2 to 45% of solution B (80% ACN and 20% H2O, 5% dimethyl sulfoxide -DMSO- , 0.1% formic acid -FA-) in 50 min. MS analysis was performed in data-independent acquisition (DIA) modality. Orbitrap detection was used for MS-1 measurements at a resolving power of 70 K in a range between 375 and 1500 m z-1 and with a 3 · 106 automatic gain control (AGC) target. Precursors were selected for data-independent fragmentation with an isolation window width of 34 m z-1 and 19 loop count. Higher collisional dissociation (HCD) energy was set to 27%, and MS-2 scans were acquired at a resolution of 35 k and 3 · 106 AGC target.

All DIA raw files were processed with Spectronaut version 18 using a library-free approach (direct DIA) under default settings. Enzymes / Cleavage Rules was set to Trypsin/P, Lys-C. Library was generated against Uniprot Human database (release UP000005640_9606 June 2024, 104602 Entries) and Uniprot Mouse database (release December 2021, 63656 Entries). Carbamidomethylation was selected as a fixed modification, and methionine oxidation and N-terminal acetylation were selected as variable modifications. The false discovery rates (FDRs) of peptide-spectrum matches (PSMs) and peptide/protein groups were set to 0.01. For DIA Analysis\Identification Precursor PEP Cutoff, Protein Qvalue Cutoff (Run) and Protein PEP Cutoff were set to 0.01. For quantification, Precursor Filtering was set to Identified (Q-value) and MS2 was chosen as quantity MS-level.

The Protein Quant Pivot Report generated by Spectronaut was statistically evaluated using Perseus software [109] version 1.6.15.0.

Pre-embedding immunogold labeling for electron microscopy

For TMEM151A topology investigations, HEK293 cells were plated in 2 well permanox-coated plates (Nunc, LabTek Chamber Slides, 177372) and transfected with *TMEM151A*-HA or *TMEM151A*-HA-LOOP constructs. After 24 h, cells were rinsed in PBS and fixed with 3% paraformaldehyde + 0.05% glutaraldehyde in PBS for 1 h at RT. For immunolabeling, the cells were briefly washed in PBS, permeabilized in blocking solution (50 mM NH 4 Cl, 0.5% BSA, 0.1% saponin in PBS) for 30 min and incubated overnight with primary anti-HA rabbit antibody (Thermo Fisher Scientific, #71-5500; 1:100 diluted in blocking solution), then rinsed and incubated with 5-nm gold-labeled protein A (PAG-5 nm, purchased from Utrecht University, Utrecht, The Netherlands) for 4 h at RT. After washes, cells were fixed in 2.5% glutaraldehyde in 0.1 M sodium cacodylate for 1 h at RT and postfixed in 2% OsO_4 in water for 1 h at RT, contrasted en bloc with 1% uranyl acetate for 1 h, dehydrated in a graded series of ethanol, and embedded in Epoxy resin for 2 days at 60 °C. 50 nm ultrathin sections were cut by Leica Ultracut UCT ultramicrotome and further contrasted with lead citrate and 5% uranyl acetate in ethanol. [110] Ultrathin sections were examined with an HT7800 120Kv transmission electron microscope (Hitachi, Tokyo, Japan) equipped with Megaview G3 camera and Radius 2.0 software (EMSIS, Muenster, Germany).

RNA extraction and reverse transcription

The RNA extraction kit RNeasy Mini Kit (QIAGEN, # 74104) was used for extraction from mouse primary cell cultures or iNeurons cell cultures according to the manufacturer protocol. Reverse transcription was performed through the use of the QuantiTect Reverse Transcription Kit (QIAGEN, #205311) starting from 1000ng of RNA for each sample.

Real time PCR

The real time PCR experiments have been carried out through the BioRad CFX 96 instrument using the SsoAdvanced™ Universal SYBR® Green Supermix (BioRad; Cat.#1725271).

Used primers are listed below:

Target	Forward primer 5'-3'	Reverse primer 5'-3'
mTmem151a #1	CTGCTCGGATGGCTACCTG	CATGACCGCACATGACAGT
mTmem151a #2	ATGGGGACGCCTATACCACC	CTCTGCGTGAGGTACGAGG
mTmem151a #3	CCTCGCCTACCCTTCAGTC	GTCTCCGTGGACAATGAGCAC
mGapdh	GAACATCATCCCTGCATCCA	CCAGTGAGCTTCCCGTTCA
m18S rRNA	CGGACAGGATTGACAGATTGAT	CCAGAGTCTCGTTCGTTATCG
mHPRT	TGAGGCGGCGAGGGAGAG	AAGCGGTCTGAGGAGGAAG
hTMEM151A #1	ACCTGAAGGACGTAGACTTCC	CACGAGCCAGAAGACCCAG
hTMEM151A #2	CAGCTATCACTACGTGCG	TGCGCCGAGTAGTCAAACTC
hTMEM151A #3	GAGTTTGACTACTCGGCGCA	CTGAAGCACTTGGTGAAGCG
hMAP2	TGAGGCTACACAGGACATGA	TTGGCCACCTTCTCTTTGAC
hGAPDH	ACAACTTTGGTATCGTGGAAGG	GCCATCACGCCACAGTTTC
hHPRT	CCTGGCGTCGTGATTAGTGAT	AGACGTTCAGTCCTGTCCATAA
hGUSB	GTCTGCGGCATTTTGTCGG	CACACGATGGCATAGGAATGG

Quantitative real-time PCR (qRT-PCR) was performed to evaluate relative gene expression levels using the comparative Ct ($2^{-\Delta Ct}$) method. Briefly, the threshold cycle (Ct) value, defined

as the number of PCR cycles required for the fluorescent signal to exceed a predefined threshold, was determined for both the target gene and an endogenous reference (housekeeping) gene for each sample. The results have been analyzed by mediating the Ct value of 3 replicates for each condition. To normalize for variations in RNA input, reverse transcription efficiency, and overall PCR performance, the Ct value of the target gene was normalized to that of the housekeeping gene (GAPDH, HPRT, 18s rRNA, GUSB), by calculating the ΔCt value according to the following equation:

$$\Delta Ct = Ct\ target - Ct\ housekeeping\ gene$$

Relative gene expression levels were then calculated as $2^{-\Delta Ct}$. The resulting values were used for statistical analysis and samples comparison and graphical representation of gene expression data. For iNeurons data about TMEM151A relative expression, samples were all compared to the ISO #B5 28 div sample, set as 100%. Regarding MAP2 relative expression data, samples were compared within each ISO #B5 and #C2 couple (same div), by setting each ISO #B5 sample at 100 %.

Patch clamp on HEK293 cells

The patch clamp technique in the whole-cell configuration allows us to measure the electrical activity across the entire cell membrane of a single cell: it enables the recording of ionic currents that flow through ion channels in the membrane.

The extracellular solution contained: 145 mM NaCl, 5 mM KCl, 1.8 mM $CaCl_2$, 1 mM $MgCl_2$, 10 mM HEPES, adjusted to pH 7.4. The internal solution consisted of: 40 mM CsCl, 10 mM NaCl, 80 mM CsF, 11 mM EGTA, 10 mM HEPES, 1 mM $CaCl_2$, adjusted to pH 7.3.

Series resistance (Rs) ranged between 2 and 4 MΩ, and cell capacitance ranged between 10 and 25 pF, as measured using the amplifier's compensation circuit. Data were analyzed using the Ana program (available at http://users.ge.ibf.cnr.it/pusch/programs-mik.htm) and IgorPro 8.0.4 software (WaveMetrics, Lake Oswego, OR, USA). The holding potential was set to –90 mV. The standard I–V protocol involved applying 20-ms voltage steps from –60 mV to +90 mV (in 10 mV increments).

The whole-cell sodium conductance (GNa) was calculated using the equation:

$$GNa\ =\ I\ /\ (V\ -\ Erev)$$

where I is the peak current, V is the applied voltage, and Erev is the sodium reversal potential, estimated by linear regression of the I–V curve for each cell.

To evaluate the voltage dependence of activation, normalized GNa values were plotted as a function of membrane potential and fitted with the Boltzmann equation:

$$G/Gmax\ =\ 1\ /\ (1\ +\ exp[(V\ -\ V_{1\ /\ 2})/k])$$

where $V_{1\ /\ 2}$ is the half-activation voltage, and k is the slope factor describing voltage sensitivity.

To investigate fast inactivation, a double-pulse protocol was used: 500-ms conditioning pulses ranging from –120 mV to 0 mV (in 10 mV increments) were followed by a test pulse to –10 mV. The resulting steady-state inactivation curve was fitted using the Boltzmann equation:

$$I/Imax\ =\ 1\ /\ (1\ +\ exp[(V\ -\ V_{1\ /\ 2})/k]).$$

Activation time constant was obtained from a single exponential fit in response to the applied potential. Inactivation kinetics were assessed by measuring the decay of the current from the peak to 40 ms from the stimulus onset with a single exponential fit. The recovery of fast inactivation protocol was a two-pulse protocol with varying time intervals with a -10 mV test pulse. Recordings were performed at room temperature (22–25°C).

Related to the PRRT2 – NaV1.2 interaction experiments, the patch clamp methods are the following. To obtain better clamp control of cells under recording, isolated cells were used for electrophysiological experiments. Thus, transfected cells were enzymatically dissociated and plated at low density about 24 hours post-transfection. All recordings were performed 24 hours after plating; transfected cells were identified by fluorescence of co-transfected green fluorescent protein (GFP) as previously described [41], [47], [48]. Voltage-clamp recordings of voltage-gated Na^+ currents were performed using the following solutions: extracellular (140 mM NaCl, 3 mM KCl, 1 mM $MgCl_2$, 1 mM $CaCl_2$, 10 mM HEPES, 10 mannitol, pH 7.3 with NaOH) and intracellular (140 mM CsCl, 10 mM NaCl, 2 mM EGTA, 10 mM HEPES, pH 7.3 with CsOH). Patch pipettes, made of borosilicate glass (Hilgenberg) were pulled and heat-polished to a final resistance of 3-5 MΩ when filled with standard internal solution. Whole-cell currents were recorded using an EPC-10 amplifier (HEKA Elektronic), and for all electrophysiological experiments data acquisition was performed using PatchMaster programs (HEKA Elektronic). Whole-cell voltage-clamp recordings of NaV currents were acquired at 20 kHz and low-pass filtered at 4 kHz. Recordings with leak currents > 200 pA or series resistance > 10 MΩ were discarded. Data acquisition was performed using the PatchMaster program (HEKA Elektronik GmbH). Series resistance was compensated 80% (2 µs response time) and the compensation was readjusted before each stimulation. The membrane potentials in whole-cell recordings were uncorrected for Donnan liquid junction potentials of ~ 9 mV. All experiments were performed at room temperature (22–24 °C). Whole-cell family currents of fast inactivating Nav channels were evoked by 5 mV step depolarization (100 ms in duration) from -80 to 40 mV and cells were held at a holding potential (Vh) of -100 mV. To minimize space-clamp problems, we selected only isolated cells with a soma diameter of about < 30 µm for recordings. Membrane capacitance artifacts and leakage currents were eliminated by P/N leak subtraction procedure. The Na^+ current density (J) was obtained by dividing the peak inward current by the cell capacitance (nA/pF). In the experiments shown, the cell was considered without current when the maximal current recorded in the cell (corresponding to the value of V = -10 mV) was below 100 pA.

Micro-electrode Array Recordings on iNeurons

The neuronal cultures were plated on commercial 48-well devices (CytoView MEA plate, Axion BioSystems, Atlanta, GA, USA). The devices integrate 16 electrodes for each well characterized by 50 µm in electrode size and arranged in a 4 × 4 grid (electrode spacing 350 µm). The electrophysiological recordings were performed with the Maestro Original (Axion BioSystems, Atlanta, GA, USA), once a week (± 2 days), from DIV 7 until DIV 56. Briefly, we let the cultures settle for 3 min at 37 °C. We performed the electrophysiological recordings of the spontaneous activity for 8 min sampled at 12.5 kHz. Data were collected applying a band pass filter, which high-pass-filter and low-pass-filter cutoff were set to 200 Hz and 3000 Hz, respectively. Off-line data analyses were performed by exploiting the Axion Software (Axion BioSystems, Atlanta, GA, USA). Briefly, the spike detection was performed with a hard-threshold detection which threshold was set to five times the standard deviation of the baseline noise. A channel was considered active whether its MFR was greater than 0.1 spikes/s [41]. From the spike detection, we extrapolated the MFR and the percentage of active

channels. Moreover, based on the MFR trend from DIV 7 to DIV 56, we evaluated the maximum reached from the curve (i.e., DIV 49). We then performed a filtering of the dataset: we excluded from further analysis the wells with less than 10 over 16 active electrodes at DIV 49 to avoid considering cultures with no electrophysiological activity. Afterwards, the burst detection was performed based on the logarithmic ISI distribution [42, 43]. Bursts were detected by setting a threshold of the minimum number of spikes belonging to a burst equal to 5 spikes. Channels with a MBR lower than 0.4 bursts/min were excluded from the bursting analysis [44]. From the burst detection, we extrapolated the MBR, the BD, and the percentage of RS. Lastly, we defined an event as network burst if the activity was composed by consecutive bursts within a 100 ms window recruited from at least 30% of the channels. From the network burst detection, the NBR was computed. Neuronal network activity was recorded following acute chemical administration (APV 75 µM, CNQX 35 µM, and BIC 30 µM) at DIV 49. In the text, the values related to the electrophysiological features are reported as mean ± standard deviation.

Computational Neuronal Modeling

Regarding the A1659V NaV1.2 computational neuronal modeling, we started from typical optimized models of a rat neocortical or hippocampal CA1 pyramidal cell. The neocortical model, kindly provided by Roy Ben-Shalom, was used as reported in Garcia et al. [111], after replacing both NaV1.2 and NaV1.6 with the NaV1.2 channel here reported. For the hippocampal neuron, we referred to Vitale et al. [112], substituting the standard literature Hodgkin-Huxley Na^+ channel with the NaV1.2 native kinetics described here, across all compartments and using a three-dimensional morphological reconstruction from Migliore et al. [113]. In the case of the A1659V substitution, we ran simulations substituting 50% of the native channels with the variant channel. Current-clamp simulations were conducted by injecting increasing current steps to the soma and recording the number of AP from both the soma and AIS. For synaptic stimulation, conducted on the hippocampal model, we colocalized one excitatory synapse and one inhibitory synapse, both belonging to the standard NEURON class Exp2Syn() [114], on the oblique dendrites, and localized following the rationale reported in Vitale et al. [112]. Peak conductances were initially set at 1e-5 nS and 0.5 nS for the inhibitory and excitatory synapses, respectively, with random activation at 40 Hz. We then increased the peak conductance of the excitatory synapses by multiplying it by an increasing factor. All simulations were carried out using the NEURON simulation environment [115].

Imaging analyses procedures and statistical analysis

Fluorescence Intensity and transfection efficiency quantification

Fluorescence intensity quantification was performed using ImageJ. The image was first opened and adjusted as needed to optimize contrast and clarity, and a threshold was then applied on the channel of interest by selecting an appropriate range of pixel intensities, to isolate the signal. Once the threshold was defined, the mean pixel intensity within the selected area was measured to quantify the fluorescence signal. The transfection efficiency (%) was calculated as the proportion of fluorescent (or positively marked) cells relative to the total cell population for each analysed field. The reported results derived from at least n=3 experiments.

Subcellular localization analysis

For the analysis of TMEM151A subcellular localization, the total cellular TMEM151A signal intensity was first quantified for each analyzed cell. Subsequently, regions of interest (ROIs) were manually drawn over specific organelle markers (GM130 for Golgi apparatus, Calreticulin for endoplasmic reticulum), and TMEM151A fluorescence intensity within these ROIs was measured. The proportion of TMEM151A localized to each organelle was calculated by dividing

the TMEM151A signal within the ROI by the total TMEM151A fluorescence of the entire cell. This ratio represents the relative distribution of TMEM151A in each subcellular compartment, independently of potential differences in total TMEM151A expression between experimental conditions. These measurements were then used to compare different TMEM151A variants to the control condition, allowing the identification of potential alterations in subcellular localization.

Neurites Length

Neurite length analysis was carried out using the NeuronJ plugin of ImageJ. Prior to neurite tracing, image calibration was performed to ensure accurate measurements by entering the appropriate scale value according to microscope magnification (e.g., 0.320 µm/pixel for 20x, 0.160 µm/pixel for 40x). Neurites were traced manually. NeuronJ calculated and displayed the total neurite length (SumLen), which was subsequently analysed for comparison towards a control condition, set as 100%.

Sholl Analysis

Sholl analysis was performed using ImageJ with the NeuronJ and Concentric Circles plugins. After tracing all neurites as previously described for the Neurites length analysis, a snapshot containing only the drawn tracings was saved, and the soma center was identified (its X/Y coordinates recorded). The Concentric Circles plugin was then used to generate 10 concentric rings centered on the soma, distanced each other by 15 µm. Neurite intersections with each circle were manually counted. Data are reported as means of the number of neurites intersections with each circle.

Statistical Analysis

Data were presented as means ± standard error of the mean (SEM), with the number of cells (n) specified in the figure legends. Normality of data distribution was assessed using the D'Agostino-Pearson normality test. Variance between two groups was compared using the F-test. For comparisons between two normally distributed groups, the unpaired two-tailed Student's T-test was applied. In case of non-normal distribution, the Mann-Whitney U-test was used. When comparing more than two normally distributed groups, one-way ANOVA followed by post hoc multiple comparison tests was employed. A significance level of 0.05% (corresponding to 95% confidence intervals) was applied to all statistical tests. Statistical analyses were performed using Prism software (GraphPad Software, Inc.).

Results – Aim 1: *SCN2A*

NaV1.2 A1659V

Clinical Features suggesting unforeseen response to sodium blockers

Pathogenic variants in the *SCN2A* gene are associated with a broad phenotypic spectrum, including Benign Familial Infantile seizures, intellectual disability, developmental and epileptic encephalopathy, and autism. As previously described, GOF variants manifest with seizures in the neonatal period and may respond to SCBs, whereas LOF variants generally present later in infancy or childhood and are nonresponsive to SCBs.

We focused on the NaV1.2 A1659V variant, identified in three unrelated individuals. Notably, despite the very early onset of seizures—suggesting a GOF effect—the patients showed unexpected or limited response to SCBs, representing an unforeseen pharmacological profile [116].

Individual 1: A 1-year-and-1-month-old boy, born to healthy, non-consanguineous parents. Seizures started on the first day of life, including limb dystonia, facial dyskinesia, apnea, and tachycardia. Multiple anti-seizure medications, including phenytoin (15 mg/kg/day), were ineffective. Seizures (>50/day) severely impaired development; at last follow-up (at 1 year and 1 month of age), he is non-verbal, lacks eye contact, and cannot sit or roll over. Brain MRI at 5 months was normal; EEG showed burst suppression at onset and multifocal epileptiform activity at follow-up.

Individual 2: A 25-year-old woman with focal motor seizures from day three of life. She continues to experience daily seizures and has severe intellectual disability, being non-verbal and showing pyramidal signs. Lamotrigine and valproate were ineffective. Brain MRI at 12 months was unremarkable; EEG at 3 years showed slow background activity with multifocal spikes.

Individual 3: A 1-year-old boy with myoclonic and short tonic seizures plus apnea starting on day one. Multiple anti-seizure medications were ineffective; adverse events included neutropenia (carbamazepine) and QT prolongation (mexiletine). He has severe developmental delay and comorbidities including transient SIADH and hip dysplasia. MRI showed mildly enlarged lateral ventricles and corpus callosum T2 hyperintensity; EEG showed burst suppression during sleep.

NGS revealed the *SCN2A* de novo missense variant c.4976C>T (p.A1659V) in our probands. The Ala 1659 is localized in the intracellular loop between the S4 and S5 segments of the NaV1.2 fourth domain (Fig. 2A) and is highly conserved both in other human sodium channels and in orthologs of other species (Fig. 2B).

Notably, despite similar clinical manifestations (Table 1), we identified the variant in a mosaic state in patients 1 and 3, with approximately 20% expression in blood lymphocytes. In proband 1, the mutant allele frequency was 26% (73/279 alleles), while in proband 3, the allele frequency was 20% (94/462) based on read counts of NGS; the mosaic was confirmed by Sanger sequencing (Fig. 2C). To understand if the variant is also expressed in other tissues, we verified its presence using fibroblast from punch biopsies. For both probands Sanger sequencing showed the same percentage of mosaicism (data not shown).

We used shinyapp prediction tool, a machine learning method that predicts functional effects of genetic missense variants in voltage-gated sodium and calcium channels, to evaluate the variant predicted impact on the patients, and found this variant predicted to be pathogenic

with a probability of 0.96 as GOF. In addition, the Franklin tools (https://franklin.genoox.com, Franklin by Genoox) based on the American College of Medical Genetics guidelines also indicates p.A1659V as strong pathogenic [19].

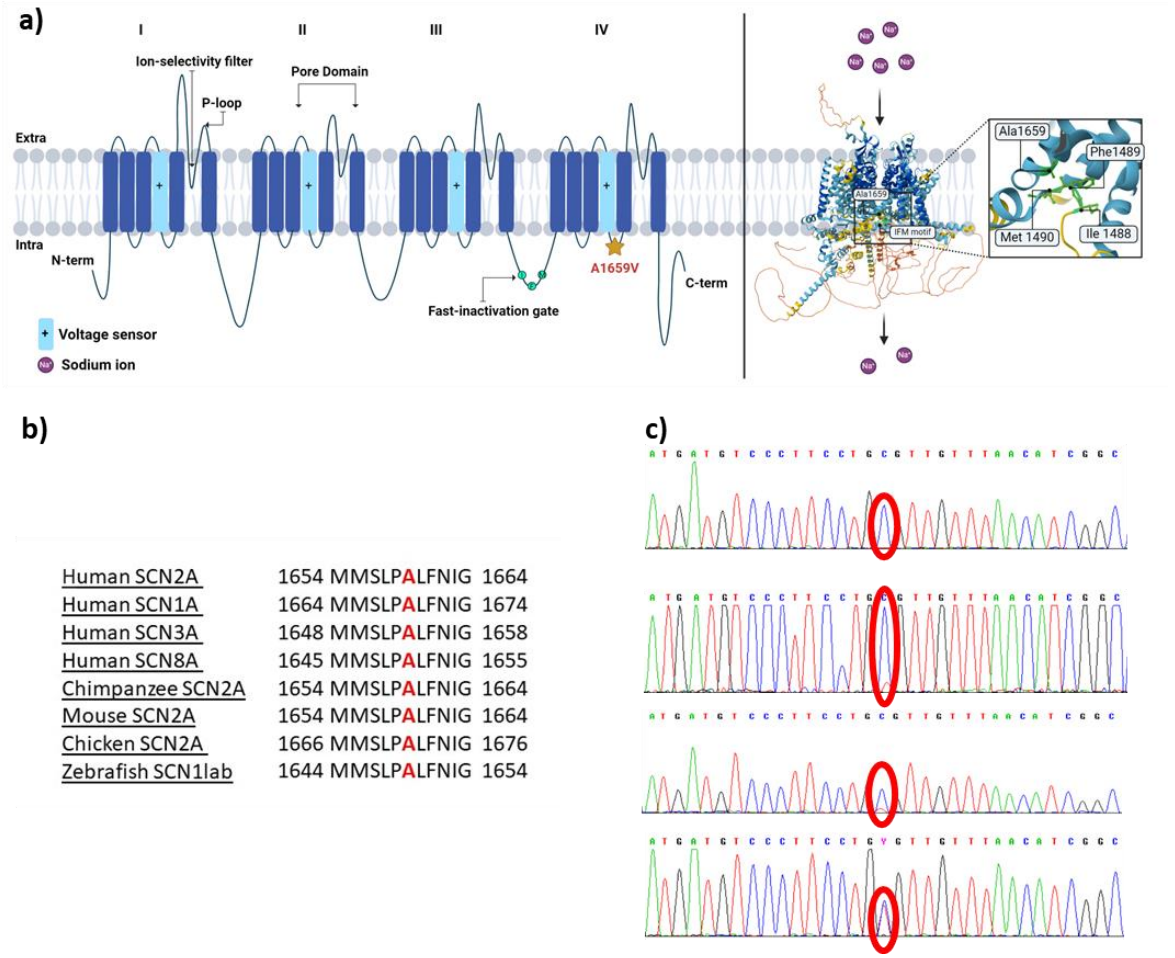

Figure 2: p.A1659V location in NaV1.2 channel. A: Schematic representation of the topology of the NaV1.2 α-subunit showing its four homologous domains. Orange star indicates the p.A1659V variant. Right panel shows the AlphaFold structure prediction of the human NaV1.2 α-subunit. The A1659 residue and the IFM motif are highlighted in the box on the right. B: Protein alignment highlights that p.A1659 is conserved in human and in other species NaV α-subunits. C: Chromatographs of the three patients with the same SCN2A variant in comparison to a sequence of a healthy control (top panel), central and bottom panels show the sequences of patient 1 and 3 (variant in mosaic state) and the sequence of patient 2 (variant in heterozygous state), respectively. Adapted from Corradi et al. 2026 [116].

The A1659V variant does not affect NaV1.2 channel expression.

We then investigated changes in the expression profile and biophysical properties of the A1659V mutant NaV1.2 channel. Recombinant cerebral NaVs show high rate of recombination when propagated in bacteria, hindering DNA manipulation and functional studies, we therefore used the stabilized pIR-CMV-*SCN2A* plasmid encoding for NaV1.2 to insert the pathogenic variant (p.A1659V) by site-directed mutagenesis to overcome these technical difficulties. [105]

We initially assessed the impact of the variant on channel expression. To this aim, NaV1.2 WT and A1659V mutant were transfected in naïve HEK293 cells, and the protein extracts were analyzed by western blot (Fig. 3A, left). The NaV1.2 A1659V mutant showed no significant differences in the expression levels compared to the WT NaV1.2 (Fig. 3A, right). We also verified the absence of endogenous expression of NaV1.2 channel by HEK293 cells (Fig. 3A,

left first lane). Transfected HEK293 were also analyzed by immunofluorescence using anti-PanNaV antibody (Fig. 3B, left). No differences in the number and fluorescent intensity of transfected cells (Fig. 3B, right) and in signal distribution (Fig. 3C) were identified between NaV1.2 WT and A1659V mutant. Moreover, image analysis by confocal microscopy did not display difference in the quantification in cells transfected with WT or A1659V variant (Fig. 3C). We conclude that the A1659V variant does not impact on the expression level of NaV1.2 channels.

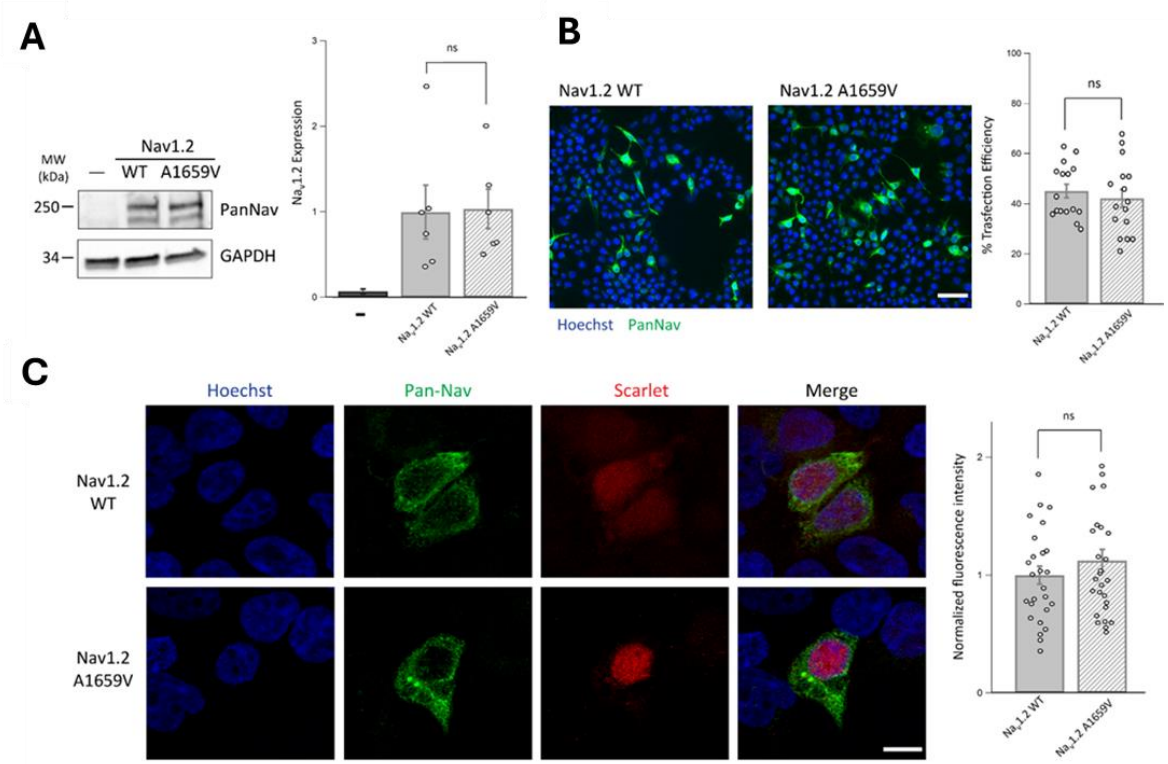

Figure 3: The A1659V variant does not affect NaV1.2 channel expression. A Left: Protein extracts from HEK293 cells transfected with either WT or A1659V NaV1.2 or untrasfected (indicated with a horizontal bar) were analyzed by western blotting using anti-PanNav antibody. Representative immunoblot. Right: Densitometric analysis of the immunoreactive bands. GAPDH was used as loading control. The expression levels were normalized on NaV1.2 WT mean expression value and are shown as means +/- SEM of n=6 independent experiments. B: Representative images of HEK293 cells transfected with either WT or A1659V NaV1.2 and immunolabelled with anti-PanNav antibody (green). DAPI staining was used to visualize nuclei (blue). Scale bar, 50 µm. Right: The percentage of transfection efficiency was calculated as the ratio between the anti-PanNav positive cells and total cells in the same field. Data represent means +/- SEM with superimposed individual values from n=3 independent experiments. C Left: representative confocal images of HEK293 cells transfected with either WT or A1659V NaV1.2 and immunolabelled with anti-PanNav antibody (green). DAPI staining was used to visualize nuclei (blue) and Scarlet signal is indicative of transfection (red). Scale bar, 5 µm. Right: Quantification of PanNav fluorescence intensity calculated as the ratio between the total PanNav fluorescence signal and the number of PanNav positive cells in the same field. The fluorescence intensity levels were normalized on NaV1.2 WT mean intensity value and are shown as means +/- SEM with superimposed individual values from n=3 independent experiments. Statistical analysis was done using Unpaired Student's t-test. Adapted from Corradi et al. 2026 [116].

The A1659V variant modifies NaV1.2 channel activity and biophysical properties.

We investigated functional properties of A1659V variant by patch-clamp technique in whole-cell configuration in transiently transfected HEK293 cells with either WT or A1659V NaV1.2 variant. We observed a strong reduction of inward sodium currents in cells transfected with mutant channel (Fig. 4A). Notably, the A1659V mutant exhibited a significantly smaller current density with a reduction of about 80% with respect to the WT in response to all depolarizing stimuli that activate the voltage-gated sodium-channel (Fig. 4B, C).

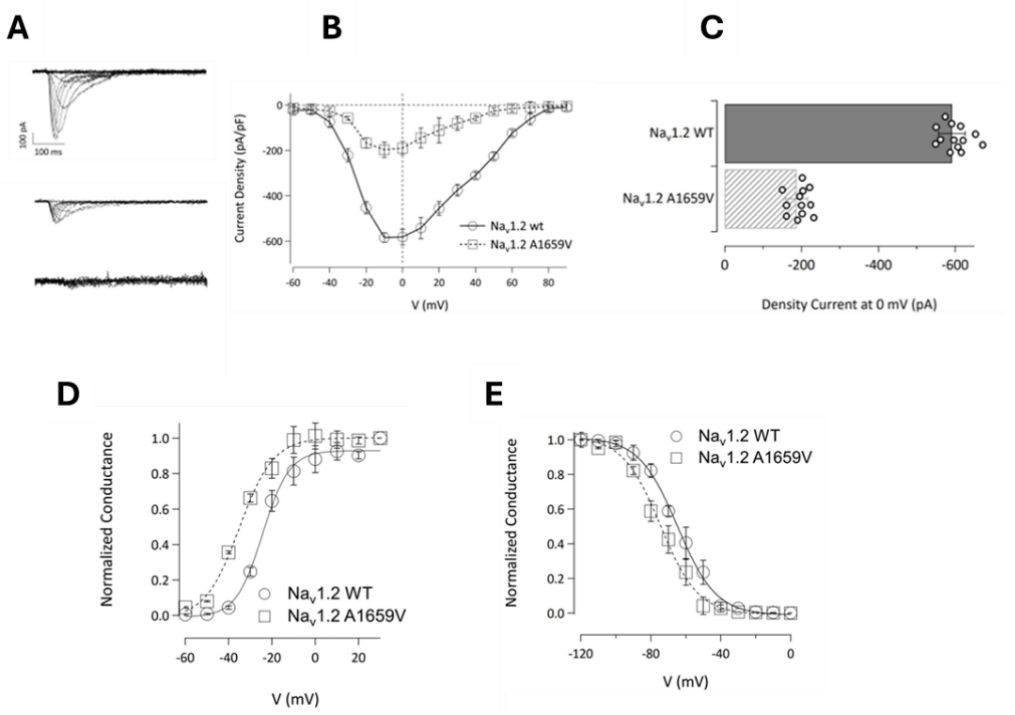

Figure 4: The A1659 variant exhibits a smaller Na^+ current with respect to the NaV1.2 WT channel. A: Whole-cell sodium representative current traces recorded from cells transiently expressing WT (top panel), or A1659V (central panel) cDNA constructs or only CD8 (bottom panel). Currents were elicited from a holding potential of -90 mV with 20 ms depolarizing voltage steps between –60 and +90 mV. B: Average current density-voltage relationships for HEK293 cells transfected with cDNA WT (dot symbols and solid lines) or mutated NaV1.2 (square symbols and dashed lines) as indicated. C: Mean of density current values measured at 0 mV (Ipeak) for indicated channels (WT NaV1.2, filled bar; A1659V NaV1.2, striped bar). Data are expressed as mean±SEM from n≥12 independent experiments. D: Overlay of voltage dependence of steady-state activation curves recorded from cells expressing WT channel (dot symbols and solid lines) or mutated (square symbol and dashed and lines) cDNAs. E: Overlay of voltage dependence of steady-state inactivation curves recorded from cells expressing WT channel (dot symbols and solid lines) or mutated (square symbols and dashed lines) cDNAs. Symbols represent mean values with SEM. Lines represent averaged Boltzmann fits to the data. Quantitative data for the kinetics and voltage dependence of activation are presented in the table 1. Data are expressed as mean±SEM from n≥12 independent experiments. Adapted from Corradi et al. 2026 [116].

In addition, we observed that the A1659V variant showed significant changes in the voltage dependence of activation and inactivation channel properties; a leftward shift of about -10 mV in voltage dependence of activation (Fig. 4D and Table 1) and a shift of about +10 mV in the voltage of half inactivation (Fig. 4E and Table 1).

Variant	$V_{1/2}$ Activation (mV)	Slope activation (mV)	$V_{1/2}$ Inactivation (mV)	Slope Inactivation (mV)
NaV1.2 WT	-24.40 ± 0.77	6.8 ± 0.1	-64.77 ± 0.83	5.99 ± 0.77
NaV1.2 A1659V	-35.10 ± 0.20 *	7.8 ± 0.3	-74.51 ± 1.23 *	6.75 ± 1.11

*Table 1: Functional features of WT and A1659V NaV1.2 channels. **Legend:** $V_{1/2}$ is voltage of half maximal activation or inactivation as indicated. Slope factor describes voltage sensitivity of the channel. Data are expressed as mean±SEM from n≥12 independent experiments. *p<0.01 versus WT determined by Student's test.*

Computational modeling in neocortical and hippocampal rodent pyramidal cells

To gain insights into the effect of the variant on single-cell firing behaviour, we decided to test the kinetics of both native and A1659V NaV1.2 (Fig. 4) by computational modelling. We used two previously published models of neocortical and hippocampal rat pyramidal cells as templates [111], [112] for neocortical and hippocampal neuron respectively, replacing the standard Hodgkin-Huxley Na^+ channels, originally inserted, with the NaV1.2 model described

in the present study. After configuring the native cell model, we substituted half of the healthy channels with the A1659V variant. Figures 5 A, B, and C clearly show that replacing 50% of the channels with the variant leads to increased firing frequency and a lowered action potential threshold in all simulated cells. This effect is especially pronounced in hippocampal neurons where the minimum current required to evoke an AP decreases from 0.6 nA to 0.2 nA, and at 0.6 nA the number of APs triples. This phenomenon is illustrated by the example traces in Figures 5 D, E, and F, where both neocortical and hippocampal neurons, under current injection and synaptic activation, show a narrower inter-spike interval along the AP train in the presence of the NaV1.2 variant.

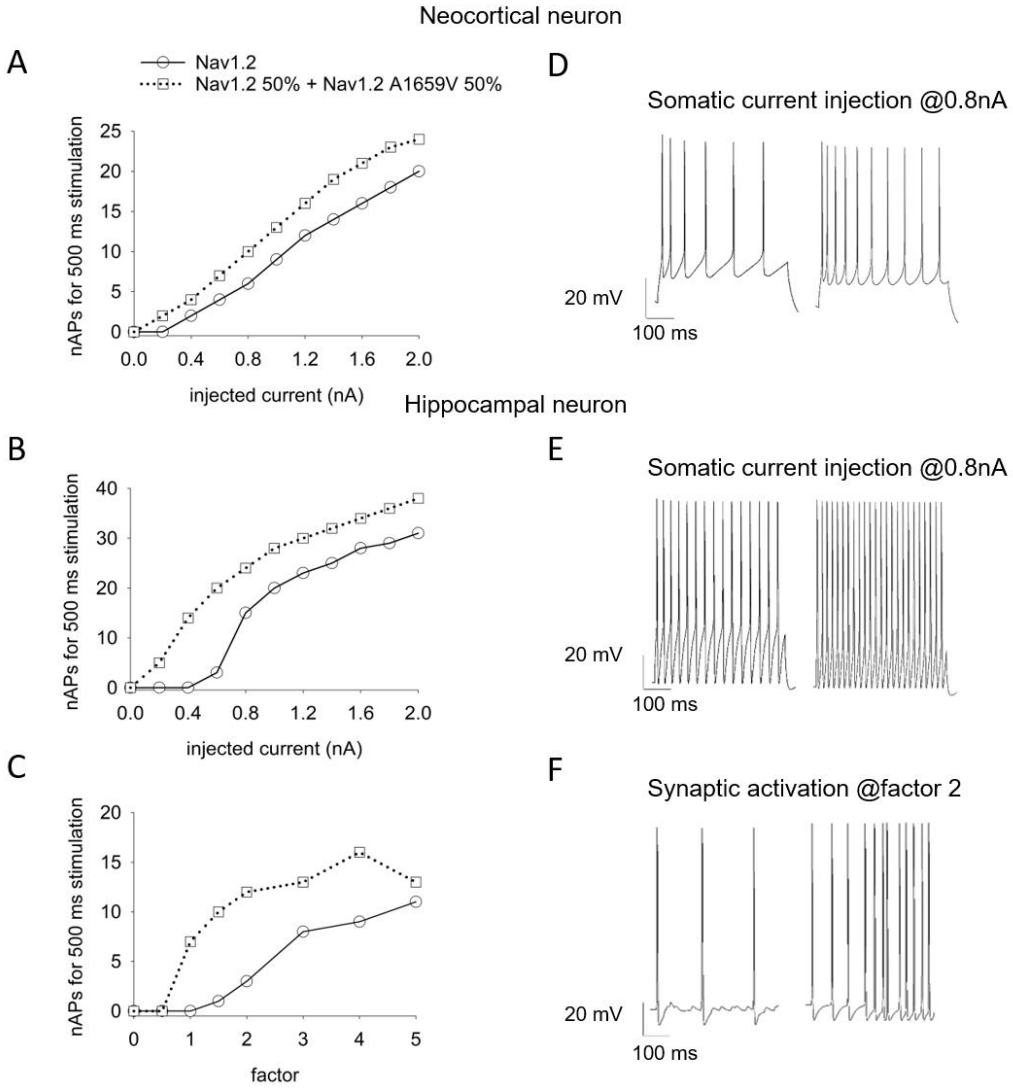

Figure 5: Simulated neuronal excitability in a mouse cortical and a rat hippocampal pyramidal cell. The cell expresses either native NaV1.2 (circular symbol and solid line) or a combination of NaV1.2 and the NaV1.2 A1659V variant, each contributing 50% to the total channel density (square symbol and dotted line). Number of spikes as a function of the current injected through somatic stimulation for 500 ms, in a (A) neocortical neuron and (B) hippocampal neuron; (C) number of spikes in response to 40 Hz synaptic stimulation for 500 ms in a hippocampal neuron. Example of modeled traces in response to 0.8 nA current injections in a (D) neocortical neuron and (E) hippocampal neuron (left NaV1.2 and right NaV1.2 A1659V); (F) example of modeled traces under synaptic stimulation with a doubling of the weight of the netcon linking the excitatory synapses to the soma (left NaV1.2 and right NaV1.2 A1659V). Adapted from Corradi et al. 2026 [116]

While the computational analysis unambiguously demonstrates a GOF impact, manifested as increased excitability and reduced firing threshold, the functional study of the A1659V variant

reveals that this substitution alters the channel's biophysical properties, producing both GOF and LOF effects compared to the reference protein. Together, these two approaches support the hypothesis that the variant exhibits mixed functional properties.

SCN2A I237N

More recently, we enrolled a second pediatric patient who met the criteria established for this functional study: the presence of a mosaic *SCN2A* variant causative of an extremely severe phenotype, associated with the lack of efficacy of conventional pharmacological treatment.

Clinical Features suggesting unforeseen response to sodium blockers

The patient is a 4-year-old boy who developed epileptic spasms within the first days of life. At the most recent follow-up, he presents with intellectual disability, absence seizures, and movement disorders. Treatment with sodium channel blockers, such as carbamazepine (CBZ), was ineffective, and multiple antiepileptic drugs were administered over time without clinical benefit.

This second case allowed us to investigate the missense variant of the *SCN2A* gene, c.710T>A (p.I237N), which had not previously been functionally characterized. In this patient as well, the clinical phenotype was suggestive of a gain-of-function effect; nevertheless, SCBs were administered without therapeutic efficacy. NGS analysis, extended to the parents, identified the de novo missense variant c.710T>A (p.I237N) as the only causative variant in the proband, present in a mosaic state with approximately 20% of cells carrying the mutation. The variant was subsequently confirmed by Sanger sequencing (Fig. 6B).

Residues I237 and A1659 are both located in the intracellular loop between the S4 voltage sensor and the S5 transmembrane segment of their respective functional domains (I237 in the first domain and A1659 in the fourth one), suggesting a similar role for these two residues in the channel inactivation process (Fig. 6A).

The I237N variant does not affect NaV1.2 channel expression.

We assessed the impact of the I237N variant on channel expression as previously done for the A1659V variant. To this aim, NaV1.2 WT and I237N mutant were transfected in naïve HEK293 cells, and the protein extracts were analyzed by western blot (Fig. 6C). The NaV1.2 I237N mutant showed no significant differences in the expression levels compared to the WT NaV1.2 (Fig. 6C, right). Transfected HEK293 were also analyzed by immunofluorescence using anti-PanNaV antibody (Fig. 6 D, E). No differences in the number and fluorescent intensity of transfected cells and in signal distribution were identified. Moreover, image analysis by confocal microscopy did not display difference in the quantification in cells transfected with WT or I237N variant. We conclude that the I237N variant does not impact on the expression level of NaV1.2 channels.

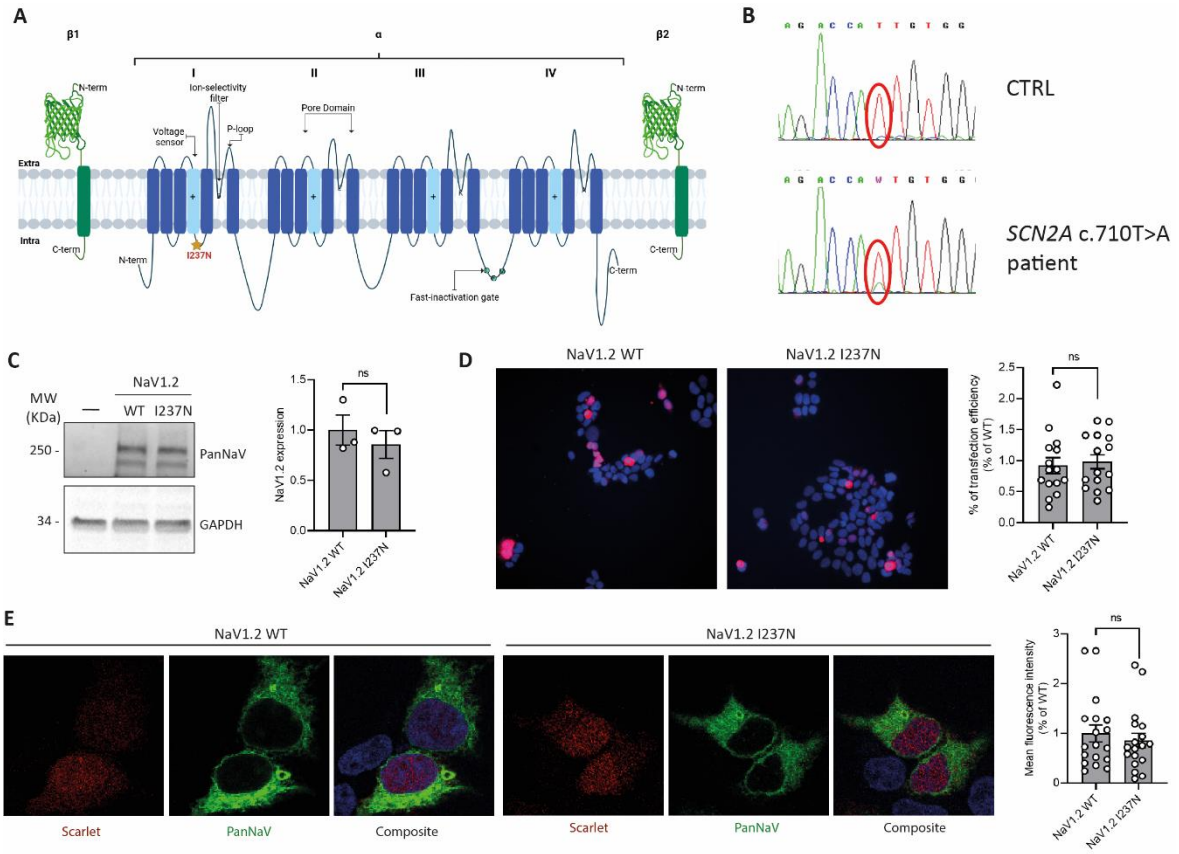

Figure 6: The I237N variant does not affect NaV1.2 channel expression. A: Schematic representation of the topology of the NaV1.2 α-subunit showing its four homologous domains. Orange star indicates the p.I237N variant. B: Chromatograph of the I237N patient in comparison to a sequence of a healthy control (top panel). C Left: Protein extracts from HEK293 cells transfected with either WT or I237N NaV1.2 or untrasfected (indicated with a horizontal bar) were analyzed by western blotting using anti-PanNaV antibody. Representative immunoblot. Right: Densitometric analysis of the immunoreactive bands. GAPDH was used as loading control. The expression levels were normalized on NaV1.2 WT mean expression value and are shown as means +/- SEM of n=3 independent experiments. D: Representative images of HEK293 cells transfected with either WT or I237N NaV1.2 and immunolabelled with anti-PanNaV antibody (green). DAPI staining was used to visualize nuclei (blue). Right: The percentage of transfection efficiency was calculated as the ratio between the Scarlet positive cells and total cells in the same field. Data represent means +/- SEM with superimposed individual values from n=3 independent experiments. E Left: representative confocal images of HEK293 cells transfected with either WT or I237N NaV1.2 and immunolabelled with anti-PanNaV antibody (green). DAPI staining was used to visualize nuclei (blue) and Scarlet signal is indicative of transfection (red). Right: Quantification of PanNaV fluorescence intensity calculated as the ratio between the total PanNaV fluorescence signal and the number of PanNaV positive cells in the same field. The fluorescence intensity levels were normalized on NaV1.2 WT mean intensity value and are shown as means +/- SEM with superimposed individual values from n=3 independent experiments. Statistical analysis was done using Unpaired Student's t-test. Unpublished results.

The I237N variant modifies NaV1.2 channel activity, but does not impact on the channel biophysical properties.

To evaluate the impact of the variant on NaV1.2 channel function, we applied the same stimulation protocols used for the A1659V mutation to HEK293 cells transiently transfected with either the wild-type or mutant channel. The I237N variant alters NaV1.2 channel activity; specifically, we observed an approximately 50% reduction in inward sodium current density compared to the wild-type channel (fig. 7 A, B, Table 2).

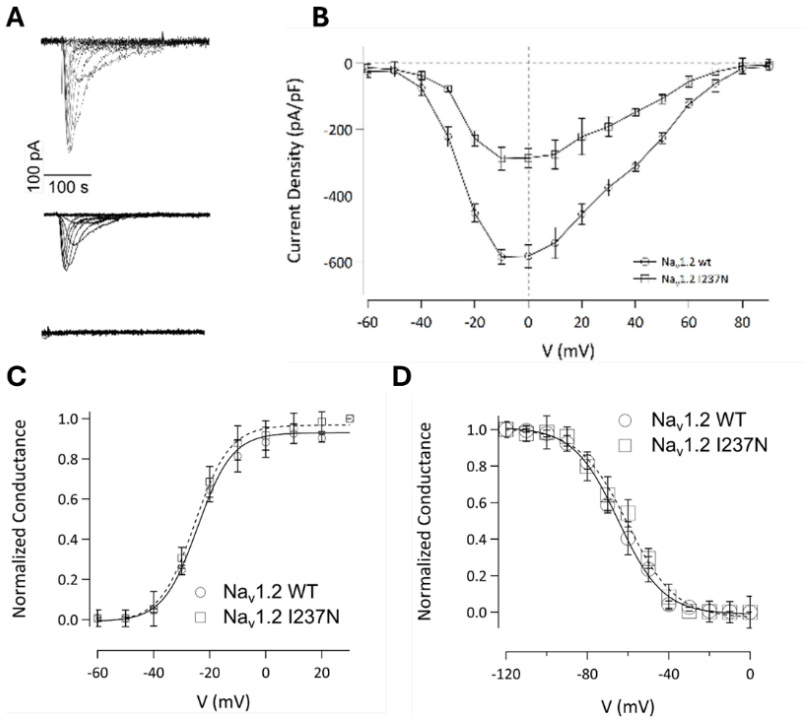

Figure 7: The I237N variant exhibits a reduced Na^+ current compared with the wild-type channel. A: Representative Na^+ current traces recorded from HEK293 cells transfected with the WT plasmid (top panel), the mutant plasmid (middle panel), or the reporter gene alone (bottom panel). B: Mean current–voltage (I–V) relationships for HEK293 cells transfected with the wild-type channel (circles, solid line) or the mutant channel (squares, dashed line), as indicated. C: Overlay of voltage dependence of steady-state activation curves. D: Overlay of voltage dependence of steady-state inactivation. Both panels C,D were recorded from cells expressing WT channel (dot symbols and solid lines) or mutated (square symbols and dashed lines) cDNAs. Symbols represent mean values with SEM. Lines represent averaged Boltzmann fits to the data. Quantitative data for the kinetics and voltage dependence of activation are presented in the table 2. Data are expressed as mean±SEM from n≥12 independent experiments. Unpublished results.

Surprisingly, the I237N variant does not induce any alteration in the voltage dependence of channel activation or inactivation; the only effect observed relative to the native protein was a reduction in channel conductance (Fig. 7 C, D).

Variant	$V_{1/2}$ Activation (mV)	Slope activation (mV)	$V_{1/2}$ Inactivation (mV)	Slope Inactivation (mV)
NaV1.2 WT	-24.40 ± 0.77	6.8 ± 0.1	-64.77 ± 0.83	5.99 ± 0.77
NaV1.2 I237N	-25.32 ± 0.63	6.2 ± 0.6	-60.33 ± 1.48 *	8.84 ± 1.4

Table 2: Functional features of WT and I237N NaV1.2 channels. Legend: V1/2 is voltage of half maximal activation or inactivation as indicated. Slope factor describes voltage sensitivity of the channel. Data are expressed as mean±SEM from n≥12 independent experiments.

Discussion – Aim 1: *SCN2A*

The four homologous neuronal voltage-gated sodium channel (i.e., NaV1.1, NaV1.2, NaV1.3, and NaV1.6) are critical for the electrical firing of neurons, but also for the macroscopic anatomical development of the brain [117]. Their expression profile and microscopic neuronal position changes in the brain. *SCN2A* is mainly expressed at the axon initial segments and nodes of Ranvier of myelinated nerve fibers during early development, then, in the adult, it locates at the AIS of unmyelinated axons [21]. Consequently, changes in NaV1.2 biophysical properties can result in diverse neurodevelopmental disorders (NDs).

Within phenotypic heterogeneity, grouping based on genetic/functional features has also been attempted [35]. As described, missense GOF variants commonly lead to early-onset seizures, both self-limited and with later delayed psychomotor development. Conversely, missense LOF variants are associated with later-onset epilepsies and non-epilepsy phenotypes such as ASD/ID.

From an electrophysiological perspective some variants fail to be strictly classified into GOF or LOF, exhibiting more complex biophysical properties and therefore are defined as “mixed” and they are identified in patients with epilepsy characterized by neonatal seizures [118], [119].

Here we investigated the biophysical properties of two previously uncharacterized NaV1.2 missense variant leading to a severe, encephalopathic phenotype in the affected patients. Peculiarly, the variant reached clinical attention due to the unexpected treatment response. All subjects, for both variants studied, had clinical features compatible with a GOF variant and showed a poor clinical response to commonly used sodium channel blockers (SCBs) (i.e, carbamazepine, phenytoin, lamotrigine). When characterizing the *in vitro* properties of the c.4976C>T (p.A1659V) and the c.710T>A (p.I237N) variants, we observed no impact on the NaV1.2 channel expression with respect to the WT channel; hence our missense variants do not impact the protein synthesis and maturation processes. Then, we measured the current passing through the mutated channels and observed smaller currents in both variants compared to native protein. Based on this, we hypothesized that the variants caused a LOF mechanism. However, the A1659V variant also altered the voltage-dependence of activation and inactivation. The hyperpolarizing shift of the activation curve is in principle a GOF effect, whereas the leftward shift of the inactivation curve represents a LOF. In a similar study, Miao et al. analyzed two de novo *SCN2A* variants: p.P1658S (adjacent to p.A1659V) and p.A1773T in the S6 segment of domain IV [118]. They demonstrated that both missense variants were either LOF (P1658S) or mixed (A1773T). Specifically, P1658S caused a complete loss of detectable currents, while A1773T resulted in a significant reduction in current density, accompanied by a hyperpolarizing shift of the voltage dependence of activation and a hyperpolarizing shift in fast inactivation. Therefore, the functional profiles of the A1773T and P1658S variants were very similar to the electrophysiological alterations recorded for the A1659V and I237N variants, respectively, supporting the hypothesis of a possible functional correlation between these residues or their localization within the intracellular S4–S5 loop of homologous domains.

To better understand the association between the A1659V variant and the patients’ phenotype, we used a computational model based on rodent neurons. Models expressing both the native channel and the A1659V NaV1.2 variant exhibited a higher firing frequency and a lower spiking threshold compared to the reference channel alone, across the full range of injected currents and under more physiological conditions achieved through synaptic stimulation. These results suggest that, in these systems, the variant is associated with a GOF effect. This effect was also consistent, across all tested configurations, with the increased neuronal excitability previously observed for the M1770L variant using a similar modeling strategy [120].

We assume that the two substitutions of A1659V or I237N could change the conformation of the S4-S5 linker of DIV or DI, a region of the channel that regulates the NaV1.2 fast inactivation mechanism [121], [122]. Noteworthy both the P1658S and A1773T variants, as well as the

A1659V and I237N, map to the channel sequences involved in fast inactivation processes [123], causing decreased currents and LOF-associated phenotypes.

Clinically, Miao's variants exhibited LOF or mixed properties [118], including reduced current density and enhanced fast inactivation. However, patients with these variants displayed milder phenotypes compared to the severe cases observed in our cohort. The mean age at seizures onset was 7 months and the impact on development was moderate or absent. All our four patients (three carrying the A1659V variant and one carrying the I237N variant) had severe developmental delay/intellectual disability. These findings suggest that even pathogenic variants in adjacent aminoacidic residues may lead to fine differences in the biophysical channel properties with diverse phenotypic expression.

Our probands do not respond to SCB, like other patients carrying mixed-effect variants (A1773T, R1312T, and E1211K), with electrophysiological properties similar to those identified for the A1659V variant here described. In vitro application of SCB to these variants results in a further reduction of channel function, thereby explaining the lack of treatment efficacy in these patients. We hypothesize that, in the case of the A1659V variant as well, these compounds may fail to produce a beneficial effect [118], [119]. Furthermore Garcia and collaborators recently demonstrated, in vitro and in vivo, that the specific blockade of the NaV1.2 channel paradoxically induces neuronal hyperexcitability. Based on this finding, we hypothesize that LOF variants could also lead to an epileptic phenotype in pediatric patients and it may also account for the lack of efficacy of SCB in epileptic patients carrying specific NaV1.2 variants, as observed in the probands described here. The reduced channel activity, resulting from LOF or mixed variants, likely underlies the pharmaco-resistance [111]. Based on the clinical pharmaco-resistance to SCB and the mixed functional effects observed in vitro, alternative treatment strategies may be considered. Given the presence of GOF features such as enhanced neuronal excitability in computational models, agents acting on excitatory-inhibitory balance (e.g., GABAergic modulators) or non-sodium channel targeted therapies (e.g., cannabidiol, steroids, or mTOR pathway modulators) might offer therapeutic benefit in selected cases. However, the variable phenotype underscores the importance of personalised approaches and the need for further functional testing to guide treatment selection.

The impact of the studied variants on channel function is reinforced not only by the severity of the epileptic phenotype of patients, but also by the fact that three of them (two for A1659V and one for I237N variant) carried the variant at the mosaic state. We found approximately 20% of mutated cells in two analyzed tissues (lymphocytes and fibroblasts) for both children (pts #1, #2 and #4). Based on this observation we can hypothesize that the variant expression in the brain may also be present with a similar percentage of mosaicism. If this hypothesis is true, it would be sufficient that the variants are expressed in a reduced percentage of neurons to cause impaired network dynamics and determine severe clinical manifestation, highlighting the importance of the A1659 and I237 residues for the physiological NaV1.2 channel function.

The investigation of these two first *SCN2A* mosaic variants led to the research in clinical databases of other *SCN2A* mosaic variants that may help to identify a pattern of behavior in the disease condition. This led us to identify other mosaic variants, found at different percentages in the patients' fibroblasts, paving the way to further studies in this direction.

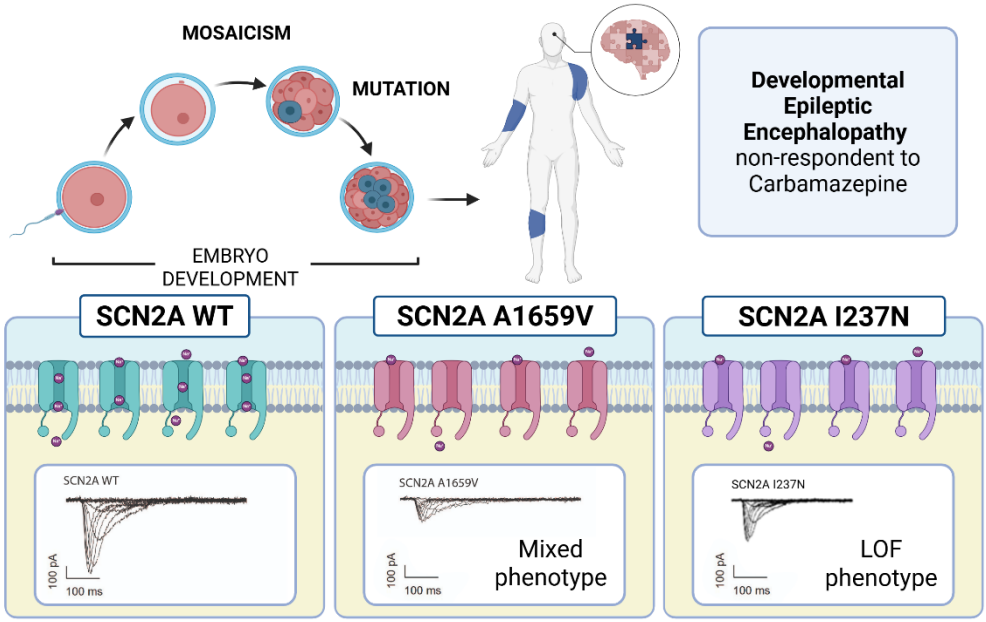

Graphical abstract Aim 1: SCN2A. Created with BioRender.com

Results – Aim 2: PRRT2

PRRT2 variants

To date, sixty PRRT2 missense variants have been reported (Fig. 8), the majority of which [70] are clustered within the COOH-terminal transmembrane (TM) domain, a region implicated in the modulation of NaV1.2 and NaV1.6 channels. This TM domain has been characterized by *in-silico* molecular dynamics simulations as a structured and stable region of the protein. However, investigating the pathogenic mechanisms of PRRT2 variants is particularly challenging, as most reported mutations—including the most frequent pathogenic variant—result in a near-complete or complete loss of protein expression, precluding functional analyses.

We therefore hypothesized that a subset of missense variants might retain detectable expression and thus allow the investigation of PRRT2-dependent pathogenic mechanisms. Following an extensive review of the literature, we identified four COOH-terminal missense variants previously reported to be expressed. In addition, we systematically screened additional missense variants within the same domain and identified four further mutants that preserved protein expression (not shown).

Using this selected panel of eight expressed COOH-terminal PRRT2 missense mutants (Fig. 9), we investigated the pathogenic mechanisms of PRRT2 dysfunction by assessing their impact on PRRT2–NaV1.2 interaction and sodium channel modulation.

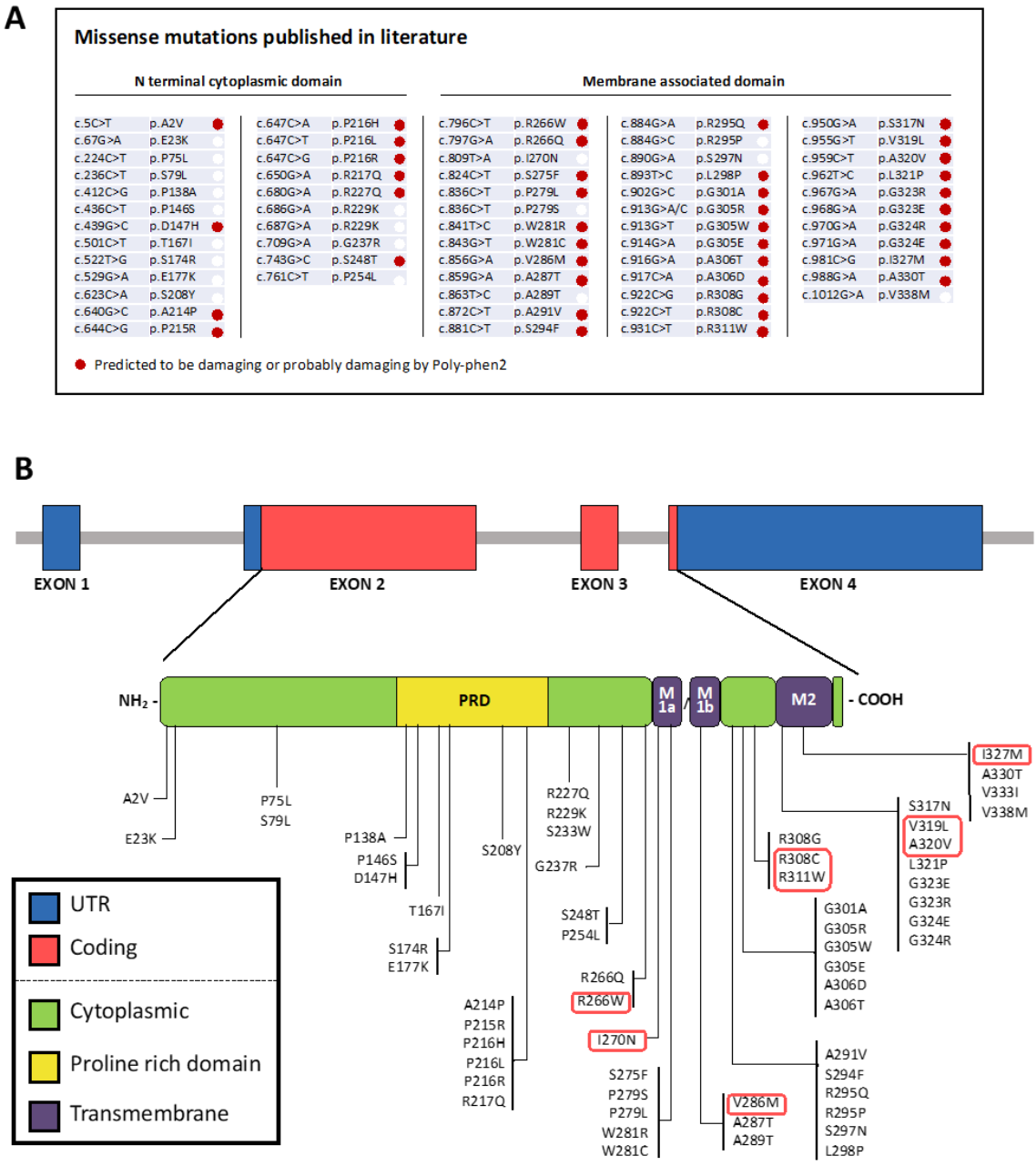

Figure 8: The PRRT2 missense variants described in the literature. A: Table listing the PRRT2 missense variants published in literature (updated by January 2023). Red dots indicate variants predicted to be damaging or probably damaging by Poly-phen2. Sources: National Center for Biotechnology Information (NCBI)[Internet]. Bethesda (MD): National Library of Medicine (US), National Center for Biotechnology Information; [1988] – [cited 2023 Jan 31]. Available from: https://www.ncbi.nlm.nih.gov/. B: Schematic view of the PRRT2 gene and protein structures with superimposed the reported pathogenic missense mutations. The variants of interest are indicated in red squares. UTR, untranslated region. Reproduced from Sterlini et al. 2023 [74].

The choice of PRRT2 variants

We focused on 8 COOH-terminal missense pathogenic variants (Fig. 9), as previously described. The four mutants that were already reported to be expressed in heterologous systems are R266W, R308C, R311W, I327M. The four further point variants that were not previously investigated are I270N, V286M, V319L, A320V (see Table 3 for references).

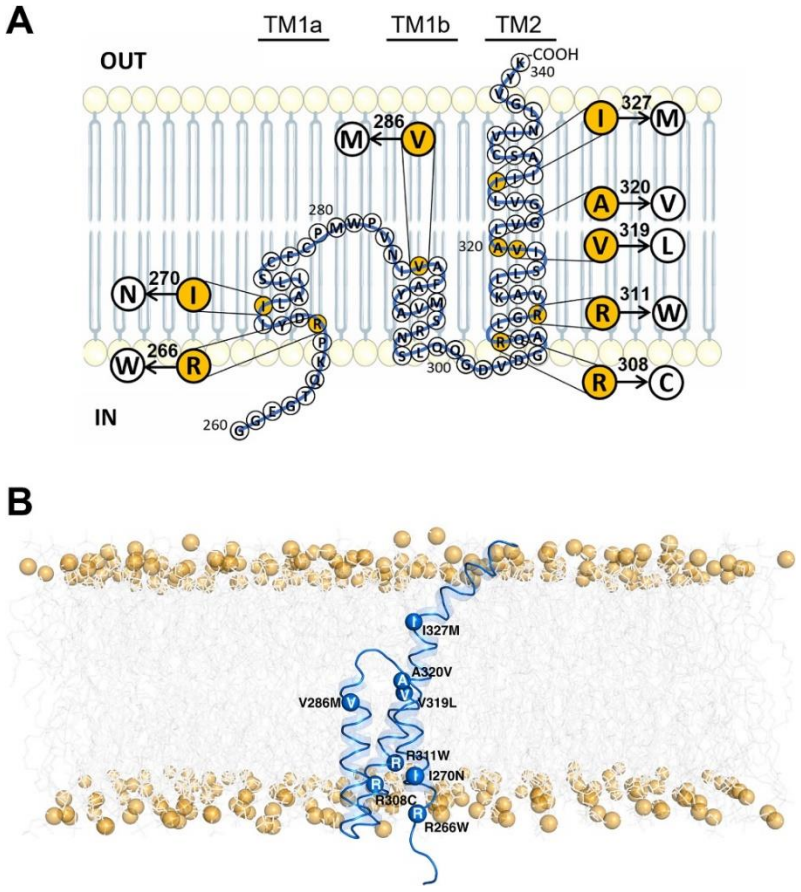

Figure 9: Multidimensional maps of missense variants within the PRRT2 membrane-associated domain. A: Schematic 2D view of the PRRT2 TM domain. The eight PRRT2 missense pathogenic variants investigated in this study are highlighted. B: Snapshot of the TM domain of PRRT2 extracted from an MD trajectory. The backbone of the protein is represented as a blue transparent ribbon; α-carbons of mutated residues are shown as navy blue spheres; phospholipid acyl tails are depicted as transparent grey sticks; phosphate atoms are shown as orange spheres. Water molecules are not included for clarity. Reproduced from Sterlini et al. 2023 [74].

PRRT2 variant		**Phenotype**	**Poly-phen2**	**Protein expression**	**Plasma membrane targeting**	**Reference**
c.796C > T	R266W	PKD	Probably damaging/ damaging	Expression similar to WT (100%)	Expression similar to WT (100%)	[71]
c.809T > A	I270N	PKD	Unknown	Unknown	Unknown	[124]
c.856G > A	V286M	PKD	Probably damaging	Unknown	Unknown	[125]
c.922C > T	R308C	PKD	Probably damaging/ damaging	Expression 50% of WT	Expression 50% of WT	[70], [71]
c.931C > T	R311W	PKD, EA	Probably damaging	Expression similar to WT (100%)	Expression similar to WT (100%)	[70], [71]
c.955G > T	V319L	PKD	Probably damaging	Unknown	Unknown	[126]
c.959C > T	A320V	PKD, BFIE	Probably damaging	Unknown	Unknown	[127]
c.981C > G	I327M	PKD, BFIE	Probably damaging/ damaging	Expression similar to WT (100%)	Expression similar to WT (100%)	[70], [71]

Table 3: List of the selected missense pathogenic variants in the PRRT2 membrane-associated domain and their phenotypic characterization. PKD, paroxysmal kinesigenic dyskinesia; EA, episodic ataxia; BFIE, benign familial infantile epilepsy; WT, wild type.

The PRRT2 missense mutants display physiological expression levels and membrane targeting

Pathogenic PRRT2 mutants were generated by site-directed mutagenesis in the pKH3-PRRT2-HA vector encoding for the human PRRT2 cDNA tagged at COOH-terminal with the 3xHA epitope [42]. Western blot analysis of PRRT2 mutants transfected in the naïve HEK293 cell line (Fig. 10A, left) revealed that the expression of the eight chosen mutants was only slightly decreased with respect to WT-PRRT2, although none of these differences approached statistical significance (Fig. 10A, right). Missense variants are often causative of PRRT2 mislocalization and altered trafficking to the plasma membrane. Thus, we investigated the membrane expression of the mutant isoforms by immunofluorescence on live cells, taking advantage of the extracellular HA epitopes fused at the COOH-terminus of PRRT2. Transfected cells were imaged by confocal microscopy (Fig. 10B, left), and the surface fluorescent signals were normalized to the respective transfection efficiency. Interestingly, all studied variants preserved a correct targeting to the membrane similar to WT-PRRT2 (Fig. 10B, right). We conclude that the missense variants analyzed do not significantly affect protein expression and membrane localization and thereby can be subjected to the functional study of the interactions with NaV channels.

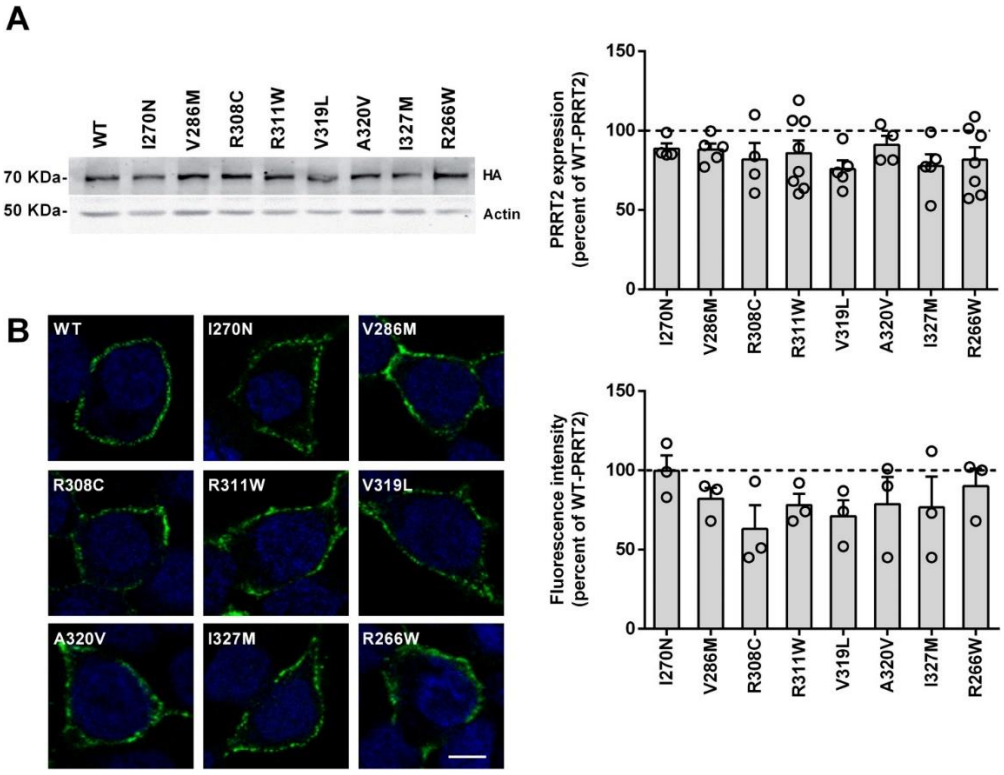

Figure 10: Expression levels and membrane targeting of missense PRRT2 mutants. A: Protein extracts from naïve HEK293 cells transfected with either WT or mutant PRRT2-HA variants were analyzed by western blotting using anti-HA antibodies. Left: Representative immunoblot. Right: Densitometric analysis of the immunoreactive bands. Actin was used as loading control. The expression levels of PRRT2 mutants are shown in percent of the immunoreactivity of WT-PRRT2 as means ± sem of n = 4–8 independent experiments (horizontal line; mean ± sem: 100 ± 0.49). B: Left: Representative confocal images of naïve HEK293 cells transfected with either WT or mutant PRRT2-HA variants and live surface-immunolabelled with anti-HA antibodies (green). DAPI staining (blue) was used to visualize nuclei. Scale bar, 5 µm. Right: Quantification of HA fluorescence intensity. Fluorescence intensity was calculated as the ratio between the total HA fluorescence signal and the transfection efficiency in the same field and expressed in percent of WT-PRRT2 (horizontal line). Data represent means ± sem with superimposed individual values from n = 3 independent experiments. Statistical analysis was done using one-way ANOVA/Holm- Šídák tests. Reproduced from Sterlini et al. 2023 [74].

PRRT2 missense variants do not impact on the structural stability of the membrane-associated domain

We investigated how the pathogenic variants affect the conformation of PRRT2 TM domain. In lack of an experimentally derived structure, we previously generated an all-atom model of the native protein domain (residues G261-K340), and we thoroughly refined it in a membrane-water environment using molecular dynamics (MD) simulations [41], [42]. Here, we performed eight independent, 1 μs-long MD simulations of the PRRT2 mutants using the HMR protocol already employed for the WT simulations. In all cases, we observed that the protein structure remains stable: the α-carbon RMSDs of all systems are stationary after 300 ns (Fig. 11). According to these results, the variants do not alter the integrity of the PRRT2 fold, despite their distinct locations along the protein sequence.

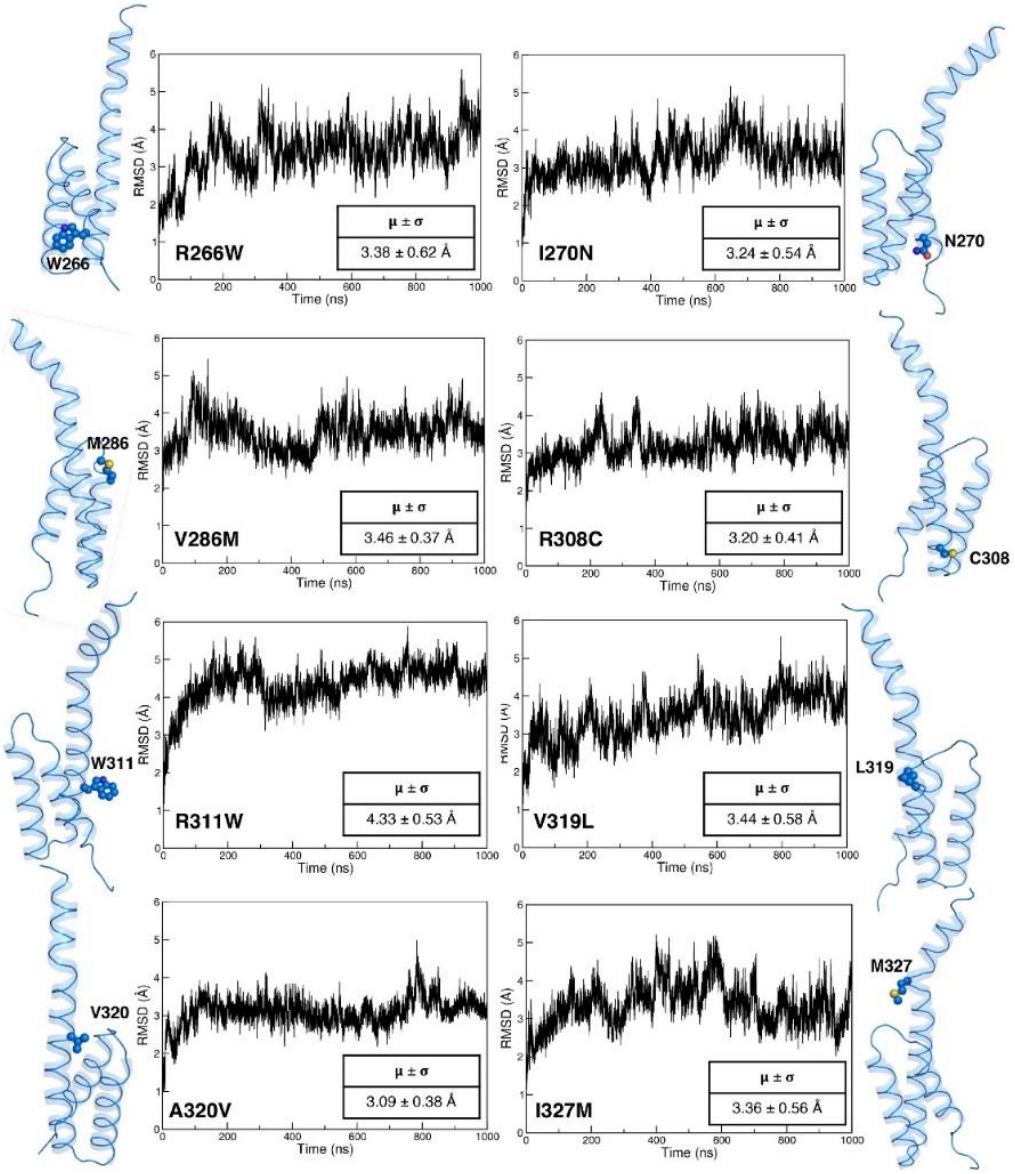

Figure 11: Structural stability assessment for PRRT2 modelled mutants by Molecular Dynamics simulations. Time-evolution of the α-carbon RMSDs in the mutant simulations, with average values (μ) reported. The mutated spots are highlighted as spheres in the structural models shown for each system. Reproduced from Sterlini et al. 2023 [74].

The V286M and A320V variants have opposite effects on the interaction between PRRT2 and NaV1.2

We next studied whether these variants could affect the binding between PRRT2 and NaV1.2 channels. Pull-down experiments were performed to investigate whether the PRRT2 mutants could bind the NaV1.2 channel with the same efficiency as WT-PRRT2. We expressed HA-tagged PRRT2 variants in *naïve* HEK293 and affinity purified them therefrom. Then, we set on-bead binding assays by challenging PRRT2-HA isoforms with extracts of HEK293 cells stably expressing the NaV1.2 channel α-subunit (HEK-NaV1.2). An additional construct, encoding for the unrelated protein BAP, also tagged with HA, was used as a negative control. PRRT2 variants were pulled down and the bound NaV1.2 channels detected by western blotting with anti-panNaV antibodies (Fig. 12A). While 6 of the 8 mutants displayed a NaV1.2 binding similar to WT-PRRT2, the A320V and V286M mutants showed a significant alteration in their binding to the channel (Fig. 12B). In particular, V286M pulled down a higher amount of NaV1.2, suggesting a binding higher than WT-PRRT2, while the isoform A320V immunoprecipitated a smaller amount of the channel. The altered NaV1.2 binding of PRRT2 mutants may cause channel dysregulation and contribute to the onset of PRRT2-related pathologies.

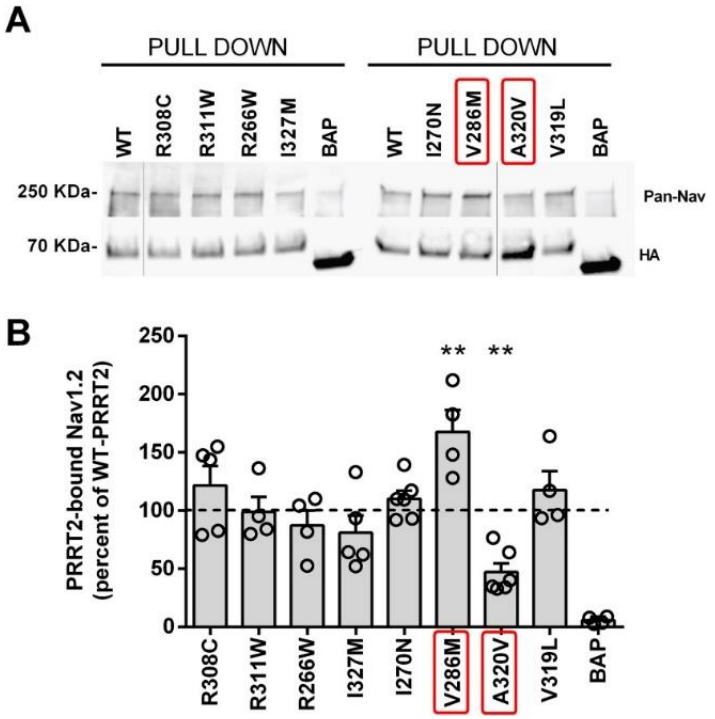

*Figure 12: Binding of missense PRRT2 mutants to NaV1.2 channels. The binding ability of PRRT2 mutants to the NaV1.2 channel was analyzed by pull down assays. A. Naïve HEK293 cells were transfected with HA-tagged WTPRRT2, mutant PRRT2 variants or the control unrelated protein BAP, extracted and immunoprecipitated using anti-HA beads. HA-bound proteins were subsequently incubated with lysates of NaV1.2-expressing HEK293 stable cell clones. HA-pulled-down samples were analyzed by western blotting using anti-panNav antibodies. Representative immunoblots are shown. Vertical grey lines in the blots indicate that the lanes were on the same gel but have been repositioned. B. Quantification of the panNav immunoreactivity in PRRT2 immunoprecipitates. Immunoblots were analyzed by densitometry of the fluorograms. The intensity of NaV1.2 immunoreactivity was normalized to the PRRT2 recovery within the same sample. The binding of PRRT2 mutants to NaV1.2 is expressed in percent of WT-PRRT2 (horizontal line; mean ± sem: 100 ± 8.27). Red boxes indicate the PRRT2 variants that showed altered NaV1.2 binding and were subjected to further analysis. Data represent means ± sem with superimposed individual values from n = 4–6 independent experiments. **p < 0.01, one-way ANOVA/ Holm-Šídák tests. Reproduced from Sterlini et al. 2023* [74].

The PRRT2 A320V mutant increases the surface exposure of NaV1.2 channels

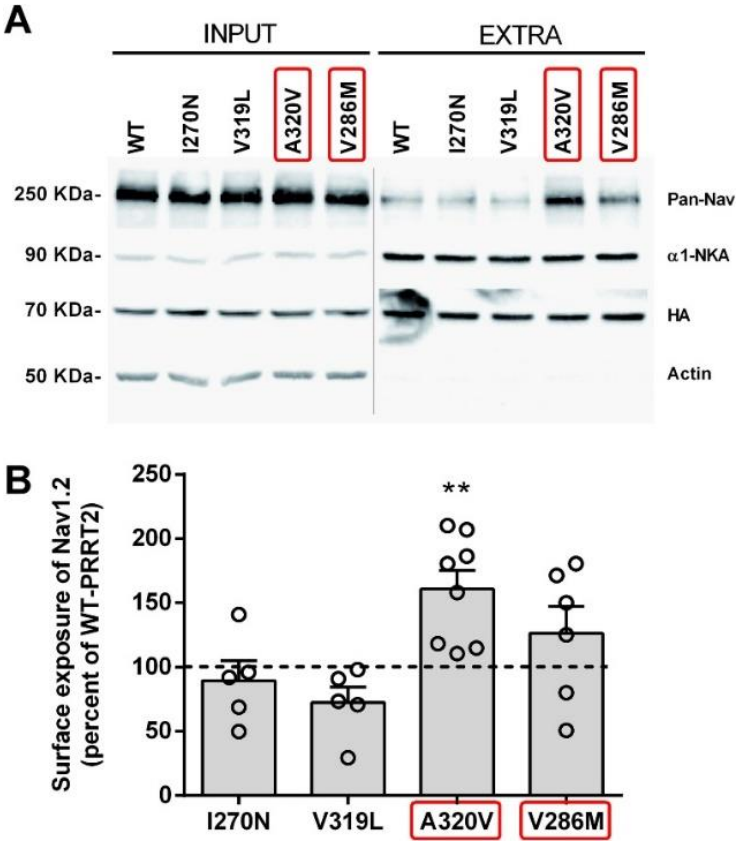

*Figure 13: Effects of missense PRRT2 mutants on the surface exposure of NaV1.2 channels. A. Representative immunoblots of biotinylation assays. HEK293 cells stably expressing NaV1.2 channels were transfected with either WT or mutant PRRT2-HA variants. Total lysates (INPUT) and biotinylated (cell surface, EXTRA) fractions were analyzed by western blotting with antibodies to HA and panNav. Na^+/K^+- ATPase α1-subunit (α1-NKA) and actin were used as markers of cell surface and intracellular fractions, respectively. Vertical grey lines in the blots indicate that the lanes were on the same gel but have been repositioned. B. Quantification of NaV1.2 surface exposure after normalization to α1-NKA. Data are expressed in percent of the respective WT-PRRT2 values (horizontal line; mean ± sem: 100 ± 5.04). Red boxes indicate the PRRT2 variants with altered NaV1.2 binding that were subjected to electrophysiological analysis. Data represent means ± sem with superimposed individual values from n = 5–8 independent experiments. **p < 0.01; one-way ANOVA/ Holm- Šídák tests. Reproduced from Sterlini et al. 2023 [74].*

Since PRRT2 interaction with NaV1.2/NaV1.6 channels modulates their plasma membrane expression [47], we investigated whether the altered binding of the A320V and V286M mutants affects membrane targeting of NaV1.2. To this end, we performed biotinylation experiments in HEK-NaV1.2 cells transfected with either WT-PRRT2 or its variants and measured the amount of NaV1.2 expressed in the membrane biotinylated protein fraction. In addition to the A320V and V286M, two additional mutants characterized by unchanged NaV1.2 binding (I270N and V319L) were tested as controls in addition to WT-PRRT2. The results showed that the A320V mutant increases the membrane expression levels of NaV1.2 compared to WT-PRRT2, suggesting that this mutant lack the ability to negatively regulate the NaV1.2 membrane exposure (Fig. 13). No significant differences in NaV channels exposure were found for the I270N, V286M and V319L variants.

The PRRT2 V286M and A320V mutants have opposite effects on the steady-state inactivation kinetics of NaV1.2 channels

We investigated in detail the functional effects of the altered interaction of the A320V and V286M mutants with NaV1.2 channels by patch-clamp electrophysiology of HEK-NaV1.2 transiently transfected with either variant (Fig. 14A). Consistent with the biotinylation studies,

the A320V mutant was significantly less effective than WT-PRRT2 in downregulating transient macroscopic Na^+ currents, and not significantly different from MOCK-transfected cells. On the other hand, the V286M mutant was still able to significantly decrease Na^+ conductance with respect to MOCK-transfected cells, and its effect was not significantly different from WT-PRRT2 (Fig. 14 B,C). Being unaffected by WT-PRRT2, the activation dynamics of NaV1.2 was not modified by either PRRT2 mutant (Fig. 14 D, E). The analysis of the NaV1.2 inactivation kinetics confirmed the previously reported left-shift of the steady-state inactivation curve by WTPRRT2 with respect to MOCK-transfected cells. Interestingly, the magnitude of this effect was increased by the V286M mutant, with a significant additional left shift of the inactivation curve (GOF), while the PRRT2 effect was lost with the A320V mutant that became similar to MOCK-transfected cells (LOF) (Fig. 14 F,G).

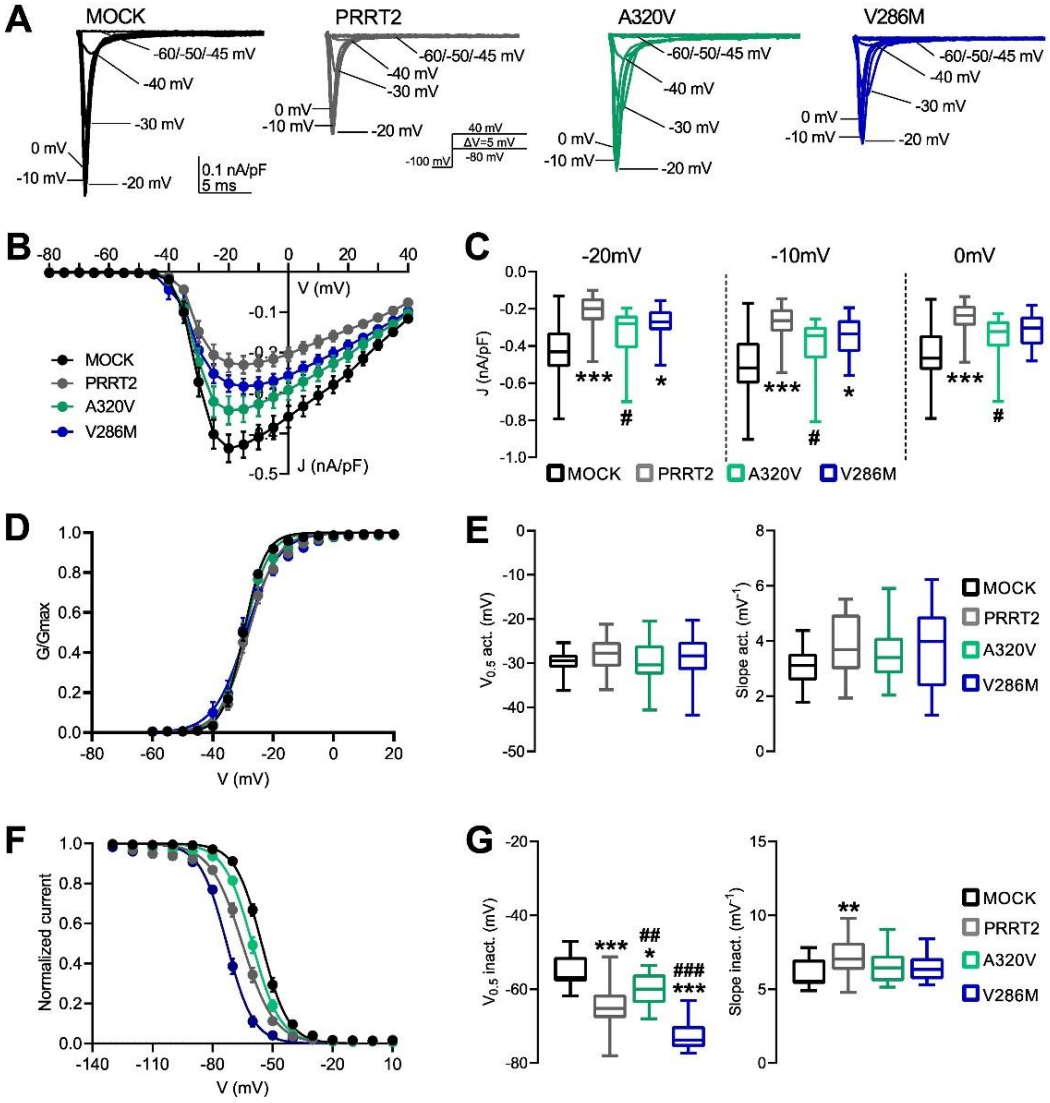

*Figure 14: Effects of the V286M and A320V mutants of PRRT2 on the transient Na^+ current and biophysical properties of NaV1.2 channels. A-C. Macroscopic Na^+ current. A. Representative whole-cell Na^+ current density (J) traces recorded from HEK293 -NaV1.2 transiently transfected with the empty pKH3 control plasmid (black), WT-PRRT2 (grey), A320V PRRT2 (green) or V286M PRRT2 (light blue). Currents were elicited by 5 mV depolarizing step from − 80 mV to 40 mV and cells were held at − 100 mV (inset). B. Current density to voltage relationship for conditions as in A. C. Box plots of the J values at three representative voltages (− 20/− 10/0 mV). Data are shown as means ± sem (MOCK, n = 21; PRRT2, n = 20; A320V n = 19; V286M n = 18). D,E. Voltage-dependence of activation. The lines are the best-fitted Boltzmann curves (D). Box plots of the half-maximal voltage of activation (V0.5 act) and slope (E). Data are shown as means ± sem (MOCK, n = 21; PRRT2, n = 20; A320V n = 19; V286M n = 18). F,G. Steady-state inactivation curves. The lines are the best-fitted Boltzmann curves (F). Box plots of the half-maximal voltages for inactivation (V0.5 inact) and slopes (G). (MOCK, n = 21; PRRT2, n = 27; A320V n = 18; V286M n = 14). *p < 0.05, **p <*

*0.01, ***p < 0.001 vs MOCK; #p < 0.05, ##p < 0.01, ###p < 0.001 vs WTPRRT2; one-way ANOVA/Tukey's tests. Reproduced from Sterlini et al. 2023 [74].*

The A320V and V286M PRRT2 mutants have opposite effects on the recovery from inactivation of NaV1.2 channels

It was previously reported that WT-PRRT2 slows down and decreases the magnitude of the recovery from inactivation of NaV1.2/1.6 channels [47]. Interestingly, the PRRT2- mediated inhibition of NaV1.2 recovery was totally lost with the A320V mutant, confirming its LOF phenotype and suggesting a key role for this PRRT2 residue in the modulation of the biophysical properties of the NaV1.2 channel (Fig. 15 A,B). In contrast, the V286M mutant confirmed the GOF observed on the inactivation kinetics by showing a decrease in the plateau recovery of the same extent of WT-PRRT2, but characterized by slower kinetics with a two-fold significant increase in the time constant (Fig. 15 A,B). Since WT-PRRT2 anticipates the entry of NaV1.2 channels in the inactivated state and reduces their recovery from inactivation (Fig. 14F and Fig. 15A), it is likely that, during high-frequency stimulation, a progressive increase in NaV1.2 inactivation occurs in the presence of PRRT2. To determine the effects of PRRT2 and its mutants in accumulating inactivated channels, a series of depolarizing pulses from a holding potential of − 100 mV to 10 mV at a frequency of 20 Hz were applied (Fig. 15C). In HEKNaV1.2 cells expressing WT-PRRT2, stimulation at 20 Hz induced a progressive and significant reduction of Na^+ current amplitude with respect to MOCK-transfected cells, consistent with an increased proportion of inactivated NaV1.2 channels (Fig. 15D). In this context, the A320V mutant induced a significantly slower and reduced depression of the current, confirming its LOF phenotype, while the V286M mutant accelerated the depression in current amplitude due to frequency inhibition with respect to WT-PRRT2 (GOF), while reaching a similar inhibition plateau (Fig. 15 D,E).

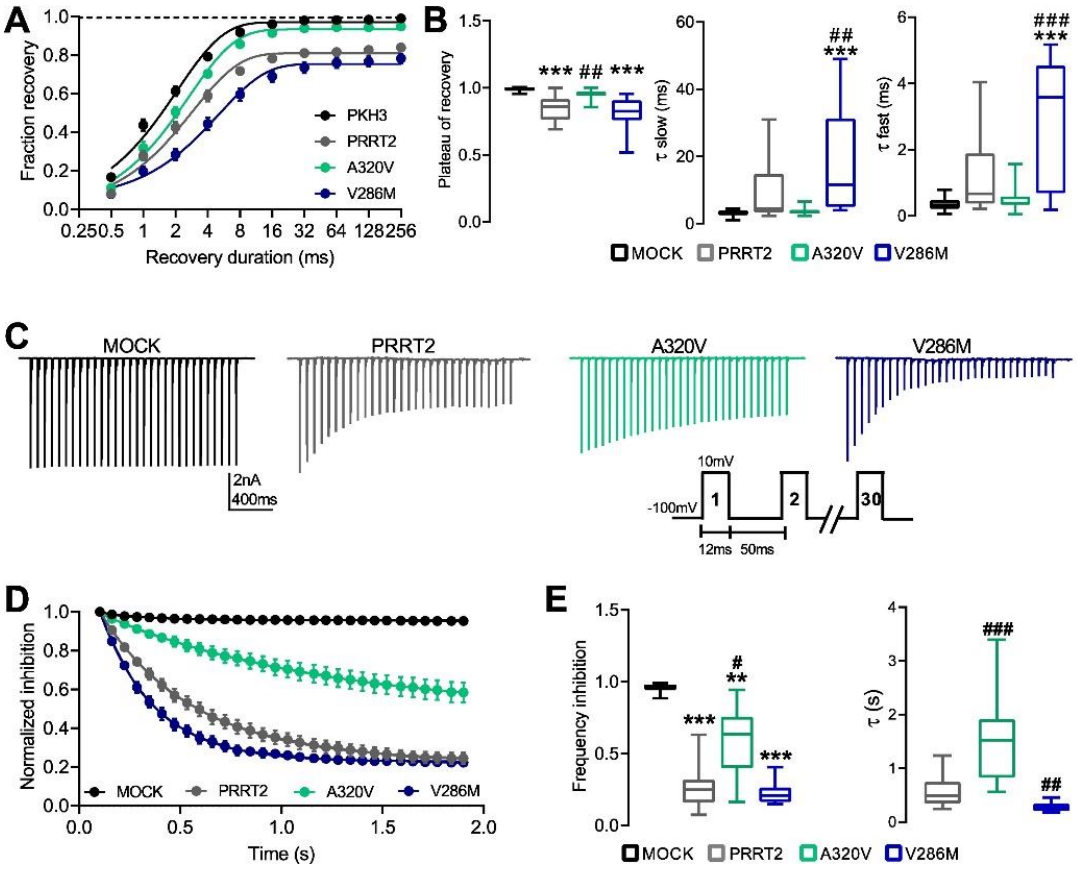

*Figure 15: Effects of the V286M and A320V PRRT2 mutants on the recovery from inactivation of NaV1.2 channels. A,B: Time-courses of the recovery from inactivation of peak currents at − 100 mV recorded in HEK293 cells stably expressing NaV1.2 and transiently transfected with empty vector (MOCK, black), PRRT2 (grey), A320V (green) or V286M (light blue) and plotted on a semi-logarithmic scale (A). Box plots of τ and plateau of recovery estimated from two-phase decay fit to the data (B). (MOCK, n = 22; PRRT2, n = 24; A320V n = 22; V286M n = 18). C-E: Frequency-dependent inhibition. C: Representative whole-cell currents recordings in the four experimental conditions shown in A. Frequency-dependent inhibition was determined using a depolarizing pulse to 10 mV from a holding potential of − 100 mV for 12 ms at a frequency of 20 Hz. Peak current was normalized to the first pulse in each experiment. D: Time-course of the frequency-dependent inhibition for the genotypes described in A. E: Box plots of the plateau and the τ values estimated from one-phase decay fit to the data. (MOCK, n = 23; PRRT2, n = 24; A320V, n = 19; V286M, n = 14). **p < 0.01, ***p < 0.001 vs MOCK; #p < 0.05, ##p < 0.01, ###p < 0.001 vs WT-PRRT2; one-way ANOVA/Tukey's tests (B) and Kruskal-Wallis/Dunn's tests (E). Reproduced from Sterlini et al. 2023 [74].*

NaV1.2-PRRT2 molecular interface

PRRT2 was shown to act as a negative modulator of membrane exposure and biophysical properties of NaV1.2, which are primarily expressed in brain neurons. Direct transmembrane binding of PRRT2 to NaV1.2 has been demonstrated extensively [47], [74]. To identify the PRRT2-NaV1.2 interaction surface we are using both computational (all-atom docking and multi-scale MD simulations) and experimental (biochemical and electrophysiology essays) approaches, following the pipelines reported below (Fig. 16). Shedding light on the structural details of the specific NaV1.2 modulation by PRRT2 will greatly improve our knowledge of the mechanisms driving associated channelopathies, paving the way for tailored therapeutic strategies.

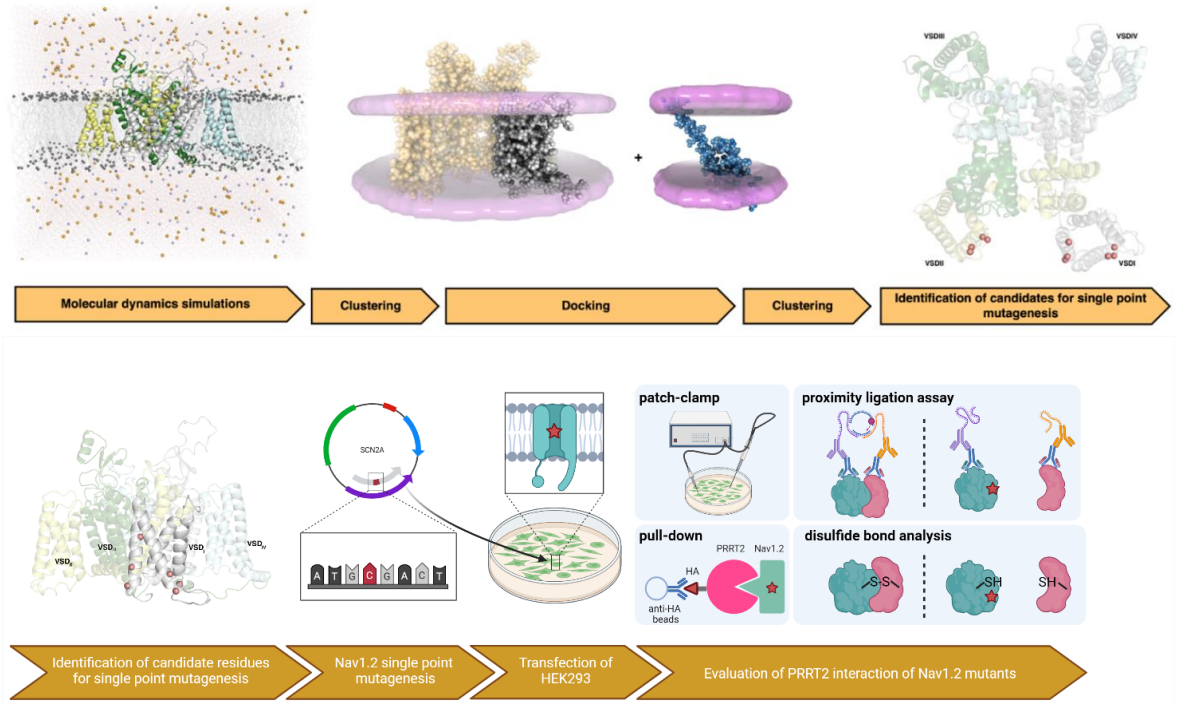

Figure 16: In-silico and experimental pipelines for the identification of NaV1.2 – PRRT2 interacting interfaces. Upper panel: in-silico simulation pipeline. Lower panel: experimental pipeline to validate candidate interfaces.

Molecular docking simulations of PRRT2-NaV1.2 interface were performed by analyzing each of the four voltage sensor domains (VSDs) of NaV1.2 separately. For each VSD, two clusters made of three candidates residues defining an interaction surface were identified by docking simulations. An example of NaV1.2 VSD investigation is reported in Figure 17: for each residue identified in the potential docking interface, a ranking score has been assigned in order to determine its importance in the cluster. After the definition of the candidate residues, we generated the triple mutated constructs encoding for mutant NaV1.2, aimed at defining potentially impaired interactions with PRRT2.

Mutagenesis candidates for the VSDII:

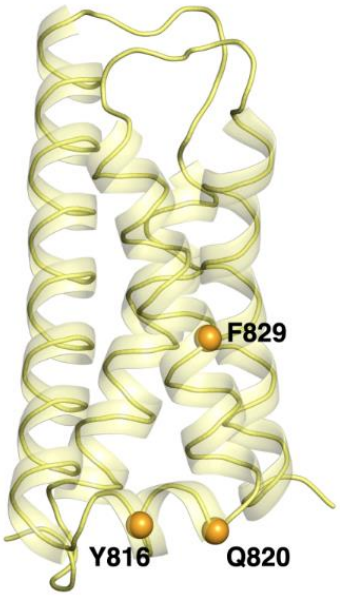

	Ranking		
	Residue	n° of contacts ($\mu \pm \sigma$)	Occurrence
1	Y816	16.60 ± 10.85	5
2	Q820	14.50 ± 9.33	4
3	F829	13.50 ± 1.53	4

Alanine scanning for the VSDII:

- Y816 → A816
- Q820 → A820
- F829 → A829

Figure 17: Mutagenesis candidates for the VSDII, example. Left panel: three-dimensional representation of the SCN2A VSDII domain, with the three candidate residues shown. Right panel: table of the candidate residues ranking values. Definition of the alanine scanning ranking for the VSDII domain. Unpublished results.

The identified clusters are listed in table 4: the residues are in descending order of interaction probability, grouped into two clusters of three residues (so cluster 2 always has a lower probability of interaction with PRRT2 than cluster 1). The identified residues were then selectively mutated in alanine to abolish the potential binding ability with the mutation reported in Table 4 (aa mutation – base # - from – to).

We tested the expression levels of these mutant constructs and compared them to WT. This step of expression evaluation is fundamental to permit further functional analyses. If mutant channels show impaired expression, differences in the electrophysiological features may be misinterpreted for an altered PRRT2 regulation. If no significant differences were found in protein expression levels between mutant constructs and WT one, we then tested the ability of these mutants to interact with WT-PRRT2 through electrophysiological characterization of Na^+ currents performed in HEK293 cells. In particular, we recorded macroscopic transient whole-cell currents from HEK293 cells co-transfected with NaV1.2 (either WT or mutant) and PRRT2 WT using a voltage-step protocol by patch-clamp method (Fig. 18).

For each cluster, the electrophysiological characterization was focused on the corresponding triple mutant, carrying all the missense substitutions within the cluster, as this construct is expected to recapitulate the combined effects of the individual variants on the interaction with PRRT2. A possible positive outcome, defined as a significant alteration of the functional interaction between PRRT2 and NaV1.2, would have prompted further analyses on double and single mutants to identify the specific residues involved.

If alterations in the protein expression levels were found (see Table 4, Expression column), the screening pipeline required to go back to double mutant constructs, reverting the variant in the position of lower binding probability, as described in the Reverse mutagenesis column of the Table 4. Double mutants were generated from the triple ones via site-directed mutagenesis and verified by sequencing, as reported in the materials and methods section. Double mutants were then tested newly for protein expression and if still alterations were found, single mutants were generated as previously described, otherwise they were analyzed for electrophysiological features in combination with PRRT2 WT.

		aa mutation	base #	from	to	Expression	Reverse mutagenesis			
VSDI	Cluster 1	N132S	1377	A	G	Ok	No			
		L134A	1382	C	G					
			1383	T	C					
		L130A	1370	T	G					
			1371	T	C					
	Cluster 2	L175I	1505	C	A	Ok	No			
		I174A	1502	A	G					
			1503	T	C					
		L171A	1493	C	G					
			1494	T	C					
VSDII	Cluster 1	Y816A	2446	T	G	Ok	No			
			2447	A	C					
		Q820A	2458	C	G					
			2459	A	C					
		F829A	2485	T	G					
			2486	T	C					
	Cluster 2	I801A	2401	A	G	Very low	I801A	2401	A	G
			2402	T	C			2402	T	C
		L771A	2371	C	G		L771A	2371	C	G
			2372	T	C			2372	T	C
		V797A	2390	T	C		A797V	2390	C	T
VSDIII	Cluster 1	F1213A	3637	T	G	Ok	No			
			3638	T	C					
		F1210A	3628	T	G					
			3629	T	C					
		V1248A	3743	T	C					
	Cluster 2	D1283A	3848	A	C	Ok	No			
		F1266A	3796	T	G					
			3797	T	C					
		V1287A	3860	T	C					
VSDIV	Cluster 1	F1527A	4712	T	G	Absent	F1527A	4712	T	G
			4713	T	C			4713	T	C
		L1573A	4850	C	G		L1573A	4850	C	G
			4851	T	C			4851	T	C
		S1536A	4739	A	G		A1536S	4739	G	A
			4740	G	C			4740	C	G
	Cluster 2	F1610A	4961	T	G	Very low	F1610A	4961	T	G
			4962	T	C			4962	T	C
		R1586A	4889	C	G		R1586A	4889	C	G
			4890	G	C			4890	G	C
		F1590A	4901	T	G		A1590F	4901	G	T
			4902	T	C			4902	C	T

Table 4: Candidate residues of different VSDs of NaV1.2 potentially involved in PRRT2 interaction. The mutated bases are identified. In the right columns expression data are summarized and need for reverse mutagenesis identified.

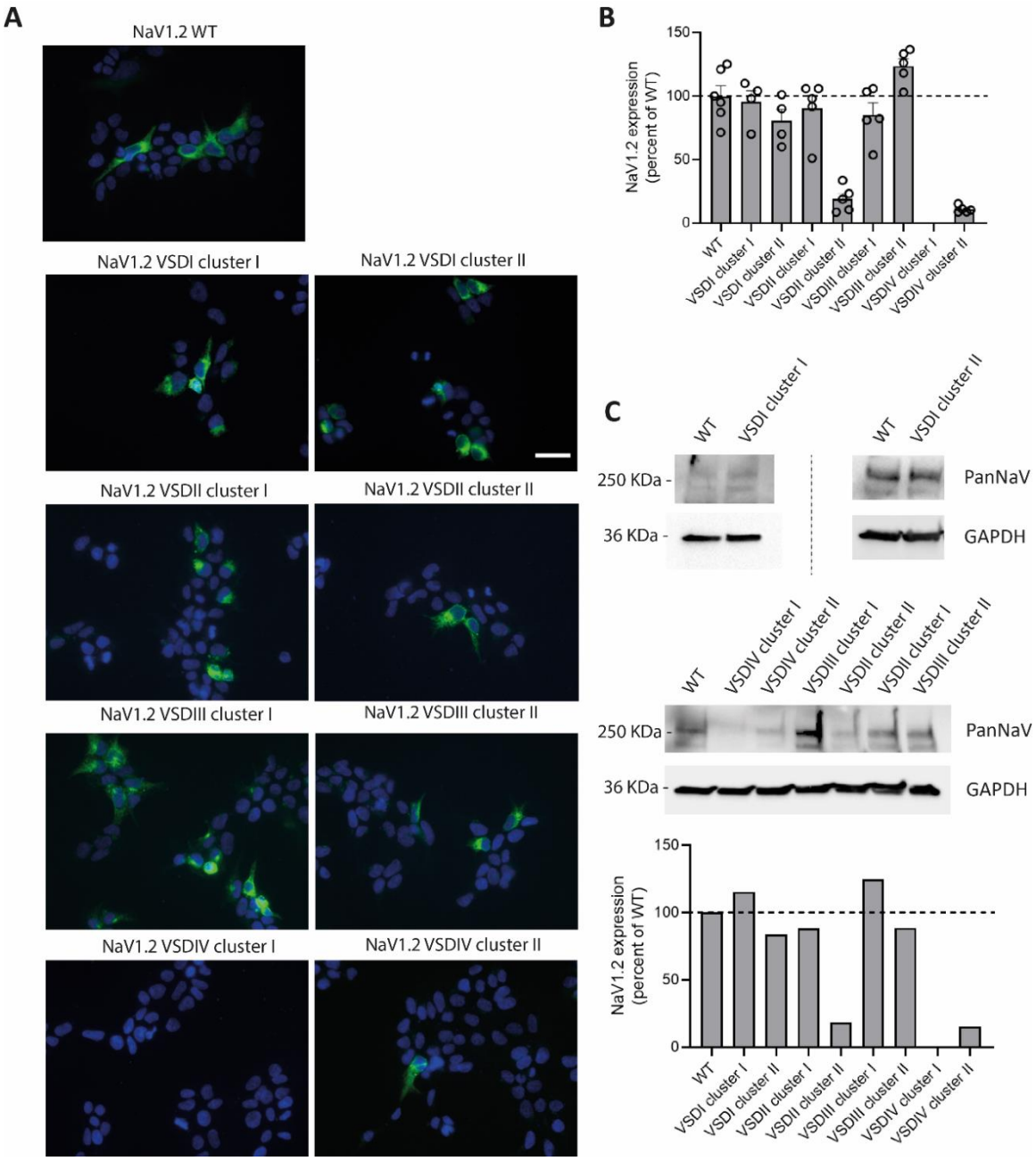

Figure 18: NaV1.2 VSDs cluster mutants expression levels. A: Representative confocal images of HEK293 cells transfected with NaV1.2 mutants. Immunofluorescence with anti-panNaV (green) antibody; cell nuclei are depicted in blue. B: NaV1.2 mutants transfection efficiency is represented in percentage of WT. Data are represented as means ± sem (horizontal line shows 100%). C: Protein extracts from naïve HEK293 cells transfected with either WT or mutant NaV1.2 variants were analyzed by western blotting using anti-panNaV antibodies. Upper panels: Representative immunoblot. Lower panel: Densitometric analysis of the immunoreactive bands. GAPDH was used as loading control. The expression levels of NaV1.2 mutants are shown in percent of the immunoreactivity of WT (horizontal line). Unpublished results.

The *SCN2A* WT and VSDs mutant constructs were transfected in naïve HEK293 cells, and the protein extracts were analyzed by western blot (Fig. 18C). The VSDII cluster II, and VSDIV clusters showed almost or completely absent NaV1.2 expression levels. The other VSDs cluster mutants (namely VSDI cluster I and II, VSDII cluster I and VSDIII clusters I and II) showed NaV1.2 expression comparable to WT. Transfected HEK293 were also analyzed by immunofluorescence using anti-panNaV antibody (Fig. 18A). The transfected cells were analyzed for transfection efficiency (Fig. 18B), which showed the same result already found in by the western blotting analysis. We conclude that the NaV1.2 constructs presenting variants

in VSDII cluster II, and in both VSDIV clusters are unable to express NaV1.2 and therefore they can't be used for electrophysiological characterization. Therefore, for the up-mentioned clusters, reverse mutagenesis is ongoing to remove the third mutation in each cluster (the one with lower ranking score, or predicted involvement in the PRRT2 binding interface). For those mutant *SCN2A* constructs that are instead able to express sufficient NaV1.2 amounts, electrophysiological characterization in combination with PRRT2 has been performed.

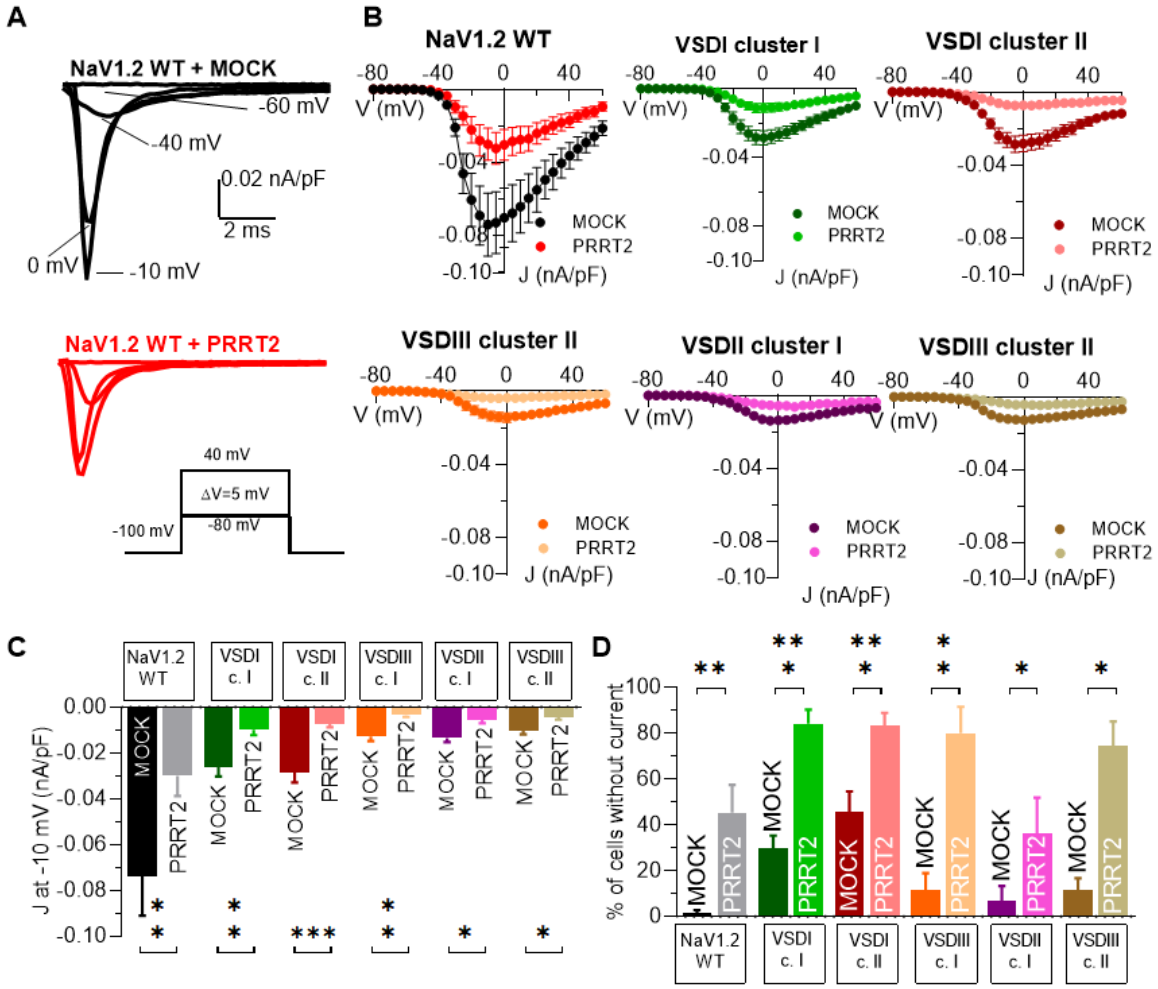

*Figure 19: Effects of the missense variants on the NaV1.2 transient currents. A: Representative whole-cell transient Na^+ currents evoked in cells transfected with NaV1.2 WT + MOCK (black, top) or NaV1.2 WT + PRRT2 (red, bottom) by the protocol depicted in the inset. B: Current density (J) versus voltage (V) relationship for the tested conditions. C: Statistical analysis of J at the value of voltage corresponding to the current peak (-10 mV). D: Percentage of cells with current below 100 pA in Hek-293 naïve cells transiently transfected with the wt channel (NaV1.2 WT) or the different NaV1.2 mutants tested. Data are shown as means ± SEM (NaV1.2 wt + MOCK, n = 14; NaV1.2 + PRRT2, n=8; VSDI c.I + MOCK, n=20; VSDI c.I + PRRT2, n = 12; VSDI c. II + MOCK, n=10; VSDI c. II + PRRT2 n=9; VSDIII c.I + MOCK, n=19; VSDIII c.I + PRRT2, n=10; VSDII c.I + MOCK, n=9; VSDII c.I + PRRT2, n=5; VSDIII c. II + MOCK, n=15; VSDIII c.II + PRRT2, n=8) ***p<0.001, **p<0.01 *p<0.1. Student's t-test/ Mann-Whitney. Unpublished results.*

We systematically analyzed the functional properties of NaV1.2 mutants by patch-clamp recordings in HEK293 cells transiently transfected with either WT or mutant NaV1.2 in each case co-expressed with WT-PRRT2. In cells transfected with NaV1.2 WT and PRRT2, the maximal transient Na^+ current recorded during the step protocol is significantly lower compared to the current recorded in cells transfected with NaV1.2 WT and MOCK, suggesting that the variants in the NaV1.2 sequence do not affect the functional interaction of PRRT2 and NaV1.2 (fig 19B-C, black vs. red). This observation is consistent with the well-documented role of PRRT2 as negative modulator of NaV1.2 functionality, but we also observed that PRRT2

causes a reduction in the transient Na^+ current of mutant channels, and this was observed for all the different mutants tested (Fig. 19B-C). The modulatory effect of PRRT2 on voltage-gated Na^+ currents is clearly recognizable by analyzing the current recorded at the value of potential of -10 mV (Fig. 19C), showing how PRRT2 reduces the maximal current when co-transfected with the WT or mutant NaV1.2. In addition to the effect on the current amplitude, a significant increase in the percentage of cells showing no current during the application of the step protocol (current threshold: 100 pA, see Materials and Methods) was observed in cells co-transfected with PRRT2 compared to MOCK (Fig. 19D). All data show that the effect of PRRT2 on the channel carrying the missense variants is similar to the effect on the NaV1.2 WT, defining no clear impairment in the interaction given by the variants themselves.

As previously mentioned, reverse mutagenesis is ongoing on those triple mutant *SCN2A* constructs leading to low or absent protein expression, namely VSDII cluster II, VSDIV clusters I and II. Subsequent analyses will be performed on the resulting double mutants about protein expression and eventually electrophysiological modulation by PRRT2.

PRRT2 L336X

Variants in the *PRRT2* gene are most commonly associated with BFIS and PKD, as previously discussed. However, not all *PRRT2* variants result in these classical phenotypes. Here, we describe a novel and atypical clinical presentation associated with a truncating *PRRT2* variant.

Clinical description

Very recently a new truncation variant has been identified in a two-and-a-half year old child. The patient had adequate neuromotor developmental milestones until the age of 15 months, when focal and generalized epileptic seizures associated with severe developmental regression (complete loss of neuromotor and language skills) occurred. He currently has a drug-resistant epileptic encephalopathy associated with a dyskinetic movement disorder. Brain MRI at 20 months showed cortical and subcortical atrophy, not described in previous examinations. Genetically, aCGH, mitochondrial DNA sequencing and exome analysis were performed in trio (in two different laboratories). The first two tests were negative while the trio revealed a de novo variant in the *PRRT2* gene. This is a truncating variant (ENST00000358758.12:c.1007T>G_p.Leu336X). Carbamazepine causes a worsening of the condition.

PRRT2 L336X variant slightly lowers protein expression

We initially assessed the impact of the variant on PRRT2. To this aim, I generated a HA N-terminally tagged PRRT2 construct in order to generate the L336X mutant construct. The WT and L336X mutant constructs were transfected in naïve HEK293 cells, and the protein extracts were analyzed by western blot (Fig. 20A). The L336X PRRT2 mutant showed no significant differences in the expression levels compared to the WT. Transfected HEK293 were also analyzed by immunofluorescence using anti-HA antibody (Fig. 20B). No differences in the transfection efficiency was found. On the other hand, image analysis by confocal microscopy found a significant lowering in the quantification of fluorescence of cells transfected with the L336X variant with respect to the WT PRRT2 (Fig. 20B). We conclude that the L336X variant does not strongly impact on the expression level of PRRT2, but that the lower single cell expression results in a tendency of decreased total expression, visible with the western blot analysis.

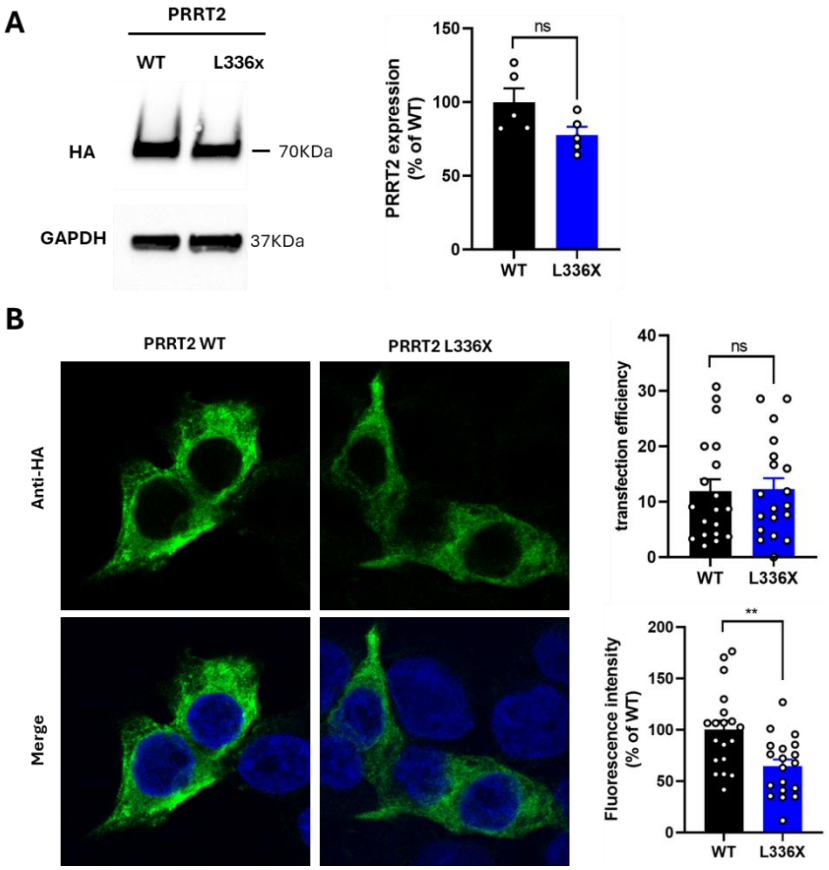

Figure 20: Expression levels of truncating PRRT2 L336x mutant. A: Left: Protein extracts from HEK293 cells transfected with either WT or L336X PRRT2-HA were analyzed by western blotting using anti-HA antibody. Representative immunoblot. Right: Densitometric analysis of the immunoreactive bands. GAPDH was used as loading control. The expression levels were normalized on PRRT2-HA WT mean expression value and are shown as means +/- SEM of n=5 independent experiments. B: Left: representative confocal images of HEK293 cells transfected with either WT or L336X PRRT2-HA and immunolabelled with anti-HA antibody (green). DAPI staining was used to visualize nuclei (blue). Right top: quantification of transfection efficiency calculated as the ratio between the HA positive cells and the total number of cells in the same field. Right bottom: Quantification of HA fluorescence intensity calculated as the ratio between the total HA fluorescence signal and the number of HA positive cells in the same field. The fluorescence intensity levels were normalized on PRRT2-HA WT mean intensity value and are shown as means +/- SEM with superimposed individual values from n=3 independent experiments. Statistical analysis was done using Unpaired Student's t-test. Unpublished results.

The L336X PRRT2 variant does not affect the PRRT2 functional interaction with NaV1.2

Considering the potential effect of the L336X mutation of PRRT2 on the interaction with NaV1.2, we performed an electrophysiological characterization of NaV1.2 whole-cell transient currents in presence of PRRT2 L336X compared to PRRT2 WT. In this perspective, we co-transfected HEK293 cells with NaV1.2 WT and PRRT2 L336X, we recorded whole-cell transient Na^+ currents from those cells through patch-clamp experiments in the voltage clamp configuration and compared their current amplitude and kinetics with the ones of cells co-transfected with NaV1.2 WT and PRRT2 WT (Fig. 21A). If the hypothesis was confirmed, an alteration in the Na^+ current amplitude or kinetics was expected in cells co-transfected with NaV1.2 and PRRT2 L336X. However, the analysis of the current amplitude/ voltage (J/V) relationship showed that PRRT2 L336X did not cause a significant change in NaV1.2 current amplitude compared to PRRT2 WT (Fig. 21B). Moreover, the percentage of cells with peak currents < 50 pA was not significantly different between the two conditions (Fig. 21C). The analysis of activation and steady-state inactivation kinetics showed no significant difference between PRRT2 WT and PRRT2 L336X in the modulatory effect on NaV1.2 (Fig. 21 D-F). Taken

together, these data suggest that the L336X mutation does not affect the modulatory activity of PRRT2 on NaV1.2 electrophysiological properties.

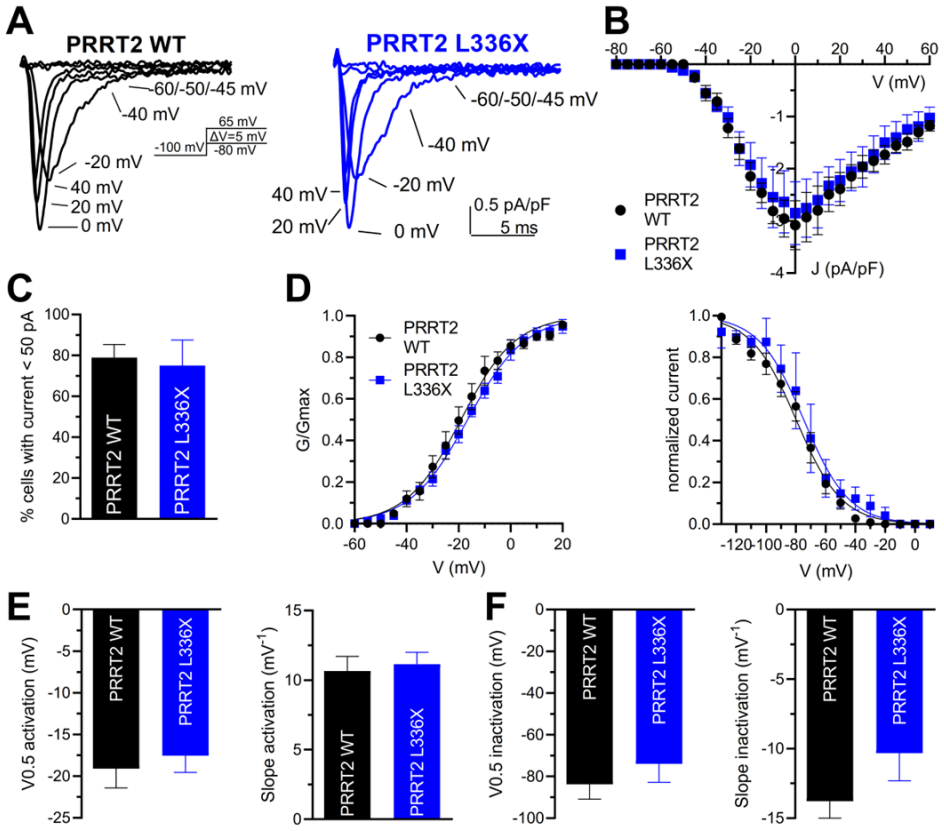

Figure 21: Effect of the L336X PRRT2 mutation on the transient Na current and biophysical properties of NaV1.2 channels. A: Representative whole-cell Na^+ current density (J) traces recorded from HEK293 cells transiently transfected with NaV1.2 and PRRT2 WT (black) or PRRT2 L336X (blue). Currents were elicited by 5 mV depolarizing steps from -80 mV to 40 mV and cells were held at -100 mV (inset). B: Current density vs. voltage relationship for conditions depicted in A. C: Percentage of cells with peak currents < 50 pA on the total number of recorded cells. Peak currents were recorded at the step of voltage equal to 0 mV. D: Voltage dependence of activation (left) and steady-state inactivation (right) curves for the tested conditions. The lines are the best-fitted Boltzmann curves. E: Statistical analysis of the half-maximal voltages for activation (V0.5 act) and slope. F: Statistical analysis of the half-maximal voltages for inactivation (V0.5 inact) and slope. All data are means ± SEM. (PRRT2 WT, n=12; PRRT2 L336X, n=8). Mann-Whitney U-test. Unpublished results.

Discussion – Aim 2: PRRT2

The disease mechanisms for paroxysmal disorders associated with nonsense/frameshift variants in the *PRRT2* gene are largely dependent on the LOF of the mutated allele product due to degradation of either the mRNA by NMD or the truncated protein which has escaped NMD [69], [128], [129]. The few pathogenic missense PRRT2 mutants that are expressed to some extent display lack of membrane targeting of the mutant protein, thus conforming to a general LOF pathogenetic mechanism [69], [70], [71]. On the other hand, a few missense pathogenic variants do not greatly affect protein expression and membrane targeting of PRRT2. In this case, the pathogenic mechanism can be more difficult to identify, depending on the potential disruption of interactions of PRRT2 with downstream cellular effectors. The investigation of these mutants can provide useful hints for understanding the structure-function relationships and the functional role of single residues and specific protein regions, as well as for identifying potential new target for therapeutic strategies. One interesting observation regards the molecular distribution of the *PRRT2* missense pathogenic variants that are largely concentrated in the short and highly conserved COOH-terminal domain of the protein, that

therefore may have a function in regulating fundamental membrane effectors such as NaV channels. We analyzed an array of missense pathogenic variants targeting the PRRT2 TM domain (4 mutants already reported to be expressed in heterologous systems and 4 point-variants that were not previously analyzed) and investigated the effects on their downstream effector NaV1.2 in terms of binding, membrane targeting and biophysical properties. Notably, all the considered mutated residues (R266, I270, V286, R308, R311, V319, A320 and I327) are fully conserved across mammalian species, testifying their important structural/functional role within the COOH-terminal domain of PRRT2. The study resulted in the identification of two residues that significantly alter the interactions of PRRT2 with the NaV1.2 channel. The A320V mutant was characterized by a clear LOF phenotype in both the membrane targeting and biophysical properties of NaV1.2 channels. On the other hand, the V286M mutant showed a GOF phenotype with respect to WT-PRRT2 in the modulation of the NaV1.2 biophysical properties (steady-state inactivation and recovery from inactivation), while it did not significantly affect the membrane targeting of the channel. This suggests that the inhibition of the membrane exposure of NaV1.2 channels and the modulation of their inactivation kinetics/recovery from inactivation may involve distinct residues of the TM region of PRRT2. Our results indicate that A320 is an important site for the interaction with the NaV1.2 channel. As far as the V286M mutant located in the TM1b region is concerned, a pathogenetic mechanism based on the observed GOF activity on NaV1.2 channels is apparently less consistent with the current knowledge of PRRT2 being a regulator of NaV activity. However, it has very recently been reported that overexpression of PRRT2 in the mouse model of 16p11.2 duplication, which in humans is associated with ASD, epilepsy and intellectual disability, causes hypersynchronous activity, increased glutamate release and seizure propensity [130]. It is therefore possible that both insufficient or excessive levels of PRRT2, and thereby LOF or GOF PRRT2 mutants, are detrimental to the stability of neuronal networks and cause paroxysmal manifestations, being PRRT2 a network stability gene [45], [56], [58], [60], [131]. However, in the present study, the PRRT2 mutants were investigated only for their NaV1.2 interaction activity, and the possibility exists that they also alter PRRT2 activities at the presynaptic level or on other effectors. The results may help understanding the molecular bases of the inhibitory effects of PRRT2 on neuronal excitability and the pathogenetic mechanisms leading to paroxysmal attacks in PRRT2 patients.

We found that the A320V and V286M mutants have a clear phenotype on the PRRT2-NaV1.2 functional interactions with the former characterized by LOF and the latter by an unexpected gain-of-function (GOF) with respect to wild-type PRRT2 (WT-PRRT2). The data confirm the key role played by NaV channel dysregulation in the pathogenesis of PRRT2- linked disorders and suggest that circuit instability and paroxysmal manifestations may arise when PRRT2 activity exits its physiological range.

We then aimed to identify the molecular interface underlying the functional interaction between PRRT2 and NaV1.2, by combining *in-silico* docking and molecular dynamics simulations with targeted mutagenesis and functional electrophysiological assays. We performed a systematic interrogation of candidate interaction surfaces located within the four VSDs of NaV1.2.

Computational analyses predicted discrete clusters of residues within each VSD with a high probability of contributing to PRRT2 binding. These residues were grouped into two clusters per domain, ranked according to their predicted interaction probability, and experimentally tested through alanine-scanning mutagenesis. This strategy was designed to maximize the likelihood of disrupting the PRRT2–NaV1.2 interface while minimizing indirect effects on

channel structure or function. The use of triple mutants for the initial screening allowed us to assess the combined contribution of spatially proximal residues, under the assumption that PRRT2 binding involves extended interaction surfaces rather than single-point contacts.

Protein expression analyses revealed that most triple mutant constructs were expressed at levels comparable to NaV1.2 WT, indicating that the majority of the selected residues are not essential for channel biosynthesis, folding, or stability. This finding supports the validity of the *in-silico* predictions in identifying surface-exposed residues potentially involved in protein–protein interactions rather than residues critical for the structural integrity of the channel. However, a subset of triple mutants—namely those corresponding to VSDII cluster II and VSDIV clusters I and II—showed markedly reduced or absent protein expression. This suggests that at least one residue within these clusters may play a structural role or be involved in trafficking or membrane insertion of NaV1.2. For these constructs, a reverse mutagenesis approach was implemented to disentangle structural effects from potential disruption of PRRT2 binding.

Electrophysiological characterization of the expressed triple mutants revealed that PRRT2 retains its inhibitory effect on NaV1.2-mediated sodium currents across all tested constructs. This suggests that none of the tested clusters, when simultaneously mutated, is individually required for PRRT2-mediated functional modulation.

Taken together, these findings indicate that the PRRT2–NaV1.2 binding interface has not yet been conclusively identified. The preservation of PRRT2-mediated functional modulation across all electrophysiologically characterized triple mutants suggests that the residues analyzed so far are not individually sufficient to disrupt the interaction. However, this does not exclude the existence of a specific binding site, which may involve residues located within clusters that could not be functionally evaluated due to low or absent protein expression.

In this context, the clusters currently undergoing reverse mutagenesis represent particularly strong candidates for PRRT2 interaction. The reduced expression observed in these constructs may reflect the presence of structurally or functionally critical residues whose simultaneous mutation compromises channel stability, thereby preventing electrophysiological assessment of PRRT2 modulation. Ongoing reverse mutagenesis will allow the generation of double and single mutants that preserve channel expression and will be essential to determine whether one or more of these residues are directly involved in PRRT2 binding.

Therefore, the present data support the conclusion that the PRRT2–NaV1.2 interaction site remains to be defined and that its identification likely requires the functional characterization of the clusters not yet accessible to electrophysiological analysis. Completion of this step will be crucial to establish whether PRRT2 engages NaV1.2 through a discrete interaction interface or through a combination of residues distributed across specific VSD regions.

The PRRT2 L336X truncating variant has been associated with an unusually severe clinical phenotype, distinct from the spectrum of neurological disorders classically linked to PRRT2 loss-of-function. This observation prompted us to investigate whether this variant alters the PRRT2-mediated modulation of NaV1.2, particularly in light of the patient's resistance to carbamazepine and other sodium channel blockers. Given the established role of PRRT2 as a negative regulator of NaV1.2 membrane exposure and functional activity, a disruption of this interaction represented a plausible pathogenic mechanism underlying both disease severity and pharmacoresistance. However, our electrophysiological analyses did not reveal detectable differences in NaV1.2 functional behavior when co-expressed with PRRT2 L336X

compared to PRRT2 WT. In both conditions, PRRT2 retained its ability to reduce NaV1.2-mediated sodium currents, indicating that the truncation at position L336 does not abolish the modulatory effect of PRRT2 on this channel, at least under the experimental conditions employed. These findings suggest that impaired regulation of NaV1.2 is unlikely to be the primary mechanism driving the severe phenotype associated with the L336X variant. Several interpretations may account for this result. First, the PRRT2 regions required for NaV1.2 interaction and modulation may be located upstream of the L336 residue, such that the truncated protein retains functional competence toward NaV1.2. Alternatively, the experimental overexpression system used in this study may partially compensate for deficits in PRRT2 stability, localization, or interaction dynamics that could be more pronounced in native neuronal contexts. Thus, while our data argue against a direct loss of PRRT2–NaV1.2 functional coupling, they do not fully exclude subtler or context-dependent effects that may emerge in more physiological models.

Importantly, the absence of an effect on NaV1.2 modulation raises the possibility that the pathogenicity of the L336X variant involves PRRT2 functions beyond sodium channel regulation. PRRT2 has been proposed to act as a multifunctional synaptic protein, potentially interacting with other classes of ion channels or components of the excitability machinery. In this regard, potassium channels represent particularly compelling candidates, given their central role in shaping action potential repolarization, firing frequency, and neuronal excitability, as well as their known contribution to epileptic phenotypes and drug responsiveness.

Consistent with this hypothesis, future studies aimed at evaluating the impact of the PRRT2 L336X variant on potassium channel function may provide critical insights into alternative disease mechanisms. Functional assays assessing PRRT2-dependent modulation of specific potassium channel subtypes could help explain both the severity of the clinical presentation and the lack of therapeutic efficacy of sodium channel blockers in the affected patient. More broadly, these investigations may contribute to redefining the role of PRRT2 in neuronal excitability, extending it beyond sodium channel regulation and offering new perspectives for targeted therapeutic interventions.

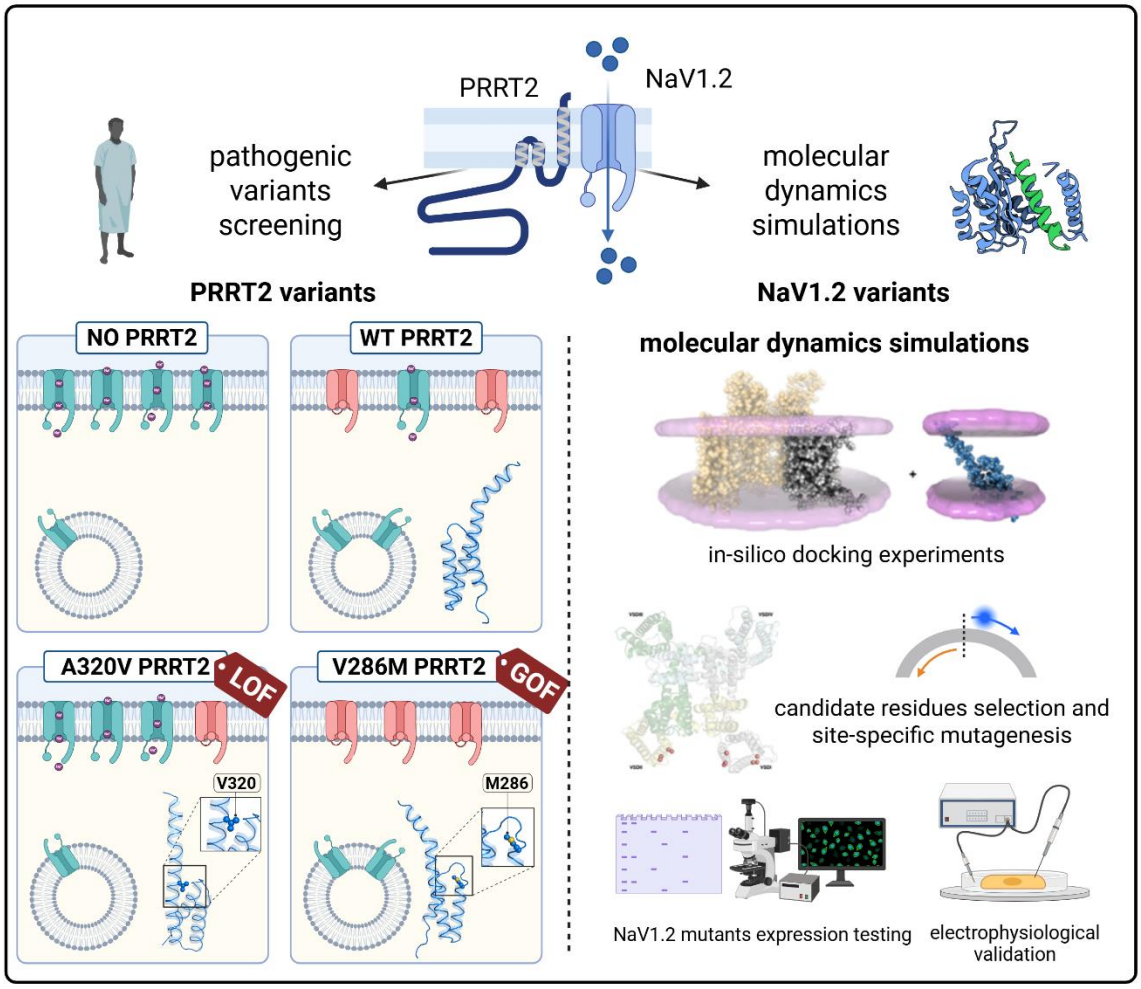

Graphical abstract Aim 2: PRRT2 – NaV1.2 interaction. Created with BioRender.com

Results – Aim 3: TMEM151A

TMEM151A membrane topology

TMEM151A is a virtually unknown protein that has recently been associated with PKD, a movement disorder causing frequent dyskinesial attacks, highly impacting the quality of life of patients, mostly children or adolescents. It is therefore of pivotal importance to understand the function of TMEM151A in order to improve therapies. As a first step to understand its biological function, we studied the membrane topology of TMEM151A protein.

Structural Modeling of TMEM151A

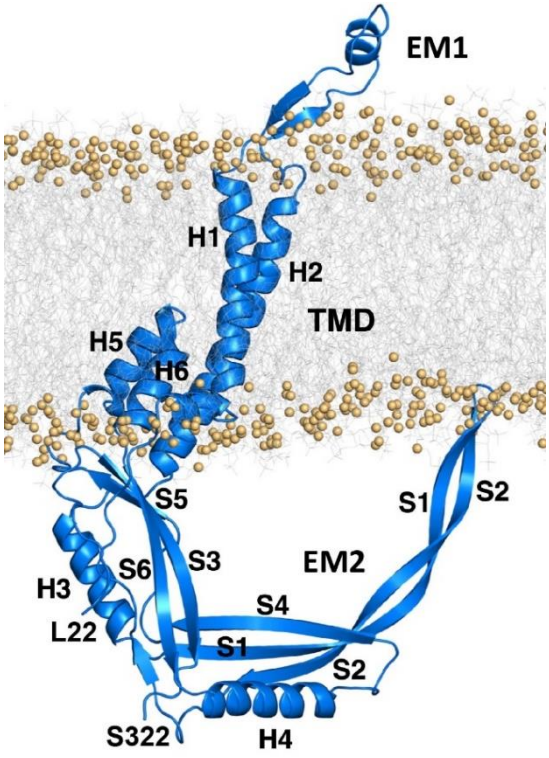

Figure 22. TMEM151A model structure. The AF2 predicted high-confidence domain L22 to S322 of TMEM151A is represented as blue cartoon embedded in the phospholipid bilayer; phospholipids heads as yellow spheres and tails as gray sticks. The predicted features are described. ECL: extracellular domain, TMD: transmembrane domain, ICD: intracellular domain, H: alpha-helix, S: β-strands. Reproduced from Morinelli et al. 2024 [85].

We retrieved the AlphaFold2 (AF2) predicted model of full-length TMEM151A. The model displays a short unstructured N-terminal segment, an all-α-helix domain, a mixed α-helix/β-sheet domain and a long mostly unstructured C-terminal region. The domain comprised between residues L22 to S322 has the highest degree of model confidence, as shown by the AF2 per-residue confidence estimation (pLDDT), whose values are mostly larger than 90 over 100 in this region.

All-atom Molecular Dynamics Simulations of Truncated TMEM151A

We used MD simulations to refine and assess the TMEM151A AF2 structural model, considering only the high-confidence segment from L22 to S322. The OPM-PPM web server yielded the predicted position of the protein embedded in a membrane, and a free-energy difference of transfer from water to the membrane of -28.3 kcal/mol [88], a value that characterizes integral membrane proteins. The protein was then inserted in a POPC membrane and solvated with water and ions. The whole system was energy-minimized and equilibrated with MD by extending the CHARMM-GUI standard protocol. The conformation of the protein within the membrane at the end of the equilibration stage is shown in Figure 22. Based on this structure, we identified the following motifs. A transmembrane domain (TMD), comprising two membrane-spanning alpha helices, H1 (residues L33-L64) and H2 (Y98-Q126), and a helix-hinge-helix motif with the short helices H5 (A285-A294) and H6 (L296 to G307), located further on the protein sequence. H1 and H2 helices are connected by an extramembrane loop (V67-A91) including a short helix (extramembrane domain 1, EM1), while on the other side of the membrane is a much larger soluble domain, formed by residues A127 to R284 and T308 to S322 (extramembrane domain 2, EM2). The EM2 includes two antiparallel

beta-sheets, β1 and β2, each of which contacts an α-helix (H3, formed by A132-Q144, and H4, by A229-N246). β1 is formed by strands S1-S2 (P147-R169 and D172-E192) and S4 (Y252-L261), with the first two extending into a long β-hairpin motif. β2 includes strands S3, S5 and S6, identified by residues A215-F226, S269-F273 and A309-F319, respectively. In the conformation at the end of the equilibration, the tip of the β-hairpin interacts with the membrane's leaflet via the linker between strands S1 and S2 (residues R167-A173).

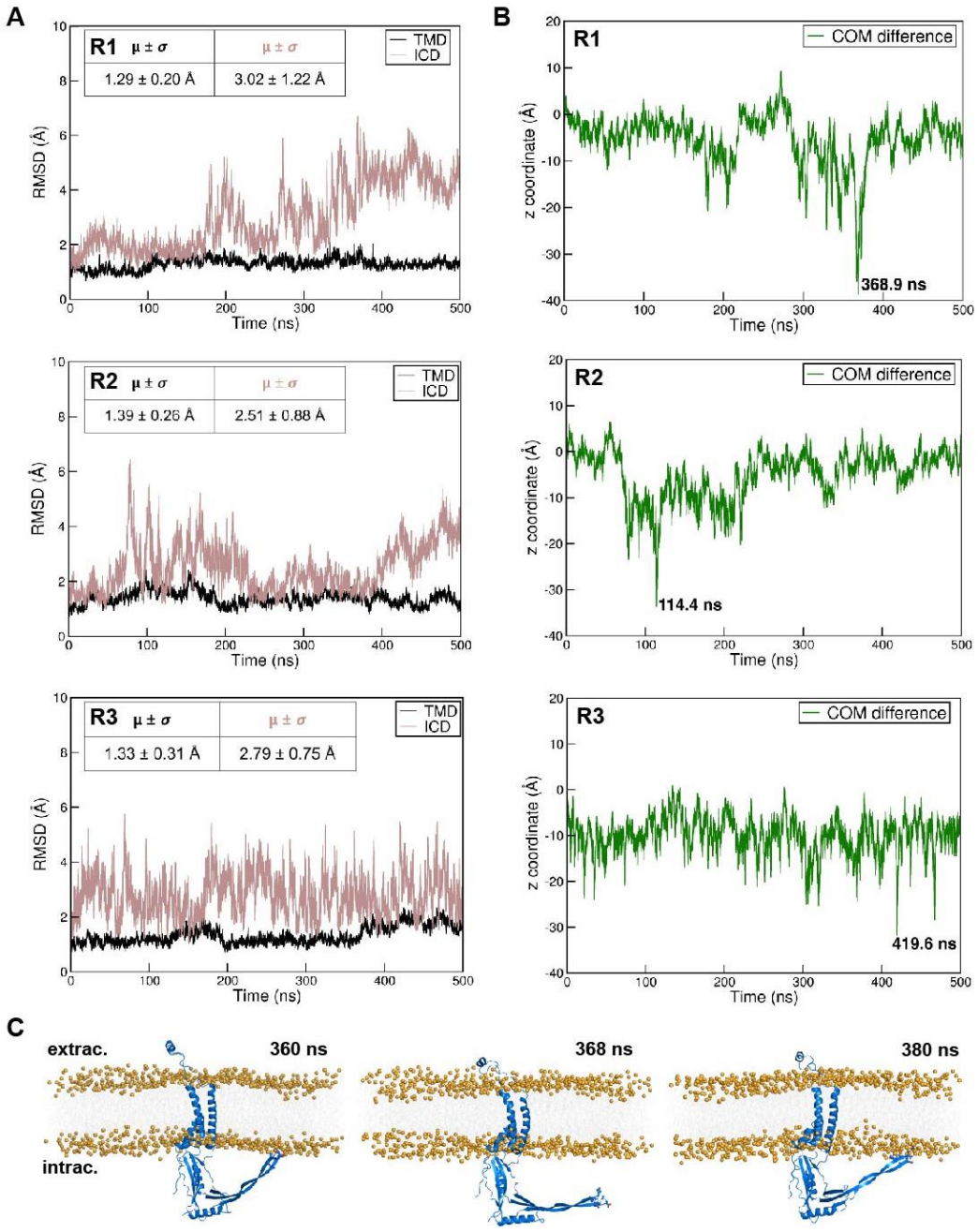

Figure 23. Molecular dynamics simulations of TMEM151A. A: Time evolution of backbone RMSD for shortened TMEM151A in the three replicated trajectories (R1-R3), for the α transmembrane domain (TMD, black), and the intracellular domain (ICD, brown). For each profile, average (μ) and Standard deviation (σ) values are reported. B: Time evolution of the distance along the z axis between the COM of R167-A173 alpha carbons and the COM of the phosphorus atoms in the lower leaflet. Frames corresponding to peak values are labelled. C: Snapshots extracted from R1 MD trajectory portraying a dissociation event between the TMEM151A β-hairpin motif and the membrane. The protein is rendered in blue cartoon while residues R167-A173 of the β-hairpin's tip are represented as sticks and spheres. Phosphorus atoms of both POPC leaflets are shown as orange spheres, while alkyl chains are presented as transparent gray sticks; water molecules are hidden for clarity. Reproduced from Morinelli et al. 2024 [85].

After equilibration, three independent 500-ns long simulations were performed. In all trajectories, the overall three-dimensional structure of the protein was conserved, as revealed by backbone root-mean-square deviation (RMSD) (Fig. 23A). In particular, very limited structural fluctuations were observed for the TMD, whose stability was additionally confirmed by the time-evolution of inter-helices cross-distances, while the EM2 showed larger fluctuations. Indeed, along the simulations we observed different conformations for the long β-hairpin, in which its tip is associated to the membrane, near to, or, only occasionally, quite far from it (completely dissociated). To monitor this heterogeneity, we computed the time-evolution of the distance between the center of mass (COM) of residues R167-A173 and the COM of leaflet's phosphorous atoms (Fig. 23B). Snapshots illustrating distinct characteristic conformations are reported in Fig. 23C.

The per-residue contribution to protein conformational fluctuations was assessed by calculating each residue's Euclidean distance (defined shift) from the starting position of the simulation after structural alignment (Fig. 24 A,B). In all the three replicas, the β-hairpin motif and the EM1 appear as the most mobile segments.

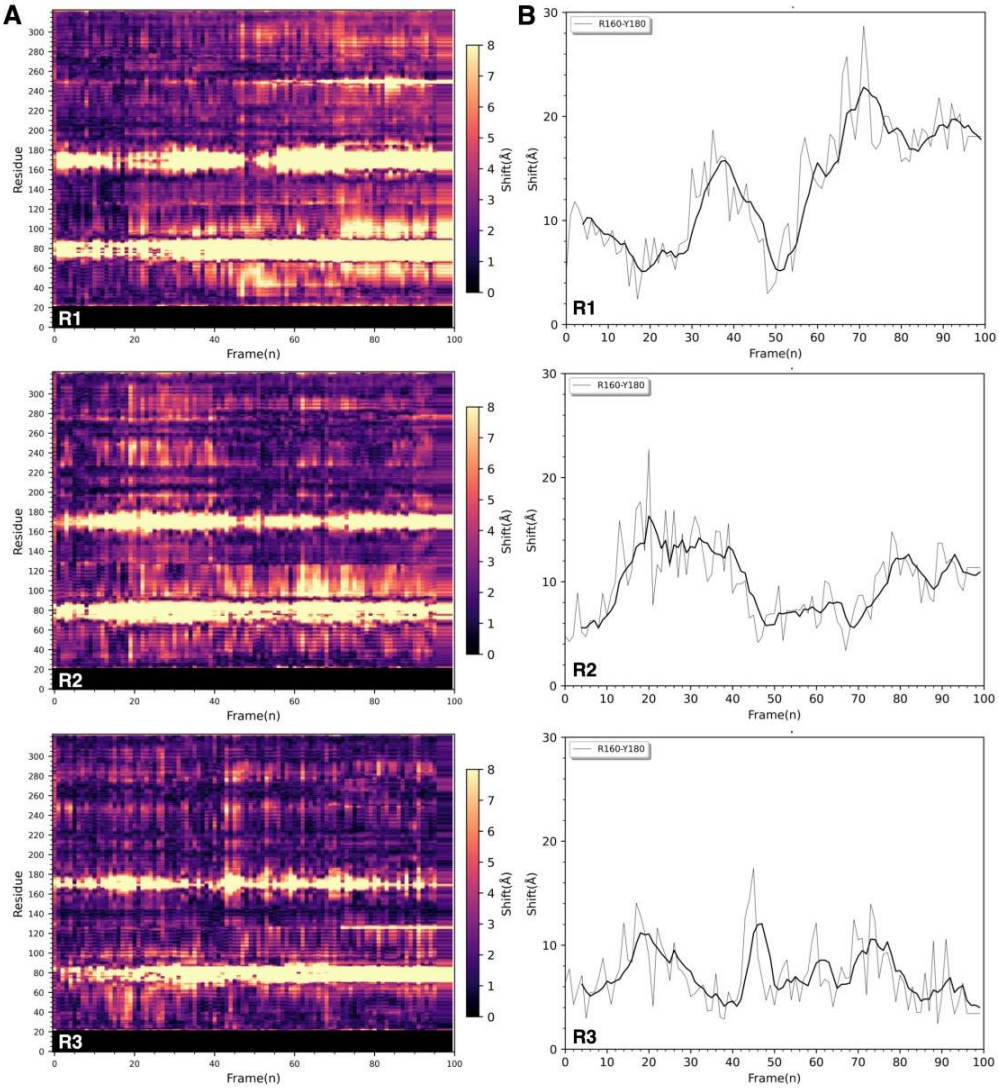

Figure 24: Protein's atomic fluctuations. A: Time evolution of each residue's backbone shift (the Euclidean distance after alignment) from the starting position in the three trajectories, colored according to their amplitude (see color bar). B: Time evolution of residue's backbone shift for TMEM151A β-hairpin (R160-Y180). Thick black lines represent moving average computed with a stride of 5 frames for each replica. Reproduced from Morinelli et al. 2024 [85].

Live-labeling immunofluorescence defines the orientation of TMEM151A in the membrane

To determine the orientation of the EM1 and EM2 domains resulting from the in-silico simulations, we generated four distinct constructs (schematized in Fig. 25A) bearing a triplet or duplet of HA tags alternatively at the N terminus (HA-TMEM151A), at the C terminus (TMEM151A-HA), within the loop (EM1) connecting the two transmembrane helices H1 and H2 (TMEM151A-HA-LOOP) or in the β1 structure at the level of the β-hairpin tip connecting the two β-strands S1-S2 (TMEM151A-HA-βsheet). AF2 generated models of the constructs show that the inserted tags do not alter the secondary or tertiary structure of truncated TMEM151A. While the pLDDT scores of the tag segments were very low, those of the protein were the same as the original model.

We transfected HEK293 cells with the four constructs and performed a live-labeling IF with anti-HA antibody followed by permeabilization and standard IF with anti-TMEM151A antibody (targeting an intracellular epitope) as schematized in Supplementary 1 to figure 25. During the live-labeling protocol cells preserve the cell membrane integrity, therefore, only the HA-epitopes which are exposed extracellularly can be recognized by the antibody. In these conditions, HA antibodies exclusively recognized the TMEM151A-HA-LOOP isoform expressing cells, confirming exposure of this loop to the extracellular surface (Fig. 25B, upper lane), whereas no signal could be detected in live cells transfected with the other constructs, confirming that the N and C termini, as well as the β-hairpin tip loop, are located intracellularly. After permeabilization, we performed standard IF with anti-TMEM151A antibody, aimed to visualize the total TMEM151A expression and that the cells negative for live labeling are actually transfected. After this step, all four TMEM151A isoforms were detected with comparable expression levels (Fig. 25B, middle lane).

To have a further validation of the described membrane topology, we generated a double tagged *TMEM151A* construct presenting a duplet of HA tag in the EM1 loop and a V5 tag at the C terminus of the protein (Supplementary 2 to fig 25). Live-labeling IF using anti-HA antibody resulted in a positive membrane staining, while no signal was present by anti-V5 antibody labeling. In the standard IF performed afterwards, the permeabilization led both anti-HA and anti-V5 antibodies to give positive cellular signals. Therefore, only the combination of the anti-HA live labeling signal (in green) with the anti-V5 permeabilized signal (in red) resulted in a merged signal (yellow) at the membrane level. These results demonstrate that EM1 connecting H1 and H2 helices is extracellular whereas the large soluble EM2 domain is oriented towards the cytosol, as schematized in Figure 22.

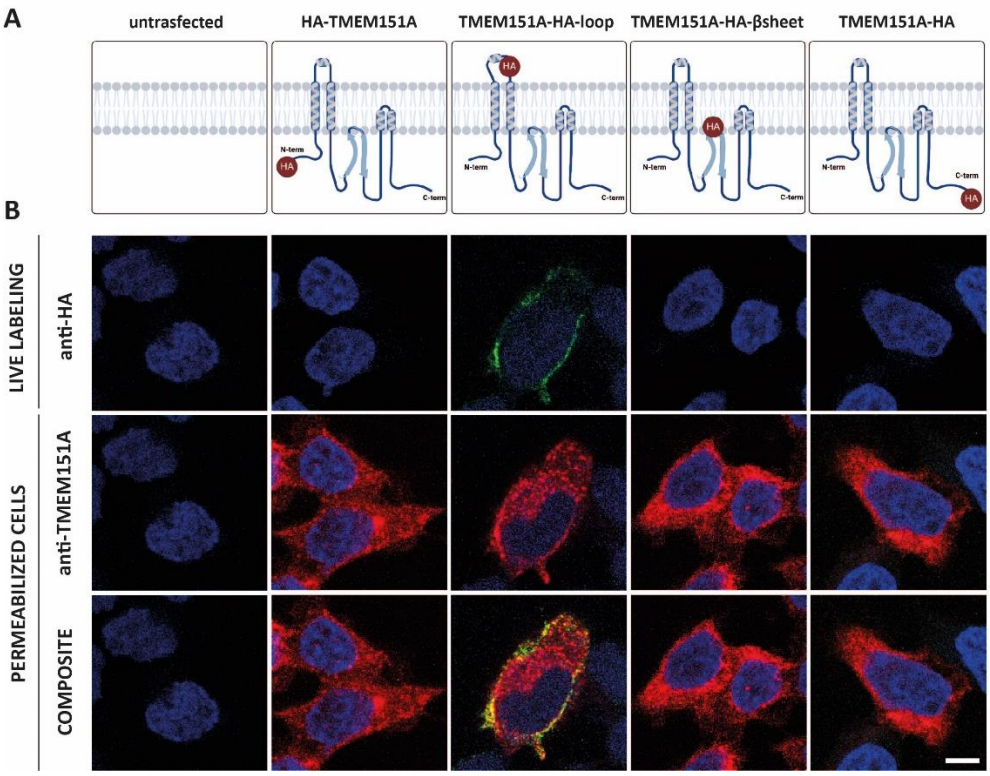

Figure 25: Live-labeling immunofluorescence validates in-silico modeling of TMEM151A. A: Schematic representation of HA tags positioning in the predicted TMEM151A membrane topology. B: Representative confocal images of HEK293 cells transfected with either HA-TMEM151A, TMEM151A-HA-LOOP, TMEM151A-HA-βsheet or TMEM151A-HA, live-labeled with anti-HA antibody (upper panel, green) and labeled with anti-TMEM151A (middle panel, red). Merged images (bottom panel). Scale bar 5 µm. Reproduced from Morinelli et al. 2024 [85].

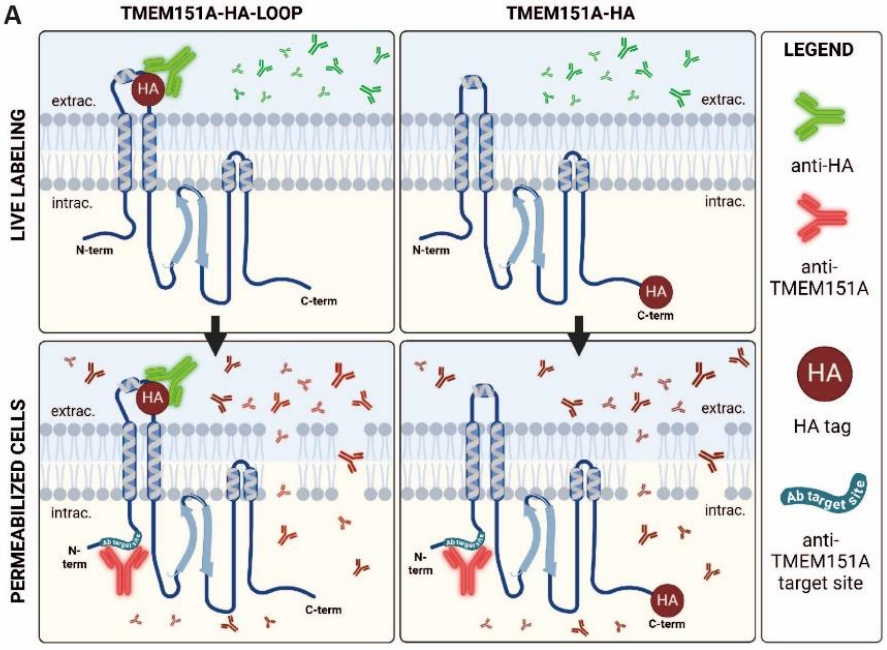

Supplementary 1 to figure 25: Live labeling validation tools. A: Live-labeling and standard immunofluorescence protocol. Upper panel: Schematic representation of anti-HA live-labeling immunofluorescence protocol applied toTMEM151A-HA-LOOP and TMEM151A-HA. Bottom panel: Schematic representation of anti TMEM151A standard immunofluorescence protocol applied to TMEM151A-HA-LOOP and TMEM151A-HA, previously treated with the anti-HA live-labeling immunofluorescence. Reproduced from Morinelli et al. 2024 [85].

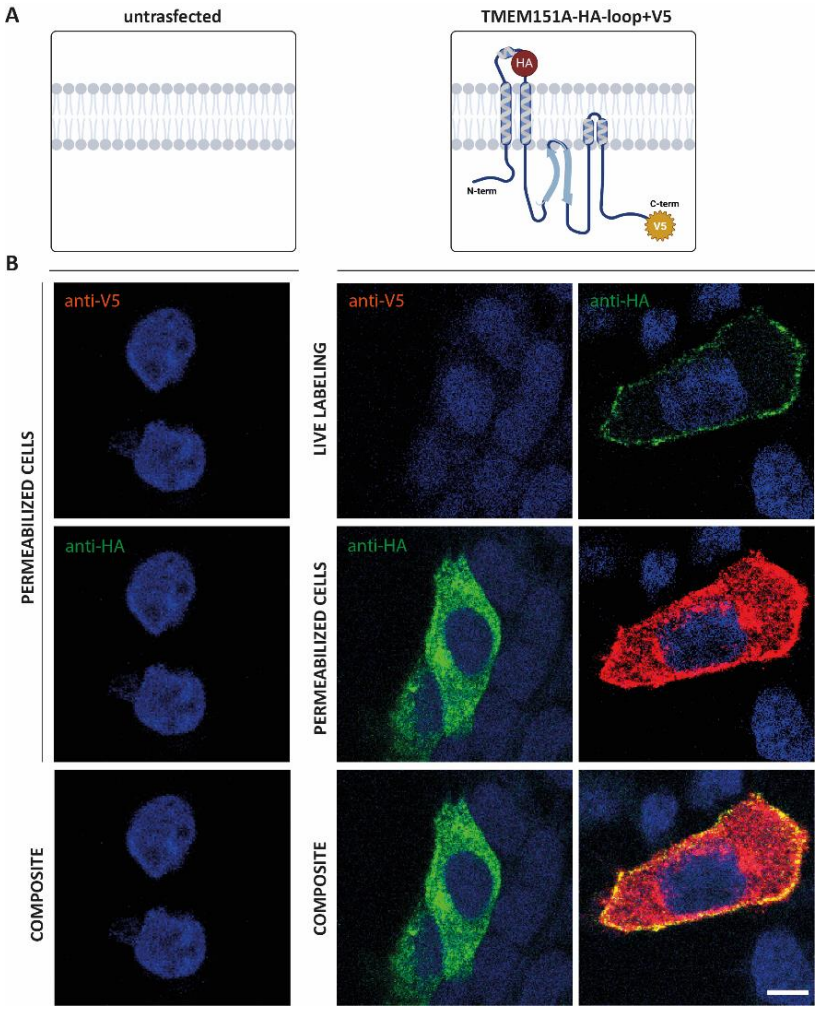

Supplementary 2 to fig 25: Live-labeling topology validation via TMEM151A double tagged molecule. A: Schematic representation of untransfected cells and cells transfected with TMEM151A-HA-loop+V5 to show the HA and V5 tags positioning in the predicted TMEM151A membrane topology. B: Left: Representative confocal images of untransfected HEK293 cells immunolabeled with anti-V5 (red– upper image) and anti-HA (green– middle image) antibodies. Bottom image: merge. Right: Representative confocal images of HEK293 cells transfected with TMEM151A-HA-LOOP+V5. Upper panel: live-labeling with anti-V5 (red) and anti-HA antibody (green). Middle panel: standard labeling with anti-HA (green) and anti-V5 (red). Bottom panel: merge images. Scale bar 5 µm. Reproduced from Morinelli et al. 2024 [85].

Electron microscopy confirms TMEM151A membrane topology

To analyze the TMEM151A topology in a greater detail, we transfected HEK293 cells with TMEM151A-HA-LOOP and TMEM151A-HA constructs, that expose HA epitopes on the opposite sides of the membrane (see Fig. 25), and performed immunogold labeling followed by electron microscopy analysis. As expected, cells transfected with TMEM151A-HA-LOOP showed the gold particles localized outside of the plasma membrane (Fig. 26A, upper images) and, although more rarely, in the internal part of putative endosomes (Fig. 26A, bottom images). On the contrary, in the cells transfected with the TMEM151A-HA, gold particles are visualized at the internal side of the plasma membrane (Fig. 26B, upper image) and more frequently at the cytosolic face of the ER (Fig. 26B, lower images) and of the endosomes (Fig. 26B, upper images). These results confirm an opposite localization of the HA epitopes of the TMEM151A-HA-LOOP and the TMEM151A-HA constructs with respect to the cellular membranes and further confirm the predicted topology. In addition, taken together, our confocal and electron microscopy data support the results by Li et al. regarding the presence of TMEM151A overexpressed protein at the level of intracellular membranes, in particular of

the ER and endosomal structures, as well as provide new information about its localization at the plasma membrane [76].

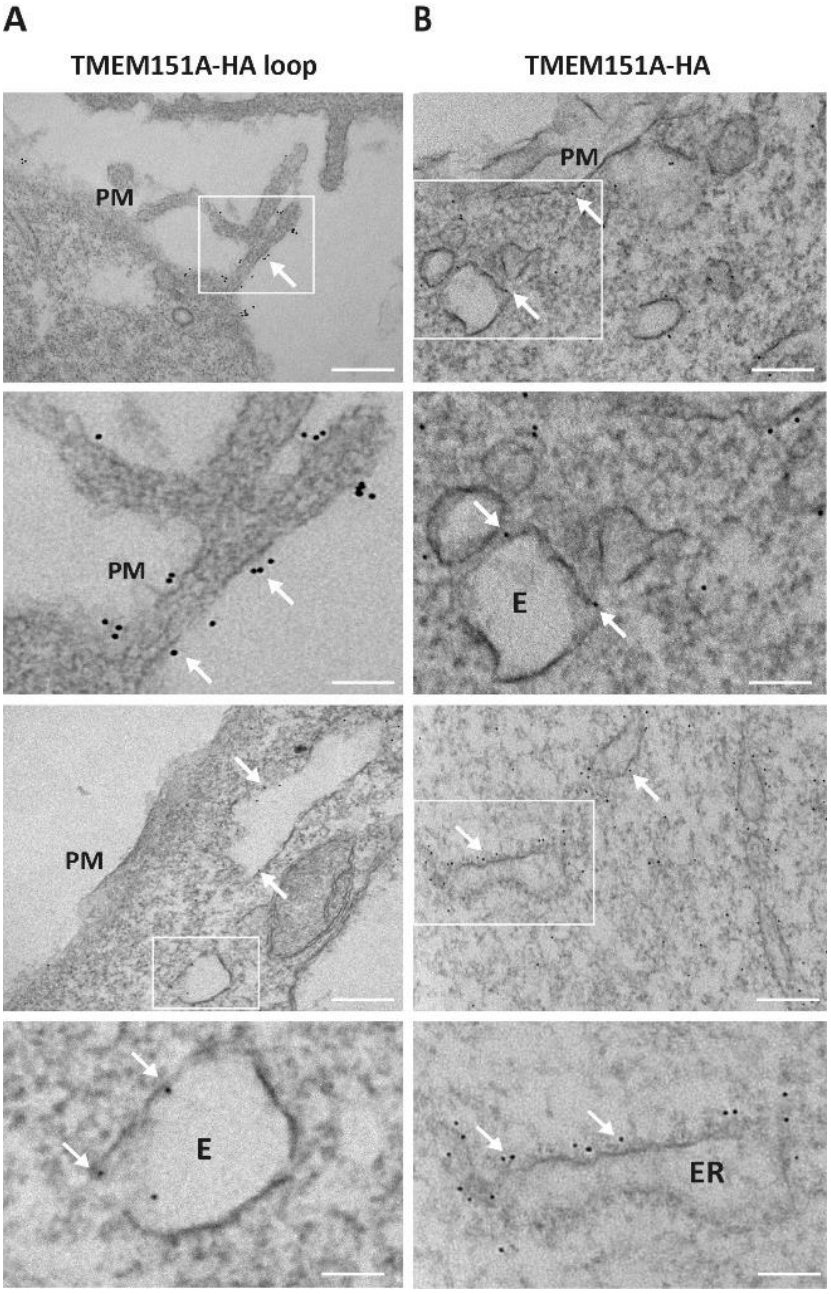

Figure 26: Electron microscopy confirms TMEM151A predicted topology. A: Electron micrographs depict gold particles localization of TMEM151A-HA-LOOP on the outer plasma membrane side (upper image) and on the inner side of a putative endosome structure (bottom image). B: Images depict gold particles localization of TMEM151A-HA on the inner side of plasma membrane and on the outer side of endosome structure (upper image) and endoplasmic reticulum (bottom image). OUT: extracellular. IN: intracellular. Scale bar 100 nm. Reproduced from Morinelli et al. 2024 [85].

Taken together, our results validate a starting AlphaFold model of TMEM151A and reveal that it comprises a transmembrane domain with two membrane-spanning alpha helices connected by a short extracellular loop and an intramembrane helix-hinge-helix structure. Notably, most of the protein is oriented towards the intracellular side of the membranes with a large cytosolic domain, as well as the protein N- and C-termini. Moreover, we demonstrated that TMEM151A localizes both at the plasma membrane and in intracellular organelles' membranes.

TMEM151A variants

Generation of six TMEM151A pathogenic variants

To date, 34 *TMEM151A* variants have been found, including 22 missense variants, 11 truncated variants, and a non-frameshift deletion (Fig. 27). Most of these variants cluster in the C-terminal cytosolic domain, highlighting the functional importance of this region. The majority of *TMEM151A*-positive PKD patients are sporadic. No clear genotype-phenotype correlations are established for *TMEM151A*-related PKD, and unlike the *PRRT2* high-frequency variant c.649dupC, no hotspot variant was found in *TMEM151A*. Functional assays performed by Li et al. indicated a significantly decreased protein expression of some mutant (non-truncated) *TMEM151A* isoforms, suggesting a potential loss of function mechanism. Additionally, TMEM151A-deficient mice showed spontaneous dyskinesia-like behaviors, supporting this hypothesis. However, a dominant-negative effect through impaired protein interactions is also possible.

As a second approach to gain comprehension of *TMEM151A* function, we decided to investigate some of the pathological variants of *TMEM151A*. Understanding the alterations of pathogenetic variants can provide valuable information regarding the function of the *TMEM151A*. Starting from the literature, we selected six *TMEM151A* variants, based on variants' frequency in distinct families, variant type, and severity of the phenotype (Table 5). Among the six chosen variants, three of them are missense, therefore they cause the change of one amino acid in a different one (G56R, V264A, S297L), two cause a precocious truncation (C125*, L300Pfs*118) and one cause the deletion of one amino acid (V149del).

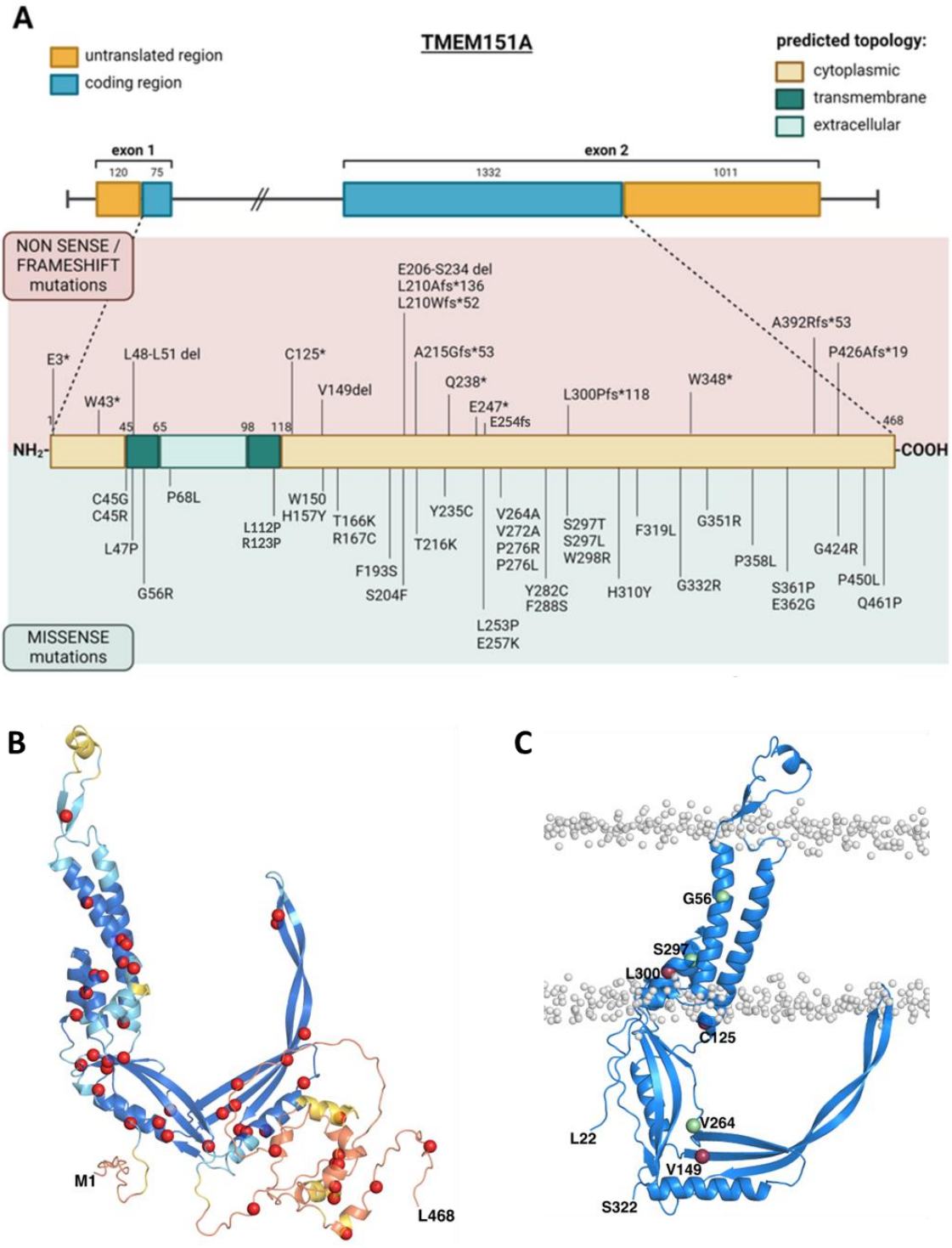

Figure 27: A: Schematic representation of the TMEM151A gene and protein structure. All the currently published in literature variants of TMEM151A are depicted. B: Structural mapping of pathogenetic variants on the AF2 predicted model for TMEM151A. Amino acids M1-L468 are portrayed as cartoon and coloured by estimated model confidence (blue, high; yellow, medium; red, low). Alpha carbons of pathogenetic residues are rendered as red spheres. C: Structural mapping of candidates selected for single-point in vitro mutagenesis. TMEM151A residues L22-S322 are embedded in a POPC bilayer. α-carbons of the 6 pathogenetic residues considered are shown. The α-carbons giving rise to truncations and missense variants are rendered as spheres and coloured in brown and green respectively. Manuscript in preparation.

TMEM151A variants' characterization.

We generated six pathogenetic variants of *TMEM151A* and characterized them by in vitro experiments for the protein expression levels and cellular sub-localization. The first step in

characterizing the mutated isoforms was to examine their total expression in comparison to the wild type of protein. To this end, TMEM151A wild type and variants were transfected in naïve HEK293 cells, and the protein extracts were analyzed by western blotting (Fig. 28 A left). Some mutant isoforms expression levels are statistically different from hTMEM151A WT (Fig. 28 B). Specifically, three of them (G56R, V149del and S297L) have a lower expression than the wild type, around the 50% of the WT one. The truncated isoforms C125* and L300Pfs* 118 have a lower molecular weight than the TMEM151A WT, while their expression level is not decreased, but rather increased in the case of the C125* mutant. The V264A missense variant causes a significant increase in protein expression.

Transfected HEK293 were also analyzed by immunofluorescence using anti-HA antibody (Fig. 28 B). No statistically significant differences in fluorescent intensity of transfected cells were identified, with the exception of the G56R variant, which showed a decreased mean fluorescence intensity (Fig. 28D). It is anyway visible a non-significant trend of increase in mean fluorescence intensity for both the truncated variants. The immunolabeled cells were also analyzed for the number of transfected cells and all the mutants showed a significantly lower transfection efficiency, with the exception of the V264A variant, which has comparable values to the respective WT (Fig. 28 C). Taken together, these results are consistent with the western blotting analysis.

DNA	protein	type	Citation	# patients	# families	Phenotype
c.166G>C	G56R	Missense	[80]	1	1	PKD
c.375C>A	C125*	Truncation	[37], [76]	5	3	PKD, dystonia
c.445_447delGTC	V149del	Microdeletion	[82]	1	1	PKD, chorea
c.791T>C	V264A	Missense	[37], [77]	4	3	PKD
c.890C>T	S297L	Missense	[82]	1	1	PKD, dystonia
c.897_912del	L300Pfs*118	Truncation	[76], [77]	7	6	PKD, dystonia

Table 5: table of the six selected variants and the resulting phenotypes.

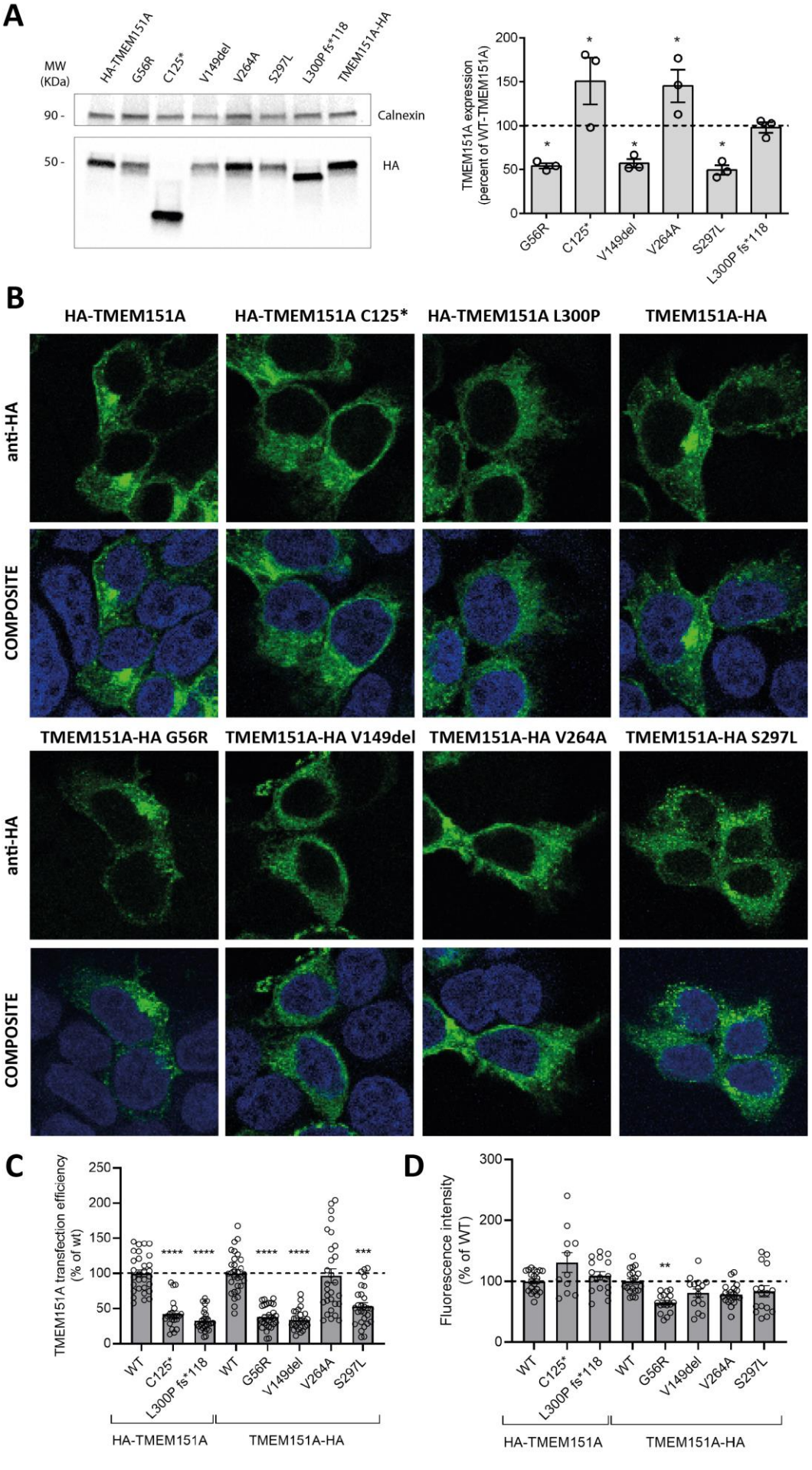
A
MW (KDa)
HA-TMEM151A
G56R
C125*
V149del
V264A
S297L
L300P fs*118
TMEM151A-HA
90 -
Calnexin
50 -
HA
TMEM151A expression (percent of WT-TMEM151A)
200
150
100
50
0
G56R
C125*
V149del
V264A
S297L
L300P fs*118
B
HA-TMEM151A
HA-TMEM151A C125*
HA-TMEM151A L300P
TMEM151A-HA
anti-HA
COMPOSITE
TMEM151A-HA G56R
TMEM151A-HA V149del
TMEM151A-HA V264A
TMEM151A-HA S297L
C
TMEM151A transfection efficiency (% of wt)
250
200
150
100
50
0
****
****
****
****
***
WT
C125*
L300P fs*118
WT
G56R
V149del
V264A
S297L
HA-TMEM151A
TMEM151A-HA
D
Fluorescence intensity (% of WT)
300
200
100
0
**
WT
C125*
L300P fs*118
WT
G56R
V149del
V264A
S297L
HA-TMEM151A
TMEM151A-HA

Figure 28: TMEM151A mutants expression levels. A: Protein extracts from naïve HEK293 cells transfected with either WT or mutant TMEM151A-HA variants were analyzed by western blotting using anti-HA antibodies. Left: Representative immunoblot. Right: Densitometric analysis of the immunoreactive bands. Calnexin was used as loading control. The expression levels of TMEM151A mutants are shown in percent of the immunoreactivity of WT as means ± sem of n = 3 independent experiments (horizontal line; mean ± sem). B: Representative confocal images of HEK293 cells transfected with TMEM151A-HA mutants. Immunofluorescence with anti-HA (green) antibody; cell nuclei are depicted in blue. C: TMEM151A-HA mutants transfection efficiency is represented in percentage of WT. D: TMEM151A-HA mutants fluorescence quantification is represented in percentage of WT. Data are represented as means ± sem of n = 3 independent experiments (horizontal line shows 100%). Manuscript in preparation.

TMEM151A subcellular localization in overexpression experiments

Studying so-called T dark genes is particularly challenging due to the limited availability of specific reagents for their detection and functional characterization. We tested both commercially available and custom-made antibodies targeting TMEM151A; however, as frequently happens for scarcely investigated proteins, none of them specifically recognized the endogenous protein but the overexpressed isoform. As previously reported in the characterization of TMEM151A membrane topology, a commercial anti-TMEM151A antibody is able to detect the overexpressed isoform by recognizing an intracellular epitope of the protein. Due to the lack of functional antibodies capable of recognizing endogenous TMEM151A, most of our experiments were performed under overexpression conditions using anti-HA antibodies to detect HA epitopes fused to TMEM151A. We favored anti-HA antibodies over anti-TMEM151A antibodies because of their higher efficiency and well-established specificity.

By transfecting TMEM151A in HEK293 we investigated its sub-cellular localization through co-staining experiments with markers typically specific for the Golgi apparatus (GM130) the endoplasmic reticulum (calreticulin) and the plasma membrane (ZO1). As is visible from the figure 29, TMEM151A under overexpression conditions strongly co-localize with Golgi apparatus and spreads also in the endoplasmic reticulum membranes. Its co-localization with ZO1 is not so strong as for the previous two markers, suggesting that the membrane localization (previously demonstrated) of TMEM151A is a lower fraction of its total expression.

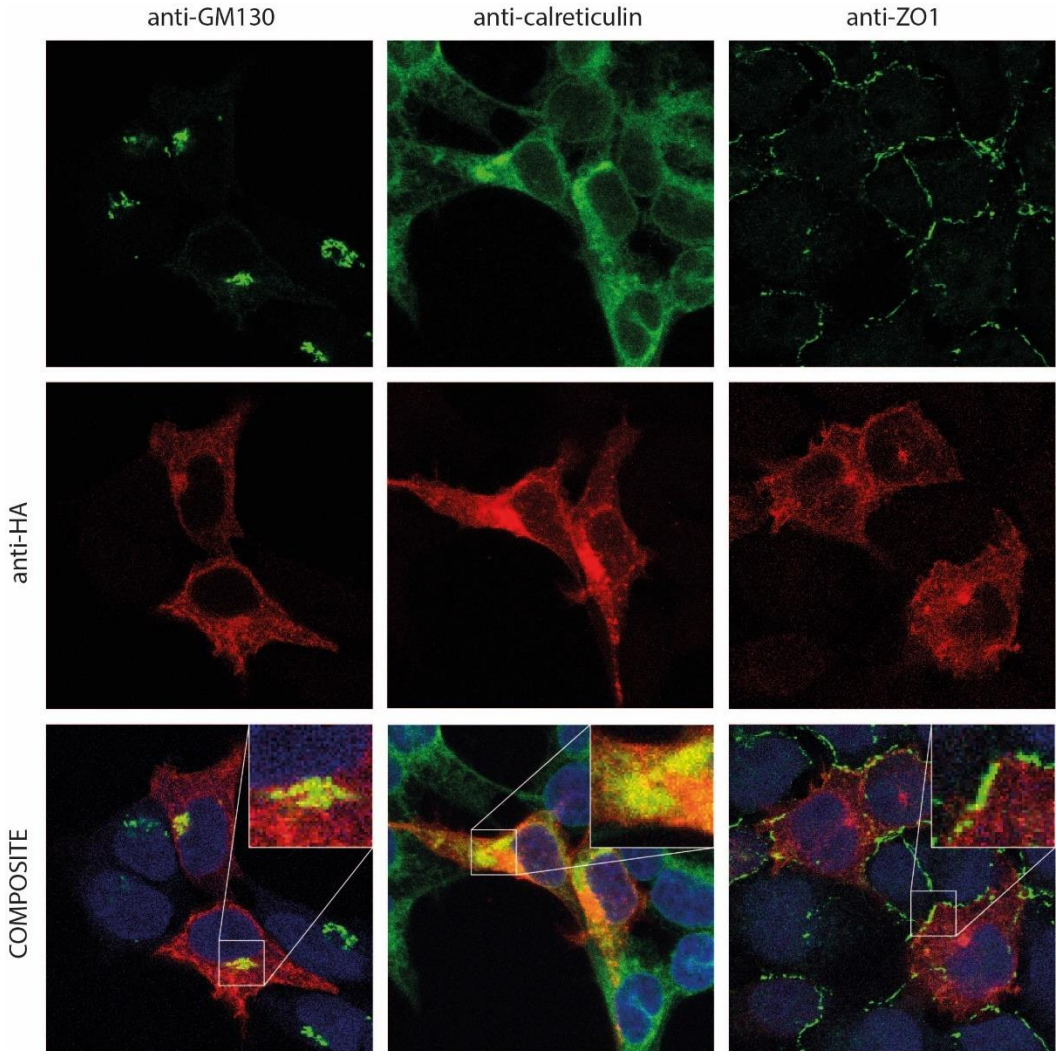

Figure 29: Representative confocal images of HEK293 cells, with zoom-in panels, transfected with TMEM151A-HA labelled with anti-HA antibody (red) and anti-GM130 for Golgi apparatus staining, or anti-calreticulin for endoplasmic reticulum staining or anti-ZO1 for plasma membrane staining. Co-localization is visible in yellow. Manuscript in preparation.

TMEM151A variants lose membrane localization

The live labeling experiment shown before demonstrated that TMEM151A is expressed at the plasma membrane and clarify its membrane topology. Therefore, we decided to investigate the impact of the pathogenic variants on TMEM151A surface expression. For live labeling experiments the use of the construct TMEM151A-HA LOOP is needed in which the HA tag is inserted in the extracellular domain. Therefore, we generated the six variants in the TMEM151A-HA LOOP construct by site-directed mutagenesis as described before for the HA-TMEM151A and TMEM151A-HA constructs. After checking the sequence of the different variants, we performed a live- labelling immunofluorescence with anti-HA antibody tagging the external HA epitope, followed by the classical assay as previously described. As shown in the figure 30, although all mutants are expressed in HEK293 as demonstrated by the anti-TMEM151A red staining of the permeabilized cells only the V264A variant maintains the correct membrane localization similar to WT protein, as shown by the green staining of the live labeled cells with the anti-HA antibody. Moreover, the membrane fluorescence quantification of TMEM151A-HA-LOOP WT and V264A isoforms does not show differences in the protein amounts at the plasma membrane levels. For the other five variants (G56R, C125*, V149del, S297L and L300Pfs*118) no green live staining by the anti- HA antibody was observed,

suggesting the lack of these TMEM151A variants from the plasma membrane. Therefore, these variants lead to altered subcellular localization of the protein compared with the WT.

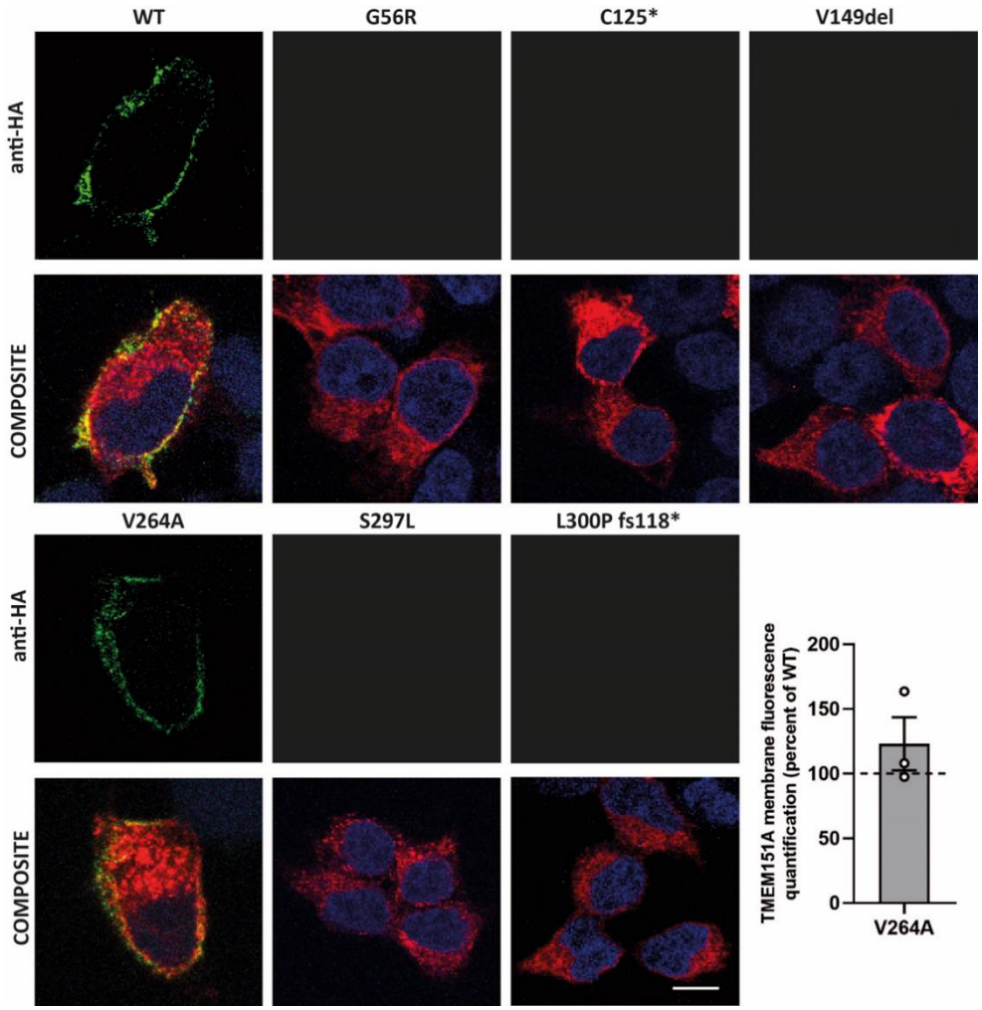

Figure 30: Representative confocal images of HEK293 cells transfected with TMEM151A-loop-HA WT and mutant isoforms live labelled with anti-HA antibody (green) and labelled with anti-TMEM151A (red). Scale bar 5 µm. Bottom right: Quantification of live HA fluorescence intensity calculated for the single cells. Only V264A mutant is shown because the others have no membrane fluorescence. The fluorescence intensity level of TMEM151A-loop-HA V264A mutant was normalized on TMEM151A-loop-HA WT mean membrane intensity value, which is depicted as dashed line and are shown as means +/- SEM with superimposed individual values from n=3 independent experiments. Statistical analysis was done using One-way Anova. Manuscript in preparation.

Subcellular localization of mutant TMEM151A isoforms

To evaluate whether the selected TMEM151A variants affect Golgi localization, we performed immunofluorescence using the Golgi GM130 marker in permeabilized HEK293 cells expressing WT or mutant constructs. As shown in Supplementary 1 to figure 30, all isoforms displayed a Golgi distribution similar to the WT. Immunolabeled cells were analyzed by evaluating the amount of TMEM151A co-localizing with GM130 over the total TMEM151A present in the transfected cell. Comparing the mutant isoforms with the WT one, no differences were found in the amount of TMEM151A located in this organelle. This measure is independent to the total TMEM151A expression previously determined in figure 28. These findings suggest that the analyzed variants do not impair TMEM151A accumulation in the Golgi compartment. The same approach has been conducted on the endoplasmic reticulum localization (Supplementary 2 to Fig. 30) using the endoplasmic reticulum specific Calreticulin marker and also in this case, no significant mis-localization has been found.

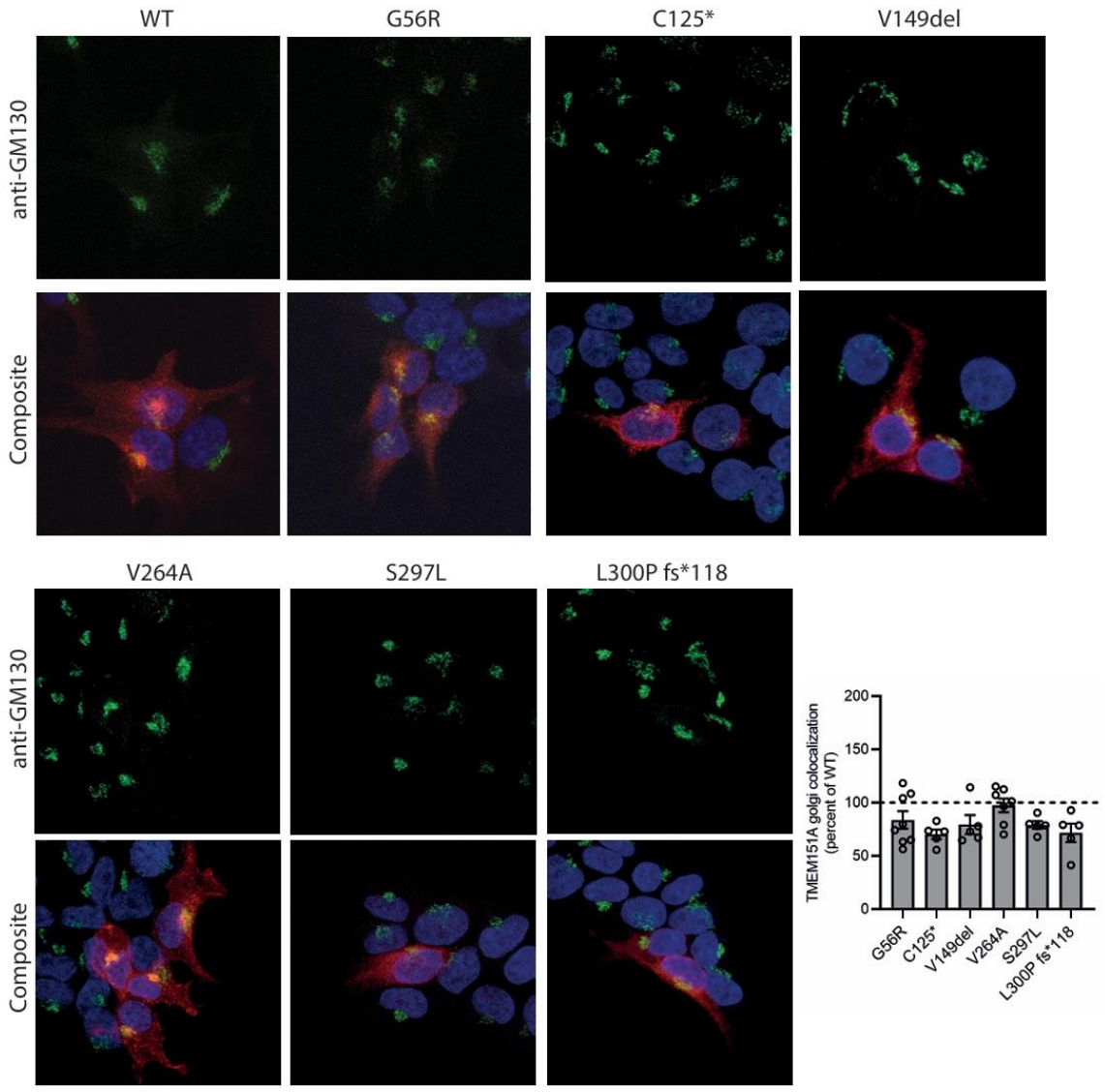

Supplementary 1 to figure 30: Representative confocal images of HEK293 cells transfected with TMEM151A-HA and its variants labelled with anti-HA antibody (red) and anti-GM130 for Golgi apparatus staining. Co-localization is visible in yellow. Bottom right panel: TMEM151A variants Golgi apparatus localization expressed in comparison of WT (percent of WT, shown as dashed line). Manuscript in preparation.

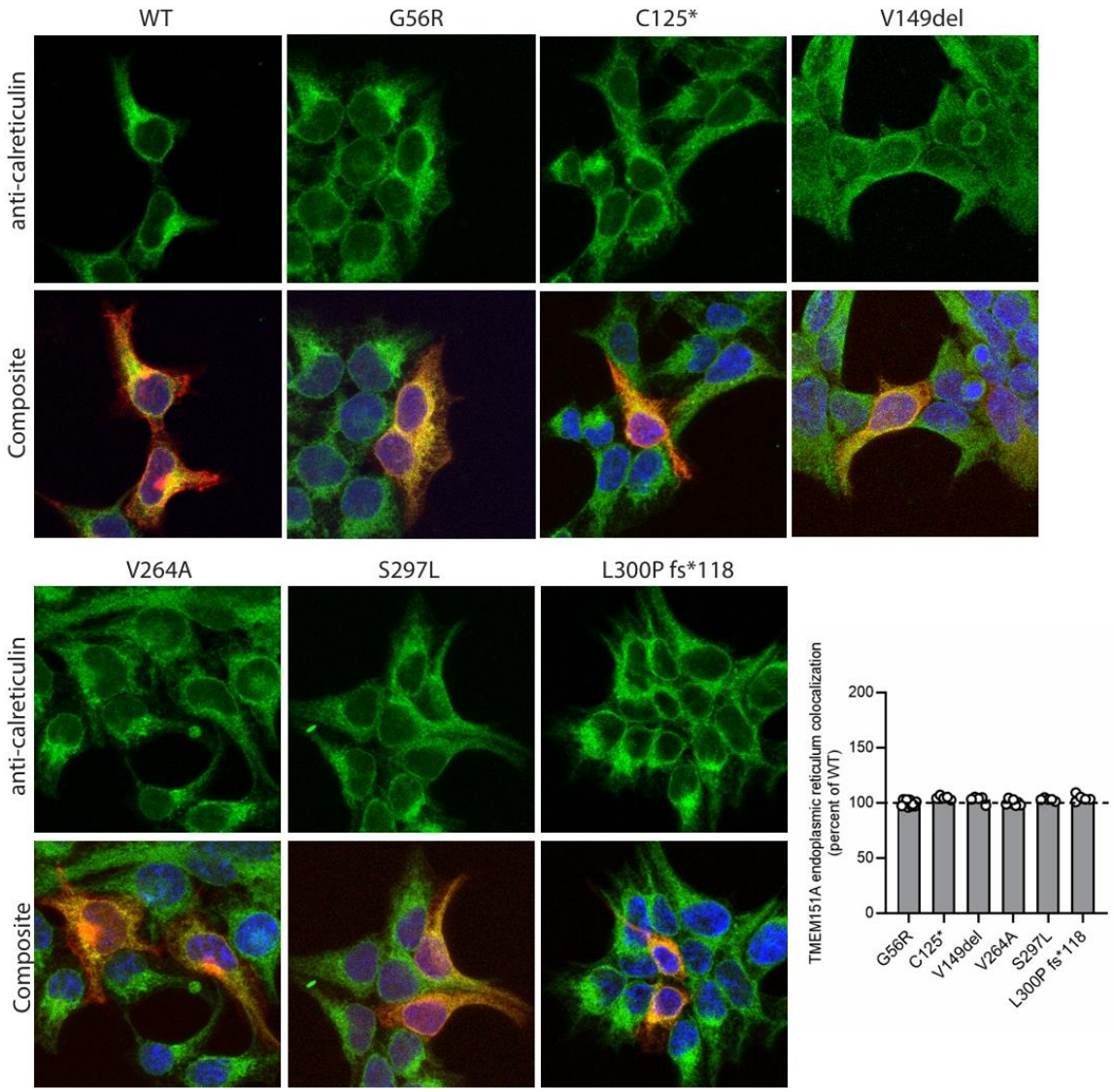

Supplementary 2 to figure 30: Representative confocal images of HEK293 cells transfected with TMEM151A-HA and its variants labelled with anti-HA antibody (red) and anti-calreticulin for endoplasmic reticulum staining. Co-localization is visible in yellow. Bottom right panel: TMEM151A variants endoplasmic reticulum localization expressed in comparison of WT (percent of WT, shown as dashed line). Manuscript in preparation.

Role of TMEM151A in mouse neuronal development

TMEM151A has been implicated in neurodevelopmental processes, as affected patients typically present with disease onset during childhood or adolescence. As previously described, studying TMEM151A, as other T-Dark genes, is particularly challenging due to the lack of specific antibodies recognizing the native form of the protein. Nevertheless, some information on TMEM151A mRNA expression in mouse tissues has been previously reported [76], [86] defining a developmentally regulated expression pattern of TMEM151A in the mouse brain, suggesting a role during nervous system maturation. Based on these observations, we sought to investigate the function of TMEM151A in neuronal development using primary mouse neurons.

TMEM151A expression is developmentally regulated

To further characterize the temporal expression profile of TMEM151A during neuronal development in vitro, TMEM151A mRNA levels were analyzed in primary mouse neuronal

cultures derived from cortex and hippocampus at 0, 3, 7, 14, 21, and 28 days in vitro (div). Primary mouse neuronal cultures represent a widely used and well-established experimental model for the study of neuronal development and maturation, and are particularly suitable for investigating the temporal regulation and functional role of genes involved in these processes.

As shown in Figure 31A, TMEM151A mRNA expression was detectable at all analyzed time points in both cortical and hippocampal cultures, although with distinct temporal dynamics. In cortical neurons, TMEM151A expression was low at early stages (0–3 div), increased markedly at 7 div, and remained elevated at later stages, with a peak observed around 14–21 div, followed by a slight decrease at 28 div.

In hippocampal neuronal cultures, TMEM151A expression also appeared low at early time points but showed a more pronounced increase starting from 7 div, reaching higher relative expression levels at 14 and 21 div compared to cortical cultures, before declining at 28 div.

Overall, these data indicate that TMEM151A expression is developmentally regulated in primary neuronal cultures, with a temporal pattern consistent with a potential role during neuronal maturation, particularly in hippocampal neurons, and consistent with patients' phenotype arising during late childhood and adolescence.

TMEM151A has a positive effect on dendritic arborization in hippocampal neurons

Given the expression pattern of TMEM151A in primary neurons, we decided to evaluate a possible effect of TMEM151A itself on their development through overexpression experiments.

Overexpression studies in primary neuronal cultures are particularly challenging, as neuronal development can be strongly affected by the transfection procedure itself, often to a greater extent than by the overexpressed construct. Therefore, to test the basic conditions and identify a potential effect of the transfection of TMEM151A WT itself, we transfected hippocampal neurons at DIV7 with either pKH3-GFP or pKH3-TMEM151A-GFP constructs and evaluated the impact of TMEM151A on neuronal morphology, branching and development. The selection of 7 days in vitro (DIV7) as a time point for transfection (see Materials and Methods) was based on the observed increase in expression of TMEM151A at this stage (Fig. 31A), furthermore, according to the patient phenotype, we had the intention to investigate early effects on dendritic arborization, which typically occur during active phases of neuronal development.

I generated the pKH3-GFP and pKH3-TMEM151A-GFP constructs as reported in the material and methods section. Immunofluorescence experiments were carried out in hippocampal neurons transfected with either TMEM151A-HA, TMEM151A-GFP or GFP as control. Confocal microscopy was used to acquire high-resolution images for the quantitative assessment of neurite length and arborization (see Materials and Methods).

Neurons transfected with GFP alone present a slightly simpler and lower in length arborization with respect to neurons transfected with TMEM151A-HA or TMEM151A-GFP (Fig. 31B). Neurites length analysis shows no significant differences in the TMEM151A conditions with respect to the GFP alone one (Fig. 31C). Sholl analysis measures the number of intersections between the neurites and 10 concentric circles drawn from the center of the cell body at constant distance. Neurons overexpressing TMEM151A have a significantly higher number of branches with respect to the ones overexpressing GFP alone (Fig. 31D) at the distance of 60 µm from the cell body center, and a non-significant higher number of branches at almost all the measured distances. No differences were found in comparing the TMEM151A-HA and TMEM151A-GFP conditions. These results suggest a role of TMEM151A in positively regulating the neuronal branching development and probably network formation.

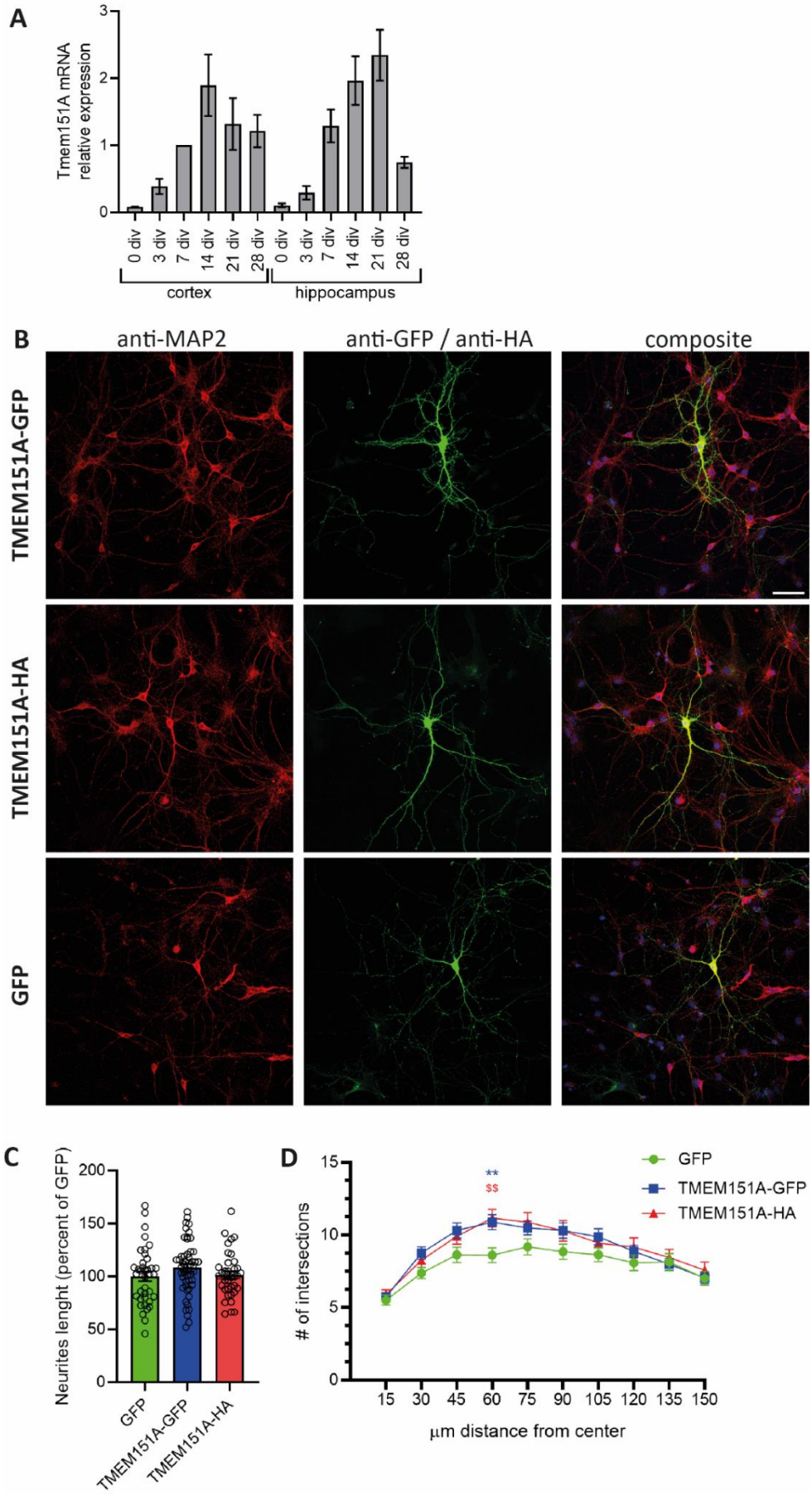

Figure 31: Effects of TMEM151A WT on Hippocampal Neurons. A: TMEM151A relative mRNA expression. TMEM151A relative mRNA expression in mouse neuronal primary cultures of cortical and hippocampal neurons at different

days in vitro (div). Data are resulting from n>3 independent experiments. Data are normalized on cx 7div samples internally at each experiment. B: Representative confocal images of hippocampal neuronal cells transfected at 7div with pKH3 GFP, pKH3-TMEM151A-HA or pKH3-TMEM151A-GFP labelled with anti-GFP antibody (green) or anti-HA antibody (green). Anti-MAP2 staining shows neuronal culture (red). Scale bar 50 µm. C: Quantification of neurites length calculated for the single cells. Data are normalized on pKH3-GFP mean neurites length and are shown as means +/- SEM with superimposed individual values from n=3 independent experiments. D: Sholl analysis showing the number of intersections between neuron's processes and concentric circles radiating from the soma at 15 µm intervals. Statistical analysis was done using One-way Anova. Manuscript in preparation.

TMEM151A variants have a negative effect on dendritic arborization in hippocampal neurons

To investigate the effects of TMEM151A variants on its role at the neuronal developmental stages, transfection of TMEM151A WT and mutant constructs was performed in hippocampal neurons at DIV7.

To assess potential defects of neuronal maturation given by the TMEM151A variants overexpression compared to WT, following confocal image acquisition, neurite length analysis was performed to compare neurite outgrowth between WT and mutant-expressing neurons. This analysis revealed that the G56R, C125*, V149del, S297L and L300fs*118 variants produced a significant decrease in neurite length compared to TMEM151A WT (Fig. 32 A, B). The V164A variant does not show any difference compared to the WT in neurites length. Regarding the Sholl analysis, all studied TMEM151A mutants caused a strong reduction in neuritic arborization, highlighting a clear impact on neuronal development (Fig. 32 C, D).

Taken together these results suggest a role for TMEM151a in promoting and regulating neuronal development, which is strongly impaired in the presence of pathogenic variants.

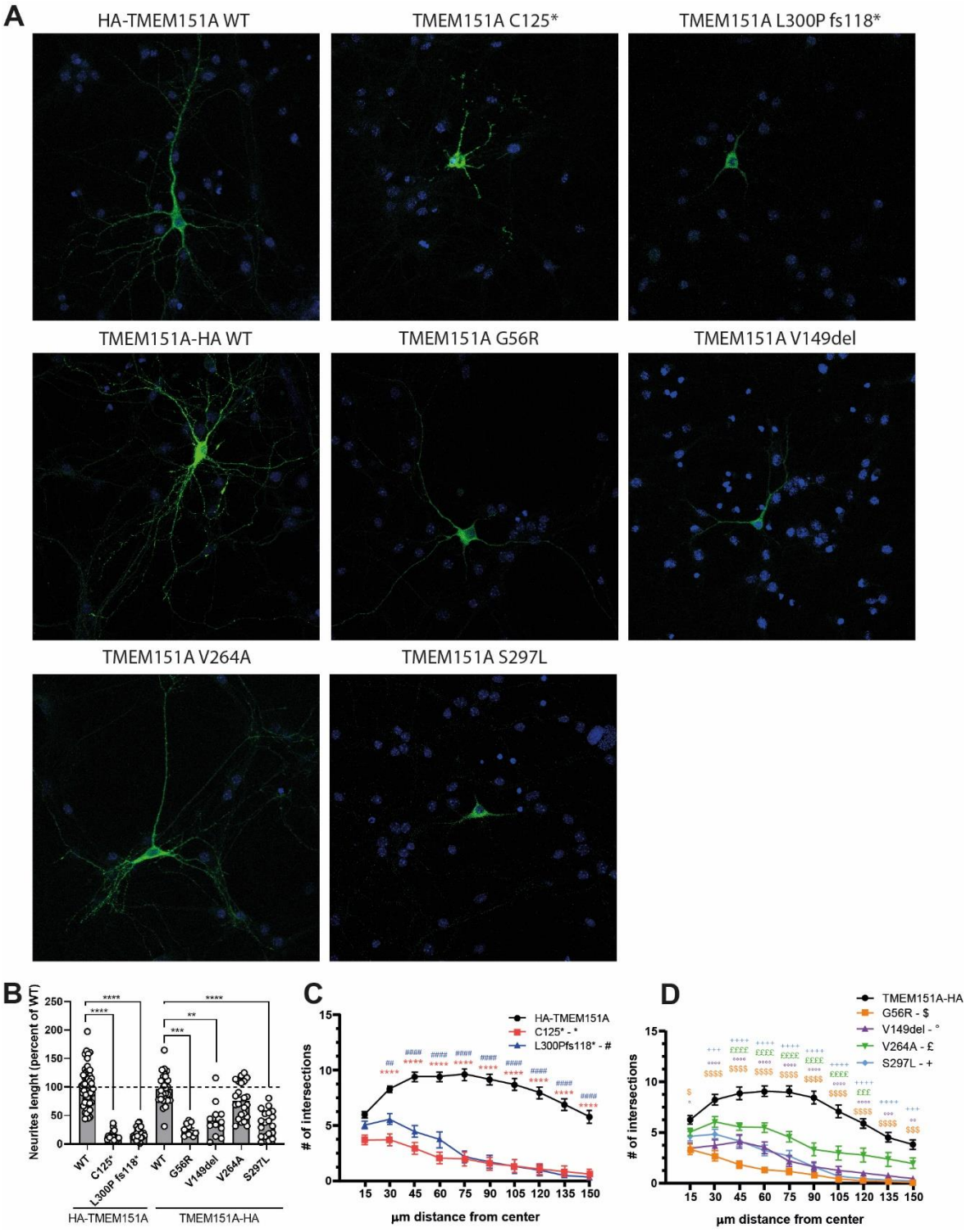

Figure 32: Effects of TMEM151A Variants on Hippocampal Neuron Development. A: Representative confocal images of hippocampal neuronal cells transfected at 7div with TMEM151A WT and mutants labelled with anti-HA antibody (green). B: Quantification of neurites length calculated for the single cells. Data are normalized on TMEM151A WT mean neurites length and are shown as means +/- SEM with superimposed individual values from n=3 independent experiments. Statistical analysis was done using One-way Anova. C-D: Sholl analysis represented as # of intersections of neurites with circles at progressive distance from the center. Significant differences are reported with different symbols for different mutants (for C125*, # for L300Pfs118*, $ for G56R, ° for V149del, £ for V264A, + for S297L). Manuscript in preparation.*

Role of TMEM151A in human neuronal development

TMEM151A associated PKD has an autosomal dominant inheritance pattern, which suggests that a single functional copy of the gene, present in the heterozygous patients, is insufficient to maintain normal neuronal function (haploinsufficiency). Since TMEM151A variants frequently lead to reduced protein expression, disease pathogenesis is best modeled as a loss-of-function. Importantly, our previous data on its variants show that TMEM151A plays a critical role in neuronal development (see Fig. 31, 32), therefore human induced pluripotent stem cells (iPSCs) provide an ideal system to study its role during neuronal differentiation and maturation. Moreover, Zhou and colleagues demonstrated that TMEM151A is mostly expressed in glutamatergic neurons [86], suggesting that a model of glutamatergic iNeurons may be useful to clarify the involvement of TMEM151A in neuronal development.

iPSCs generation and characterization

We purchased an iPSCs line that has been engineered by CrisprCas9 to KO the TMEM151A gene in heterozygous manner (that will be called #C2) and an isogenic control wild-type line (ISO #B5), as described in the materials and methods section. The CrisprCas9 editing targeted the exon 1 of ENST00000327259.5 TMEM151A-201 through the use of 2 guide RNAs that have been chosen based on the predictive activity and off-target analysis. This heterozygous approach is modelling in a more precise manner, than a complete knock-out, the patients condition.

The cells have been cultured and expanded so to have a good storage of all the clones. The iPSCs colonies have been checked for shape and growth and no differences have been noticed between the two cell lines (Fig. 33A). Furthermore, the cells have been checked for the presence of the mutation generated by gene editing, by extracting the genomic DNA and performing PCR using primers (Fg and Rg) as reported in the scheme in figure 32B. The ISO #B5 extract and the WT allele of the #C2 clone gave an amplified band of 491 bp, while the mutant allele of the #C2 clone gave a shorter amplicon of 210 bp, due to the deletion of part of the 5' UTR and of the first exon of *TMEM151A*, leading to the loss of the ATG codon as well (Fig. 33 B,C). The amplicons have been sequenced in order to verify the correctness of the sequence and the loss of the ATG codon (Fig. 33 C).

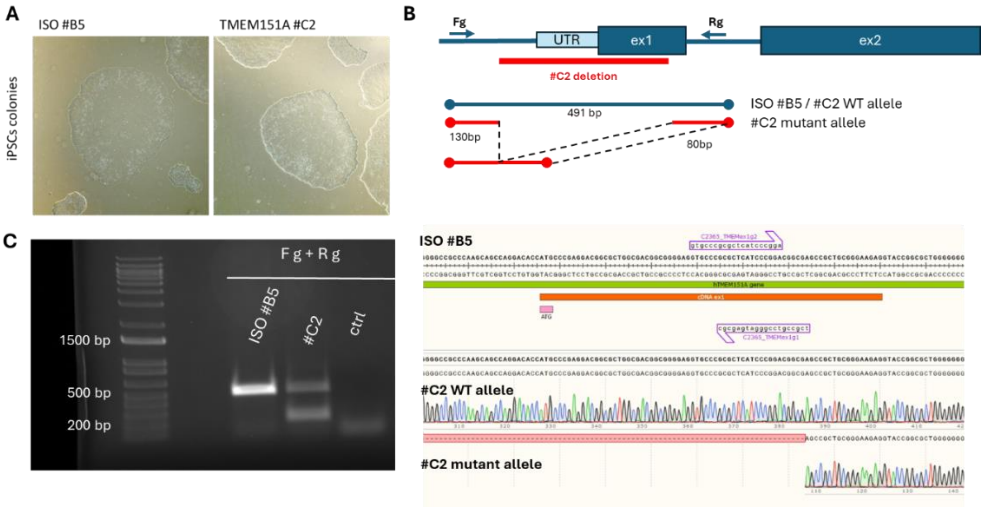

Figure 33: iPSCs cell cultures representatives and genomic DNA checks. A: Representative images of iPSCs colonies. Images have been taken at the EVOS XL-core microscope (ThermoFisher Scientific). B: Schematic representation of the genomic DNA structure and of the generated amplicons by primers Fg and Rg. C: Left: Representative agarose gel of PCR analysis on genomic DNA, resulting from the use of Fg and Rg primers. Right: Sequencing results. Screenshot of the SnapGene software showing the PCR amplicons sequenced by Sanger

Sequencing and aligned to the ISO #B5 sequence. Guide RNAs are shown in violet. cDNA sequence is shown in orange. Both PCR resulting bands for the #C2 clone have been extracted and sequenced and the results are found at the bottom right of the panel. Unpublished results.

iNeurons induction

Two main strategies are mostly used nowadays to generate neurons from iPSCs: (i) extrinsic factors to mimic the stepwise processes of neurogenesis, directing cells through different progenitor states and toward distinct cell lineages (such as Dual smad inhibition eventually followed by different morphogens), or (ii) the induced expression of lineage-specifying transcription factors to directly differentiate cells to a specific fate, often bypassing the progenitor stage.

Contrasting with extrinsic factors differentiation approaches, transcription factor programming-based protocols significantly expedite neuronal production, demonstrating reduced heterogeneity and enhanced consistency across various stem cell lines [132]. Among these, the most used is Neurogenin 2 (NGN2), a bHLH transcription factor that has received particular attention for its application for the in vitro differentiation of fibroblasts and iPSCs into glutamatergic neurons and, less frequently, in a range of other neuronal subtypes such as dopaminergic, serotonergic, motor, sensory neurons and astrocytes. However, based on current literature, the standardization of post-reprogramming processes, especially in neuronal differentiation, remains deficient. Indeed, there are numerous shortcomings within the protocols developed to date. One of the main concerns of the current protocols is the extreme variability of the number of copies of NGN2 expressed by the starting iPSC, due to the random infection procedure and leading to differentiated neurons at different levels of maturation.

Therefore, I used a standardized and optimized protocol, developed in my lab, for generating iPSC-derived glutamatergic neurons (iGluNeurons) through the inducible overexpression of NGN2 [133]. Key improvements include:

- selecting a population with homogeneous integration of NGN2 cassettes to reduce heterogeneity caused by variable NGN2 expression levels,
- incorporating an intermediate step during neuronal differentiation to store neuronal progenitors, thereby facilitating their use across multiple experiments and reducing variability.

We used a vector in which NGN2 is linked to GFP through a T2A sequence and chose to isolate a subpopulation of iPSCs exhibiting both median and homogeneous expression of GFP (and thereby of NGN2) by Flow-activated cell sorting (FACS) sorting (Fig. 34, upper panel). Our methodology involved lentiviral transduction of iPSCs using the “all-in-one” vector to express rtTA and the NGN2/GFP transcript under the control of the Tetracycline response element promoter (TREtight promoter). Following infection, iPSCs underwent puromycin selection for 4 days, allowing subsequent expansion to perform FACS sorting. The transduced and resistance-selected iPSCs do not exhibit any fluorescence, demonstrating well-controlled expression by TREtight promoter without any leakage. Upon induction with tetracycline, a significant proportion of cells ranging from 30% to 80% appear negative for GFP, while the positive ones exhibit a strong heterogeneity in GFP expression. After a 12-hour induction with doxycycline, we isolated the subpopulation exhibiting a consistent median level of GFP-NGN2 expression by FACS sorting [45].

These cells were then plated in Stemflex media, without doxycycline, on Petri dishes to expand iPSC pools. The sorted iPSCs that have integrated the 'all-in-one' cassettes into their genome

(iPSC-NGN2) took approximately 7 to 10 days to form colonies of medium size and then were subsequently split using Versene. This crucial step allowed us to store a substantial number of cells at the same passage with comparable integration of the 'all-in-one Tet-on' cassette, increasing the intra- and inter-experimental homogeneity.

To differentiate iGluNeurons, we employed a two-step protocol schematized in Fig. 34, bottom panel [133]. The initial phase, termed the "pre differentiation step" (pre-diff step), spans 3 days and involves the induction of NGN2 with doxycycline in a medium supplemented with neurotrophic factors (induction media). As iPSCs grow in colonies, an initial single-cell dissociation step is crucial prior to doxycycline treatment to ensure an optimal environment for subsequent neuronal differentiation. iPSCs were plated in Induction Media, DMEM/F12, a nutrient-rich medium widely acknowledged for iPSC cultures, was chosen to provide an ideal milieu for this phase.

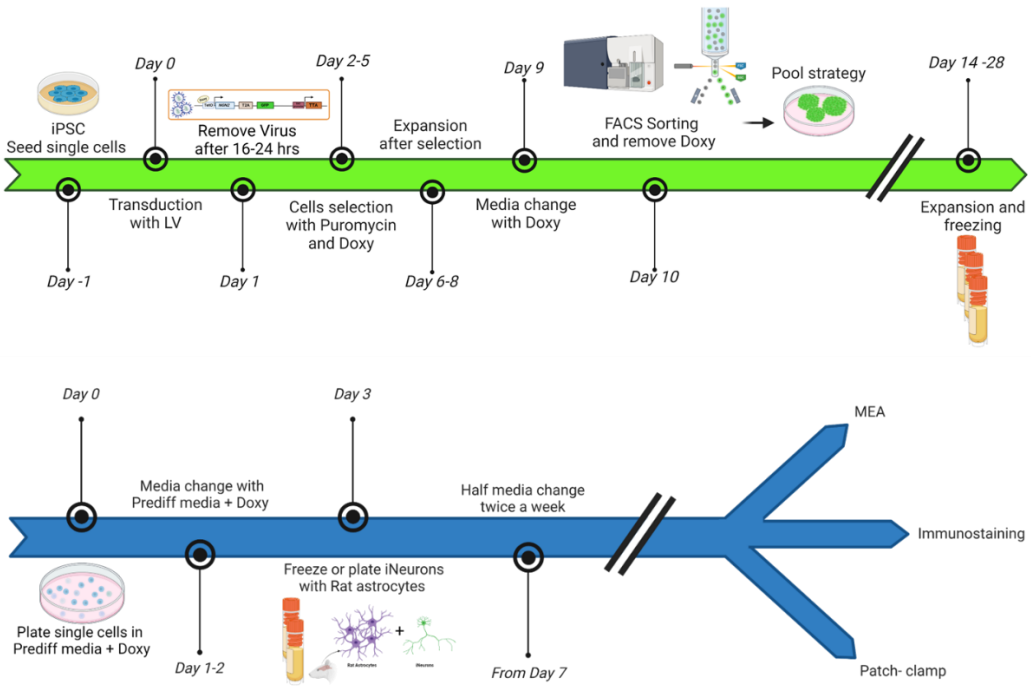

Figure 34: Upper panel: Schematic representation of protocol of iPSCs induction to pre-diffentiated glutamatergic iNeurons through the infection with a lentivirus bringing the all-in-one NGN2 inducible construct. Bottom panel: Schematic representation of pre-differentiated cells induction in iNeurons, with the subsequent applications. Adapted from Servetti et al. 2025 [133].

Over a 3-day in vitro (DIV), a progressive morphological transformation towards the neuroprogenitor fate (characterized by neurites elongation and arborization) is observed. By DIV 3, cells uniformly exhibit the typical neuron-like morphology and differentiated into NPC (neuro-progenitor cells). At this stage, NPC cells could be cryopreserved as large batches. Overall, this scalable protocol for the generation of cryopreserved batches of NPCs provides a high level of standardization for subsequent analysis. Subsequently, NGN2-NPCs were thawed and plated together with rat astrocytes (Fig. 34). Without astrocyte support, NPCs can survive only up to DIV12-14, an insufficient time for achieving adequate neuronal maturation. Cells were plated at a density of 100 cells/mm^2 for immunofluorescence experiments and at a density of 1,200 cells/mm^2, comprising 800 neurons and 400 rat astrocytes for MEA recordings [134]. The maturation status was evaluated by immunocytochemistry for several neuronal markers. Starting from 4-5 weeks of differentiation, iGluNeurons exhibited markers

typical of mature neurons such as neuronal specific markers (neuronal nuclear protein - NeuN), markers of synaptic specialization (synapsins I/II – Syn1/2) and dendritic processes (MAP2) (Fig. 35 C).

TMEM151A KO heterozygous iNeurons show impaired development and maturation

To assess the developmental regulation of TMEM151A expression, RT–qPCR analysis was performed in wild-type (ISO #B5) and TMEM151A heterozygous (#C2) iPSCs and iPSC-derived neurons at multiple stages of differentiation. In wild-type neurons, TMEM151A expression increased progressively during neuronal maturation, with a significant upregulation observed at 35 and 42 DIV compared to earlier time points (Figure 35A). In contrast, heterozygous neurons exhibited significantly reduced TMEM151A mRNA levels at all analyzed stages. While a modest difference between genotypes was detected at early differentiation stages, heterozygous neurons failed to show the marked developmental upregulation of TMEM151A observed in wild-type cultures at later time points, resulting in highly significant differences at 35 and 42 DIV.

To evaluate whether reduced TMEM151A expression was associated with altered neuronal maturation, the expression of the neuronal marker MAP2 was analyzed in parallel (Figure 35 B). TMEM151A heterozygous neurons displayed a progressive reduction in MAP2 expression when compared to the WT neurons, which became significant from 28 DIV onward and was further exacerbated at later stages. These data indicate that heterozygous neurons exhibit impaired neuronal maturation and/or dendritic development concomitant with reduced TMEM151A expression.

To better clarify the role of TMEM151A in the neuronal development, we performed immunofluorescence analyses at different developmental stages of the iNeurons cultures. iNeurons were analyzed for their neurites length and arborization as it was performed for mouse primary cultures before. The progressive maturation of neuronal networks across long-term differentiation in vitro was analyzed from 7 to 56 days in vitro. ISO neurons show a time-dependent increase in neurite outgrowth and network complexity, culminating in a dense and highly interconnected neuronal network at late stages (35–56 DIV) (Fig. 36A). In contrast, neurons carrying a heterozygous deletion of *TMEM151A* (#C2) exhibit visibly reduced neuritic arborization and a less organized network architecture, particularly evident from 21 DIV onward (Fig. 36A). Quantitative analysis of neurites length reveals no significant differences between ISO and #C2 cultures at early developmental stages (7–14 DIV), whereas a significant decrease in total intersections is observed in #C2 neurons at intermediate and late time points (21–56 DIV), indicating impaired structural maturation (Fig. 36B). Consistently, Sholl analysis demonstrates that ISO neurons develop progressively higher branching complexity at proximal and intermediate distances from the soma, while *TMEM151A* heterozygous neurons show a marked reduction in the number of intersections across multiple radii starting at 21 DIV (Fig. 36C). Together, these data indicate that partial loss of TMEM151A compromises neuronal morphogenesis and network maturation during later stages of in vitro development.

Immunofluorescence analysis revealed that ISO #B5 and ##C2 cultures are positive to both neuronal and synaptic markers (namely MAP2, NeuN and Syn1/2) (Fig. 35 C). As it is visible from the representatives, possible differences may be identified in the Syn1/2 staining, coherently with the previously described evidences regarding the lower network complexity. Further analyses will be performed to clarify if this heterozygous culture shows a lower synaptic density.

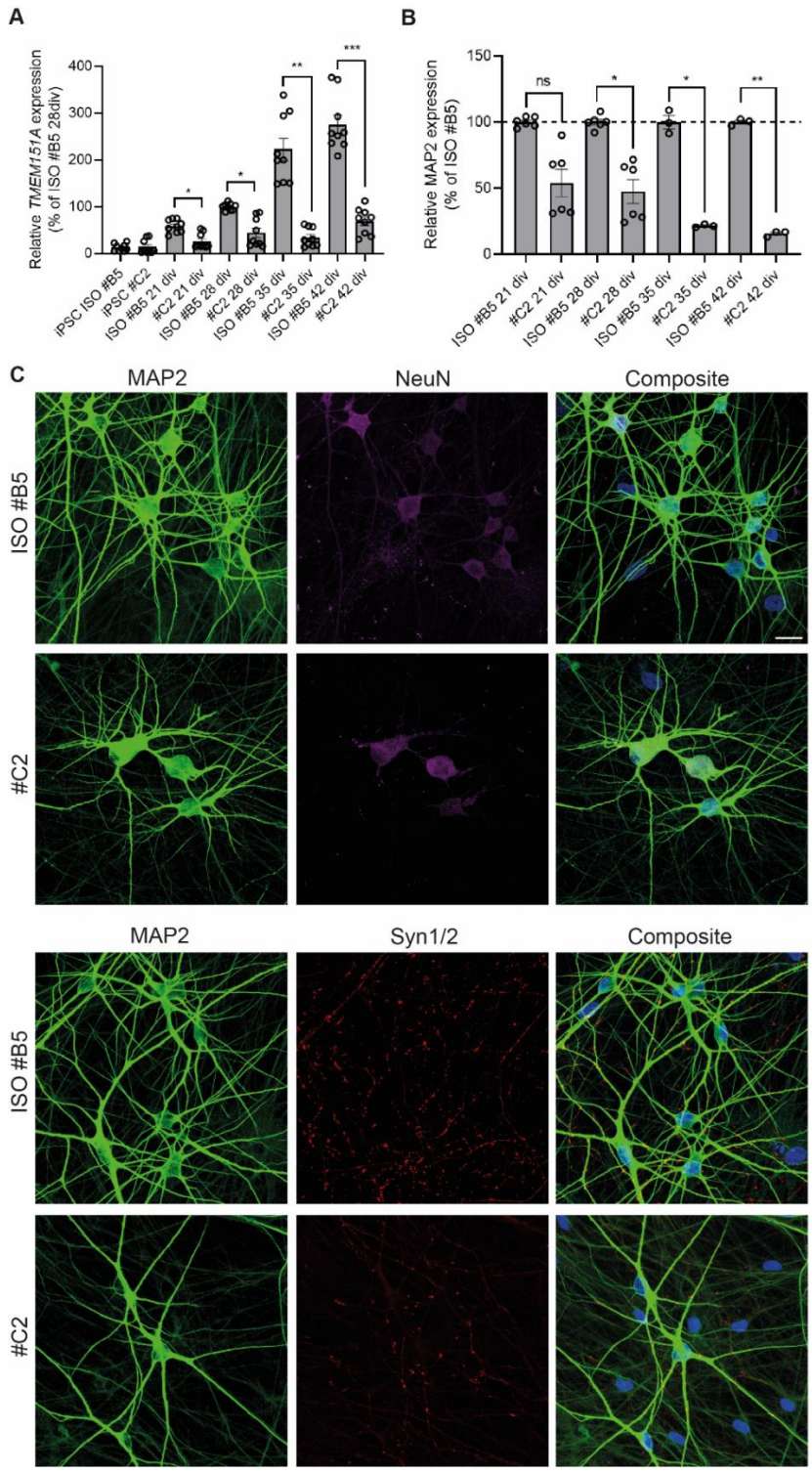

Figure 35: TMEM151A iNeurons characterization. A: Developmental regulation of TMEM151A expression in wild-type and TMEM151A heterozygous iPSC-derived neurons. RT–qPCR analysis of TMEM151A expression in wild-type (ISO #B5) and TMEM151A heterozygous (#C2) iPSCs and derived neurons at 21, 28, 35, and 42 days in vitro (DIV). Expression levels were normalized to housekeeping gene and afterwards to ISO #B5 28 DIV and are shown as percentage values. B: RT–qPCR analysis of the neuronal marker MAP2 in the same conditions and time points. Expression levels were normalized to housekeeping gene and afterwards to ISO #B5 internally to each time point and are shown as percentage values (dashed line 100%). Data are presented as mean ± SEM with individual data points overlaid. Statistical significance is indicated as ns (not significant), $p < 0.05$, $p < 0.01$, $p < 0.001$. B: C: Representative confocal images of iNeurons at 42 div of maturation labelled with anti-MAP2 (green), anti-NeuN (Magenta). B: Representative confocal images of iNeurons at 42 div of maturation labelled with anti-MAP2 (green), anti-Syn1/2 (red). Dapi staining for nuclei (blue). Images have been taken at the Leica SP8 confocal microscope (40X magnification). Scale bar 20 um. Unpublished results.

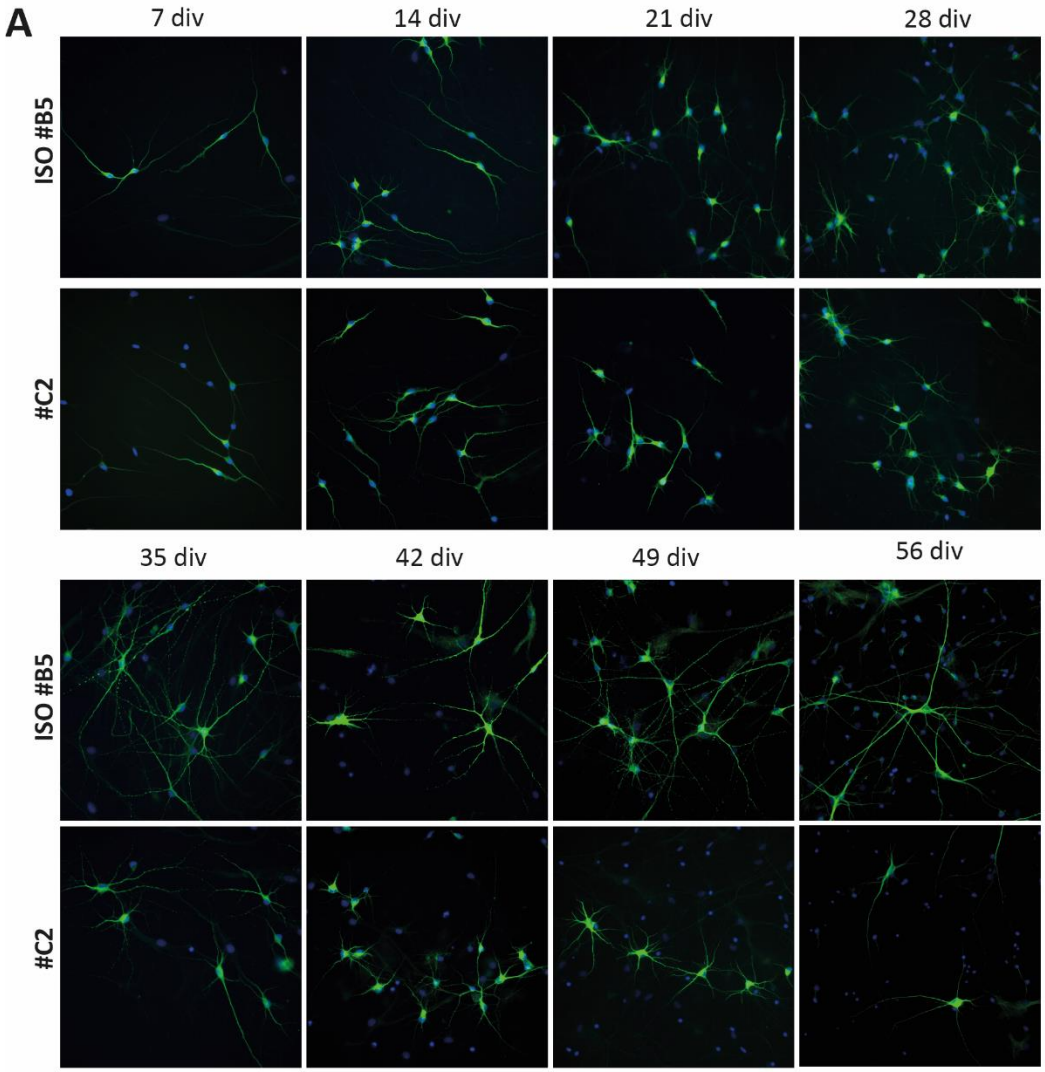
A
7 div
14 div
21 div
28 div
ISO #B5
#C2
35 div
42 div
49 div
56 div
ISO #B5
#C2

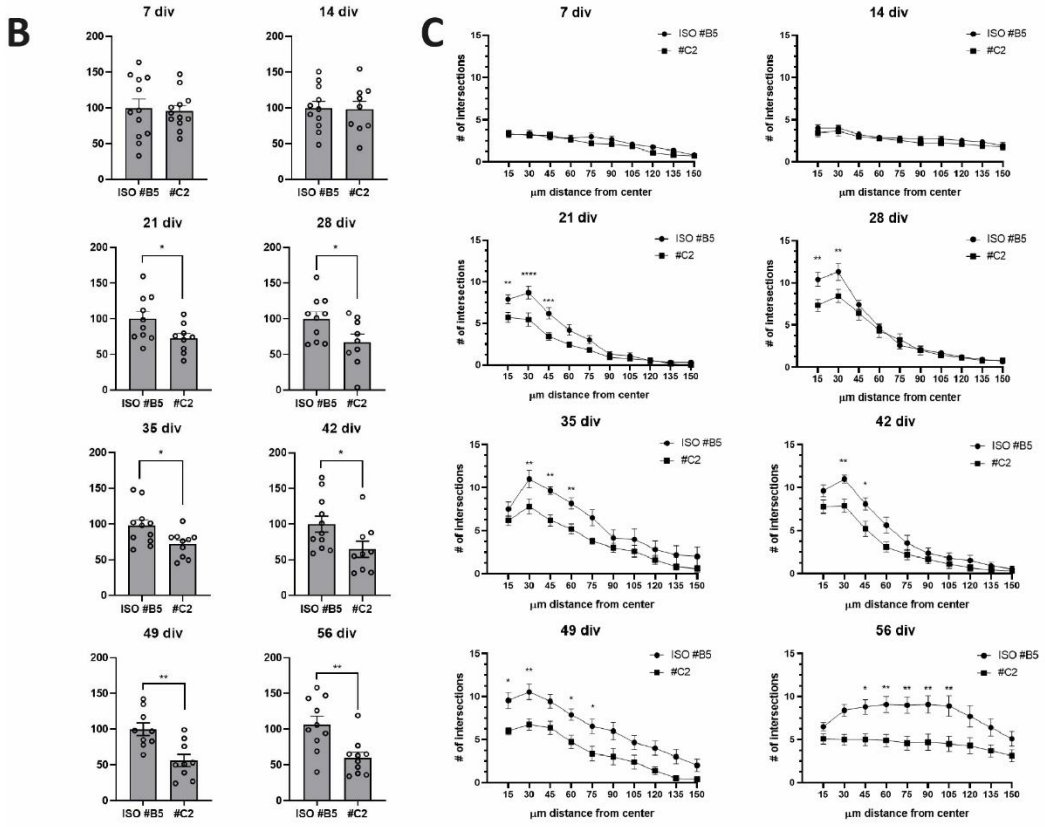
B
7 div
14 div
21 div
28 div
35 div
42 div
49 div
56 div
ISO #B5
#C2
C
7 div
14 div
21 div
28 div
35 div
42 div
49 div
56 div
ISO #B5
#C2
# of intersections
µm distance from center

Figure 36: iNeurons maturation. A: Representative epifluorescence images of iNeurons maturation at different time points, labelled with anti-MAP2 (green). Nuclei are depicted in blue. B: Quantification of neurites length calculated for the single cells. Data are normalized on ISO #B5 mean neurites length and are shown as means +/- SEM with superimposed individual values. C: Sholl analysis showing the number of intersections between neuron's processes and concentric circles radiating from the soma at 15 µm intervals. Statistical analysis was done using One-way Anova. Unpublished results.

TMEM151A KO heterozygous iNeurons show impaired network activity

To study the activity of iNeurons networks, we plated them on Micro-electrode array (MEA) devices (Supplementary to Figure 37). MEA recordings were performed every 7 days from 7 to 56 days in vitro.

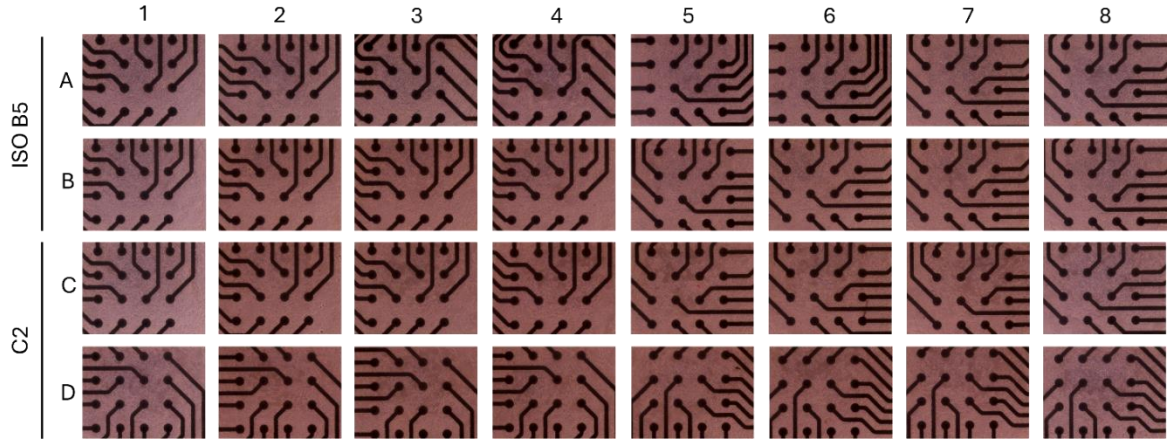

Supplementary to Figure 37: MEA Axion 48 wells (16 electrodes) cultures representative. Unpublished results.

Neuronal network activity increased progressively over time in both ISO #B5 and #C2 cultures, consistent with ongoing maturation across days in vitro. However, despite this overall increase, #C2 cultures followed a clearly altered developmental trajectory compared to controls, indicative of delayed and impaired network maturation. Multiple electrophysiological parameters converge to describe this phenotype from complementary perspectives.

In control ISO #B5 networks, maturation was characterized by a rapid recruitment of active electrodes, which reached a plateau at mid-developmental stages. In contrast, #C2 cultures exhibited a delayed and incomplete recruitment of active sites, resulting in a persistently smaller pool of active neurons throughout development (Fig. 37 A). This reduced recruitment was paralleled by a lower weighted mean firing rate, which, although gradually increasing over time, remained significantly reduced in #C2 cultures compared to ISO #B5 networks at later stages (Fig. 37 B). Together, these findings indicate that TMEM151A-deficient networks mature with both fewer active neurons and diminished overall firing output.

Beyond changes in activity levels, the temporal organization of spiking was profoundly altered in #C2 cultures. While bursting activity emerged in both conditions, ISO #B5 networks displayed an earlier increase and rapid stabilization of burst dynamics. In contrast, #C2 cultures showed a delayed onset of bursting during early and intermediate stages of development (Fig. 37 C). Strikingly, at later time points, burst frequency in #C2 cultures continued to rise and exceeded that of control networks, despite the reduced number of active electrodes and lower firing rates. This shift was accompanied by significantly shorter burst durations, indicating that in the absence of TMEM151A, bursts become more frequent but less sustained (Fig. 37 C, D).

Consistent with this altered bursting profile, #C2 cultures retained a higher proportion of random, non-bursting spikes throughout maturation, whereas ISO #B5 networks rapidly transitioned toward more structured firing patterns (Fig. 37 E). The progressive recruitment of neurons into coordinated bursting activity was also delayed in #C2 cultures, as reflected by the slower increase in the proportion of bursting electrodes. Although this parameter eventually approached control levels, it did so at later stages and in the context of persistently altered burst structure (Fig. 37 F).

At the network level, large-scale synchronization was similarly delayed and dysregulated. Network bursts emerged earlier and more robustly in ISO #B5 cultures, whereas #C2 networks exhibited a delayed onset of global synchronization (Fig. 37 G). As observed for single-burst activity, network burst frequency in #C2 cultures surpassed control levels at later stages of maturation. However, this increase in frequency was not accompanied by stable network dynamics, as network burst duration remained shorter during intermediate stages and only partially converged with controls at the latest time points (Fig. 37 H).

Overall, these data indicate that loss of TMEM151A profoundly alters the developmental trajectory of neuronal network activity. TMEM151A-deficient networks are characterized by delayed neuronal recruitment, reduced firing output, persistent disorganization of spiking, and a late-emerging shift toward more frequent but shorter and potentially unstable burst and network burst events. This pattern is consistent with a neurodevelopmental network phenotype and suggests that TMEM151A is required not only for timely network maturation, but also for the stabilization and proper regulation of synchronous activity as neuronal circuits develop.

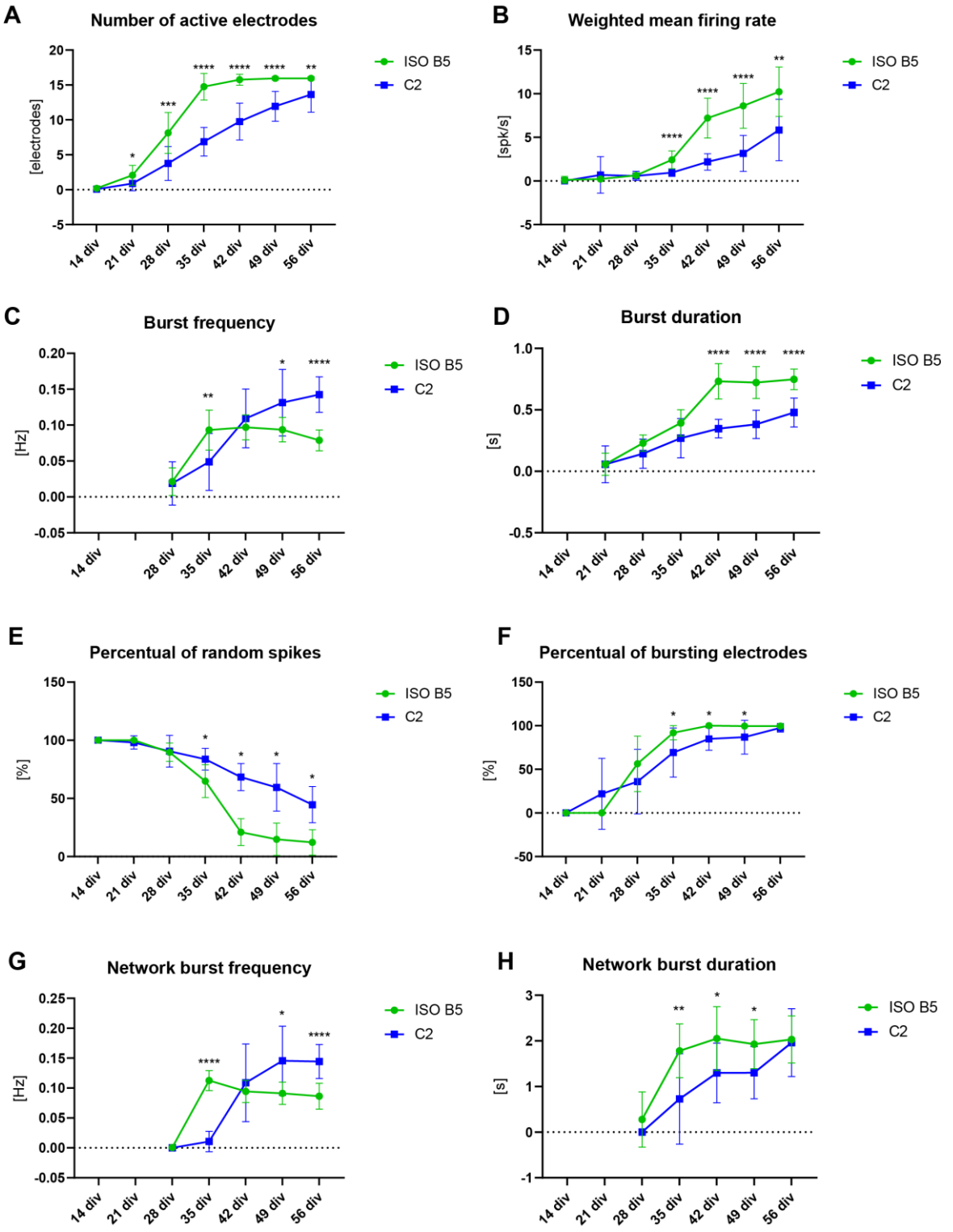

Figure 37: Spontaneous electrophysiological activity of the iNeurons network. iGluNeurons were plated on MEA chips. A-H: Scatter plots of Number of active electrodes, weighted Mean Firing Rate, percentage of Active Electrodes, burst frequency, burst duration, percentual of random spikes, percentual of bursting electrodes, networks burst frequency and network burst duration. Data are shown as means ± SEM. n = 16. Unpublished results.

TMEM151A interactomics

To investigate the interactome of TMEM151A, we adopted two complementary strategies: a targeted approach aimed at assessing its direct interaction with NaV channels, motivated by the phenotypic and therapeutic similarities with PRRT2-related disorders, and an unbiased proteomic approach to systematically identify additional interacting partners. Together, these

approaches enable the identification of the molecular pathways in which TMEM151A is involved, thereby providing insight into its role in neuronal development and into the pathogenic mechanisms underlying TMEM151A-related neurological disorders when the gene is mutated.

TMEM151A regulates NaV1.1 kinetics

Previous evidences show how PRRT2 negatively regulates the activity of NaV1.2 channels [47], [74]. Both PRRT2 and TMEM151A PKD patients are responsive to Carbamazepine treatment, a sodium channel blocker. Therefore, we decided to test if TMEM151A, as PRRT2, has a regulatory effect on one or more voltage-gated Na^+ channels.

HEK293 cells were co-transfected with constructs encoding NaV1.2 (SCN2A) or NaV1.6 (SCN8A) together with either pKH3-TMEM151A-HA or the empty pKH3 control. We recorded whole-cell transient Na+ currents through patch-clamp experiments and compared the current amplitude and kinetics between cells transfected with NaV channels and the empty vector and those co-transfected with TMEM151A WT (Fig. 38A). Current–voltage (I–V) relationships (Fig. 38 B, F) revealed comparable current densities across the full range of tested membrane potentials between control conditions and TMEM151A-coexpressing cells for both channel isoforms. Consistently, the voltage dependence of activation (Fig. 38 C, G) and steady-state inactivation (Fig. 38 D, H) was not significantly shifted by TMEM151A co-expression, as indicated by overlapping normalized conductance curves and similar half-activation and half-inactivation voltages.

Overall, electrophysiological recordings revealed no significant differences in current density or in the activation and inactivation kinetics of evoked currents in the presence or absence of TMEM151A, indicating that TMEM151A does not exert a detectable regulatory effect on these sodium channels under these experimental conditions.

In contrast, co-transfection of pKH3-TMEM151A-HA with the sodium channel NaV1.1 resulted in a significant alteration of channel gating properties. Representative whole-cell Na^+ currents recorded from HEK293 cells expressing NaV1.1 together with the empty control vector or TMEM151A are shown (Fig. 39 A). While the peak current amplitude appeared largely comparable between conditions, co-expression of TMEM151A was associated with a visibly faster decay of the evoked currents, suggesting accelerated inactivation.

Consistently, analysis of the current–voltage (I–V) relationship (Fig. 39 B) revealed no significant differences in current density across the tested voltage range between control and co-expressing TMEM151A NaV1.1 transfected cells, indicating that TMEM151A does not substantially affect channel expression levels or macroscopic current amplitude.

Superimposition of normalized current traces (Fig. 39 C) further highlighted the pronounced acceleration of inactivation kinetics in the presence of TMEM151A, with currents decaying more rapidly following peak activation. Quantitative analysis confirmed this observation, as the inactivation time constant (τ) was significantly reduced across multiple test potentials when TMEM151A was co-expressed (Fig. 39 D).

Together, these results demonstrate that TMEM151A selectively modulates the functional properties of NaV1.1 by accelerating channel inactivation, thereby reducing channel open time without affecting current density. This functional effect phenocopies a LOF behavior of NaV1.1, supporting a role for TMEM151A as a negative modulator of NaV1.1 channel activity under these experimental conditions (Fig. 39).

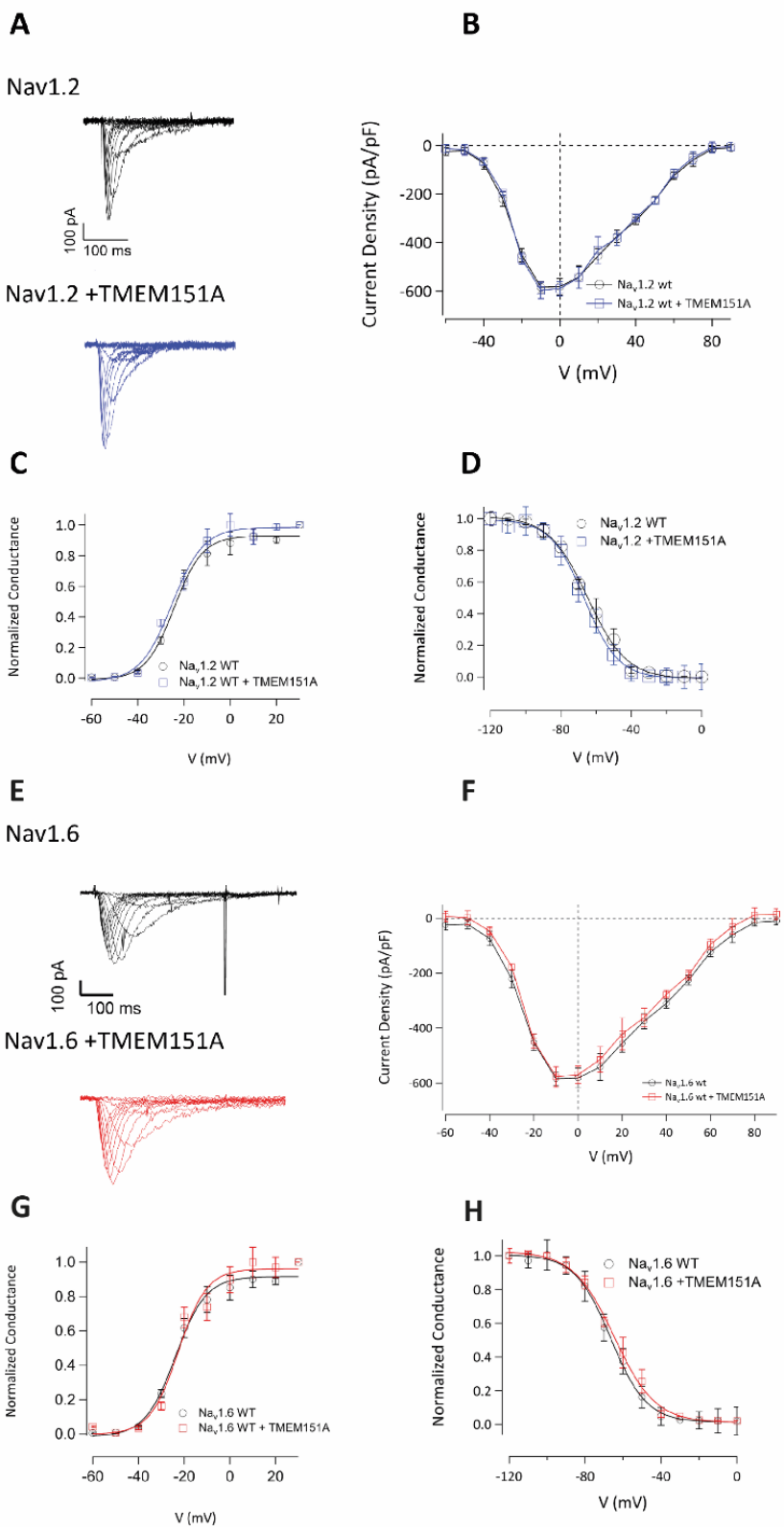

Figure 38: The co-expression of TMEM151A with NaV1.2 and NaV1.6 channels does not alter the biophysical properties of either channel. A-E: Whole-cell sodium representative current traces recorded from cells transiently expressing WT NaV channel alone (top panel, black trace), or with TMEM151A (middle panel, colored trace) cDNA constructs. Currents were elicited from a holding potential of –90 mV with 20 ms depolarizing voltage steps between –60 and +90 mV. B-F: Average current density–voltage relationships. C-G: Superimposed voltage-dependence curves of steady-state activation. D-H: Superimposed voltage-dependence curves of steady-state inactivation for HEK293 cells transfected with wt Nav channel alone (black symbols and lines) or with TMEM151A (colored symbols and lines) as indicated. Data are expressed as mean ± SEM from n ≥ 20 independent experiments. Manuscript in preparation.

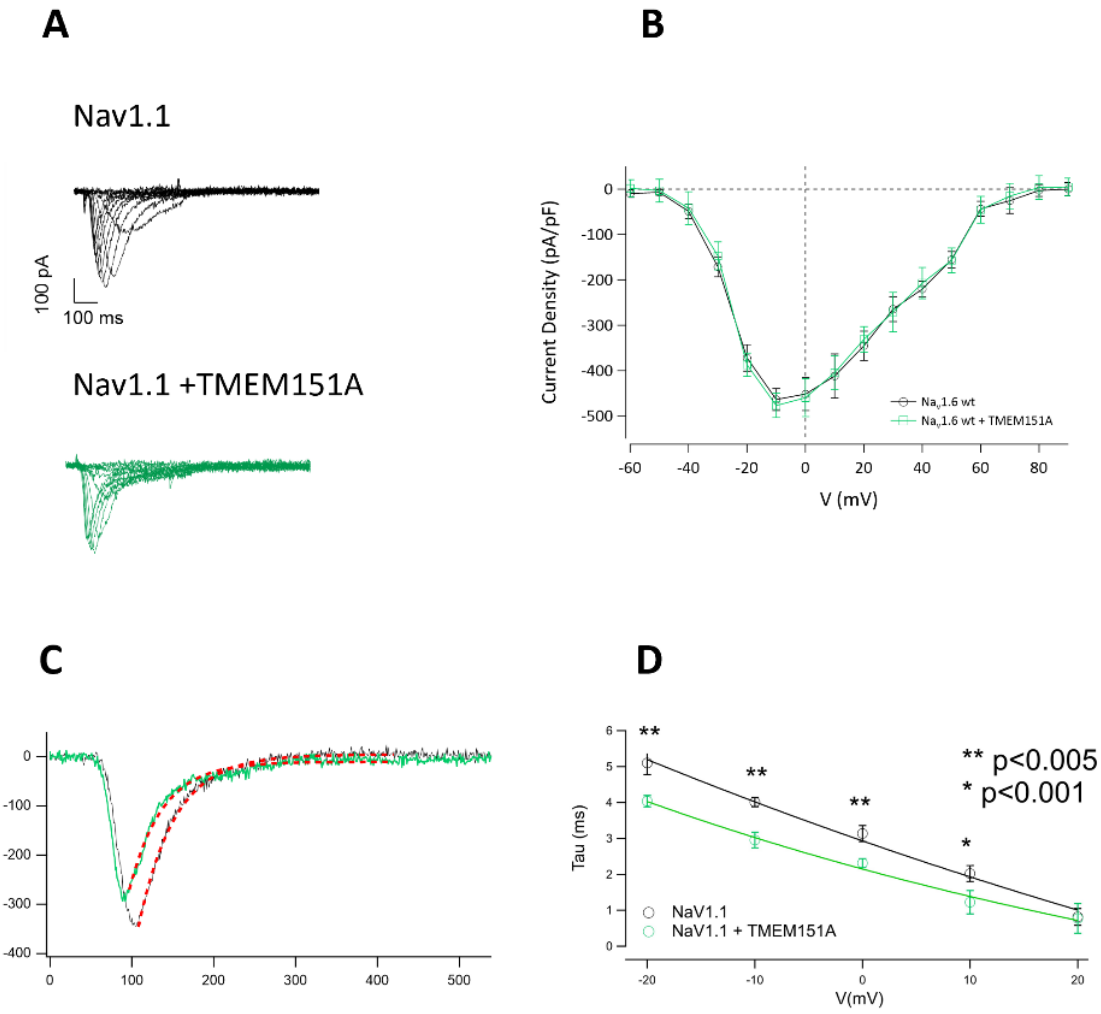

Figure 39: The co-expression of TMEM151A with NaV1.1 channel alters the biophysical properties of the channel. A: Whole-cell sodium representative current traces recorded from cells transiently expressing NaV1.1 channel alone (top panel, black trace), or with TMEM151A (middle panel, green trace) cDNA constructs. Currents were elicited from a holding potential of –90 mV with 20 ms depolarizing voltage steps between –60 and +90 mV. B: Average current density–voltage relationships. C: Example of fitting with a single exponential function to obtain the inactivation time constant in response to the applied potential. Inactivation kinetics were assessed by measuring the decay of the current from the peak to 40 ms from the stimulus onset with a single exponential fit. D: Voltage dependence of time constants for the onset of fast inactivation at the indicated membrane potentials in HEK293 cells transfected with NaV1.1 channel alone (top panel, black trace), or with TMEM151A (middle panel, green trace) as indicated. Data are expressed as mean ± SEM from n ≥ 20 independent experiments. Manuscript in preparation.

TMEM151A variants lose the regulatory effect on NaV1.1 kinetics

To confirm the specificity of the TMEM151A effect on NaV1.1, and to understand if the regulatory effect of TMEM151A on NaV1.1 may be implicated in the pathogenic mechanism associated to the TMEM151A disease variants, electrophysiological studies have been conducted by combining some of the variants in study with NaV1.1.

We selected two TMEM151A variants that result in truncated proteins, presumably leading to a LOF mechanism, to assess their effect on NaV1.1 channel inactivation. In transiently transfected HEK293 cells, co-expression of the mutated TMEM151A with NaV1.1 did not alter the Na^+ current amplitude generated by the channel. In contrast to the WT TMEM151A, both truncating variants failed to accelerate NaV1.1 inactivation. Instead, the inactivation kinetics were significantly slower and closely resembled those observed in cells co-expressing NaV1.1 with the empty control vector. Quantitative analysis of the inactivation time constant (τ) across

multiple test potentials confirmed a loss of the modulatory effect exerted by WT TMEM151A on channel inactivation (Fig. 40).

Together, these data indicate that the truncating TMEM151A variants behave as LOF alleles with respect to NaV1.1 regulation: while they do not affect channel current density, they abolish the ability of TMEM151A to promote rapid channel inactivation. The resulting prolongation of NaV1.1 open time is expected to dysregulate sodium channel activity in inhibitory neurons, providing a potential mechanistic link between TMEM151A pathogenic variants and neuronal hyperexcitability.

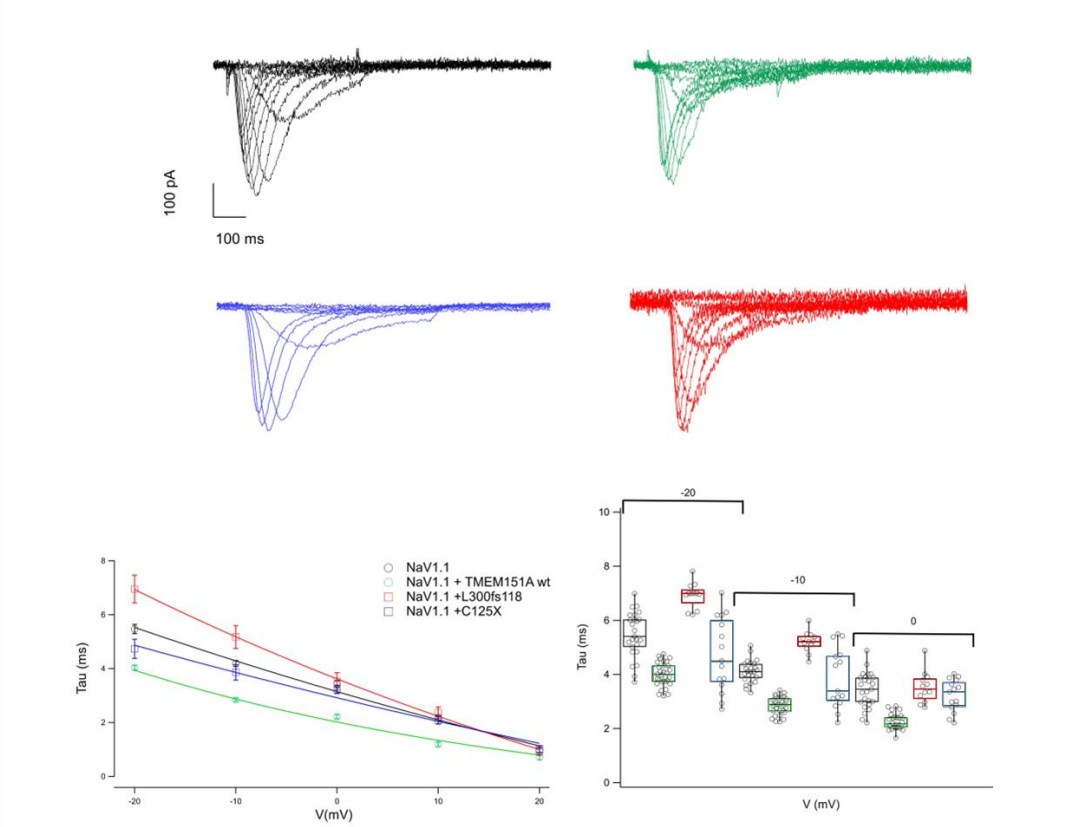

Figure 40: The co-expression of mutated TMEM151A with WT NaV1.1 channel restores the inactivation kinetics of the channel. Upper panel: Whole-cell sodium representative current traces recorded from cells (top panel) transiently expressing WT NaV1.1 channel alone (black trace), or with WT and mutated TMEM151A (WT green traces, mutant C125 blue traces and L300Pfs*118 red traces) cDNA constructs. Currents were elicited from a holding potential of –90 mV with 20 ms depolarizing voltage steps between –60 and +90 mV. Lower panel: Voltage dependence of time constants for the onset of fast inactivation at the indicated membrane potentials in HEK293 cells transfected with WT NaV1.1 channel alone (black trace), or with WT and mutated TMEM151A (WT green traces, mutant C125* blue traces and L300Pfs*118 red traces) as indicated.* Manuscript in preparation.

TMEM151A proteomics investigation reveal potential interactors

We performed pull-down experiments as described in the materials and methods section to identify the potential interactors of TMEM151A in the mouse brain, as reported in the scheme below (Fig. 41 A).

The experiment was performed with three different bates in order to identify specific TMEM151A interactors: HA-Tmem151a, Tmem151a-HA and BAP-HA (bacterial alkaline phosphatase). The three constructs were overexpressed in the heterologous system of the HEK293 cells. After bates isolation via immunoprecipitation, they have been incubated with mouse whole brain lysate to allow the establishment of bate-interactors bonds. The resulting

material was then analyzed by mass-spectrometry, as described in the material and methods section. From the mass-spectrometry data, different parameters can be evaluated to determine the most promising interactors of TMEM151A. The data analysis followed the following pipeline:

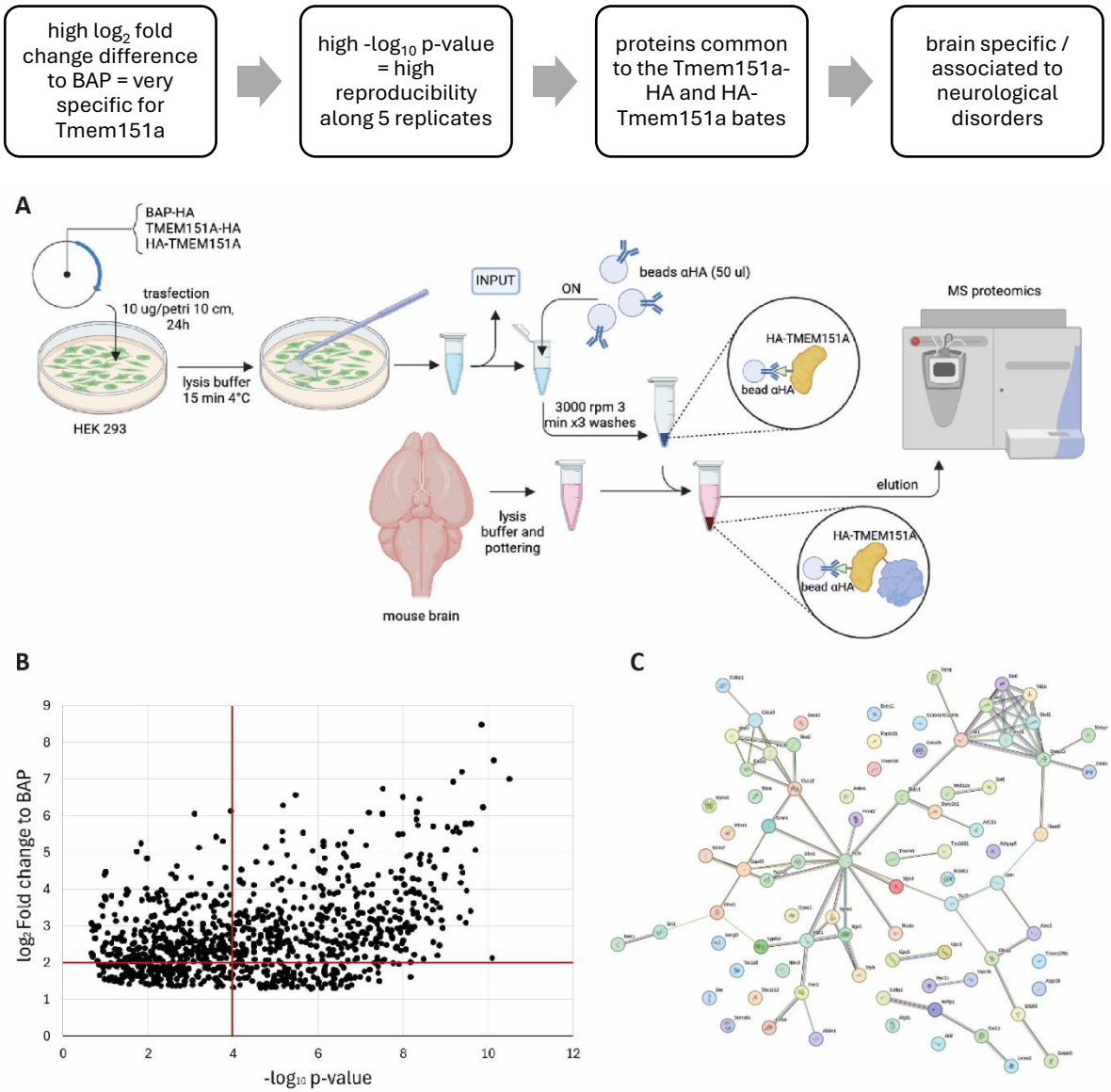

Figure 41: TMEM151A interactomics study. A: Schematic representation of the TMEM151A proteomics experimental setting. B: Volcano plot graph showing the TMEM151A interactors. On the y axis the log_2 fold change difference to BAP-HA is shown. On the x axis, the $-log_{10}$ p-value significance is shown, obtained from 5 replicates. C: String graph showing the TMEM151A interactors with log2 fold change to BAP higher than 4 and -log10 p-value higher than 1,5. Unpublished results.

A total of 5,833 proteins were identified across all samples. For statistical analyses, we considered the 4,440 proteins that were present at 100% completeness in at least one of the three experimental groups. Of these, 2,792 proteins (63%) were classified as Homo sapiens.

In order to further filter proteins annotated as Homo sapiens, proteins identified in the HEK empty-vector control samples from a preliminary pilot experiment were subtracted from each group. Data were plotted according to the log_2 fold change to BAP, in order to discriminate the most specific ones and according to the $-log_{10}$ p-value derived from five independent replicates of the experiment.

Subsequently, only proteins showing a fold change greater than 2 were retained. This filtering strategy reduced the dataset to 1,758 proteins, of which 690 (39%) were still classified as Homo sapiens. Further comparisons were done to retain only the proteins with $-\log_{10}$ p-value greater than 4, defining higher reproducibility along the 5 replicates for each bate (Fig. 41B). Among these proteins further considerations can be done about the concomitance of proteins in the two Tmem151a bates experimental conditions and about the involvement of these proteins in neurological diseases or known neuronal pathways.

Protein–protein interaction analysis was performed on the resulting proteins using the STRING database to investigate the molecular context of TMEM151A (Fig. 41C). The resulting network reveals a highly interconnected architecture, characterized by the presence of distinct functional clusters. The most prominent module is centered on ACTB (β-actin) and includes multiple actin-binding and cytoskeleton-associated proteins such as MYH4, MYO1B, DBN1, TAGLN3, STMN1/2, and RAC2, indicating a strong association of TMEM151A with cytoskeletal organization and actin dynamics.

A second major cluster comprises components of the vesicle trafficking and membrane fusion machinery, including SNAP23, multiple syntaxins (STX1A, STX1B, STX6, STX8), VTI1B, and GOSR1, suggesting a potential role for TMEM151A in intracellular transport and membrane remodeling processes. Additional clusters are enriched in proteins involved in cell cycle regulation and mitotic spindle organization (e.g., SKA1–3, PRC1, ESCO2, CCNB2), as well as motor proteins and microtubule-based transport factors such as DYNC2H1 and DNM1.

Notably, the presence of integrins (ITGA1, ITGA11, ITGB1) and galectins (LGALS8) links TMEM151A to pathways regulating cell adhesion interactions.

Discussion – Aim 3: TMEM151A

TMEM151A membrane topology

As a first step to understand its biological function, we identified the topology of TMEM151A by a combination of computational and experimental approaches. Structural modeling and refinement by MD identified well-separated transmembrane and extramembrane domains. TMD (transmembrane domain) encompasses two major helices (H1 and H2) that span the whole membrane and are connected by a short loop and two shorter helices (H5 and H6), closer to the C terminus, forming a helix-turn-helix motif. A large extramembrane domain encompasses β-strands (S1-S6) and α-helices (H3 and H4). A remarkable feature of this domain (EM2) is the extended hairpin formed by the S1-S2 strands, whose tip is most of the time interacting with the membrane leaflet. MD simulations showed stability of the whole TMD, whereas the EM2 domain displayed higher fluctuations due to occasional loss of the interaction with the membrane.

The orientation of TMEM151A extramembrane domains has been defined by two different wet experimental approaches such as live-IF and electron microscopy. The HA epitope in the loop among the H1 and H2 helices (TMEM151A-HA-LOOP) is facing outwards from the plasma membrane validating the predicted topology. In addition, electron microscopy images confirm its localization on the extracellular side of the plasma membrane as well as in the inner side of the intracellular vesicles. On the contrary, the HA epitope at the C-term (TMEM151A-HA) is associated to the cytosolic face of the plasma membrane, ER or endosome membranes. Taken together these results indicate that TMEM151A has a short extracellular loop, a structured and stable transmembrane domain and a large cytosolic domain featuring several

secondary structures, suggesting the involvement of TMEM151A in processes occurring in the cytosol or at the membrane level but not extracellularly.

From the topological point of view PRRT2 is characterized by an unstructured cytosolic domain and a particular membrane associated domain with a helix-hinge-helix not crossing the plasma membrane contiguous to a single transmembrane helix, that is a hallmark of several Dispanins, the class to which PRRT2 belongs [42], [135], [136]. This particular structure is a feature of proteins involved in intracellular (or vesicles) trafficking and membrane fusion events. Interestingly, a similar domain is also present in the TMD of TMEM151A, providing insights into its putative function. However, the helix-hinge-helix motif of TMEM151A is adjacent to transmembrane helices in 3D structure but not contiguous to them in the protein sequence. On the contrary, the intracellular domain of TMEM151A is very different from the unstructured cytosolic domain of PRRT2 suggesting that the two proteins may share some functions at the membrane level but are involved in different processes in the cytosol.

From our topology data it can be concluded that TMEM151A plays its role in the membrane of intracellular organelles and in the plasma membrane as well as in the cytosolic cellular compartment. Overall, this work may contribute in directing the future research to specific groups of molecular interactors and molecular targets for pharmacological interventions.

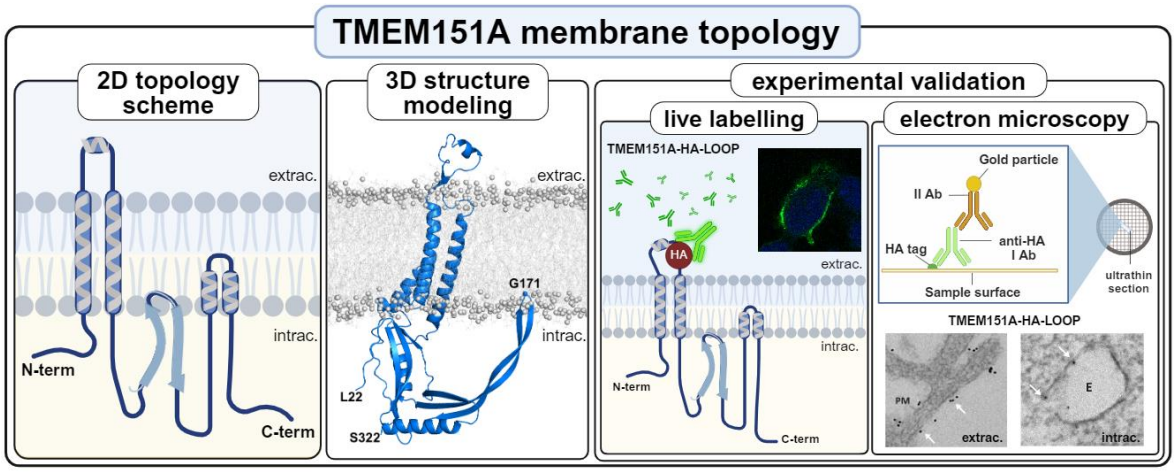

Graphical abstract Aim 3: TMEM151A membrane topology. Created with BioRender.com

TMEM151A variants characterization

Since TMEM151A is a largely uncharacterized gene, the study of pathogenic variants represents a valuable approach to elucidate its physiological function and the pathophysiological mechanisms underlying TMEM151A-associated paroxysmal disorders. The functional characterization of six pathogenic TMEM151A variants provides important insights into the molecular mechanisms involved in PKD. While some missense variants (G56R, V149del and S297L) displayed a significant reduction in total protein expression, other variants—including the truncating C125* and the missense V264A—showed normal or even increased expression levels. As previously reported for other PKD-associated proteins, such as PRRT2, both decreased and increased protein expression can contribute to paroxysmal disease phenotypes [74]. Accordingly, it is plausible that TMEM151A variants may exert either loss-of-function or gain-of-function effects, ultimately leading to a hyperexcitable neuronal phenotype through disruption of the physiological balance within neuronal networks.

The truncated isoforms C125* and L300Pfs*118 exhibited a lower molecular weight compared to the WT TMEM151A protein, as expected, while their overall expression levels were not

reduced and were even increased in the case of the C125* variant. The loss of substantial portions of the protein structure in these variants is likely to impair normal TMEM151A function, independently of total protein abundance.

Notably, live-labeling experiments revealed that five out of the six analyzed variants completely lost plasma membrane localization, despite being clearly expressed intracellularly. This observation strongly suggests that correct membrane targeting of TMEM151A is a critical requirement for its physiological activity. In contrast, the V264A variant retained membrane localization comparable to the WT protein, indicating that alternative pathogenic mechanisms—such as impaired intrinsic protein function or altered protein–protein interactions—may contribute to disease in this case.

Importantly, all variants preserved normal localization to the Golgi apparatus and the ER, indicating that early intracellular trafficking of TMEM151A is not impaired and that the defect likely arises at a later step of membrane targeting, stabilization, or retention. Given that TMEM151A function is expected to be tightly linked to its three-dimensional structure, alterations in amino acid composition may induce structural changes that ultimately impair its membrane targeting or activity. In this regard, molecular dynamics simulations of mutant proteins, starting from the AlphaFold2 structural model described above, could provide valuable insights into how specific variants affect protein stability and conformation.

An in-depth analysis of truncating variants may further contribute to the understanding of the functional relevance of distinct TMEM151A domains. Leveraging our findings on TMEM151A membrane topology, we demonstrated that several pathogenic variants fail to reach the plasma membrane. The loss of membrane targeting observed in these mutants may be associated with reduced total expression levels (as observed for G56R, V149del and S297L) or may result from improper protein folding. The C125* variant introduces a truncation at the end of the first membrane-associated domain, immediately after the second major α-helix, leading to the loss of part of this domain as well as the entire intracellular C-terminal region. Despite showing increased total expression levels, similar to the V264A variant, the C125* mutant — as well as the L300Pfs*118 variant, which displays expression levels comparable to the WT — fails to localize to the plasma membrane. These observations indicate that the membrane-associated domain alone is not sufficient to ensure correct membrane localization of TMEM151A and suggest that additional regions of the protein, including the C-terminal domain, are required for proper membrane targeting.

Collectively, these findings support a model in which most TMEM151A pathogenic variants primarily act through a loss-of-function mechanism. Nevertheless, these conclusions should be interpreted with caution, as all experiments were conducted under overexpression conditions in heterologous systems. Although this strategy is necessary in the absence of specific tools to detect endogenous TMEM151A, it may influence protein stability, trafficking, or subcellular distribution, and therefore may not fully reflect the physiological behavior of the protein in native neuronal contexts.

TMEM151A role in mouse neuronal development

The results presented indicate that TMEM151A plays an important role in promoting and regulating neuronal development, particularly during stages of active dendritic growth and maturation. Consistent with previous reports describing a developmentally regulated expression of TMEM151A in the mouse brain, our analysis of primary cortical and hippocampal neurons revealed a clear temporal regulation of TMEM151A mRNA expression in vitro. The

progressive increase in expression during neuronal maturation, with peak levels observed between 14 and 21 days in vitro, supports a role for TMEM151A in later phases of neuronal development rather than in early neurogenesis. This temporal pattern is particularly pronounced in hippocampal neurons and is in line with the clinical observation that TMEM151A-associated paroxysmal disorders typically manifest during late childhood or adolescence.

Based on this expression profile, we investigated the functional impact of TMEM151A on neuronal morphology using overexpression approaches in primary hippocampal neurons. Neurons overexpressing TMEM151A displayed increased dendritic branching compared to control neurons, as revealed by Sholl analysis. Given the importance of dendritic architecture for network formation and signal integration, TMEM151A may contribute to the establishment of functional neuronal circuits during development.

In contrast, the overexpression of pathogenic TMEM151A variants resulted in a marked impairment of neuronal maturation. Most variants analyzed (G56R, C125*, V149del, S297L and L300Pfs*118) caused a significant reduction in both neurite length and dendritic arborization compared to TMEM151A WT-expressing neurons. These findings indicate that pathogenic variants interfere with key functional domains of TMEM151A required for its developmental role, ultimately leading to defective neuronal growth and branching. Such alterations could contribute to aberrant circuit formation and increased network excitability, providing a cellular substrate for the paroxysmal phenotypes observed in patients.

Notably, the V264A variant did not significantly affect neurite length and showed a milder phenotype compared to the other variants, suggesting a variant-specific impact on TMEM151A function. This observation is consistent with previous data showing preserved plasma membrane localization of the V264A mutant and supports the idea that not all pathogenic variants equally disrupt TMEM151A-dependent developmental processes. Instead, different variants may act through distinct molecular mechanisms, resulting in variable degrees of functional impairment.

Taken together, these results support a model in which TMEM151A promotes dendritic branching and neuronal maturation, and in which pathogenic variants disrupt these processes, leading to impaired neuronal development. Although these experiments were performed under overexpression conditions, they provide important functional evidence linking TMEM151A to neuronal morphogenesis and offer a mechanistic framework to understand how *TMEM151A* variants may contribute to the pathophysiology of paroxysmal movement disorders.

Since many *TMEM151A* pathogenic variants lead to reduced protein expression, a loss-of-function mechanism could be modeled by selectively knocking down TMEM151A in mouse neurons using shRNA. This approach would allow the study of TMEM151A function at endogenous expression levels, avoiding the limitations associated with overexpression systems. A major limitation of this strategy is the current lack of specific antibodies able to reliably detect endogenous TMEM151A, which prevents direct validation of protein downregulation. As an alternative, shRNA efficiency could be indirectly assessed at the transcript level using RNAscope or quantitative real-time PCR to confirm TMEM151A mRNA silencing. Overall, RNA-based knockdown approaches represent a promising direction for future studies aimed at dissecting the physiological role of TMEM151A in neuronal contexts.

TMEM151A role in human neuronal development

The morphological analysis of iNeuron maturation revealed that partial loss of *TMEM151A* impairs the progressive structural development of neuronal cultures, particularly at intermediate and late stages of differentiation. *TMEM151A*-deficient neurons exhibited reduced neuritic arborization and diminished network complexity, suggesting compromised neuronal integration during maturation and confirming in a completely different system the developmental defect observed in mouse neurons overexpressing the *TMEM151A* variants described above. These structural defects provide an important framework for interpreting the functional alterations observed at the network level.

Collectively, MEA recordings demonstrate that loss of *TMEM151A* leads to a delayed and incomplete maturation of neuronal network activity. *TMEM151A*-deficient (#C2) cultures showed reduced recruitment of active electrodes, lower firing rates, and a persistent prevalence of uncoordinated spiking compared to isogenic controls. Although bursting activity and network bursts were eventually established, they emerged later, involved fewer neurons, and were shorter in duration, indicating an impaired ability to sustain coordinated activity. These findings suggest that *TMEM151A* is not strictly required for the generation of neuronal activity per se, but is instead critical for the timely organization, synchronization, and stabilization of network dynamics during maturation.

The persistence of random spiking activity and the reduced stability of bursts in *TMEM151A*-deficient networks point to defective synaptic integration and/or an altered balance in network signaling. At the network level, the delayed onset and reduced robustness of network bursts further indicate compromised large-scale coordination, supporting the idea that TMEM151A contributes to the proper assembly and functional refinement of neuronal circuits. Together with the morphological defects observed in dendritic development, these functional alterations suggest that loss of TMEM151A disrupts the coupling between structural maturation and emergent network activity.

Overall, the MEA phenotype supports a role for TMEM151A in functional network integration and maturation, consistent with its implication in human paroxysmal movement disorders, where subtle but significant alterations in neuronal excitability and synchronization are thought to underlie episodic motor symptoms. Importantly, the current model is limited to a single excitatory neuronal population. To more closely recapitulate physiological conditions, future studies will exploit the same TMEM151A-mutant and isogenic control iPSC lines to generate GABAergic neurons through doxycycline-inducible expression of ASCL1 and DLX2. The establishment of mixed excitatory–inhibitory co-cultures will enable a more accurate assessment of excitation–inhibition balance and provide deeper insight into the circuit-level mechanisms underlying TMEM151A-associated pathophysiology.

TMEM151A interactomics

TMEM151A – NaV1.1 modulation

Our electrophysiological data identify TMEM151A as a selective modulator of NaV1.1 channel kinetics. In heterologous HEK293 cells, co-expression of TMEM151A did not affect sodium current density or amplitude mediated by NaV1.2, NaV1.6, or NaV1.1, indicating that TMEM151A does not influence channel expression levels or membrane availability under these conditions. However, TMEM151A selectively altered the inactivation properties of NaV1.1, significantly accelerating the entry of the channel into the fast-inactivated state. This

effect was not observed for NaV1.2 or NaV1.6, suggesting a specific functional interaction between TMEM151A and NaV1.1.

The inactivation time constant (τ) represents a key kinetic parameter governing the duration of sodium influx during an action potential. A reduction in τ reflects a faster transition of the channel from the open to the inactivated state, thereby shortening channel open time and limiting sodium entry. Functionally, this behavior is equivalent to a loss-of-function effect at the channel level, as it constrains the ability of neurons to sustain repetitive firing. Notably, NaV1.1 is preferentially expressed in GABAergic inhibitory interneurons, where it plays a critical role in maintaining inhibitory tone and network stability.

In this context, the TMEM151A-dependent modulation of NaV1.1 inactivation provides a mechanistic link between TMEM151A dysfunction and altered neuronal excitability. Pathogenic TMEM151A truncating variants (C125* and L300Pfs*118) completely lose this regulatory effect. While these variants do not alter sodium current amplitude or density, they fail to modulate NaV1.1 inactivation kinetics, which revert to values comparable to control conditions. This loss of modulation suggests that intact TMEM151A is required for proper fine-tuning of NaV1.1 gating and that disease-associated variants act through a loss-of-function mechanism at the level of channel regulation.

At first glance, this mechanism may appear counterintuitive. TMEM151A WT accelerates NaV1.1 inactivation, whereas loss of TMEM151A function would be expected to slow inactivation and thereby increase NaV1.1 activity. Given that NaV1.1 is predominantly expressed in inhibitory interneurons, increased NaV1.1 function would classically be predicted to enhance inhibition rather than promote hyperexcitability. However, this apparent paradox is consistent with previous observations showing that GOF variants of NaV1.1 can also lead to epileptic phenotypes, as reported for specific *SCN1A* variants [137]. These studies indicate that excessive or dysregulated NaV1.1 activity can disrupt interneuron firing precision, impair network synchronization, and ultimately destabilize excitation–inhibition balance.

Importantly, the effect of TMEM151A on NaV1.1 kinetics is subtle and highly specific, affecting channel gating rather than overall current amplitude or expression. Although modest at the biophysical level, such kinetic modulation may have a disproportionate impact on neuronal firing dynamics, particularly in fast-spiking inhibitory interneurons, where precise timing of action potentials is critical. Small changes in inactivation kinetics can influence spike frequency adaptation, action potential reliability, and network oscillations

The clinical relevance of this mechanism is further supported by the therapeutic response of TMEM151A-related patients to carbamazepine, a sodium channel blocker. The effectiveness of carbamazepine suggests that abnormal sodium channel function contributes directly to disease pathophysiology and reinforces the idea that altered NaV1.1 gating, even in the absence of large changes in current amplitude, can be sufficient to drive paroxysmal motor symptoms. In this respect, *TMEM151A* appears functionally convergent with other paroxysmal disorder genes, such as *PRRT2*, which also modulate sodium channel activity and show similar pharmacological sensitivity.

Together, these findings support a model in which TMEM151A contributes to neuronal network stability by fine-tuning NaV1.1 inactivation kinetics in inhibitory neurons. Loss of this modulatory function, as observed for pathogenic *TMEM151A* variants, is likely to impair inhibitory control and promote network instability. While these experiments were conducted

in a heterologous overexpression system, they provide a coherent mechanistic framework that integrates molecular, cellular, and clinical observations and strongly motivate future studies in neuronal and circuit-specific models to validate the physiological relevance of TMEM151A–NaV1.1 interaction.

TMEM151A proteomics

The interactomics approach used in this study provides initial insights into the molecular context of TMEM151A and suggests its involvement in multiple cellular pathways relevant to neuronal and neurodevelopmental function. By combining a pull-down strategy with mass spectrometry and applying stringent filtering criteria, we aimed to identify robust and biologically meaningful interaction partners while minimizing non-specific associations.

A relevant aspect of the dataset is the presence of proteins annotated as Homo sapiens. This is expected, as TMEM151A was overexpressed in HEK293 cells for 24 hours prior to incubation with mouse brain lysate. During this time, the bait protein can establish interactions with endogenous HEK293 proteins. These interactions should not be considered purely artifactual, as they may involve conserved and ubiquitously expressed housekeeping proteins that are also present in mouse brain tissue. Importantly, the subsequent incubation with mouse brain lysate allows the formation of additional interactions with brain-derived proteins, supporting the idea that the identified interactome reflects a combination of conserved cellular interactions and brain-relevant binding events.

Protein–protein interaction network analysis highlights a strong association of TMEM151A with cytoskeletal components, particularly actin-related proteins, together with motor proteins and regulators of microtubule dynamics. Given the central role of cytoskeletal organization in neuronal development, morphology, and intracellular transport, these interactions suggest that TMEM151A may contribute to key processes such as neurite outgrowth, growth cone dynamics, dendritic spine remodeling, and neuronal migration. These processes are essential for the establishment of functional neuronal circuits during brain development and rely on tightly coordinated actin–microtubule remodeling.

In parallel, the enrichment of proteins involved in vesicle trafficking and membrane fusion points toward a potential role for TMEM151A in intracellular transport and membrane remodeling. Efficient trafficking of synaptic vesicles, receptors, and adhesion molecules is required for synaptogenesis, synaptic maturation, and activity-dependent plasticity. Alterations in these pathways during development could lead to long-lasting effects on neuronal connectivity and excitability.

Additional interactions with cell adhesion molecules, including integrins and galectins, further support a role for TMEM151A in neuron–extracellular matrix interactions and mechanotransduction pathways. These mechanisms are known to regulate neuronal positioning, axon guidance, and synaptic stabilization. Moreover, the association with proteins involved in cell cycle regulation and cytoskeletal organization during mitosis raises the possibility that TMEM151A may also influence neural progenitor proliferation or differentiation, although this aspect requires further investigation.

In the context of neurological disease, the interaction networks identified in this study suggest that alterations in TMEM151A-associated pathways may impact neuronal excitability and network stability. Disruption of cytoskeletal dynamics, membrane trafficking, or adhesion-related mechanisms in developing or mature neurons could contribute to the pathophysiology of movement disorders associated with TMEM151A dysfunction.

Overall, although further experimental validation is required, this study provides a first molecular framework for understanding TMEM151A function. The identified interaction networks suggest that TMEM151A may act at the interface between cytoskeletal regulation, membrane trafficking, and adhesion-related pathways, all of which are critical for neuronal development and function. Future studies will focus on validating selected interactors and determining how disease-associated *TMEM151A* variants affect these molecular pathways, with the aim of clarifying the role of *TMEM151A* in brain development and neurological disease.

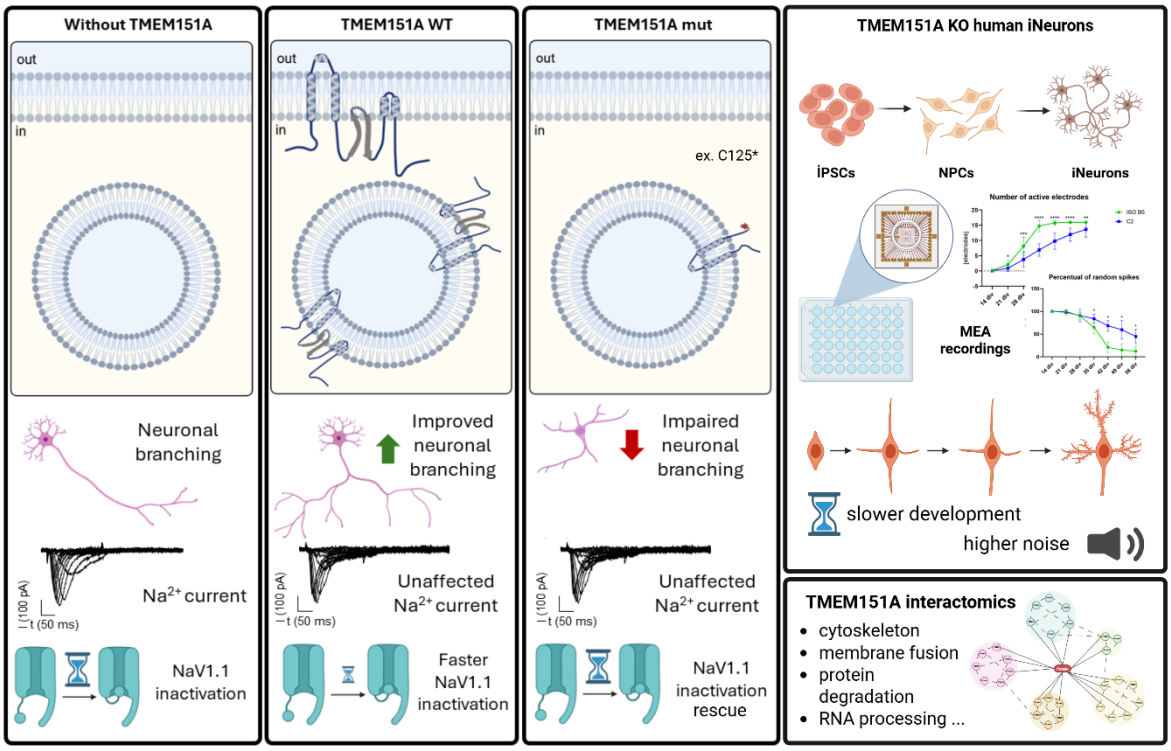

Graphical abstract Aim 3 – TMEM151A. Created with BioRender.com

Conclusion

This PhD thesis aimed to investigate the molecular and functional mechanisms underlying epilepsy and paroxysmal movement disorders by focusing on three genes - *SCN2A*, *PRRT2*, and *TMEM151A* - which, despite encoding proteins with distinct structures and primary functions, converge on the regulation of neuronal excitability and network stability. By integrating clinical data, functional assays, molecular interaction studies, and cellular and animal models, this work provides a comprehensive view of how alterations at different levels of neuronal signaling can lead to paroxysmal neurological phenotypes.

A central theme emerging from this thesis is the concept of excitability imbalance as a unifying pathogenic mechanism. In *SCN2A*-related disorders, this imbalance arises directly from alterations in the biophysical properties of voltage-gated sodium channels, whereas in *PRRT2*- and *TMEM151A*-associated disorders, it emerges indirectly, through dysregulation of sodium channel modulation, synaptic transmission, or network synchronization. Despite these differences, all three conditions manifest with episodic neurological symptoms, highlighting how subtle perturbations in excitability control can translate into dramatic clinical events.

The analysis of *SCN2A* mosaic variants underscored the complexity of genotype–phenotype correlations in sodium channelopathies. The functional characterization of the A1659V and I237N variants revealed unexpected loss-of-function profiles despite clinical features suggestive of a gain-of-function mechanism. These findings challenge the traditional dichotomous classification of *SCN2A* variants and emphasize the importance of direct functional testing, particularly in mosaic conditions where the proportion and distribution of mutant cells may critically shape disease severity and treatment response. From a clinical perspective, these results reinforce the need for precision medicine approaches, as therapeutic strategies based solely on predicted functional classes may be misleading and potentially harmful.

The work on PRRT2 further expanded the understanding of how neuronal excitability can be modulated by non-channel proteins. By dissecting the interaction between PRRT2 and the NaV1.2 channel, this thesis demonstrated that PRRT2 exerts a finely tuned inhibitory control over sodium channel function. Importantly, both loss- and gain-of-function effects of *PRRT2* missense variants were shown to disrupt this balance, supporting the idea that PRRT2 operates within a narrow physiological range. When this range is exceeded in either direction, neuronal network instability and paroxysmal manifestations may arise. This concept aligns with emerging evidence that PRRT2 dosage and functional integrity are critical determinants of network behavior and highlights PRRT2 as a key homeostatic regulator rather than a simple inhibitory factor.

The identification of specific residues involved in the PRRT2–NaV1.2 interaction represents an important step toward understanding the molecular basis of *PRRT2*-related disorders. At the same time, the absence of detectable effects of the severe PRRT2 L336X variant on NaV1.2 function suggests that PRRT2 pathogenicity may extend beyond sodium channel modulation, potentially involving other ion channels or presynaptic mechanisms. This observation underscores the multifunctional nature of PRRT2 and points to the need for broader investigative approaches to fully capture its role in neuronal physiology.

A major contribution of this thesis is the comprehensive characterization of *TMEM151A*, a gene that until recently remained largely uncharacterized, and recently associated with paroxysmal kinesigenic dyskinesia. The detailed analysis of TMEM151A expression revealed a strong

enrichment in the nervous system and a marked developmental regulation, with higher expression during postnatal stages and reduced levels in adulthood. This temporal profile mirrors the clinical course of PKD, which typically manifests in childhood or adolescence and often remits later in life, suggesting a direct link between TMEM151A expression dynamics and disease susceptibility.

Functional studies demonstrated that TMEM151A plays a role in neuronal maturation, dendritic arborization, and network organization. Loss of TMEM151A function resulted in impaired dendritic development and delayed network synchronization, as shown by electrophysiological analyses in human iNeuron models. Importantly, TMEM151A deficiency did not abolish neuronal activity per se but rather disrupted the timing and coordination of network maturation, a phenotype consistent with paroxysmal disorders in which baseline neurological function is preserved between episodes. These findings support the view that TMEM151A acts as a stabilizing factor for neuronal circuits, ensuring proper integration and synchronization rather than controlling excitability at the level of single action potentials.

The identification of TMEM151A molecular interactors, including proteins involved in synaptic function and membrane trafficking, further supports its role in network-level regulation. Moreover, the observation that TMEM151A modulates sodium channel kinetics - particularly NaV1.1 - provides a mechanistic link to the efficacy of sodium channel blockers in *TMEM151A*-associated PKD. Together with recent in vivo evidence from murine models, these results position TMEM151A alongside PRRT2 as a critical regulator of motor circuit stability and reinforce the idea that PKD is fundamentally a disorder of network excitability rather than a primary channelopathy.

Across all three genes studied, a recurrent theme is the disruption of finely balanced regulatory systems. Whether through direct channel dysfunction (*SCN2A*), altered channel modulation and synaptic regulation (*PRRT2*), or impaired network maturation and synchronization (*TMEM151A*), the resulting phenotypes converge on episodic neurological dysfunction. This convergence helps explain the shared responsiveness to sodium channel blockers across distinct genetic etiologies and highlights common therapeutic vulnerabilities.

In conclusion, this thesis provides new insights into the molecular and functional bases of epilepsy and paroxysmal movement disorders, emphasizing the importance of regulatory mechanisms that maintain neuronal and network stability. By integrating genetic, molecular, and functional approaches, this work contributes to a more nuanced understanding of disease mechanisms and lays the groundwork for future studies aimed at identifying novel therapeutic targets and improving genotype-guided treatment strategies. Ultimately, the findings presented here support a shift from a gene-centric to a network-centric view of paroxysmal neurological disorders, in which diverse molecular defects converge on shared principles of neuronal excitability and circuit stability.

Acknowledgements

I would like to express my sincere gratitude to all those who contributed, directly or indirectly, to the completion of this PhD thesis.

First and foremost, I am deeply grateful to my supervisor, Prof. Anna Corradi, for her guidance, support, and scientific insight throughout the course of this project. Her expertise, critical thinking, and constant encouragement were fundamental to my scientific growth and to the development of this work. I also thank my co-supervisor and mentor, Prof. Bruno Sterlini, for his valuable advice, constructive discussions, and availability at different stages of my PhD. Moreover, I want to thank Prof. Fabio Benfenati for his supervision on the PRRT2 project and his invaluable mentorship at different stages of this work.

I would like to thank all the members of the laboratory for creating a stimulating and supportive working environment. Their scientific input, technical assistance, and everyday collaboration greatly contributed to this project. In particular, I am grateful to colleagues, especially to Dott. Martina Muià and Dott. Martina Servetti, with whom I shared experiments, ideas, and challenges, and whose support made the laboratory experience both productive and enjoyable.

I also wish to acknowledge all collaborators and co-authors who contributed their expertise to different aspects of this work, including clinical characterization, computational modeling, electrophysiological recordings. In particular, I would like to thank Dott. Beatrice Corradi and Prof. Luca Maragliano for computational modeling on both PRRT2 and TMEM151A. Moreover, I would like to thank Dott. Giacomo Mazzoni, Dott. Francesca Franchi, Prof. Pierluigi Valente for the electrophysiological studies on the PRRT2-NaV1.2 interaction and Dott. Loretta Ferrera for the electrophysiological studies on NaV1.2 mutants and on the TMEM151A-NaV interaction. Regarding the electron microscopy analyses, I want to thank Dott. Pietro Arnaldi and Prof. Katia Cortese. Regarding the proteomics investigation of TMEM151A interactors, I want to thank Dott. Martina Bartolucci and Dott. Andrea Petretto. Their contributions were essential to the multidisciplinary nature of this thesis.

I am grateful to the clinicians and patients involved in the genetic studies described in this work. I also thank the technical staff for their invaluable assistance and for ensuring the smooth functioning of the research infrastructure, in particular I would like to thank Dott. Antonella Marte and Dott. Silvia Casagrande.

I acknowledge the funding agencies, especially Telethon/Cariplo Foundations – Italy (Grant GJC22066 to A. Corradi and F. Zara) for funding the project entitled “Molecular and functional investigation of the role of TMEM151A in the pathogenesis of movement disorders” and the Ministry of University and Research (MUR), National Recovery and Resilience Plan (NRRP), for funding the MNESYS project (PE0000006) entitled “A Multiscale integrated approach to the study of the nervous system in health and disease” (DN. 1553 October 11, 2022) to A. Corradi and F. Zara and institutions (Università di Genova and Italian Institute of Technology) that supported this work and provided the resources necessary to carry out this research. Their support made possible the development of this project and the dissemination of its results.

Finally, I would like to thank my family, my boyfriend and friends for their constant support, patience, and encouragement throughout these years. Their understanding and motivation were essential during both challenging and rewarding moments of this journey. This thesis is dedicated to them.

References

[1] R. S. Fisher *et al.*, 'ILAE Official Report: A practical clinical definition of epilepsy', *Epilepsia*, vol. 55, no. 4, pp. 475–482, 2014, doi: 10.1111/epi.12550.

[2] 'ILAE classification of the epilepsies: Position paper of the ILAE Commission for Classification and Terminology - Scheffer - 2017 - Epilepsia - Wiley Online Library'. Accessed: Dec. 02, 2025. [Online]. Available: https://onlinelibrary.wiley.com/doi/10.1111/epi.13709

[3] C. Rastin, L. C. Schenkel, and B. Sadikovic, 'Complexity in Genetic Epilepsies: A Comprehensive Review', *Int J Mol Sci*, vol. 24, no. 19, p. 14606, Sep. 2023, doi: 10.3390/ijms241914606.

[4] O. K. Steinlein, 'Genetic mechanisms that underlie epilepsy', *Nat Rev Neurosci*, vol. 5, no. 5, pp. 400–408, May 2004, doi: 10.1038/nrn1388.

[5] C. M. de Gusmão, L. Garcia, M. A. Mikati, S. Su, and L. Silveira-Moriyama, 'Paroxysmal Genetic Movement Disorders and Epilepsy', *Front Neurol*, vol. 12, p. 648031, Mar. 2021, doi: 10.3389/fneur.2021.648031.

[6] J. Spillane, D. M. Kullmann, and M. G. Hanna, 'Genetic neurological channelopathies: molecular genetics and clinical phenotypes', *J Neurol Neurosurg Psychiatry*, p. jnnp-2015-311233, Nov. 2015, doi: 10.1136/jnnp-2015-311233.

[7] C. Reynolds, M. D. King, and K. M. Gorman, 'The phenotypic spectrum of SCN2A-related epilepsy', *European Journal of Paediatric Neurology*, vol. 24, pp. 117–122, Jan. 2020, doi: 10.1016/j.ejpn.2019.12.016.

[8] I. Favre, E. Moczydlowski, and L. Schild, 'On the structural basis for ionic selectivity among Na+, K+, and Ca2+ in the voltage-gated sodium channel', *Biophys J*, vol. 71, no. 6, pp. 3110–3125, Dec. 1996, doi: 10.1016/S0006-3495(96)79505-X.

[9] X. Li *et al.*, 'Structural basis for modulation of human NaV1.3 by clinical drug and selective antagonist', *Nat Commun*, vol. 13, no. 1, p. 1286, Mar. 2022, doi: 10.1038/s41467-022-28808-5.

[10] W. Stühmer *et al.*, 'Structural parts involved in activation and inactivation of the sodium channel', *Nature*, vol. 339, no. 6226, pp. 597–603, Jun. 1989, doi: 10.1038/339597a0.

[11] S. J. Sanders *et al.*, 'Progress in Understanding and Treating SCN2A-Mediated Disorders', *Trends in Neurosciences*, vol. 41, no. 7, pp. 442–456, Jul. 2018, doi: 10.1016/j.tins.2018.03.011.

[12] M. Duménieu, M. Oulé, M. R. Kreutz, and J. Lopez-Rojas, 'The Segregated Expression of Voltage-Gated Potassium and Sodium Channels in Neuronal Membranes: Functional Implications and Regulatory Mechanisms', *Front. Cell. Neurosci.*, vol. 11, Apr. 2017, doi: 10.3389/fncel.2017.00115.

[13] M. H. P. Kole and G. J. Stuart, 'Signal processing in the axon initial segment', *Neuron*, vol. 73, no. 2, pp. 235–247, Jan. 2012, doi: 10.1016/j.neuron.2012.01.007.

[14] W. Tian, L. Peng, M. Zhao, L. Tao, P. Zou, and Y. Zhang, 'Dendritic Morphology Affects the Velocity and Amplitude of Back-propagating Action Potentials', *Neurosci Bull*, vol. 38, no. 11, pp. 1330–1346, Nov. 2022, doi: 10.1007/s12264-022-00931-9.

[15] E. V. Gazina *et al.*, '"Neonatal" Nav1.2 reduces neuronal excitability and affects seizure susceptibility and behaviour', *Hum Mol Genet*, vol. 24, no. 5, pp. 1457–1468, Mar. 2015, doi: 10.1093/hmg/ddu562.

[16] W. Hu, C. Tian, T. Li, M. Yang, H. Hou, and Y. Shu, 'Distinct contributions of Na(v)1.6 and Na(v)1.2 in action potential initiation and backpropagation', *Nat Neurosci*, vol. 12, no. 8, pp. 996–1002, Aug. 2009, doi: 10.1038/nn.2359.

[17] I. A. Ademuwagun, S. O. Rotimi, S. Syrbe, Y. U. Ajamma, and E. Adebiyi, 'Voltage Gated Sodium Channel Genes in Epilepsy: Mutations, Functional Studies, and Treatment Dimensions', *Front Neurol*, vol. 12, p. 600050, 2021, doi: 10.3389/fneur.2021.600050.

[18] M. Wolff, A. Brunklaus, and S. M. Zuberi, 'Phenotypic spectrum and genetics of SCN2A-related disorders, treatment options, and outcomes in epilepsy and beyond', *Epilepsia*, vol. 60 Suppl 3, pp. S59–S67, Dec. 2019, doi: 10.1111/epi.14935.

[19] M. Meisler, S. Hill, and W. Yu, 'Sodium channelopathies in neurodevelopmental disorders', *Nat Rev Neurosci*, vol. 22, no. 3, pp. 152–166, Mar. 2021, doi: 10.1038/s41583-020-00418-4.

[20] N. Specchio and P. Curatolo, 'Developmental and epileptic encephalopathies: what we do and do not know', *Brain*, vol. 144, no. 1, pp. 32–43, Feb. 2021, doi: 10.1093/brain/awaa371.

[21] P. W. E. Spratt *et al.*, 'The Autism-Associated Gene Scn2a Contributes to Dendritic Excitability and Synaptic Function in the Prefrontal Cortex', *Neuron*, vol. 103, no. 4, pp. 673-685.e5, Aug. 2019, doi: 10.1016/j.neuron.2019.05.037.

[22] J. Oyrer, S. Maljevic, I. E. Scheffer, S. F. Berkovic, S. Petrou, and C. A. Reid, 'Ion Channels in Genetic Epilepsy: From Genes and Mechanisms to Disease-Targeted Therapies', *Pharmacol Rev*, vol. 70, no. 1, pp. 142–173, Jan. 2018, doi: 10.1124/pr.117.014456.

[23] L. F. S. Menezes, E. F. Sabiá Júnior, D. V. Tibery, L. D. A. Carneiro, and E. F. Schwartz, 'Epilepsy-Related Voltage-Gated Sodium Channelopathies: A Review', *Front Pharmacol*, vol. 11, p. 1276, 2020, doi: 10.3389/fphar.2020.01276.

[24] M. Demirkiran and J. Jankovic, 'Paroxysmal dyskinesias: clinical features and classification', *Ann Neurol*, vol. 38, no. 4, pp. 571–579, Oct. 1995, doi: 10.1002/ana.410380405.

[25] C. M. De Gusmao and L. Silveira-Moriyama, 'Paroxysmal movement disorders - practical update on diagnosis and management', *Expert Rev Neurother*, vol. 19, no. 9, pp. 807–822, Sep. 2019, doi: 10.1080/14737175.2019.1648211.

[26] G. Pisanò *et al.*, 'Paroxysmal Dyskinesias in Paediatric Age: A Systematic Review', *Journal of Clinical Medicine*, vol. 14, no. 17, p. 5925, Jan. 2025, doi: 10.3390/jcm14175925.

[27] S. McGuire, S. Chanchani, and D. S. Khurana, 'Paroxysmal Dyskinesias', *Seminars in Pediatric Neurology*, vol. 25, pp. 75–81, Apr. 2018, doi: 10.1016/j.spen.2017.12.007.

[28] J.-J. Xu, H.-F. Li, and Z.-Y. Wu, 'Paroxysmal Kinesigenic Dyskinesia: Genetics and Pathophysiological Mechanisms', *Neurosci. Bull.*, vol. 40, no. 7, pp. 952–962, Jul. 2024, doi: 10.1007/s12264-023-01157-z.

[29] A. De Rosa, B. Balint, and K. R. Kumar, 'Editorial: Genetics of Paroxysmal Movement Disorders', *Front. Neurol.*, vol. 12, Sep. 2021, doi: 10.3389/fneur.2021.752000.

[30] X.-J. Huang *et al.*, 'Paroxysmal kinesigenic dyskinesia: Clinical and genetic analyses of 110 patients', *Neurology*, vol. 85, no. 18, pp. 1546–1553, Nov. 2015, doi: 10.1212/WNL.0000000000002079.

[31] W. Sun, J. Li, Y. Zhu, X. Yan, and W. Wang, 'Clinical features of paroxysmal kinesigenic dyskinesia: report of 24 cases', *Epilepsy Behav*, vol. 25, no. 4, pp. 695–699, Dec. 2012, doi: 10.1016/j.yebeh.2012.06.019.

[32] X. Liu *et al.*, 'Clinical and genetic analyses of 150 patients with paroxysmal kinesigenic dyskinesia', *J Neurol*, vol. 269, no. 9, pp. 4717–4728, Sep. 2022, doi: 10.1007/s00415-022-11103-0.

[33] M. Mantegazza, G. Curia, G. Biagini, D. S. Ragsdale, and M. Avoli, 'Voltage-gated sodium channels as therapeutic targets in epilepsy and other neurological disorders', *Lancet Neurol*, vol. 9, no. 4, pp. 413–424, Apr. 2010, doi: 10.1016/S1474-4422(10)70059-4.

[34] Q. Zeng *et al.*, 'SCN2A-Related Epilepsy: The Phenotypic Spectrum, Treatment and Prognosis', *Front Mol Neurosci*, vol. 15, p. 809951, Mar. 2022, doi: 10.3389/fnmol.2022.809951.

[35] M. Wolff *et al.*, 'Genetic and phenotypic heterogeneity suggest therapeutic implications in SCN2A-related disorders', *Brain*, vol. 140, no. 5, pp. 1316–1336, May 2017, doi: 10.1093/brain/awx054.

[36] W.-J. Chen *et al.*, 'Exome sequencing identifies truncating mutations in PRRT2 that cause paroxysmal kinesigenic dyskinesia', *Nat Genet*, vol. 43, no. 12, Art. no. 12, Dec. 2011, doi: 10.1038/ng.1008.

[37] W.-T. Tian *et al.*, 'TMEM151A Variants Cause Paroxysmal Kinesigenic Dyskinesia: A Large-Sample Study', *Movement Disorders*, vol. 37, no. 3, pp. 545–552, 2022, doi: 10.1002/mds.28865.

[38] I.-C. Chou *et al.*, 'Successful control with carbamazepine of family with paroxysmal kinesigenic dyskinesia of PRRT2 mutation', *BioMed*, vol. 4, no. 2, p. 15, May 2014, doi: 10.7603/s40681-014-0015-0.

[39] R. Guerrini, V. Conti, M. Mantegazza, S. Balestrini, A. S. Galanopoulou, and F. Benfenati, 'Developmental and epileptic encephalopathies: from genetic heterogeneity to phenotypic continuum', *Physiological Reviews*, vol. 103, no. 1, pp. 433–513, Jan. 2023, doi: 10.1152/physrev.00063.2021.

[40] F. Valtorta, F. Benfenati, F. Zara, and J. Meldolesi, 'PRRT2: from Paroxysmal Disorders to Regulation of Synaptic Function', *Trends in Neurosciences*, vol. 39, no. 10, pp. 668–679, Oct. 2016, doi: 10.1016/j.tins.2016.08.005.

[41] F. Franchi *et al.*, 'The intramembrane COOH-terminal domain of PRRT2 regulates voltage-dependent Na+ channels', *Journal of Biological Chemistry*, vol. 299, no. 5, p. 104632, May 2023, doi: 10.1016/j.jbc.2023.104632.

[42] P. Rossi *et al.*, 'A Novel Topology of Proline-rich Transmembrane Protein 2 (PRRT2): HINTS FOR AN INTRACELLULAR FUNCTION AT THE SYNAPSE*', *Journal of Biological Chemistry*, vol. 291, no. 12, pp. 6111–6123, Mar. 2016, doi: 10.1074/jbc.M115.683888.

[43] J. Coleman *et al.*, 'PRRT2 Regulates Synaptic Fusion by Directly Modulating SNARE Complex Assembly', *Cell Reports*, vol. 22, no. 3, pp. 820–831, Jan. 2018, doi: 10.1016/j.celrep.2017.12.056.

[44] D. Ferrante *et al.*, 'PRRT2 modulates presynaptic Ca2+ influx by interacting with P/Q-type channels', *Cell Reports*, vol. 35, no. 11, p. 109248, Jun. 2021, doi: 10.1016/j.celrep.2021.109248.

[45] P. Valente *et al.*, 'Constitutive Inactivation of the PRRT2 Gene Alters Short-Term Synaptic Plasticity and Promotes Network Hyperexcitability in Hippocampal Neurons', *Cerebral Cortex*, vol. 29, no. 5, pp. 2010–2033, May 2019, doi: 10.1093/cercor/bhy079.

[46] P. Valente *et al.*, 'PRRT2 Is a Key Component of the Ca2+-Dependent Neurotransmitter Release Machinery', *Cell Reports*, vol. 15, no. 1, pp. 117–131, Apr. 2016, doi: 10.1016/j.celrep.2016.03.005.

[47] F. Fruscione *et al.*, 'PRRT2 controls neuronal excitability by negatively modulating Na+ channel 1.2/1.6 activity', *Brain*, vol. 141, no. 4, pp. 1000–1016, Apr. 2018, doi: 10.1093/brain/awy051.

[48] P. Valente *et al.*, 'A Push–Pull Mechanism Between PRRT2 and β4-subunit Differentially Regulates Membrane Exposure and Biophysical Properties of NaV1.2 Sodium Channels', *Mol Neurobiol*, vol. 60, no. 3, pp. 1281–1296, Mar. 2023, doi: 10.1007/s12035-022-03112-x.

[49] B. Sterlini *et al.*, 'An interaction between PRRT2 and Na+/K+ ATPase contributes to the control of neuronal excitability', *Cell Death Dis*, vol. 12, no. 4, Art. no. 4, Mar. 2021, doi: 10.1038/s41419-021-03569-z.

[50] H.-Y. Lee *et al.*, 'Mutations in the Gene PRRT2 Cause Paroxysmal Kinesigenic Dyskinesia with Infantile Convulsions', *Cell Reports*, vol. 1, no. 1, pp. 2–12, Jan. 2012, doi: 10.1016/j.celrep.2011.11.001.

[51] J. H. Döring *et al.*, 'The Phenotypic Spectrum of PRRT2-Associated Paroxysmal Neurologic Disorders in Childhood', *Biomedicines*, vol. 8, no. 11, Art. no. 11, Nov. 2020, doi: 10.3390/biomedicines8110456.

[52] D. Ebrahimi-Fakhari, A. Saffari, A. Westenberger, and C. Klein, 'The evolving spectrum of *PRRT2* -associated paroxysmal diseases', *Brain*, vol. 138, no. 12, pp. 3476–3495, Dec. 2015, doi: 10.1093/brain/awv317.

[53] A. R. Gardiner *et al.*, 'The clinical and genetic heterogeneity of paroxysmal dyskinesias', *Brain*, vol. 138, no. 12, pp. 3567–3580, Dec. 2015, doi: 10.1093/brain/awv310.

[54] M. Delcourt *et al.*, 'Severe phenotypic spectrum of biallelic mutations in PRRT2 gene', *J Neurol Neurosurg Psychiatry*, vol. 86, no. 7, pp. 782–785, Jul. 2015, doi: 10.1136/jnnp-2014-309025.

[55] A. Labate *et al.*, 'Homozygous c.649dupC mutation in PRRT2 worsens the BFIS/PKD phenotype with mental retardation, episodic ataxia, and absences', *Epilepsia*, vol. 53, no. 12, pp. e196–e199, 2012, doi: 10.1111/epi.12009.

[56] C. Michetti *et al.*, 'The PRRT2 knockout mouse recapitulates the neurological diseases associated with PRRT2 mutations', *Neurobiology of Disease*, vol. 99, pp. 66–83, Mar. 2017, doi: 10.1016/j.nbd.2016.12.018.

[57] G.-H. Tan *et al.*, 'PRRT2 deficiency induces paroxysmal kinesigenic dyskinesia by regulating synaptic transmission in cerebellum', *Cell Res*, vol. 28, no. 1, Art. no. 1, Jan. 2018, doi: 10.1038/cr.2017.128.

[58] F. Binda, P. Valente, A. Marte, P. Baldelli, and F. Benfenati, 'Increased responsiveness at the cerebellar input stage in the PRRT2 knockout model of paroxysmal kinesigenic dyskinesia', *Neurobiology of Disease*, vol. 152, p. 105275, May 2021, doi: 10.1016/j.nbd.2021.105275.

[59] D. J. Calame *et al.*, 'Presynaptic PRRT2 Deficiency Causes Cerebellar Dysfunction and Paroxysmal Kinesigenic Dyskinesia', *Neuroscience*, vol. 448, pp. 272–286, Nov. 2020, doi: 10.1016/j.neuroscience.2020.08.034.

[60] B. Lu *et al.*, 'Cerebellar spreading depolarization mediates paroxysmal movement disorder', *Cell Reports*, vol. 36, no. 12, p. 109743, Sep. 2021, doi: 10.1016/j.celrep.2021.109743.

[61] J. Mo, B. Wang, X. Zhu, X. Wu, and Y. Liu, 'PRRT2 deficiency induces paroxysmal kinesigenic dyskinesia by influencing synaptic function in the primary motor cortex of rats', *Neurobiology of Disease*, vol. 121, pp. 274–285, Jan. 2019, doi: 10.1016/j.nbd.2018.10.011.

[62] W. A. Catterall, M. J. Lenaeus, and T. M. Gamal El-Din, 'Structure and Pharmacology of Voltage-Gated Sodium and Calcium Channels', *Annual Review of Pharmacology and Toxicology*, vol. 60, no. 1, pp. 133–154, 2020, doi: 10.1146/annurev-pharmtox-010818-021757.

[63] M. Mantegazza, S. Cestèle, and W. A. Catterall, 'Sodium channelopathies of skeletal muscle and brain', *Physiological Reviews*, vol. 101, no. 4, pp. 1633–1689, Oct. 2021, doi: 10.1152/physrev.00025.2020.

[64] R. C. Dale, A. Gardiner, J. A. Branson, and H. Houlden, 'Benefit of carbamazepine in a patient with hemiplegic migraine associated with PRRT2 mutation', *Developmental Medicine & Child Neurology*, vol. 56, no. 9, pp. 910–910, 2014, doi: 10.1111/dmcn.12396.

[65] J. H. Döring *et al.*, 'Efficacy, Tolerability, and Retention of Antiseizure Medications in PRRT2-Associated Infantile Epilepsy', *Neurology Genetics*, vol. 8, no. 5, Oct. 2022, doi: 10.1212/NXG.0000000000200020.

[66] S. Suzuki-Muromoto, R. Kosaki, K. Kosaki, and M. Kubota, 'Familial hemiplegic migraine with a PRRT2 mutation: Phenotypic variations and carbamazepine efficacy', *Brain and Development*, vol. 42, no. 3, pp. 293–297, Mar. 2020, doi: 10.1016/j.braindev.2019.12.007.

[67] Q. Zhao *et al.*, 'PRRT2 variants and effectiveness of various antiepileptic drugs in self-limited familial infantile epilepsy', *Seizure*, vol. 91, pp. 360–368, Oct. 2021, doi: 10.1016/j.seizure.2021.07.013.

[68] J. J. Winters and L. L. Isom, ‘Chapter Eleven - Developmental and Regulatory Functions of Na+ Channel Non–pore-forming β Subunits’, in *Current Topics in Membranes*, vol. 78, R. J. French and S. Yu. Noskov, Eds, in Na Channels from Phyla to Function, vol. 78. , Academic Press, 2016, pp. 315–351. doi: 10.1016/bs.ctm.2016.07.003.

[69] Y.-T. Liu *et al.*, ‘PRRT2 mutations lead to neuronal dysfunction and neurodevelopmental defects’, *Oncotarget*, vol. 7, no. 26, pp. 39184–39196, May 2016, doi: 10.18632/oncotarget.9258.

[70] M.-H. Tsai *et al.*, ‘PRRT2 missense mutations cluster near C-terminus and frequently lead to protein mislocalization’, *Epilepsia*, vol. 60, no. 5, pp. 807–817, 2019, doi: 10.1111/epi.14725.

[71] S.-Y. Zhao *et al.*, ‘Functional study and pathogenicity classification of PRRT2 missense variants in PRRT2-related disorders’, *CNS Neuroscience & Therapeutics*, vol. 26, no. 1, pp. 39–46, 2020, doi: 10.1111/cns.13147.

[72] M. Li *et al.*, ‘PRRT2 Mutant Leads to Dysfunction of Glutamate Signaling’, *International Journal of Molecular Sciences*, vol. 16, no. 5, Art. no. 5, May 2015, doi: 10.3390/ijms16059134.

[73] A. Landolfi, P. Barone, and R. Erro, ‘The Spectrum of PRRT2-Associated Disorders: Update on Clinical Features and Pathophysiology’, *Front. Neurol.*, vol. 12, Mar. 2021, doi: 10.3389/fneur.2021.629747.

[74] B. Sterlini *et al.*, ‘Missense mutations in the membrane domain of PRRT2 affect its interaction with Nav1.2 voltage-gated sodium channels’, *Neurobiology of Disease*, vol. 183, p. 106177, Jul. 2023, doi: 10.1016/j.nbd.2023.106177.

[75] C. Michetti, A. Corradi, and F. Benfenati, ‘PRRT2, a network stability gene’, *Oncotarget*, vol. 8, no. 34, pp. 55770–55771, Jul. 2017, doi: 10.18632/oncotarget.19506.

[76] H.-F. Li *et al.*, ‘TMEM151A variants cause paroxysmal kinesigenic dyskinesia’, *Cell Discovery*, vol. 7, 2021, doi: 10.1038/s41421-021-00322-w.

[77] Y.-L. Li *et al.*, ‘Exome-Wide Analyses in Paroxysmal Kinesigenic Dyskinesia Confirm TMEM151A as a Novel Causative Gene’, *Movement Disorders*, vol. 37, no. 3, pp. 641–643, 2022, doi: 10.1002/mds.28904.

[78] H. Wang, P. Huang, M. Zhu, X. Fang, C. Wu, and D. Hong, ‘TMEM151A phenotypic spectrum includes paroxysmal kinesigenic dyskinesia with infantile convulsions’, *Neurol Sci*, vol. 43, no. 10, pp. 6095–6099, Oct. 2022, doi: 10.1007/s10072-022-06208-3.

[79] L.-Y. Ma, L. Han, M. Niu, L. Chen, Y.-Z. Yu, and T. Feng, ‘Screening of the TMEM151A Gene in Patients With Paroxysmal Kinesigenic Dyskinesia and Other Movement Disorders’, *Frontiers in Neurology*, vol. 13, 2022, Accessed: Oct. 05, 2023. [Online]. Available: https://www.frontiersin.org/articles/10.3389/fneur.2022.865690

[80] T. Wirth *et al.*, ‘De Novo Mutation in TMEM151A and Paroxysmal Kinesigenic Dyskinesia’, *Movement Disorders*, vol. 37, no. 5, pp. 1115–1117, 2022, doi: 10.1002/mds.29023.

[81] Y.-L. Chen, D.-F. Chen, H.-F. Li, and Z.-Y. Wu, 'Features Differ Between Paroxysmal Kinesigenic Dyskinesia Patients with PRRT2 and TMEM151A Variants', *Mov Disord*, vol. 37, no. 3, pp. 608–613, Mar. 2022, doi: 10.1002/mds.28939.

[82] S. Satolli *et al.*, 'Two Cases of TMEM151A-Associated Paroxysmal Dyskinesia in a Single-Center Series of PRRT2-Negative Patients', *Mov Disord Clin Pract*, vol. 10, no. 5, pp. 842–844, May 2023, doi: 10.1002/mdc3.13705.

[83] Y. Zhang *et al.*, 'Genetic and phenotypic analyses of PRRT2 positive and negative paroxysmal kinesigenic dyskinesia', *Ther Adv Neurol Disord*, vol. 17, p. 17562864231224110, 2024, doi: 10.1177/17562864231224110.

[84] S. Marx *et al.*, 'Transmembrane (TMEM) protein family members: Poorly characterized even if essential for the metastatic process', *Seminars in Cancer Biology*, vol. 60, pp. 96–106, Feb. 2020, doi: 10.1016/j.semcancer.2019.08.018.

[85] L. Morinelli *et al.*, 'Unraveling the Membrane Topology of TMEM151A: A Step Towards Understanding its Cellular Role', *J Mol Biol*, vol. 436, no. 23, p. 168834, Dec. 2024, doi: 10.1016/j.jmb.2024.168834.

[86] H.-W. Zhou *et al.*, 'TMEM151A in forebrain excitatory neurons negatively regulates seizure susceptibility', *Epilepsia*, Dec. 2025, doi: 10.1111/epi.70016.

[87] J. Jumper *et al.*, 'Highly accurate protein structure prediction with AlphaFold', *Nature*, vol. 596, no. 7873, Art. no. 7873, Aug. 2021, doi: 10.1038/s41586-021-03819-2.

[88] M. A. Lomize, I. D. Pogozheva, H. Joo, H. I. Mosberg, and A. L. Lomize, 'OPM database and PPM web server: resources for positioning of proteins in membranes', *Nucleic Acids Research*, vol. 40, no. D1, pp. D370–D376, Jan. 2012, doi: 10.1093/nar/gkr703.

[89] 'The PyMOL Molecular Graphics System, Version 2.0. (2002). Schrödinger, LLC, New York, NY. Schrödinger, LLC'.

[90] J. Lee *et al.*, 'CHARMM-GUI Membrane Builder for Complex Biological Membrane Simulations with Glycolipids and Lipoglycans', *J Chem Theory Comput*, vol. 15, no. 1, pp. 775–786, Jan. 2019, doi: 10.1021/acs.jctc.8b01066.

[91] E. Neria, S. Fischer, and M. Karplus, 'Simulation of activation free energies in molecular systems', *The Journal of Chemical Physics*, vol. 105, no. 5, pp. 1902–1921, Aug. 1996, doi: 10.1063/1.472061.

[92] J. Lee *et al.*, 'CHARMM-GUI Input Generator for NAMD, GROMACS, AMBER, OpenMM, and CHARMM/OpenMM Simulations Using the CHARMM36 Additive Force Field', *J Chem Theory Comput*, vol. 12, no. 1, pp. 405–413, Jan. 2016, doi: 10.1021/acs.jctc.5b00935.

[93] R. B. Best *et al.*, 'Optimization of the additive CHARMM all-atom protein force field targeting improved sampling of the backbone ϕ, ψ and side-chain χ(1) and χ(2) dihedral angles', *J Chem Theory Comput*, vol. 8, no. 9, pp. 3257–3273, Sep. 2012, doi: 10.1021/ct300400x.

[94] J. Huang *et al.*, 'CHARMM36: An Improved Force Field for Folded and Intrinsically Disordered Proteins', *Biophysical Journal*, vol. 112, no. 3, Supplement 1, pp. 175a–176a, Feb. 2017, doi: 10.1016/j.bpj.2016.11.971.

[95] T. Darden, D. York, and L. Pedersen, ‘Particle mesh Ewald: An N·log(N) method for Ewald sums in large systems’, *The Journal of Chemical Physics*, vol. 98, no. 12, pp. 10089–10092, Jun. 1993, doi: 10.1063/1.464397.

[96] S. Miyamoto and P. A. Kollman, ‘Settle: An analytical version of the SHAKE and RATTLE algorithm for rigid water models’, *Journal of Computational Chemistry*, vol. 13, no. 8, pp. 952–962, 1992, doi: 10.1002/jcc.540130805.

[97] S. E. Feller, Y. Zhang, R. W. Pastor, and B. R. Brooks, ‘Constant pressure molecular dynamics simulation: The Langevin piston method’, *The Journal of Chemical Physics*, vol. 103, no. 11, pp. 4613–4621, Sep. 1995, doi: 10.1063/1.470648.

[98] W. Humphrey, A. Dalke, and K. Schulten, ‘VMD: Visual molecular dynamics’, *Journal of Molecular Graphics*, vol. 14, no. 1, pp. 33–38, Feb. 1996, doi: 10.1016/0263-7855(96)00018-5.

[99] M. Kožić and B. Bertoša, ‘Trajectory maps: molecular dynamics visualization and analysis’, *NAR Genom Bioinform*, vol. 6, no. 1, p. lqad114, Mar. 2024, doi: 10.1093/nargab/lqad114.

[100] J. Abramson *et al.*, ‘Accurate structure prediction of biomolecular interactions with AlphaFold 3’, *Nature*, vol. 630, no. 8016, pp. 493–500, Jun. 2024, doi: 10.1038/s41586-024-07487-w.

[101] S. F. Altschul, W. Gish, W. Miller, E. W. Myers, and D. J. Lipman, ‘Basic local alignment search tool’, *J Mol Biol*, vol. 215, no. 3, pp. 403–410, Oct. 1990, doi: 10.1016/S0022-2836(05)80360-2.

[102] I. M. Wallace, O. O’Sullivan, D. G. Higgins, and C. Notredame, ‘M-Coffee: combining multiple sequence alignment methods with T-Coffee’, *Nucleic Acids Res*, vol. 34, no. 6, pp. 1692–1699, 2006, doi: 10.1093/nar/gkl091.

[103] S. Moretti, F. Armougom, I. M. Wallace, D. G. Higgins, C. V. Jongeneel, and C. Notredame, ‘The M-Coffee web server: a meta-method for computing multiple sequence alignments by combining alternative alignment methods’, *Nucleic Acids Res*, vol. 35, no. Web Server issue, pp. W645-648, Jul. 2007, doi: 10.1093/nar/gkm333.

[104] X. Robert and P. Gouet, ‘Deciphering key features in protein structures with the new ENDscript server’, *Nucleic Acids Res*, vol. 42, no. Web Server issue, pp. W320-324, Jul. 2014, doi: 10.1093/nar/gku316.

[105] J.-M. DeKeyser, C. H. Thompson, and A. L. George, ‘Cryptic prokaryotic promoters explain instability of recombinant neuronal sodium channels in bacteria’, *Journal of Biological Chemistry*, vol. 296, Jan. 2021, doi: 10.1016/j.jbc.2021.100298.

[106] R. R. Mattingly and I. G. Macara, ‘Phosphorylation-dependent activation of the Ras-GRF/CDC25Mm exchange factor by muscarinic receptors and G-protein beta gamma subunits’, *Nature*, vol. 382, no. 6588, pp. 268–272, Jul. 1996, doi: 10.1038/382268a0.

[107] D. B. Bekker-Jensen *et al.*, ‘A Compact Quadrupole-Orbitrap Mass Spectrometer with FAIMS Interface Improves Proteome Coverage in Short LC Gradients’, *Mol Cell Proteomics*, vol. 19, no. 4, pp. 716–729, Apr. 2020, doi: 10.1074/mcp.TIR119.001906.

[108] N. A. Kulak, G. Pichler, I. Paron, N. Nagaraj, and M. Mann, 'Minimal, encapsulated proteomic-sample processing applied to copy-number estimation in eukaryotic cells', *Nat Methods*, vol. 11, no. 3, pp. 319–324, Mar. 2014, doi: 10.1038/nmeth.2834.

[109] S. Tyanova *et al.*, 'The Perseus computational platform for comprehensive analysis of (prote)omics data', *Nat Methods*, vol. 13, no. 9, pp. 731–740, Sep. 2016, doi: 10.1038/nmeth.3901.

[110] E. V. Polishchuk and R. S. Polishchuk, 'Pre-embedding labeling for subcellular detection of molecules with electron microscopy', *Tissue and Cell*, vol. 57, pp. 103–110, Apr. 2019, doi: 10.1016/j.tice.2018.11.002.

[111] J. D. Garcia *et al.*, 'Differential roles of NaV1.2 and NaV1.6 in neocortical pyramidal cell excitability', *Elife*, vol. 14, p. RP105696, Jul. 2025, doi: 10.7554/eLife.105696.

[112] P. Vitale *et al.*, 'Different responses of mice and rats hippocampus CA1 pyramidal neurons to in vitro and in vivo-like inputs', *Front. Cell. Neurosci.*, vol. 17, Dec. 2023, doi: 10.3389/fncel.2023.1281932.

[113] R. Migliore *et al.*, 'The physiological variability of channel density in hippocampal CA1 pyramidal cells and interneurons explored using a unified data-driven modeling workflow', *PLoS Comput Biol*, vol. 14, no. 9, p. e1006423, Sep. 2018, doi: 10.1371/journal.pcbi.1006423.

[114] 'NEURON | empirically-based simulations of neurons and networks of neurons'. Accessed: Jan. 23, 2026. [Online]. Available: https://neuron.yale.edu/neuron/

[115] 'The NEURON Simulation Environment | Neural Computation | MIT Press'. Accessed: Jan. 23, 2026. [Online]. Available: https://direct.mit.edu/neco/article-abstract/9/6/1179/6087/The-NEURON-Simulation-Environment?redirectedFrom=fulltext

[116] A. Corradi *et al.*, 'Functional Characterization of a De Novo SCN2A Mixed Variant Linked to Early Infantile Developmental and Epileptic Encephalopathy', *Neurology Genetics*, vol. 12, no. 1, p. e200344, Feb. 2026, doi: 10.1212/NXG.0000000000200344.

[117] L. Liang *et al.*, 'Developmental dynamics of voltage-gated sodium channel isoform expression in the human and mouse brain', *Genome Med*, vol. 13, no. 1, p. 135, Aug. 2021, doi: 10.1186/s13073-021-00949-0.

[118] P. Miao *et al.*, 'Electrophysiological features: The next precise step for SCN2A developmental epileptic encephalopathy', *Molecular Genetics & Genomic Medicine*, vol. 8, no. 7, p. e1250, 2020, doi: 10.1002/mgg3.1250.

[119] C. Lossin, X. Shi, M. A. Rogawski, and S. Hirose, 'Compromised function in the Nav1.2 Dravet syndrome mutation R1312T', *Neurobiology of Disease*, vol. 47, no. 3, pp. 378–384, Sep. 2012, doi: 10.1016/j.nbd.2012.05.017.

[120] J. Clatot *et al.*, 'Rare dysfunctional SCN2A variants are associated with malformation of cortical development', *Epilepsia*, vol. 66, no. 3, pp. 914–928, Mar. 2025, doi: 10.1111/epi.18234.

[121] A. L. Goldin, 'Mechanisms of sodium channel inactivation', *Current Opinion in Neurobiology*, vol. 13, no. 3, pp. 284–290, Jun. 2003, doi: 10.1016/S0959-4388(03)00065-5.

[122] W. Ulbricht, 'Sodium channel inactivation: molecular determinants and modulation', *Physiol Rev*, vol. 85, no. 4, pp. 1271–1301, Oct. 2005, doi: 10.1152/physrev.00024.2004.

[123] S. Lauxmann *et al.*, 'Relationship of electrophysiological dysfunction and clinical severity in SCN2A-related epilepsies', *Hum Mutat*, vol. 39, no. 12, pp. 1942–1956, Dec. 2018, doi: 10.1002/humu.23619.

[124] G. Balagura *et al.*, 'Clinical spectrum and genotype-phenotype correlations in PRRT2 Italian patients', *European Journal of Paediatric Neurology*, vol. 28, pp. 193–197, Sep. 2020, doi: 10.1016/j.ejpn.2020.06.005.

[125] H.-F. Li *et al.*, 'Associations between neuroanatomical abnormality and motor symptoms in paroxysmal kinesigenic dyskinesia', *Parkinsonism & Related Disorders*, vol. 62, pp. 134–140, May 2019, doi: 10.1016/j.parkreldis.2018.12.029.

[126] J. Fang, S. Wang, G. Zhao, and L. Cao, 'Novel mutation of the PRRT2 gene in two cases of paroxysmal kinesigenic dyskinesia: Two case reports', *Biomedical Reports*, vol. 12, no. 6, pp. 309–312, Jun. 2020, doi: 10.3892/br.2020.1293.

[127] J. G. Lu *et al.*, 'A novel PRRT2 pathogenic variant in a family with paroxysmal kinesigenic dyskinesia and benign familial infantile seizures', *Cold Spring Harb Mol Case Stud*, vol. 4, no. 1, p. a002287, Jan. 2018, doi: 10.1101/mcs.a002287.

[128] Y. Pan *et al.*, 'PRRT2 frameshift mutation reduces its mRNA stability resulting loss of function in paroxysmal kinesigenic dyskinesia', *Biochemical and Biophysical Research Communications*, vol. 522, no. 3, pp. 553–559, Feb. 2020, doi: 10.1016/j.bbrc.2019.11.025.

[129] L. Wu *et al.*, 'PRRT2 truncated mutations lead to nonsense-mediated mRNA decay in Paroxysmal Kinesigenic Dyskinesia', *Parkinsonism & Related Disorders*, vol. 20, no. 12, pp. 1399–1404, Dec. 2014, doi: 10.1016/j.parkreldis.2014.10.012.

[130] M. P. Forrest *et al.*, 'Rescue of neuropsychiatric phenotypes in a mouse model of 16p11.2 duplication syndrome by genetic correction of an epilepsy network hub', *Nat Commun*, vol. 14, no. 1, Art. no. 1, Feb. 2023, doi: 10.1038/s41467-023-36087-x.

[131] H. Lerche, 'Synaptic or ion channel modifier? PRRT2 is a chameleon-like regulator of neuronal excitability', *Brain*, vol. 141, no. 4, pp. 938–941, Apr. 2018, doi: 10.1093/brain/awy073.

[132] F. P. McCready, S. Gordillo-Sampedro, K. Pradeepan, J. Martinez-Trujillo, and J. Ellis, 'Multielectrode Arrays for Functional Phenotyping of Neurons from Induced Pluripotent Stem Cell Models of Neurodevelopmental Disorders', *Biology (Basel)*, vol. 11, no. 2, p. 316, Feb. 2022, doi: 10.3390/biology11020316.

[133] M. Servetti *et al.*, 'Optimization of Transcription Factor-Driven Neuronal Differentiation from Human Induced Pluripotent Stem Cells for Disease Modelling and Drug Screening', *Stem Cell Rev Rep*, vol. 21, no. 3, pp. 816–833, Apr. 2025, doi: 10.1007/s12015-025-10845-4.

[134] M. Frega *et al.*, 'Rapid Neuronal Differentiation of Induced Pluripotent Stem Cells for Measuring Network Activity on Micro-electrode Arrays', *J Vis Exp*, no. 119, p. 54900, Jan. 2017, doi: 10.3791/54900.

[135] M. S. Almén, N. Bringeland, R. Fredriksson, and H. B. Schiöth, 'The Dispanins: A Novel Gene Family of Ancient Origin That Contains 14 Human Members', *PLOS ONE*, vol. 7, no. 2, p. e31961, Feb. 2012, doi: 10.1371/journal.pone.0031961.

[136] J. R. Deuis, T. Klasfauseweh, L. Walker, and I. Vetter, 'The "dispanins" and related proteins in physiology and neurological disease', *Trends in Neurosciences*, Jul. 2024, doi: 10.1016/j.tins.2024.06.004.

[137] S. Matricardi *et al.*, 'Gain of function SCN1A disease-causing variants: Expanding the phenotypic spectrum and functional studies guiding the choice of effective antiseizure medication', *Epilepsia*, vol. 64, no. 5, pp. 1331–1347, May 2023, doi: 10.1111/epi.17509.

Appendix

Publications

- Missense variants in the membrane domain of PRRT2 affect its interaction with Nav1.2 voltage-gated sodium channels
  Sterlini B*, Franchi F*, **Morinelli L***, Corradi B, Parodi C, Albini M, Bianchi A, Marte A, Baldelli P, Alberini G, Maragliano L, Valente P, Benfenati F, Corradi A.
  Neurobiol Dis. 2023 Jul;183:106177. doi: 10.1016/j.nbd.2023.106177 – * co-first author
- Unraveling the Membrane Topology of TMEM151A: A Step Towards Understanding its Cellular Role
  Morinelli L*, Corradi B*, Arnaldi P, Cortese K, Muià M, Zara F, Maragliano L, Sterlini B, Corradi A.
  J Mol Biol. 2024 Dec 1;436(23):168834. doi: 10.1016/j.jmb. 2024.168834. - * co-first author [85]
- Optimization of Transcription Factor-Driven Neuronal Differentiation from Human Induced Pluripotent Stem Cells for Disease Modelling and Drug Screening
  Servetti M, Caramia M, Parodi G, Loiacono F, Nano E, Biddau G, Ferrando L, **Morinelli L**, Valente P, Martinoia S, Escelsior A, Serafini G, Tamburro S, Baldassari S, Fassio A, Benfenati F, Corradi A, Sterlini B.
  Stem cell Reviews and Reports 2025 Apr;21(3):816-833. doi: 10.1007/s12015-025-10845-4 [133]
- Functional Characterization of a de novo SCN2A Mixed Variant Linked to Early Infantile Developmental and Epileptic Encephalopathy
  Corradi A §,*, Riva A §, Sterlini B §, **Morinelli L**, Ludovico A, Madia F, Striano P, Albini M, Vitale P, Pusch M, Lombardo G, Elia M, Chatron N, Lesca G, Zara Z, Falsaperla R °, Ferrera L °,*
  Neurology: Genetics 2026 Feb 2; 12(1):e200344.
  doi:10.1212/NXG.0000000000200344 - § co-first author; * co-corresponding authors - ° co-last author [116]
- Hints about TMEM151A function through the analysis of its pathogenic variants
  Morinelli L*, Muià M*, Ferrera L, Zara F, Sterlini B, Corradi A
  In preparation - * co-first author

Congresses

- Italian Society of Neuroscience - SINS 2023 conference – Turin (Italy)
  Poster presentation
- Italian Society of Physiology – Young Researchers in Physiology (YRP) conference 2023 - Bertinoro (Italy)
  Oral presentation
- European Federation of Neuroscience – FENS Forum 2024 – Wien (Austria)
  Poster presentation
- Italian Society of Physiology - SIF congress 2024 – Rome (Italy)
  Poster presentation
- Telethon Foundation Convention 2025 – Rimini (Italy)
  Poster presentation
- Neurogenomics conference – Human Technopole 2025 – Milan (Italy)
  Poster presentation